

NN08201, 1919

## Imaging Spectrometry and the Ronda peridotites

Online copy

20 APR. 1995

UB-CANDEX

CENTRALE LANDBOUWCATALOGUS



0000 0611 8968

907962 40951

Promotor: dr. S.B. Kroonenberg  
hoogleraar in de Geologie en Mineralogie

Co-promotor: dr. A.G. Fabbri  
hoogleraar in de Geologie, ITC, Enschede

ANNO 8701, 1919

**Freek Dirk van der Meer**

**Imaging Spectrometry and the Ronda peridotites**

**Proefschrift**

ter verkrijging van de graad van doctor  
in de landbouw- en milieuwetenschappen  
op gezag van de rector magnificus,  
dr. C.M. Karssen,  
in het openbaar te verdedigen  
op vrijdag 28 april 1995  
des namiddags te vier uur in de Aula  
van de Landbouwniversiteit te Wageningen

ISBN: 90-7962.

BIBLIOTHEEK  
LANDBOUWUNIVERSITEIT  
WAGENINGEN

CIP-GEGEVENS KONINKLIJKE BIBLIOTHEEK, DEN HAAG

Van der Meer, F.D.

Imaging spectrometry and the Ronda peridotites / F.D.

van der Meer. - [S.l. : s.n.]. - Ill.

Thesis Wageningen. - With ref. - With summary in Dutch.

ISBN 90-5485-385-9

Subject headings: remote sensing / geology

Printed in the Netherlands by Grafisch Service Centrum van de  
Landbouwwuniversiteit Wageningen



## STELLINGEN

1. De hoge spectrale resolutie van „imaging spectrometer” systemen biedt de mogelijkheid om gesteenten en mineralen vanuit de lucht te identificeren en te kaarteren.  
*Dit proefschrift*
2. De positie van de carbonaat-absorptieband in mengsels van synthetische calciet en dolomiet is afhankelijk van het percentage calciet.  
*Dit proefschrift*
3. De graad van serpentinisatie van peridotieten kan worden geschat aan de hand van de diepte van de 2.3 $\mu$ m absorptieband voor sterk geserpentiniseerde monsters.  
*Dit proefschrift*
4. De doeltreffendheid van atmosferische calibratietechnieken is verschillend per data set en afhankelijk van de spectrale signatuur van de voorkomende terreineenheden.  
*Dit proefschrift*
5. Beeldclassificatie door middel van geostatistische schattingsmethoden valt te verkiezen boven de huidige classificatiemethoden omdat deze gebruik maakt van spatiële en spectrale karakteristieken van de training data.  
*Dit proefschrift*
6. Wanneer bij beeldclassificatie spectrale banden worden gebruikt die buiten het golflengtebereik van het absorptiefenomeen liggen, neemt de betrouwbaarheid van de classificatie af.  
*Dit proefschrift*
7. Mineraalkaartering vanuit GERIS beelden bevestigt de zonering van het Ronda peridotietmassief in een granaat-, een spinel- en een plagioklaasfacies.  
*Dit proefschrift*
8. Prijsstijgingen in het openbaar vervoer staan haaks op het milieubeleid gericht op de terugdringing van het autogebruik.
9. Het gebruik van lease auto's door particulieren dient te worden ontmoedigd.
10. De duif verliest zijn geloofwaardigheid als symbool van de vrede door de mus uit de binnenstad te verdrijven.
11. De snelheid waarmee reorganisaties elkaar binnen een bedrijf opvolgen is een graadmeter voor de kwaliteit van het management.
12. De „grazende Nederlander” is de melkkoe van de fastfood industrie.

13. Naarmate de tendens om op oudere leeftijd kinderen te krijgen doorzet, zal het grootouderschap een unicum worden.

14. De bezuinigingen op de openbare groenvoorziening slaan toe in de vorm van wilde clematis en klimop.

Stellingen behorende bij het proefschrift „Imaging spectrometry and the Ronda peridotites”  
van Freek van der Meer.

Wageningen, 28 april 1995.

*Aan mijn vader*

## **Contents**

Samenvatting (Summary in Dutch).....	11
<i>Chapter 1</i>	
Introduction.....	15
1.1 Introduction.....	15
1.2 Rationale for this study.....	17
1.3 General Geology of the Betic Cordilleras.....	18
1.4 Outline of this thesis.....	21
<i>Chapter 2</i>	
Triassic-Miocene paleogeography and basin evolution of the Subbetic Zone between Ronda and Málaga.....	25
2.1 Introduction.....	26
2.2 Outline of the stratigraphy of the Ronda-Málaga region.....	26
2.2.1 Triassic.....	26
2.2.2 Jurassic.....	30
2.2.3 Cretaceous.....	31
2.2.4 Paleocene-Miocene.....	32
2.3 Triassic-Late Miocene paleogeographic reconstructions.....	36
2.3.1 Pre-Miocene.....	36
2.3.2 Late Oligocene and Miocene.....	37
2.4 Quantitative subsidence analysis and its implications for geodynamics.....	41
2.4.1 Interpretation of the subsidence record.....	44
2.5 Conclusions.....	48
<i>Chapter 3</i>	
A review of the tectonic evolution of the Ronda peridotite massif.....	51
3.1 Introduction.....	52
3.2 Regional geologic setting.....	52
3.3 A review of field and microstructures.....	54
3.3.1 The Sierra Alpujata.....	56
3.3.2 The Sierra Bermeja.....	56
3.4 New paleostress data.....	61
3.4.1 Theory.....	61
3.4.2 Results and interpretation.....	62
3.5 Discussion and conclusions.....	68

- Contents -

*Chapter 4*

Spectral reflectance of carbonate mineral mixtures and bidirectional reflectance theory.....	73
4.1 Introduction.....	74
4.2 Bidirectional reflectance theory.....	75
4.3 Reflectance spectra of carbonate minerals and rocks.....	77
4.3.1 Laboratory methods.....	77
4.3.2 Controls of carbonate absorption band positions.....	79
4.3.3 Effects of particle size.....	80
4.3.4 Effects of sorting.....	80
4.3.5 Calcite-dolomite mixtures.....	82
4.3.6 Effects of impurities.....	86
4.4 Reflectance spectra of rock samples.....	95
4.5 Conclusions.....	98

*Chapter 5*

Spectral reflectance of ultramafic rocks and the effect of serpentinization.....	101
5.1 Introduction.....	102
5.2 Reflectance spectra of ultramafic rocks.....	104
5.2.1 Laboratory method.....	104
5.2.2 Mineral spectra.....	104
5.2.3 Rock spectra.....	107
5.3 Effect of serpentinization on reflectance spectra.....	111
5.3.1 Theory.....	111
5.3.2 Reflectance spectra of serpentinites.....	112
5.4 Conclusions.....	115

*Chapter 6*

Reflectance spectra of weathered rock samples, soil, vegetation and field reflectance spectra.....	117
6.1 Introduction.....	118
6.2 Reflectance characteristics of weathered rock samples.....	118
6.2.1 Carbonates.....	118
6.2.2 Ultramafics.....	122
6.3 Soil reflectance characteristics.....	123
6.4 Vegetation reflectance spectra.....	130
6.5 Reflectance spectra characterizing the peridotite-metamorphics contact.....	133
6.5.1 The Ronda-San Pedro contact.....	133
6.5.2 The Guaitara section.....	136
6.5.3 The Jubrique section.....	139
6.6 Relation between laboratory, field and image spectra: a Case Study from the Los Pedroches batholith.....	141
6.6.1 Chemical composition of soils.....	143
6.6.2 Spectra of minerals contributing to soil reflectance.....	145
6.6.3 Spectra of soil samples.....	147
6.6.4 Image processing and analysis.....	150
6.7 Conclusions.....	156

- Contents -

*Chapter 7*

Preprocessing of imaging spectrometer data and atmospheric calibration.....	159
7.1 Introduction.....	160
7.2 Imaging spectrometer systems.....	160
7.2.1 The Airborne Visible/Infrared Imaging Spectrometer (AVIRIS).....	160
7.2.2 Geophysical Environmental Research Imaging Spectrometer (GERIS).....	163
7.2.3 Imaging spectrometer data sets used.....	165
7.3 Estimation of signal-to-noise ratio.....	167
7.3.1 The "local means and local variances method".....	168
7.3.2 The "geostatistical method".....	169
7.3.3 Results.....	170
7.4 Wavelength calibration.....	179
7.5 Atmospheric calibration techniques.....	179
7.5.1 The Flat-field correction.....	180
7.5.2 The Log-residual and Flat-field log-residual method.....	180
7.5.3 The Empirical Line method.....	181
7.5.4 The Internal Average Relative Reflectance (IARR) atmospheric correction technique.....	183
7.5.5 The Atmospheric Removal Method (ATREM).....	183
7.5.6 Performance of atmospheric calibration techniques.....	185
7.5.7 Comparison of the AVIRIS Cuprite Mining district data set and the GERIS data set from southern Spain.....	193
7.6 Conclusions.....	194

*Chapter 8*

Mineral mapping and automatic feature extraction from imaging spectrometer data.....	197
8.1 Introduction.....	198
8.2 Existing techniques for mineral mapping from imaging spectrometer data....	198
8.2.1 Comparison of pixel and laboratory spectra.....	198
8.2.2 Colour-composite images.....	200
8.2.3 Colour-coded stacked spectra.....	201
8.2.4 Binary encoding.....	202
8.2.5 Waveform characterization.....	203
8.2.6 Spectral Angle Mapping (SAM).....	204
8.2.7 Spectra Unmixing.....	206
8.3 A new indicator kriging classification method for mineral mapping.....	207
8.3.1 Conventional classification techniques in the hyperspectral space....	208
8.3.2 The indicator kriging classifier.....	210
8.3.3 Statistical zonation techniques for automatic detection of absorption features.....	215
8.3.4 Results.....	218
8.4 Conclusions.....	227
Appendix 1: Ordinary kriging of points and blocks.....	228
Appendix 2: Support correction.....	232

- Contents -

<i>Chapter 9</i>	
Imaging spectrometry and the Ronda peridotites.....	237
9.1 Introduction.....	238
9.2 Mineral mapping and the Ronda peridotites.....	239
9.2.1 Spectral unmixing.....	239
9.2.2 Mineral mapping.....	240
9.3 Case Study 1: Calcite-dolomite mineral mapping.....	246
9.3.1 GERIS data preparation.....	248
9.3.2 Estimating calcite-dolomite abundances using indicator kriging.....	249
9.3.3 Simulating calcite-dolomite abundances using conditional simulation.....	252
9.3.4 Results.....	255
9.4 Case Study 2: Mapping the degree of serpentinization.....	264
9.4.1 Data preparation.....	265
9.4.2 Sequential Gaussian Conditional Simulation (SGCS).....	266
9.4.3 Results.....	268
9.5 Conclusions.....	272
Appendix 1: Sequential Conditional Simulation.....	274
References.....	275
Acknowledgements.....	303
Bibliography.....	305
Curriculum Vitae.....	309
Plates.....	313

## ***Samenvatting (Summary in Dutch)***

Conventionele satelliet gegevens, zoals verkregen door Landsat Thematic Mapper en SPOT, hebben een spectrale resolutie in de orde van 100 tot 200 nanometers waardoor een groot deel van de informatie belangrijk voor het herkennen van mineralen (met absorptie banden in de orde van 20 tot 40 nanometers breed) in remote sensing data verloren gaat. Derhalve werden hoge spectrale resolutie sensoren ontwikkeld waarmee laboratoriumachtige spectra kunnen worden gemeten voor elk pixel. Zo ontstond de „imaging spectrometry”; een nieuwe discipline binnen de remote sensing. „Imaging spectrometry” is het verkrijgen van beeldgegevens in vele nauwe aaneensluitende spectrale banden over het 0.4µm tot 2.5µm golflengte bereik met als doel de optimale spectrale karakterisering van pixel spectra om zo mineralen en gesteenten te kaarteren vanuit vliegtuig of satelliet opnames. Toepassingen van „imaging spectrometers” gemonteerd op vliegtuigen hebben succes opgeleverd in woestijn gebieden. Relatief weinig onderzoek is gedaan naar de vertaling van deze resultaten in gedeeltelijk begroeide gebieden die een meer realistische omgeving vormen voor geologische prospectie. Dit vereist een andere aanpak waarbij nieuwe analyse methoden dienen te worden ontwikkeld. Met het oog op de toekomst, waarin verscheidene organisaties satellieten met een hoog spectraal scheidend vermogen zullen lanceren (zoals NASA te weten de HIRIS en de ASTER, en ESA te weten de MERIS en de HRIS), is veel vooronderzoek nodig. In deze dissertatie is het nut onderzocht van „imaging spectrometry” voor geologische kaartering en toepassingen binnen de olie en mineraal exploratie. Daarbij is gebruik gemaakt van AVIRIS data van het Cuprite Mining District (een NASA test gebied in de woestijn van Nevada waarvan veel gegevens beschikbaar zijn) en GERIS data uit Zuid-Spanje (hetgeen het Ronda peridotiet massief en aangrenzende carbonaat gesteenten beslaat). Een succesvolle toepassing van „imaging spectrometry” voor geologisch onderzoek vereist: een basiskennis van de geologie van het te bestuderen gebied, kennis van de spectrale eigenschappen van de te onderzoeken gesteenten, een gedegen kalibratie van de „ruwe” remote sensing data en een analyse methode die geschikt is voor beeldanalyse onder specifieke klimatologische omstandigheden. Deze aspecten komen aan de orde in deze dissertatie.



- Samenvatting -

Het gebied tussen Ronda en Málaga is onderzocht middels stratigrafische kaartering. Uit deze kaartering resulteren tijd-facies profielen die ten grondslag liggen aan een paleogeografische reconstructie. Deze reconstructie en de resultaten van kwantitatieve dalingsmodellen geven inzicht in de wordingsgeschiedenis van het Ronda-Málaga gebied. De zo gereconstrueerde deformatiegeschiedenis wordt getoetst aan bestaande geodynamische modellen voor de evolutie van het Westelijk Mediterraan gebied. Het peridotiet massief van Ronda is reeds jaren intensief onderzocht door menig onderzoeker. Een compilatie van de huidige kennis is gegeven in Hoofdstuk 3. Nieuwe paleostress analyses leveren een drietal dominante spanningsvelden op gerelateerd aan de plaatsing van de peridotieten in de continentale korst. In combinatie met de dalingsanalyse beschreven in Hoofdstuk 2 kan worden geconcludeerd dat laat orogene horizontaal bewegingen een belangrijke rol spelen in de tektonische evolutie van het Ronda peridotiet massief.

Laboratorium spectrale analyse (met een Beckman UV 5240 spectrometer) van verse gesteentemonsters afkomstig uit het onderzoeksgebied in Zuid-Spanje richt zich met name op carbonaat gesteenten en ultramafische gesteenten. Electronische- en trillingsprocessen in kristalroosters en onzuiverheden van mineralen bepalen in belangrijke mate de positie en vorm van spectrale absorptie fenomenen in carbonaat spectra. De rol van onzuiverheden in mineraalroosters is onderzocht door middel van mengsels van diverse mineralen. Tevens is gebruik gemaakt van semi-empirische modellen voor de simulatie van reflectie karakteristieken van gesteenten op basis van de eigenschappen van de hoofdcomponenten. Systematische analyse van het mineraal mengsel van calciet en dolomiet wijst op een semi-lineaire relatie tussen de positie van de carbonaat absorptieband (tussen 2.3µm en 2.35µm) en de verhouding calciet/dolomiet van het monster.

Peridotieten zijn ultramafische gesteenten die voor meer dan 40% bestaan uit olivijn en voor de rest uit pyroxenen en accessorische bestanddelen. De spectrale eigenschappen van dit soort gesteenten worden gedomineerd door ijzer absorptiebanden afhankelijk van de mineralogie van het gesteente. In veel gevallen zijn peridotiet gesteenten geserpentiniseerd: een proces waarbij olivijn hydrothermaal omzet naar serpentijn-groep mineralen met magnetiet als bijproduct. Onderzoek verricht aan geserpentiniseerde peridotiet monsters (Hoofdstuk 5) wijst op een lineaire relatie tussen de OH<sup>-</sup> absorptieband-diepte en de graad van serpentinisatie. Magnetiet heeft de eigenschap om absorptiebanden te onderdrukken. Synthetische mineraal mengsels van olivijn en serpentijn met 5% magnetiet demonstreren eenzelfde lineair verband tussen de absorptieband-diepte en de graad van serpentinisatie voor monsters met een relatief hoge concentratie serpentijn. Laboratorium analyse van verweerde gesteentemonsters, vegetatie en veldreflectie metingen vormt de link tussen laboratorium onderzoek en remote sensing gegevens.

Om pixel spectra te kunnen vergelijken met laboratorium spectra dienen „ruwe”

- Samenvatting -

„imaging spectrometer” data te worden gekalibreert waarbij atmosferische invloeden worden weggenomen. In Hoofdstuk 7 wordt uitvoerig ingegaan op deze kalibratie. Een op niet-parametrische geostatistiek gebaseerde beeldanalyse methode, waarbij laboratorium en pixel spectra kwantitatief worden vergeleken om zodoende verschillende mineralen te kunnen kaarteren, wordt belicht in Hoofdstuk 8. In vergelijking tot conventionele beeldclassificatie methoden heeft de nieuwe aanpak het voordeel dat: geen veld spectrale gegevens noodzakelijk zijn, dat spectrale zowel als spatiële informatie wordt gebruikt ter karakterisering van een mineraal component, dat geen statistische normaal-verdeling van de oorspronkelijke data noodzakelijk is en dat resultaten kunnen worden geëxtrapoleerd naar subpixel schaal. Een kritische analyse van classificatie betrouwbaarheden leert dat de optimale hoeveelheid spectrale banden in een classificatie afhankelijk is van de breedte van een te onderzoeken absorptie fenomeen. Wanneer bij de classificatie spectrale banden worden gebruikt die buiten het golflengte bereik van het absorptie fenomeen liggen, zal de classificatie betrouwbaarheid afnemen.

In Hoofdstuk 9 worden de resultaten van geologische mineraal kaartering met behulp van de GERIS data set uit Zuid-Spanje beschreven. De geëxtrapoleerde mineralen bevestigen de bekende metamorfe zonerings van het Ronda peridotiet massief in een granaat, spinel en plagioklaas facies. Verscheidene metamorfe mineralen in marmers alsmede verschillende serpentijn fasen in de peridotieten wijzen op een late fase van breuk deformatie. Een methode voor de analyse van „imaging spectrometer” gegevens in begroeide gebieden gericht op mineraal en olie exploratie is getest (Hoofdstuk 9). Deze methode berust op de volgende stappen: (1) vegetatie maskering, (2) berekening van de absorptieband-diepte uit GERIS gegevens met behulp van de „convex Hull” transformatie, (3) vertaling van deze waarde in een percentage dat de fractie van een bepaald mineraal weergeeft en (4) schatting van de percentages van verschillende mineraal voorkomens voor pixels met vegetatie door middel van geostatistische simulatie modellen. Een eerste case-study gaat in op de kaartering van dolomitatiepatronen middels het empirische model gepresenteerd in Hoofdstuk 4. Deze dolomitatiepatronen zijn van belang voor olie exploratie omdat dolomitatie van carbonaat gesteenten de porositeit van zulke gesteenten verhoogd met 12%. Daardoor zijn dolomieten vaak geschikte olie reservoir gesteenten. In een tweede case-study worden serpentinitatiepatronen in peridotiet gesteenten geanalyseerd door gebruik te maken van het model ontworpen in Hoofdstuk 5 en de vertaling hiervan naar GERIS beelden. Serpentinisatie leidt tot voorkomens van het mineral chrysotiel hetgeen de grondstof is voor 90% van de asbest in de wereld. Beide studies wijzen op het belang van „imaging spectrometry” voor geologische prospectie.

# CHAPTER 1:

## *Introduction*

### 1.1 INTRODUCTION

Remote sensing of the earth's surface from aircraft and from spacecraft provides information not easily acquired by surface observations. Until recently, the main limitations of remote sensing were that no subsurface information could be obtained and that surface information lacked detail due to the broad bandwidth of scanners available. It has been shown that orbital imaging radar can provide subsurface data in arid regions (McCauley *et al.*, 1982), and work on high-spectral resolution radiometry has shown that earth surface mineralogy can be identified using spectral information from scanner data (Goetz *et al.*, 1982). Conventional scanners (e.g. Landsat MSS and TM, and SPOT) acquire information in a few separate spectral bands of various widths (typically in the order of 100-200nm), thus filtering to a large extent the reflectance characteristics of the surface (Goetz & Rowan, 1981). Most terrestrial materials are characterized by spectral absorption features typically 20-40nm in width (Hunt, 1980). New scanner types were developed which acquire data in many small contiguous wavelengths bands, allowing laboratory-like reflectance spectra to be produced for each pixel in the image. The field of imaging spectrometry, dealing with "the acquisition of image data in many contiguous spectral bands (Goetz, 1991)", is concerned with analyzing such scanner data (Fig. 1.1).

The first airborne spectrometer data were collected in 1981 using a one-dimensional profile spectrometer developed by the Geophysical Environmental Research Company which acquired data in 576 channels covering the 0.4-2.5 $\mu$ m wavelength range (Chiu & Collins, 1978). The first imaging device was the Airborne Imaging Spectrometer (AIS), developed at the NASA Jet Propulsion Laboratory which was operational from 1983 onward. This instrument acquired data in 128 spectral bands in the range of 1.2-2.4 $\mu$ m. with a field-of-view of 3.7 degrees resulting in images of 32 pixels width (Vane & Goetz, 1985). A later version of the instrument, AIS-2, covered the 0.8-2.4 $\mu$ m region acquiring images 64 pixels wide (LaBaw, 1987). In 1989 NASA began data acquisition with an improved version of AIS

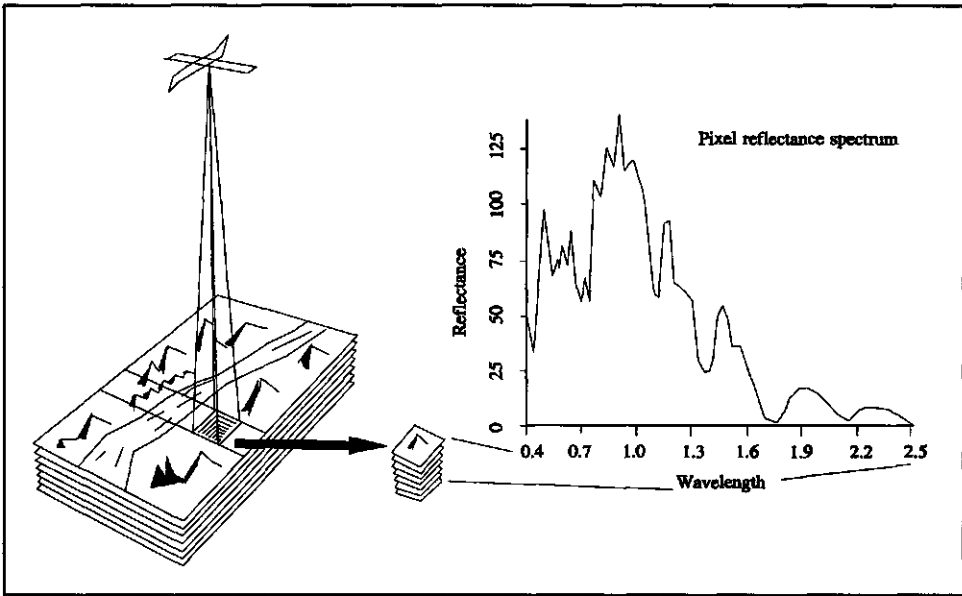


Fig. 1.1: Schematic representation of imaging spectrometry with the AVIRIS scanner. Data are collected in 224 contiguous spectral bands of 10nm bandwidth for each pixel in the scene. Each pixel has an continuous spectrum over the 0.4-2.5 $\mu$ m wavelength range which can be used to identify surface materials by comparison with laboratory spectra (after: Porter & Enmark, 1987).

called the Airborne Visible/Infrared Imaging Spectrometer (AVIRIS; Vane *et al.*, 1993). While AIS was a proof-of-concept engineering test bed, AVIRIS was proposed as a facility that would routinely supply well-calibrated data for many different purposes. The AVIRIS scanner makes possible the simultaneous collection of images in 224 contiguous bands resulting in a complete reflectance spectrum for each 20\*20 m. pixel in the 0.4 to 2.5 $\mu$ m region with a sampling interval of 10nm. (Goetz *et al.*, 1985; Vane & Goetz, 1988; 1993). The field-of-view of the AVIRIS scanner is 30 degrees resulting in a ground field-of-view of 10.5km. The signal-to-noise ratio is 100:1 at 0.7 $\mu$ m and 50:1 at 2.2 $\mu$ m. Several other imaging spectrometers systems have been developed during the last years specifically designed for particular problems rather than being suitable for a wide range of studies. Data from the Geophysical Environmental Research Imaging Spectrometer (GERIS), an imaging spectrometer system designed for geologic remote sensing, covering a strip over the Ronda peridotites and adjacent metamorphic terrains in southern Spain is used throughout this study. Furthermore, AVIRIS data from the Cuprite Mining District in Nevada, USA, is used.

A number of orbital imaging spectrometer missions are planned or being prepared

currently. HIRIS, the High Resolution Imaging Spectrometer (Goetz & Herring, 1989; Kerekes & Landgrebe, 1991) is designed to acquire images in 192 spectral bands simultaneously in the 0.4-2.5 $\mu$ m wavelength region with a ground resolution of 30m. and a swath width of 30km. This scanner has a spectral resolution of 9.4nm in the 0.4-1.0 $\mu$ m wavelength region and a 11.7nm spectral resolution in the 1.0-2.5 $\mu$ m wavelength range. The Advanced Spaceborne Thermal Emission and Reflectance Radiometer (ASTER; Kahle *et al.*, 1991) is a high spectral resolution imaging spectrometer planned for the first (A) platform of NASA's Earth Observing System (EOS-A). The instrument is designed with three bands in the visible and near-infrared spectral range with a 15m resolution, six bands in the short wave infrared with a 30m spatial resolution, and five bands in the Thermal infrared with a 90m resolution. The VNIR and SWIR bands have a spectral resolution in the order of 10nm. Simultaneously, a single band in the near-infrared will be provided for stereo capability. The swath width of an image will be 60km with 136km crosstrack and a temporal resolution of 16 days. The European Space Agency and a number of other agencies are developing two spaceborne imaging spectrometers (Rast, 1992): The Medium Resolution Imaging Spectrometer (MERIS) and the High Resolution Imaging Spectrometer (HRIS). MERIS, currently planned for the first Polar Platform to be launched in 1997, is designed mainly for oceanographic application and covers the 0.4-1.05 $\mu$ m wavelength region with 1.25nm bands at a spatial resolution of 250m or 1000m. HRIS, currently planned for the second Polar Platform to be launched around the year 2000, is a spectrometer similar to HIRIS which will cover the 0.4-2.4 $\mu$ m wavelength range with a 10nm contiguous sampling interval at a 32m ground resolution.

## 1.2 RATIONALE FOR THIS STUDY

Reflectance spectra of minerals, mineral mixtures, and rocks are studied to obtain detailed compositional information of the earth's surface, which can be related to spectral reflectance characteristics observed in remotely sensed imagery (e.g. Crowley, 1993). Similarly, it has been shown that spectral reflectance in visible and near-infrared offers a rapid and inexpensive technique for determining the mineralogy of samples and obtaining information on minor element chemistry (Gaffey, 1986). High-spectral resolution scanners, as for example AVIRIS and GERIS, acquire remotely sensed data in many contiguous spectral bands allowing direct identification of surface mineralogy by comparing pixel spectra and laboratory spectra. With the advent of such detailed remotely sensed imagery, the need exists to investigate reflectance spectra of minerals in detail to better understand the influence of mineralogy on their reflectance characteristics. Not only do we need to describe mineral

spectra but also spectra of mineral mixtures need to be evaluated leading to a characterization of rock spectra. Effects of impurities on these spectra may be of fundamental importance in establishing a link between pixel spectra from high-spectral resolution imagery and laboratory spectra of minerals and rocks. In order to establish this relation and use it in image processing, quantification of the spectral effects of impurities and mineral mixtures is needed. In practical usage of imaging spectrometer data, proper atmospheric calibration is important. The technique used for atmospheric correction is dependent on many factors related to climatic conditions, topography, availability of ground targets, etc of the study area (Carder *et al.*, 1993; Carrere & Conel, 1993; Frouin *et al.*, 1990) and on the presence and type of vegetation (Elvidge *et al.*, 1993).

Geological imaging spectrometry studies mainly focus on areas with little or no vegetation and small topographic variations (see Vane & Goetz, 1993 for a recent discussion). In this study, I have selected a moderately vegetated area which is representative of the kind of area usually studied by geologists. This yields a number of inherent problems described later in this thesis. With the advent of satellite imaging spectrometer systems in the near future, researchers should be prepared and aware of the possibilities and difficulties of hyperspectral remote sensing in vegetated areas. This thesis results from a project on imaging spectrometry, described in detail in Van der Meer (1994h), in which image processing strategies are being developed for multiband image analysis for geologic mapping purposes in the presence of vegetation. The approach followed relies largely on geostatistical techniques to simulate data at locations where spectral signature is obscured by dense vegetation. A number of image processing packages have been developed for the analysis of imaging spectrometry data sets including SPAM (Mazer *et al.*, 1988), GENESIS (Jansen, 1993), T-SPECTRA (Donoghue *et al.*, 1990). We have been using the Spectral Image Processing System (SIPS; Kruse *et al.*, 1993) using the Interactive Data Language software (IDL) running on a Hewlett Packard UNIX-based workstation under Motif window manager in 8-bit color mode. Although this package contains a number of image analysis tools suitable for mineral mapping, new processing techniques will be presented in this thesis specifically useful in vegetated terrains. Furthermore it will be demonstrated that imaging spectrometry can contribute to local geologic knowledge, in this study particularly to the metamorphic zonation of the Ronda peridotites and surrounding metamorphic sequences exposed in the Betic Cordilleras of southern Spain.

### **1.3 GENERAL GEOLOGY OF THE BETIC CORDILLERAS**

The Betic Cordilleras of southern Spain form the northern part of the Betic-Rif orogenic belt

and constitute the westernmost part of the Alpine-Mediterranean chain. Classically, the Betic Cordilleras are subdivided into a northern External Zone and a southern Internal or Betic Zone (Egeler & Simon, 1969; Torres-Roldán, 1979; Fig. 1.2). These zones are separated by flysch sediments of Early Cretaceous to Early Miocene age, which are restricted to the western Betic Cordilleras (Fontboté, 1984; Bouillin *et al.*, 1986).

The External Zone, in most tectonic models for the orogen, is regarded as the passive continental margin of the Iberian continent (Hermes, 1978; García-Hernandez *et al.*, 1980; De Smet, 1984; De Ruig, 1992). On the basis of paleogeographic criteria the External Zone is further subdivided into a Prebetic Zone in the north and a Subbetic Zone in the south separated by Intermediate Units. The Prebetic Zone represents the former shelf environment where shallow marine deposition prevails, whereas the deposits of the Subbetic Zone are characterized by a pelagic facies reflecting deeper marine environments (Fallot, 1948; De Smet, 1984). The Subbetic Zone may be subdivided into a northern and a southern Subbetic Zone mainly formed by calcareous Jurassic limestones, and a median Subbetic Zone formed by marly Jurassic limestones.

The Internal Zone consists of a stack of four nappe complexes composed of essentially metamorphic rocks of Triassic and older ages. These complexes are in descending order: (1) the Malaguide Complex, (2) the Alpujarride Complex, (3) the Mulhacen Complex, and (4) the Veleta Complex (Bakker *et al.*, 1989). The Mulhacen and Veleta Complexes formerly constituted the Nevado-Filabride Complex, but have been separated because they show a marked difference in metamorphic characteristics (De Jong, 1991). The Veleta Complex is characterized by conditions of metamorphism of relatively low pressure and temperature (Díaz de Federico *et al.*, 1979; De Jong, 1993), whereas the Mulhacen Complex shows an early phase of high-pressure-low-temperature metamorphism (Vissers, 1981; Bakker *et al.*, 1989). The Alpujarride Complex is characterized by high-pressure-low-temperature metamorphism, however, with generally lower maximum pressures as found in the Mulhacen Complex (Goffé *et al.*, 1989; Bakker *et al.*, 1989). The Malaguide Complex is nearly non-metamorphic (Egeler & Simon, 1969). The Dorsale Unit is regarded as the margin of the Malaguide Complex (Bouillin *et al.*, 1986). A fifth tectonic unit can be found in tectonic windows below the Alpujarride and Malaguide nappe complexes: the Almagrider Complex (Simon, 1987; De Jong, 1991). The Almagrider Complex consists of low-grade metamorphic red-beds, evaporites, and carbonates. Because of the similarity of the Triassic sediments found in the Almagrider Complex and the External Zone, the Almagrider Complex is presently regarded as the southernmost part of the External Zone (Simon, 1987).

The Internal Zone as a whole is often regarded as an allochthonous tectonic element (referred to as the Alboran Microplate; Andrieux *et al.*, 1971; Dercourt *et al.*, 1986), which finds its origin far to the northeast of its present position (LeBlanc & Olivier, 1984).

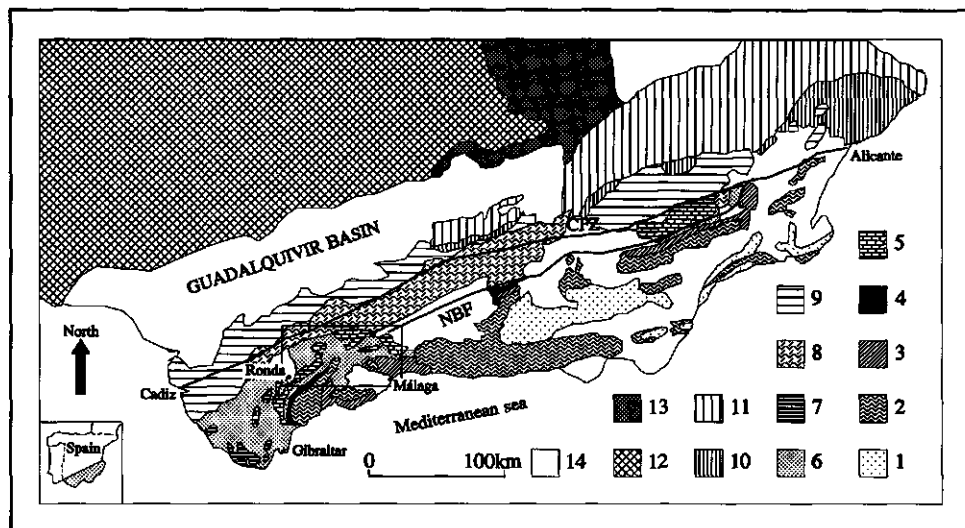


**Fig. 1.2:** Tectonic sketch map of the Betic Cordilleras (modified after Bakker *et al.*, 1989; Geel *et al.*, 1992). The area of investigation is outlined by the black box (Legend: 1-4 = Internal or Betic Zone; 1 = Veleta and Mulhacen Complex (Nevado-Filabride Complex), 2 = Alpujarride and Almagrde Complex, 3 = Malaguide Complexes, 4 = Dorsale Unit, 6-11 and part of unit 5 = External Zone; 5 = Penibetic and southern Subbetic Zone, 6 = 'flysch' units, 7 = parautochthonous External units, 8 = median Subbetic Zone, 9 = northern Subbetic Zone, 10 = Intermediate Units, 11 = Prebetic Zone, 12 = Hercynian Meseta (undifferentiated), 13 = Mesozoic cover of the Hercynian Meseta, 14 = Late Tertiary and Quarternary basins, NBF = North Betic Fault, CFZ = Crevillente Fault Zone).

Geel *et al.* (1992) argue that the Betic Zone and the Internal Zones of the African-Rif orogen formed part of an eo-Alpine orogenic belt which was the continuation of the Calabrian-Kabylian belt (Dercourt *et al.*, 1986). The Internal Zone was juxtaposed against the Iberian margin during a complex Miocene orogeny, causing the External Zone to develop into a fold-and-thrust belt (De Ruig, 1992; Geel *et al.*, 1992). In the western part of the Betic Cordilleras, the Subbetic thrust sheets border the Miocene Guadalquivir Basin, which is regarded as the foreland basin of the Betic Cordilleras (Vegas & Banda, 1982). In the eastern Betic Cordilleras, Miocene foreland-basin sediments are incorporated in the thrust sheets (De Ruig, 1992).



## 1.4 OUTLINE OF THIS THESIS

In Chapter 2, the results of detailed geologic mapping of sedimentary strata of the Subbeticum of Ronda are presented including a stratigraphic description of several sections near Ronda, El Burgo, Ardales, Teba, and Arriate in the Ronda-Málaga area. These are used to develop time-facies profiles on basis of which the paleogeography is reconstructed with emphasis on Miocene turning points. Timing of rift-related Mesozoic tectonic events, Early Miocene compressional tectonic events, and Late Miocene strike-slip tectonic events are derived from the result of a backstripping analysis using a synthetic composite stratigraphic section as input data. The final results are presented within the framework of Western Mediterranean plate tectonics yielding a number of deformation events characterizing the tectono-sedimentary evolution of the area.

A review of recent work on field and microstructures within the Ronda peridotite body is given in Chapter 3. Paleostress analysis of fault-slip data from the peridotites are discussed. These lead to three stress tensors: an extensional, a compressional, and a strike-slip related tensor. Similar work conducted on Cretaceous and Tertiary carbonates of the Subbeticum give identical stress tensors. For the carbonates, tectonic stylolites and extension veins allow to relatively date these stress tensors. This dating together with the timing of tectonic phases from the backstripping analysis is used to derive an alternative model for the emplacement of the Ronda peridotites.

Visible and near-infrared reflectance spectra of carbonate minerals, carbonate mineral mixtures, and un-weathered rock samples are discussed in Chapter 4. First, bidirectional reflectance theory is addressed forming the basis for a semi-empirical model to simulate reflectance of mineral mixtures from their single-component reflectance spectra. The following topics are discussed in the remainder of this Chapter: carbonate absorption band position, effects of particle size, effects of sorting, calcite-dolomite mixtures and the shifting 2.3 $\mu$ m absorption band, and the effects of impurities such as aqueous fluid inclusions, transition metal ions, organic matter. Finally, spectra of rock samples are discussed in relation to the mineral spectra.

Reflectance spectra of ultramafic rocks and minerals forming these rocks are discussed in Chapter 5. After a review of some earlier work, mineral spectra of olivines, orthopyroxenes, and clinopyroxenes are presented. Un-weathered rock spectra of several samples of dunites, ilmenites, harzburgites, and pyroxenites are discussed. The remainder of the Chapter is devoted to the effect of serpentinization on the reflectance spectra of ultramafic rocks. It is demonstrated that the degree of serpentinization can be quantified by using the depth of OH<sup>-</sup> features occurring near 1.4 $\mu$ m and 2.3 $\mu$ m and the brightness of a sample measured as the reflectivity at 1.6 $\mu$ m. From a study of synthetic mixtures of olivine,

serpentine, and magnetite prepared in the laboratory it is derived that the spectral quenching effect of magnetite affects the spectral properties of serpentines with 55 % serpentine minerals or less. Thus highly serpentinized areas can be mapped using the above mentioned characteristics regardless the amount of magnetite.

In Chapter 6, reflectance spectra of weathered peridotite and carbonate rock samples, soils, and vegetation, derived from the Ronda-Málaga area, are discussed. Part of this Chapter is based on a case study developed for the Los Pedroches batholith near Almadén (south-Central Spain). A total of 13 soil samples were taken over the contact aureole of the granitic intrusion and analyzed spectrally as well as chemically. The reflectance spectra of relevant minerals are discussed and subsequently the soil spectra. From these spectra, the change of albedo, Fe, AlOH absorption, H<sub>2</sub>O, and OH<sup>-</sup> absorption over the contact zone are quantified using the spectra. Field spectra using a TM simulator spectrometer are used to link the laboratory spectra and the TM image. Finally, image processing techniques using ratio images are used to map changes in iron content etc of soils over the area. This case study demonstrates the possibility of linking laboratory and pixel spectra when calibrating the data carefully using field spectrometry.

In Chapter 7, the preprocessing of the raw imaging spectrometer data is discussed. First, a technical description of the sensors used is given. These are the Airborne Visible and Infrared Imaging spectrometer (AVIRIS) and the GER imaging spectrometer. Next quantification of signal-to-noise ratios is discussed using two alternative methods. The main topic is the atmospheric calibration of imaging spectrometer data. Several methods are used: Flat-field calibration, Internal Average Reflectance method, Empirical line method, Log-residual method, and a atmospheric simulation model. The performance of these methods is compared using a number well-characterized standard field targets in the Cuprite mining district AVIRIS data set and the GERIS data set from southern Spain. Comparison of the results directly reflects the difference between atmospheric calibration in presence or absence of heavy vegetation.

If the imaging spectrometer data are properly calibrated, the next logical step would be to use the data to map surface mineralogy. Mineral mapping techniques are treated in Chapter 8. Some techniques have been proposed for this purpose which are not always very successful, many studies use conventional classification techniques. Specific imaging spectrometer techniques are introduced: inverse mixing modelling, spectral angle mapping, and band-depth analysis. The main body of the text deals with a new mineral mapping technique based on indicator kriging. This technique uses automatic zonation techniques to identify absorption features and non-parametric geostatistics to calculate the probability that a pixel belongs to a certain mineralogy. The performance of this technique is discussed in the framework of conventional image classification techniques.

*- Introduction -*

In last final Chapter 9, several techniques and methodologies discussed in previous Chapters are applied to the GER 63-channel imaging spectrometer data set flown over the Ronda peridotites and adjacent carbonates which was calibrated using techniques discussed in Chapter 7. Two Case Studies are presented to emphasize the use of imaging spectrometry for geologic mineral exploration purposes. The first Case Study deals with the problem of dolomitization which is an important parameter in oil exploration. Calcite-dolomite mixtures and dolomitization patterns are mapped using the semi-linear model for the position of the carbonate absorption band derived in Chapter 4. Conditional simulation techniques and indicator kriging are used to estimate the calcite content of pixels. The second Case Study addresses the degree of serpentinization in the peridotites; an indication for possible asbestos deposits. The approach is based on the theoretical results derived in Chapter 5. Results of mineral mapping using techniques discussed in Chapter 8, show that several minerals could be mapped using the GER data set which give information on metamorphic facies. These metamorphic minerals bear important conclusions on the conditions of metamorphism related to the emplacement of the peridotites discussed in Chapters 2 and 3.

## CHAPTER 2:

### *Triassic-Miocene paleogeography and basin evolution of the Subbetic Zone between Ronda and Málaga<sup>1</sup>*

#### ABSTRACT

During the Triassic, continental and supratidal environments prevailed in the north of the Ronda-Málaga region whereas intertidal and shallow marine environments characterize the south. From the Jurassic up to the Miocene, the Ronda-Málaga region was the scene of shallow marine environments in the north and open or deeper marine environments in the south. The Miocene reveals rapidly changing paleo-environments. During the Aquitanian a submarine fan system developed with clastic supply from an emerged area in the north. In the Burdigalian, deformation started to the south of the study area and depositional patterns completely reversed, now showing detritus supply from an emerged area in the south. The entire area emerged during Langhian and Serravallian times and several local extension basins developed in the Tortonian.

Backstripping analysis reveals four phases of accelerated subsidence related to extension in the Mesozoic: Anisian-Ladinian (241-235Ma), Norian-Hettangian (223-203Ma), Callovian-Tithonian (161-146Ma), and Cenomanian-Turonian (97-89Ma). These phases can be correlated with tectonic events in the Central Atlantic Ocean. The Tertiary subsidence record shows a change from slow to rapid subsidence in the Late Oligocene and Early Miocene related to a change from extensional to compressional tectonics. Throughout the Middle and Late Miocene and the Pliocene, strike-slip tectonics resulted in local extension and compression giving rise to renewed basin development. The paleogeographic reconstructions together with subsidence analysis allow to discuss the tectonostratigraphic evolution of the Ronda-Málaga region within the framework of western Mediterranean plate tectonics.

---

<sup>1</sup>Parts of this Chapter have been published as:

Van der Meer, F. 1994. Triassic-Miocene paleogeography and basin evolution of the Subbetic zone between Ronda and Málaga, Spain. *Geologie & Mijnbouw*, In press.

Van der Meer, F. 1994. Quantitative subsidence analysis and thermal-mechanical modelling: examples from southern Spain and Libya. *ITC-Journal*, 94(1): 52-63.

## 2.1 INTRODUCTION

In this Chapter, the stratigraphy of the Subbetic zone as exposed in the Ronda-Málaga region is outlined. A total of 29 stratigraphic sections have been investigated (Van der Meer, 1994a; Hamzah, 1992; Agbor, 1992; Yan, 1992; Shendy, 1992) have been investigated. Their locations are shown on Fig. 2.1. The stratigraphic record of the southernmost Subbetic Zone in the Ronda-Málaga region consists of sediments ranging in age from Triassic up to Pliocene. In the following text, which also incorporates observations from the literature, these are discussed focusing on the exposed sequences north and east of Ronda and Neogene deposits north of El Burgo (Fig. 2.1). From this discussion, a series of paleogeographic reconstructions follow for the Triassic upto and including the Miocene. Due to limitation in palinspatic control for the Triassic-Cretaceous period, facies distributions in this period are only described without attempting to map their distributions. A number of map reconstructions are presented for the Miocene period outlining the rapid paleoenvironmental changes related to regional tectonics. A combination of backstripping analysis and facies analysis is used in the last part of this Chapter to mark clear deformation phases related to Mediterranean plate tectonic events.

## 2.2 OUTLINE OF THE STRATIGRAPHY OF THE RONDA-MALAGA REGION

### 2.2.1 Triassic

Triassic units exposed east of Ronda (Fig. 2.1, section 1) range in age from Spathian to Rhaetian (Fig. 2.3). The earliest Triassic (Tr1) consists of a sequence of very thick to thin beds of red-coloured conglomerates and sandstones (with components up to 5 cm in size) which are fining upward to medium grained sandstones. Red beds of the same age and composition are found throughout the Betic Cordilleras (Simon, 1987). Trough-shaped and wedge-shaped cross-stratification in the order of centimetres is common in the coarser sandstones. The base of a set of cross strata may be coated with a red pelitic film. Mud cracks have been observed locally, as well as small-scale fining upward sequences. The red conglomeratic sandstones are thought to represent the lower part of a coarse grained alluvial fan whereas small-scale fining upward sequences suggest deposition by a 'meandering' type of river. This interpretation is consistent with the observations made by Roep (1972) in the Vélez-Rubio area, 200 km to the northeast. Fossils have not been found in the clastic sequence, but from geologic relations an Early-Middle Triassic (Spathian-Early Anisian) age is inferred.

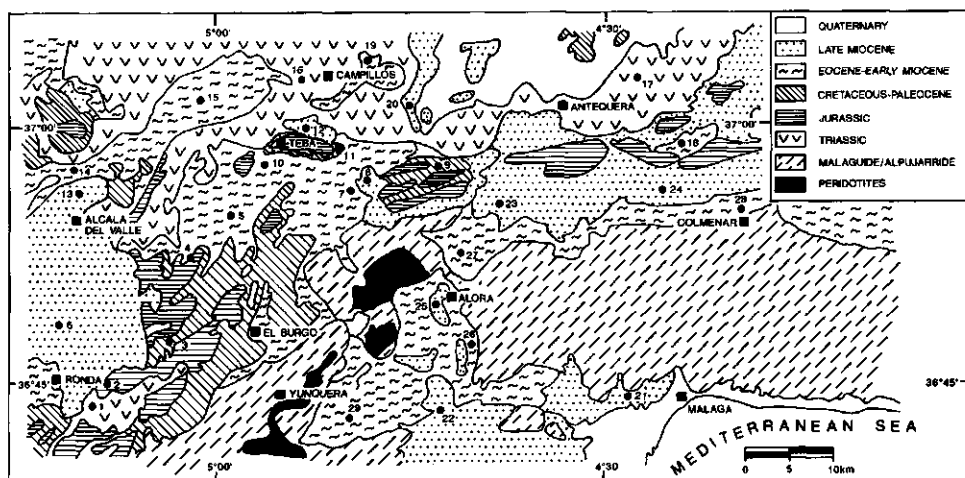


Fig. 2.1: General geologic map of the investigated area. Numbers indicate sections used for the paleogeographic reconstructions.

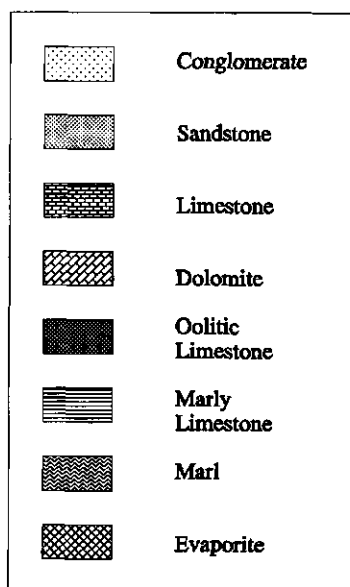


Fig. 2.2: Legend to the lithology in the stratigraphic columns of Figs 3-6 and the composite stratigraphic column of Fig. 2.11. Legend to the 'sedimentary structures': CC = caliche crusts, CL = convolute lamination, CR = current ripples, DC = desiccation cracks, FU = fining upward, GB = graded bedding, HB = herringbone cross-bedding, HCS = Hummocky Cross Stratification, OL = olistostromes, PL = parallel lamination, WR = wave ripples.

The lower part of the sequence Tr2 consists of dolomites containing *Myophoria*, *Protorcula*, and *Neritaria* together with other species yielding an Anisian age (Dürr, 1967).

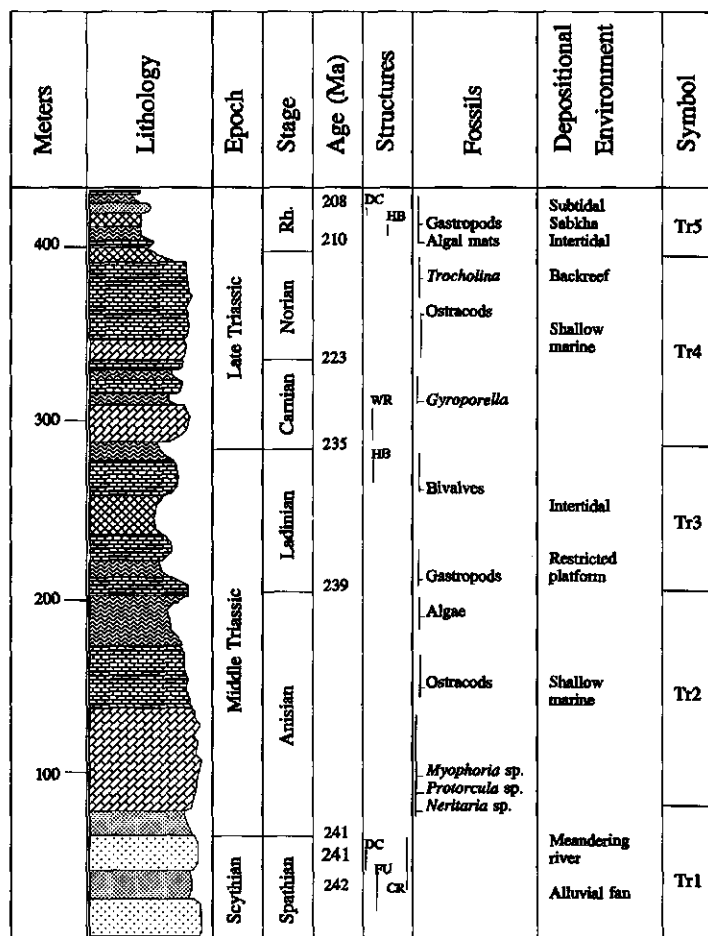


Fig. 2.3: Stratigraphic column of the Triassic deposits outcropping in the Subbetic Zone east of Ronda (location 1 on Fig. 2.1). Legend: see Fig. 2.2.

Overlying these dolomites is a series of limestones containing fragments of ostracods. Remains of algae were found in marls at the top of Tr2.

The bottom of Tr3 is formed by a resistant limestone bed containing abundant gastropods. Dürr (1967) recognized a Ladinian fauna and described local intervals of evaporites in the Tr3 sequence, although this observation is disputed by Bourgois (1978). The carbonate sequence represented by units Tr2 and Tr3 was deposited in a shallow marine, restricted platform environment.

The lower part of the Late Triassic consists of approximately 110m of limestones and dolomites with interbedded marls. This sequence (Tr4) was dated by Martín-Algarra (1980) on the basis of Dasycladacea (e.g. *Gyroporella* sp. aff. *verticillata*) as Carnian-Norian. A backreef environment of deposition is interpreted on basis of the occurrence of *Trocholina*

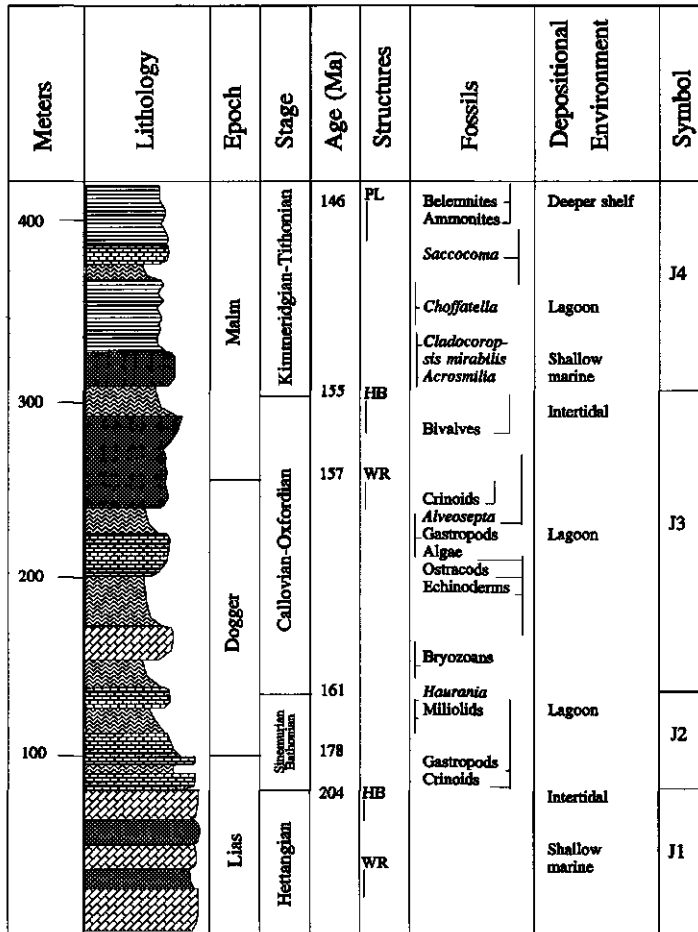


Fig. 2.4: Stratigraphic column of the Jurassic deposits outcropping in the Subbetic Zone east of Ronda (location 2 on Fig. 2.1). Legend: see Fig. 2.2.

at the top of Tr4.

This sequence is overlain by 40m of multicoloured marls alternating with sandstones and evaporites (Tr5). These marls were dated as Rhaetian by Blumenthal (1933) which is consistent with dating by Besems & Simon (1982) of similar Triassic rocks in the Murcia Province in the eastern part of the External Betic Cordilleras. Our observations agree with the general opinion that the Late Triassic facies originated in a continental or shallow marine evaporitic environment.

The Triassic north of Campillos and Antequera (see Fig. 2.1 for location) consists of 150-200m of evaporites (mainly anhydrite, gypsum, and halite) alternating with coarse alluvial fan deposits. Thin intervals of well-bedded algal stromatolites record short-term marine influences.



### 2.2.2 Jurassic

Jurassic rocks exposed near Ronda (Fig. 2.1, section 2) consist of approximately 400m of limestones, dolomites, marls, and marly limestones (Fig. 2.4; Azéma *et al.*, 1979). The earliest Jurassic and possibly the latest Triassic (Rhaetian ?) consists of a 40-70m-thick unit of light-grey, sugary dolomites interbedded with oolitic limestones (J1). This unit has been dated on the basis of the stratigraphic relationship with the overlying unit, a relatively thin (less than 50m) sequence of well bedded, grey-brown lime-mudstones and marls. These micrites are frequently laminated and contain abundant gastropods, bivalves and crinoids (J2). On the basis of the gastropod fauna, the sequence was dated Sinemurian-Bathonian by Dürr (1967). The presence of *Haurania* indicates a lagoonal environment of deposition and a Pliensbachian to Bathonian age. Therefore the age of the underlying unit J1 is inferred as earliest Jurassic.

The lower part of the Middle and Late Jurassic unit J3 consists of a 200m-thick series of well-bedded, monotonous limestones and marls with occasional dolomites (J3). In the middle and upper part of this sequence, abundant crinoids and bivalves were found. Dürr (1967) dated the series as Callovian-Oxfordian on the basis of corals and hydrozoans. The carbonates were deposited in a lagoonal environment as evidenced by the presence of *Alveosepta*. *Alveosepta* occurs only in the middle part of the sequence and indicates an Oxfordian to Kimmeridgian age. Towards the top of the sequence, the occurrences of oolitic limestones indicate wave action in a shallow marine environment.

The latest Jurassic rocks (J4) consist of a series of 120m of well-bedded oolitic limestones developing into marly limestones containing abundant belemnites and ammonites at the top of the sequence, suggesting an abrupt deepening of the depositional environment. The age of unit J4 is inferred as Kimmeridgian-Tithonian (Durand-Delga *et al.*, 1959). The base of the sequence was dated as the boundary between the Oxfordian and Kimmeridgian from the presence of *Cladocoropsis mirabilis* and *Acrosmilia* aff. *fromenteli*. The occurrence of *Saccocoma* indicates a pelagic facies and a Kimmeridgian and Tithonian age.

In the north, near Archidona (15km east of Antequera, Fig. 2.1), the thickness of the Jurassic is approximately 750m. The Hettangian-Sinemurian comprises a basal part of dolomites and algal stromatolites which are locally brecciated due to wave action or desiccation. The upper part of the Hettangian-Sinemurian contains 200m of oolitic grainstones and algal wackestones. A deepening of the depositional environment is inferred from a series of 300m of marly limestones containing radiolarians and planktonic foraminifera. These marly limestones were dated as Pliensbachian to Kimmeridgian by Delgado & Sanz de Galdeano (1981). The latest Jurassic exposed near Archidona consists of turbidites and marly units containing abundant ammonites and *Aptychus* (Delgado & Sanz de Galdeano, 1981).

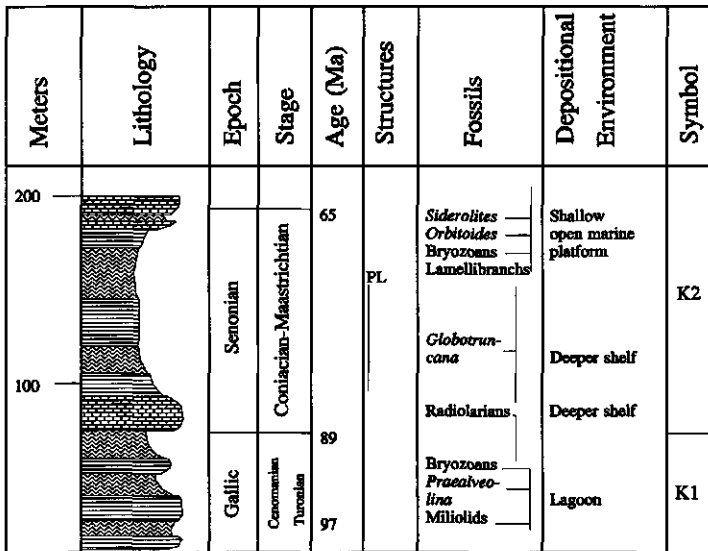


Fig. 2.5: Stratigraphic column of the Cretaceous deposits outcropping in the Subbetic Zone east of Ronda (location 3 on Fig. 2.1). Legend: see Fig. 2.2.

### 2.2.3 Cretaceous

The Cretaceous sequence exposed in the Ronda area (Fig. 2.1, section 3) is relatively thin (generally less than 300m, Fig. 2.5). The lowermost unit (K1) is composed of marls alternating with marly limestones and contains radiolarians, bryozoans, and several foraminifer species. The base of the sequence is formed by a 10m-thick layer of nodular, bituminous marly limestone. Occurrences of *Praealveolina* in the lower part of the K1 unit indicate a Late Albian to Turonian age. ITGE (1990) dated the unit K1 as Cenomanian-Turonian. This suggests a non-depositional or erosional hiatus during the Early Cretaceous. *Miliolids* and *Praealveolina* in the basal and middle part of unit K1 record a lagoonal environment and radiolarians at the top of K1 a deeper shelf environment.

The Senonian is mainly represented by a series of well-bedded, red-coloured marly limestones and marls of the 'Couches Rouges' facies (in spanish 'Capas Rojas', K2). The base of unit K2 is formed by a series of thick-bedded limestones. The marls and marly limestones contain abundant planktonic foraminifera (e.g. *Globotruncana*) which indicate a Coniacian to Maastrichtian age (Azéma, 1961) and a deeper facies. The top of the K2 sequence contains *Siderolites* and *Orbitoides* which yields a Maastrichtian age and a shallow open marine platform environment of deposition. However, Kockel (1960) mentioned *Globorotalia* species indicating a Paleocene or younger age for what is here taken as the top of unit K2. The thickness of this unit diminishes from 250m south, to less than 50m north of the study area.

Some 5km north of Antequera a more complete Cretaceous sequence occurs. The Neocomian is represented as a thin (15m) unit composed of marls and marly limestones containing abundant *Nannoconus* species indicating pelagic conditions. A series of 60m thickness of bituminous marls with radiolarians of Cenomanian-Turonian age and with *Globotruncana* and *Rotalipora* overlies this unit. The Couches Rouges facies overlying the Cenomanian-Turonian marls is represented by 200m of red-coloured marls and thin-bedded limestones containing abundant *Globotruncana* and *Rugoglobigerina* species. The sequence is passes upward into Paleocene (*Globigerina daubjergensis* zone; Dürr, 1967).

#### 2.2.4 Paleocene-Miocene

The Tertiary stratigraphy described below (Fig. 2.6) is exposed at three representative groups of locations in the western part of the study area: El Burgo (Fig. 2.1, sections 3, 5, and 6), Ardales (sections 7 and 9), and Teba (sections 10, 11, and 12).

The distribution of Paleocene deposits over the area is very irregular. In places they are lacking and Eocene deposits rest directly on top of the 'Capas Rojas' unit, in other places a thick Paleocene sequence ( $\pm 150\text{m}$ ) is found. The Paleocene in El Burgo shows in-situ *Microcodium* in detrital limestones. The occurrence of in-situ *Microcodium* is generally accepted to indicate a non-marine origin (Esteban, 1974) and it is restricted to coastal zones with predominantly non-saline water. According to Smit (1979), in-situ *Microcodium* only occurs in Paleocene-Early Eocene series although Klappa (1978) claims occurrences of *Microcodium* in the Eocene and Pleistocene. The Paleocene deposits of Ardales and Teba, on the contrary, were deposited in deeper marine environments. Occurrences of *Dictyoconus* in the Teba section indicate deposition at the platform margin. A deeper shelf environment is deduced from the occurrence of *Globigerina* and *Globorotalia* in the Ardales section.

Late Paleocene-Eocene deposits reach a maximum thickness of 300m and consist of bioclastic limestones with terrigenous clasts, marly limestones and marls. In the El Burgo area, these deposits often show convolute bedding, graded bedding and other characteristics of turbiditic sequences. On the basis of the occurrence of *Nummulites*, *Asterocyclina*, and *Discocyclina*, the Late Paleocene to Eocene age was established for the El Burgo section (Dürr, 1967). Local occurrences in the Late Paleocene-Eocene deposits of the El Burgo section of chaotic masses of blocks of limestones from Jurassic units cemented by marls containing abundant foraminifera have been interpreted as olistostromes deposited in deeper water environments. The Eocene deposits of the El Burgo and Ardales sections record a shallow open marine platform environment of deposition with the presence of *Nummulites* and *Discocyclina*. The occurrence of abundant *Miliolids* in the lower part of the Eocene deposits

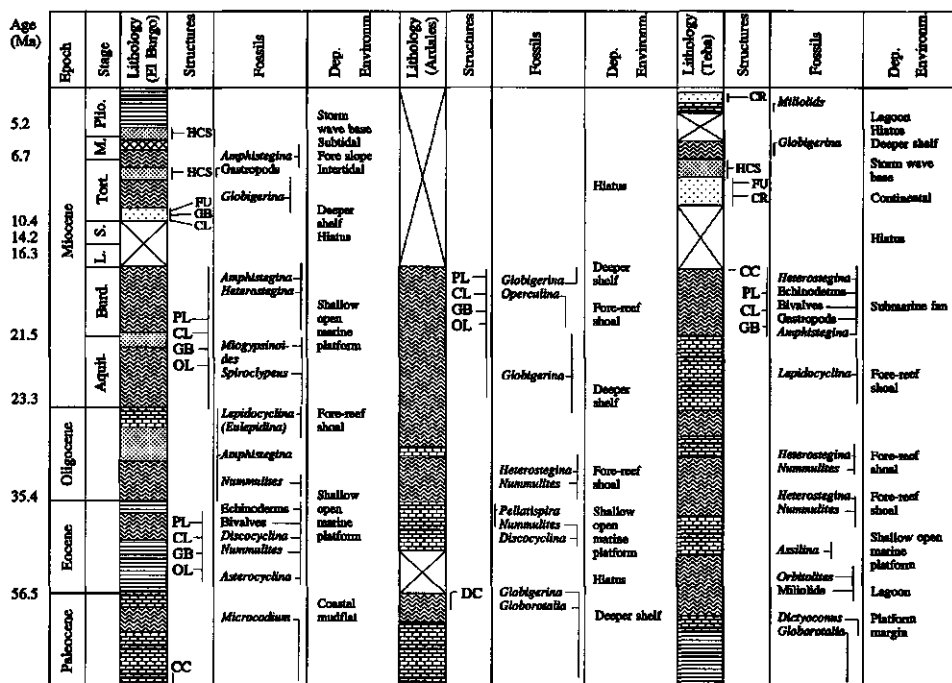


Fig. 2.6: Tertiary stratigraphy in the El Burgo section (Paleocene is number 3, Eocene-Burdigalian number 5, and Tortonian-Pliocene number 6 in Fig. 2.1), the Ardales section (Paleocene is number 9, Eocene-Burdigalian is number 7), and the Teba section (Paleocene is number 11, Eocene-Burdigalian number 10 in, and Tortonian-Pliocene number 12 in Fig. 2.1). Note that the time scale changes after Oligocene. Legend: see Fig. 2.2.

of the Teba section indicates a lagoonal environment which deepens to a shallow open marine platform environment as deduced from the presence of *Heterostegina* near the top of the Eocene section.

The Late Paleocene-Eocene deposits in the El Burgo section are overlain by a 100m-thick Oligocene sequence consisting of red marls and intercalated bioclastic limestones and sandstones. The limestones contain *Amphistegina*. Near the top of the El Burgo section, *Lepidocyclina* (*Eulepidina*) indicates a fore-reef shoal environment. *Nummulites* is present at the base of the sequence. *Heterostegina* and *Nummulites* present in the lower part of the Oligocene sections of both Ardales and Teba, which consists mainly of marls, indicate a fore-reef shoal environment of deposition. The Oligocene in both the Ardales and Teba sections reaches a maximum thickness of 150m.

The Early Miocene and possibly Late Oligocene sediments in the El Burgo and Ardales sections consist of grey-green marls and micaceous sandstones showing convolute

bedding, graded bedding, parallel lamination and other characteristics of turbiditic sequences. Occurrences of *Miogypsina* (or *Miogypsinoidea*, Peyre 1974) and *Spiroclypeus* in the El Burgo section indicate a Late Oligocene to Early Miocene age. Peyre (1974) dated the sequence as Aquitanian. The Ardales section records deeper shelf environments with the presence of *Globigerina*. A fore-reef shoal environment of deposition for the Aquitanian of the Teba section is deduced from the occurrence of *Lepidocyclina* in bioclastic limestones. The thickness of this unit is highly variable and ranges from 200 to 500m in the studied area. Similar sediments of the same age have been estimated to reach a thickness of 1000m near Gibraltar (Didon, 1960; 1969).

Turbidites of Burdigalian age in all three sections are represented by a thick sequence of marls with intercalated sandstones and conglomeratic lenses showing graded and convolute bedding. These marls contain fragments of *Microcodium* and often also reworked fossil fragments from Jurassic and Early Tertiary sediments which are present in a chaotic mass interpreted as an olistostrome. The thickness of this unit varies from 800m to locally more than 1500m (Dubois & Magre, 1972). In the El Burgo and Teba sections, the fauna in these sediments contains *Amphistegina*, *Heterostegina*, planktonic foraminifera, and reworked fragments of bryozoans and corals. It was dated by Serrano-Lozano (1979) as Burdigalian. The Aquitanian-Burdigalian boundary in the sediments of the El Burgo and Teba sections is marked by the last observance datum of *Catapsydrax dissimilis* (top of zone N5, planktonic foraminiferal zonation of Blow, 1969), whereas the Burdigalian-Langhian boundary in these sections is marked by the first appearance datum of *Praeorbulina glomerosa* (within zone N8). *Operculina* occurs in the middle and lower parts of the Burdigalian in the Ardales area, whereas *Globigerina* is abundant near the top of the Ardales section.

No Langhian and Serravallian deposits were found.

The Tortonian and Messinian sediments exposed north of Ronda (shown in Fig. 2.6 as the top of the El Burgo section) have been studied by Serrano-Lozano (1980). In these sediments, a basal series of 50m of conglomerates and arenites with an overall fining upward trend shows characteristics of a turbiditic sequence, e.g. convolute bedding and graded bedding. Overlying these conglomerates is a series of 600m of marls containing abundant *Globigerina* which are overlain by a 60m thick sequence of sandstones which contain Hummocky Cross Stratification indicating storm induced wave action below the fairweather wave base. An assemblage of *Globigerina bulloides*, *Globigerina decoraperta*, *Globigerinoides obliquus*, *Globorotalia continuosa*, and *Sphaeroidinellopsis seminulina*, found in the marls, was interpreted as Early Tortonian (Serrano-Lozano, 1980). Overlying the Early Tortonian north of Ronda is a sequence of marls (200 to 300m thick) with an upward increase of sandstone intervals containing minor halite intercalations recording a shallowing upward trend from an deeper marine to a continental and/or shallow marine environment. Dating by

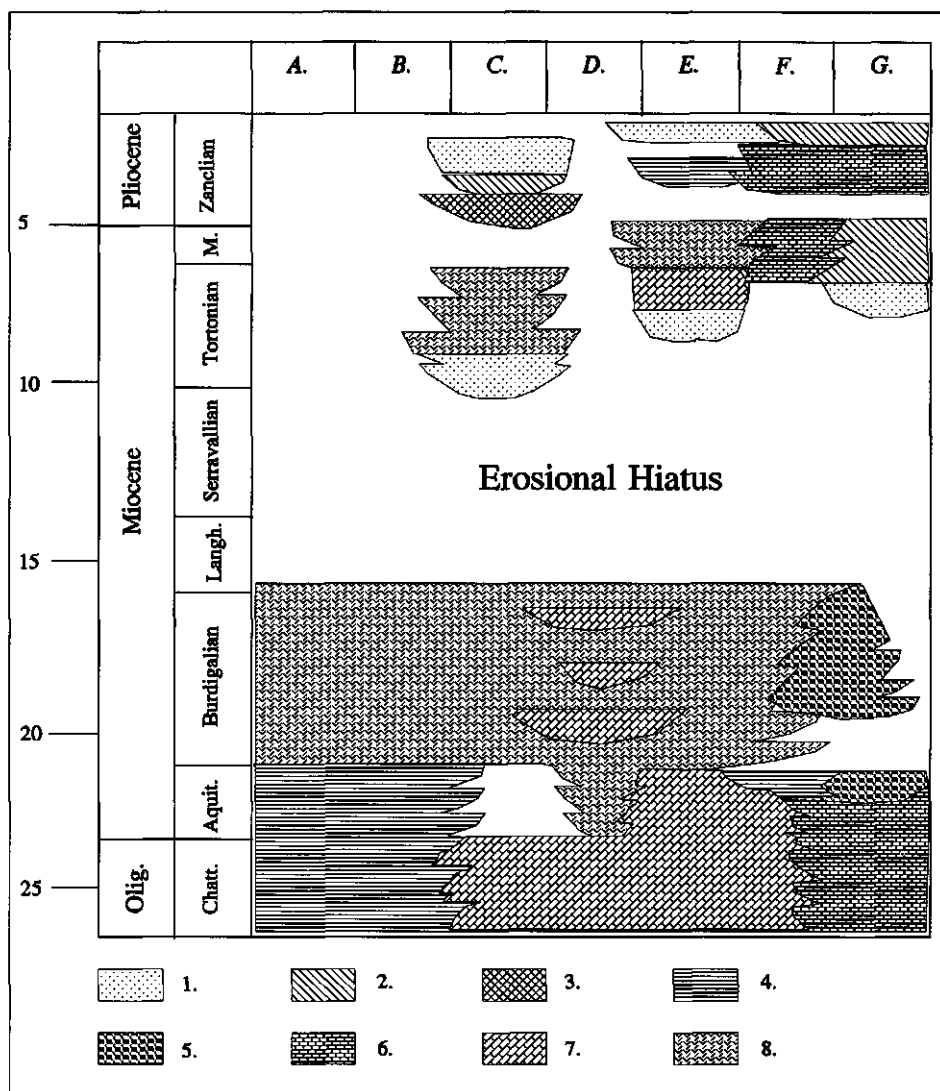


**Fig. 2.7:** Time-facies profile for the Neogene of the northern part of the Ronda-Málaga region. Legend: 1. Alluvial fan and fluvial environment, 2. Supratidal and continental sabkha, 3. Intertidal, 4. Lagoon, 5. Backreef, 6. Shallow open marine platform, 7. Fore-reef shoal, 8. Deeper shelf, A. Periana, B. Colmenar, C. Antequera, D. Ardales, E. Teba, F. Cañete la Real, G. Alcalá del Valle.

Serrano-Lozano (1980) on the basis of *Globorotalia* subzones yielded an estimate of Late Tortonian and Messinian (*Globorotalia mediterranea* subzone to *Globorotalia humerosa*

subzone). Locally, the Late Tortonian and Messinian unit is topped by a relatively thin (approximately 5-150m) marly limestone unit dated as Pliocene (Serrano-Lozano, 1980). In the Ardales section, sediments younger than Burdigalian age are absent. Middle Tortonian continental deposits (alluvial fan and braided river deposits) in the Teba area are overlain by Late Tortonian and Messinian deep-water marls containing *Globigerina*. Unconformably overlying these *Globigerina* marls are lagoonal sediments containing *Miliolids* which in turn are unconformably overlain by coarse alluvial fan deposits. The Tortonian-Pliocene sediments of the Teba section have a thickness ranging from 200 to 500m.

## 2.3 TRIASSIC-LATE MIOCENE PALEOGEOGRAPHIC RECONSTRUCTIONS

In the following text sections, paleogeographic reconstructions are presented. These are based on a total of 29 stratigraphic sections measured in the Ronda-Málaga region (Fig. 2.1) in conjunction with previous work by Dürr (1967), Serrano-Lozano (1979, 1980), Peyre (1974), González-Donoso & Serrano-Lozano (1977), Kockel (1960), and others.

From the stratigraphic sections, time-facies profiles have been constructed which were used to reconstruct the paleogeography as presented below. An example of a time-facies profile for the Neogene through the northern part of the studied region from Periana to Alcalá del Valle is shown in Fig. 2.7.

### 2.3.1 Pre-Miocene

During the Triassic the Ronda-Málaga region has been the scene of continental conditions and supratidal environments in the north and intertidal and shallow marine environments to the south. Southeast of Ronda and east of Alcalá del Valle, Triassic limestones and marls record a shallow-marine intertidal environment sometimes subjected to subaerial exposure. North of Antequera and Campillos, thick evaporite sequences indicate continental sabkha settings dominated by the interplay of fluvial and lacustrine processes. Coarse-grained, cross-bedded clastic limestones east of Antequera were formed by alluvial fans and associated braided rivers.

In the northern part of the area, Early Jurassic bioclastic limestones near Teba and north of Archidona (15km east of Antequera) were formed in a very shallow-marine high-energy environment. During the Sinemurian-Bajocian this environment deepened to a marine pelagic environment in which marls with abundant radiolarians and ammonites were deposited

showing occasional turbiditic influences. Further to the south, northeast of Ronda, a shallow-marine restricted environment existed throughout the Early and Middle Jurassic deepening to a marine pelagic environment in the Late Jurassic.

The Early Cretaceous marks a period of non-deposition in large parts of the studied region. During the Late Cretaceous, marine pelagic sedimentation prevailed with environments generally deepening to the southeast. Detritus supply was from the northwest to the southeast (e.g. Baena-Perez & Jerez-Mir, 1982).

A regional differentiation of sedimentary facies can be observed during the Paleocene. Marine deposition continued in various locations, whereas in-situ occurrences of *Microcodium* are evidence for subaerial exposure of the Triassic-Cretaceous limestones near El Burgo and between Antequera and Campillos.

Eocene conglomerates and bioclastic limestones directly overlie Cretaceous limestones and a Paleocene hardground west of Archidona. The conglomerates possibly have a continental origin, whereas the limestones were deposited in a shallow-marine high-energy environment. Waterdepth increased southward with decreasing detritus supply. Near Colmenar and Teba, marls containing abundant *Nummulites* record a shallow-marine open-shoal environment which existed throughout Eocene and Oligocene times. Near Teba, Late Eocene and Oligocene marls and limestones deposited in a fore-reef shoal environment overlie Early Eocene lagoonal sediments. West of Ardales, the stratigraphic record shows a non-depositional hiatus during the Early Eocene. Late Eocene, shallow marine carbonates rest on Paleocene deep-marine marls near Ardales. Further south, near El Burgo and south of Alora, a submarine fan system developed, characterized by mass flows and turbidites.

### 2.3.2 Late Oligocene and Miocene

During the Late Oligocene and Miocene, the Ronda-Málaga region is the scene of rapidly changing environments related to tectonic episodes. Four different periods can be recognized, each controlled by a different tectonic regime: (1) Late Oligocene-Aquitania, (2) Burdigalian, (3) Langhian and Serravallian, and (4) Tortonian and Messinian.

*Late Oligocene-Aquitania* - During the Late Oligocene and Aquitania (Fig. 2.8) a submarine fan system developed, characterized by mass flows and turbidites south of the line Casabermeja-Ardales-Teba. These turbidites are the lateral equivalents of the so-called Alozaina Formation (western Betic Cordilleras; Hermes, 1985) and the Ciudad Granada Formation (eastern Betic Cordilleras; Geel *et al.*, 1992). The Jurassic-Cretaceous limestone areas east of Ronda, north of Ardales and west of Cuevas del Becerro emerged, shedding



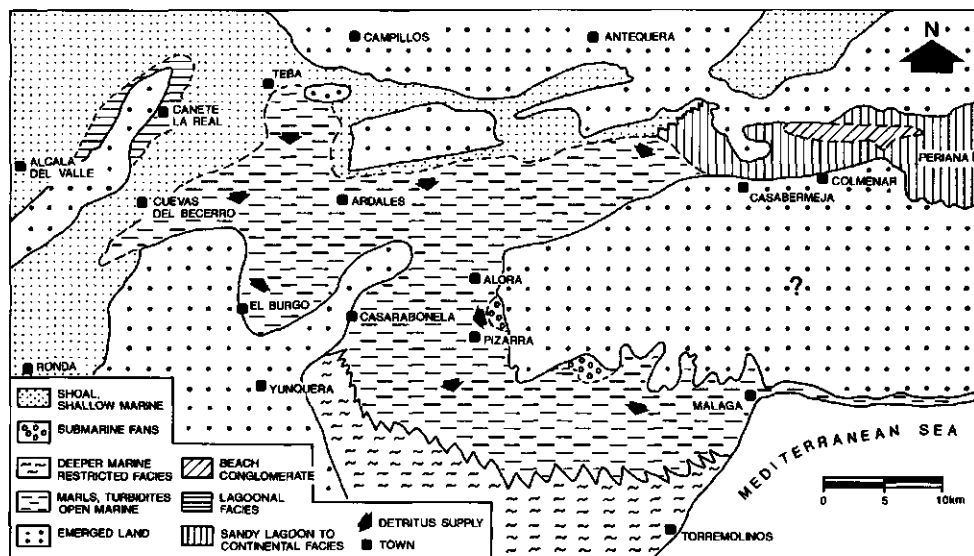


Fig. 2.8: Interpreted facies distribution for Late Oligocene-Aquitania times in the Ronda-Málaga area (see text 'Paleogeographic reconstructions').

clastics into the newly formed basins. Simultaneously, detritus was supplied from the Triassic high which stretched from Campillos to Antequera. Although the main direction of detritus supply was from north to south, some east-west oriented paleocurrent directions indicate influx of clastics from local high areas. Limestones formed in a fore-reef shoal environment evidence a shallow-marine platform situated west of the line Ronda-Teba. Lagoonal conditions prevailed in the area surrounding the emerged Jurassic limestone block of Cañete la Real. Marls and limestones containing abundant lepidocyclinids and bryozoan debris, found north-east of Ardales and south of Campillos, indicate open shoal conditions; however the occurrence of reef-building organisms may point to the existence of patch reefs or fringing reefs bordering the Triassic high (see also Peyre, 1974). North of Colmenar open marine limestones of Oligocene age containing abundant diatoms (dated by Hermes & Smit, 1975) are concordantly overlain by Aquitania sandstones showing eolian influences (see also Durand-Delga, 1980), thus pointing to a very rapid uplift in Late Oligocene-Aquitania time.

**Burdigalian** - The paleogeography in the Burdigalian (Fig. 2.9) is completely different from that of foregoing periods. Near Pizarra, Tortonian bioclastic limestones rest unconformably

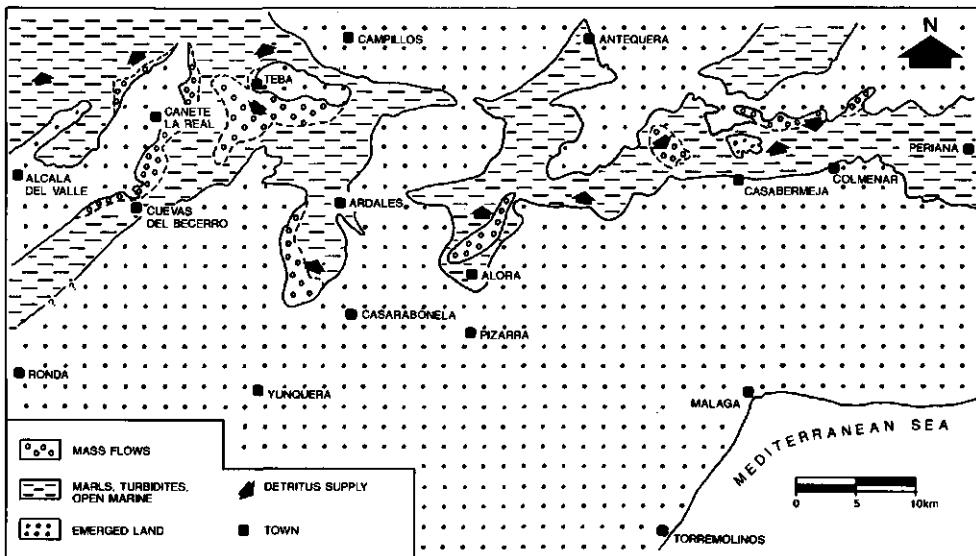
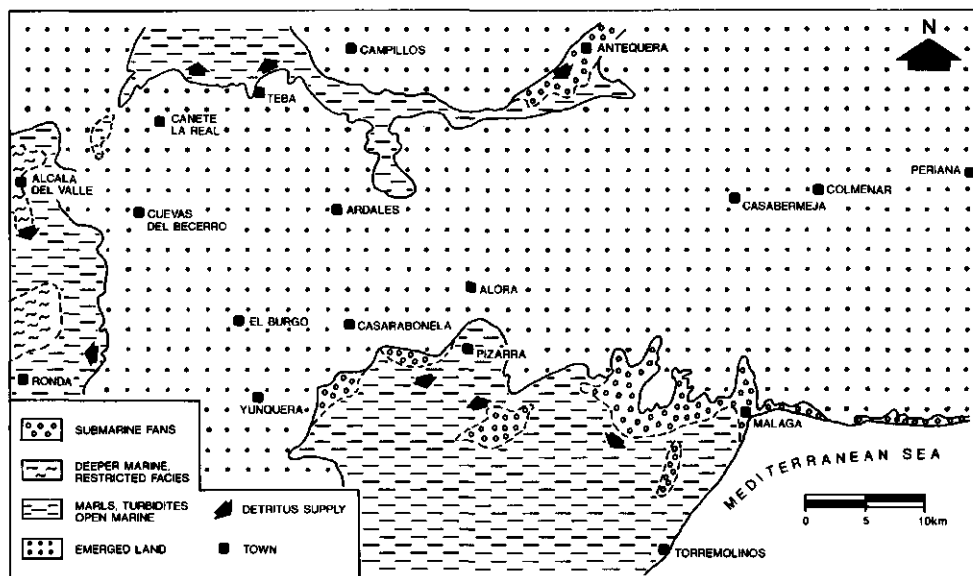


Fig. 2.9: Interpreted facies distribution for Burdigalian times in the Ronda-Málaga area (see text 'Paleogeographic reconstructions').

upon Aquitanian turbidite fan deposits, indicating an emerged landmass which stretched south of the line Colmenar-Alora-Cuevas del Becerro. Detritus supply was mainly from south to north although olistostromes south of Teba record southward supply directions from a local Jurassic limestone block north of Teba. Besides clastics derived from Triassic-Cretaceous limestone units, also marble blocks can be found in submarine fans. These marbles may have originated from Alpujarride nappe complexes to the south. Large quantities of clastics were shed into a narrow sea-arm parallel to the line Colmenar-Alora. A north-south emerged area separated this arm from a marine basin north of Teba that deepened northward. Deposition and simultaneous folding or tilting of strata is indicated by internal angular unconformities found in Burdigalian sediments northwest of Cañete la Real. Toward the close of the Burdigalian, depositional environments became more shallow as the Subbetic Zone was gradually being uplifted and incorporated in the thrust load (see also Hermes, 1977).

*Langhian and Serravallian* - Throughout the investigated area Langhian and Serravallian sediments are missing. North of Teba and northeast of Ardales, Tortonian sediments unconformably overlie Burdigalian fan deposits. Apparently large areas emerged during



**Fig. 2.10:** Interpreted facies distribution for Tortonian times in the Ronda-Málaga area (see text 'Paleogeographic reconstructions').

Langhian and Serravallian. Simultaneously, marine sedimentation continued in the Guadalquivir basin north of the investigated area (Lanaja *et al.*, 1987; Santos-García *et al.*, 1991; Tjalsma, 1971).

**Tortonian and Messinian** - During the Tortonian and Messinian (Fig. 2.10), new basins came into existence: north of Teba, around Ronda, and south of Pizarra.

Northeast of Teba, Tortonian conglomerates transgressively overlie Jurassic limestones. These conglomerates contain both Triassic components shed southward into the basin from the Campillos-Antequera high, as well as Cretaceous-Jurassic limestone pebbles. Detritus supply was mainly from the south. In northern direction, outside the area studied, this basin deepened as indicated by shallow marine limestones containing lamellibranchs and debris of bryozoans. Southeast of Campillos, coarse clastic sediments of Tortonian age were deposited in a very shallow marine environment, whereas in a narrow area northeast of Antequera (outside the area of Fig. 2.10) such sediments grade-up into yellowish white siltstones with plant debris and gastropods interpreted as lacustrine deposits.

North of Ronda, a basin was formed in the Early Tortonian which existed throughout

the Tortonian and Messinian. The infill of this basin is asymmetric and its thickness increases in northwestern direction (Serrano-Lozano, 1980). Early Tortonian continental conglomerates, interpreted as fluvial or alluvial fan deposits, are restricted to a small area north and east of Ronda, whereas coeval shallow marine conditions prevail on the northern margin of the basin (Serrano-Lozano, 1980). Throughout the Tortonian and Early Messinian this basin continued to subside. East of Ronda, Hummocky Cross Stratification indicates storm induced wave action below the fairweather wave base with NNE-SSW to W-E current directions. To the north and west, deeper marine marls were deposited which show occasional turbiditic influences. Toward the close of the Messinian the basin north of Ronda emerged and sedimentation continued only along the northern edge where algal limestones are found (Gonzalez-Donoso & Serrano-Lozano, 1977).

A third basin developed south of Alora in which marls and submarine turbidite fans were deposited during the Tortonian.

## **2.4 QUANTITATIVE SUBSIDENCE ANALYSIS AND ITS IMPLICATIONS FOR GEODYNAMICS**

The aim of backstripping analysis is to produce a graphical representation of the vertical movement of a stratigraphic horizon in a sedimentary basin as an indicator of the subsidence and uplift history in the basin since the horizon was deposited (Van Hinte, 1978). Stratigraphic data needed for a backstripping analysis include a stratigraphic column showing present-day thicknesses, rock types, ages, and estimated paleo-water depths. To obtain a subsidence curve, first the paleo-sediment and paleo-water columns are reconstructed. Sediment thicknesses are corrected for compaction. Corrections for possible changes in sea-level relative to present-day sea level yield the basement subsidence. Then the total load of sediments on the basement is removed to give the tectonic subsidence; the undistorted basin subsidence that would occur in the absence of sedimentation.

In this study, a water-loaded tectonic subsidence curve corrected for the effects of sediment loading and paleo-bathymetry was calculated for an area with pronounced Neogene subsidence. The Subbetic composite stratigraphic record (Van der Meer, 1994b; Fig. 2.11) was derived from sections 1-6 located north and northeast of Ronda (Fig. 2.1). Backstripping techniques discussed by Steckler & Watts (1978), Sclater & Christie (1980), and Bond & Kominz (1984) were used. The time scale of Harland *et al.* (1990) was adopted. Lithological effects, in particular compaction and densities of evaporites, have been corrected for, using an exponential decrease of porosity with depth (Bond *et al.*, 1983).

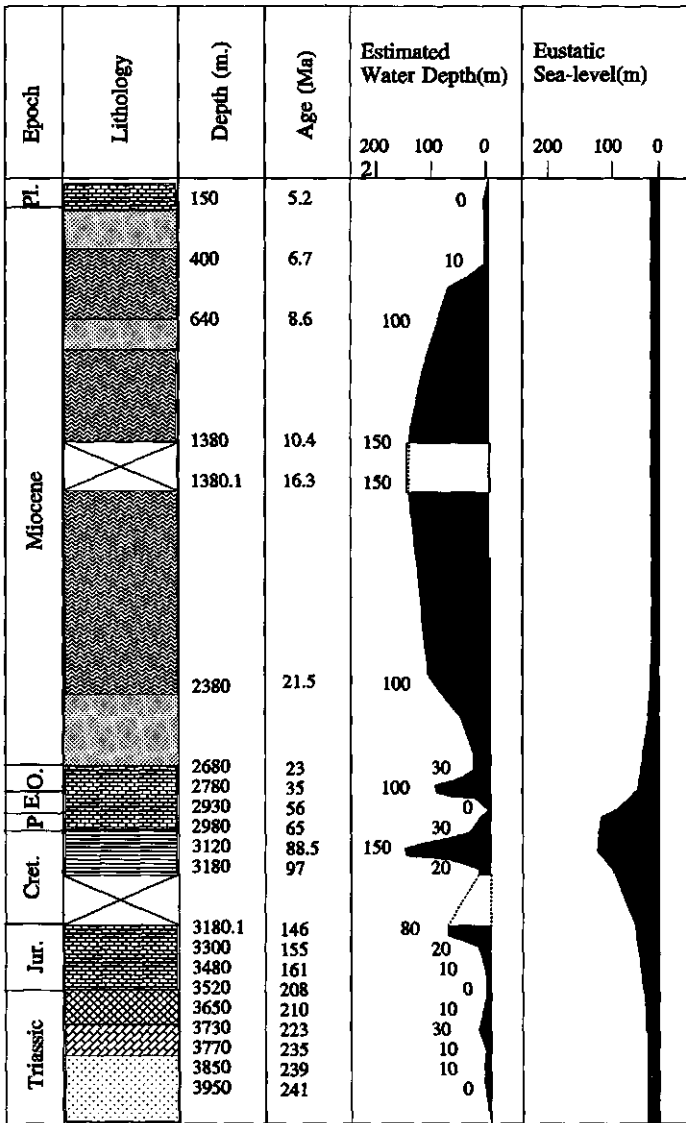


Fig. 2.11: Composite stratigraphic section for the Subbetic Zone of the Ronda-Málaga region used for backstripping analysis. The column is based on sections 1-6 of Fig. 2.1. Legend: see Fig. 2.2.

Each stratigraphic unit between two chrono-stratigraphic horizons has been assigned a sand, silt, shale, carbonate, and anhydrite percentage, with each lithology responding according to its own compaction scheme. Porosity-depth relations were defined over two intervals (a deeper and a shallow relation), therefore two exponential expressions were necessary to describe the delithification procedure and a depth at which the deeper relation takes over from

Table 2.1: Maximum (upper) and minimum (lower) compaction parameters.

Lithology	$\phi_i$	$C_i$	$\phi_o$	$C_o$	$z_p$	$\rho_{gr}$
Sand	0.29	0.216	0.40	0.51	1.0	2.65
Silt	0.42	0.375	0.60	1.00	0.5	2.68
Shale	0.50	0.475	0.70	1.10	0.5	2.72
Carbonate	0.52	0.442	0.78	1.33	0.5	2.71
Halite	0.00	0.100	0.00	0.10	0.0	2.03
Anhydrite	0.00	0.100	0.00	0.10	0.0	2.95
Sand	0.20	0.480	0.20	0.480	0.0	2.65
Silt	0.25	0.325	0.25	0.325	0.0	2.68
Shale	0.37	0.470	0.53	1.050	0.5	2.72
Carbonate	0.20	0.580	0.20	0.580	0.0	2.71
Halite	0.00	0.100	0.00	0.100	0.0	2.03
Anhydrite	0.00	0.100	0.00	0.100	0.0	2.95

$\phi_i$  = surface porosities (given as fraction) for the deep porosity-depth relation

$C_i$  = characteristic depth constants (in  $\text{km}^{-1}$ ) for the deep porosity-depth relation

$\phi_o$  = surface porosities (given as fraction) for the shallow porosity-depth relation

$C_o$  = characteristic depth constants (in  $\text{km}^{-1}$ ) for the shallow porosity-depth relation

$z_p$  = depth (in km) at which the deeper porosity-depth relation takes over from the shallow one

$\rho_{gr}$  = grain density (in  $\text{g/cm}^3$ ) of the corresponding lithology

the shallow relation (see Bond & Kominz, 1984). Minimum and maximum compaction effects have been tested using the parameters listed in Table 2.1. Other parameters used in the backstripping analysis are listed in Table 2.2. These represent the range of values commonly observed in quantitative subsidence analysis (Bond & Kominz, 1984). The results of incorporating compaction effects showed that the uncertainties in basement and tectonic subsidence related to the range in compaction parameters are in the order of several tens of metres.

Depositional depths were estimated from the sedimentary facies and faunal content, and quantified using the paleo-bathymetric scale of Ingle (1980). According to this scale, the accuracy of the paleo-waterdepth estimates obtained is within 50m for shallow-water deposits, but increases to 100-500m for deeper-water deposits.

Effects of long-term eustatic sea level changes (after Kominz, 1984) on the inferred tectonic subsidence were incorporated. Airy isostasy was assumed, thus ignoring the effect of a finite strength of the lithosphere on its response to sediment loading. This assumption, however, does not significantly affect the shape of the subsidence curve (Watts *et al.*, 1982), particularly during rift stages, when the lithosphere is mechanically weak (e.g. Hegarty *et al.*, 1988). Similarly, the reduced basement cooling resulting from the blanketing effect of sediments was ignored (Turcotte & Ahern, 1977; Lucazeau & Le Douaran, 1985). Detailed

- Chapter 2 -

*Table 2.2: Parameters other than compaction used in the backstripping analysis.*

Parameter	Symbol	Value
Initial lithospheric thickness	$L$	125 km
Initial crustal thickness	$C$	31.3 km
Coefficient of thermal expansion	$\alpha$	$3.4 \times 10^{-5} \text{ }^{\circ}\text{C}^{-1}$
Asthenospheric temperature	$T_m$	1333 $^{\circ}\text{C}$
Thermal diffusivity	$\kappa$	$0.008 \text{ cm}^2 \text{ s}^{-1}$
Mantle density	$\rho_m$	$3.33 \text{ g cm}^{-3}$
Crustal density	$\rho_c$	$2.8 \text{ g cm}^{-3}$
Isotherm describing the EET	$T_e$	333 $^{\circ}\text{C}$
Water density	$\rho_w$	$1.03 \text{ g cm}^{-3}$
Surface porosity of sediment infill	$\phi(o)$	0.55
Characteristic depth constant	$c$	$0.55 \text{ km}^{-1}$

knowledge of the thermal structure of the lithosphere throughout the evolution of the basin would be required to incorporate this effect into our analysis. However, because of the long time scale on which lithospheric cooling operates, a correction of the blanketing effect will not significantly alter the shape of the subsidence curves (Lucazeau & Le Douaran, 1985).

#### 2.4.1 Interpretation of the subsidence record

From the Mesozoic tectonic subsidence curve (Fig. 2.12) for the southern Subbetic Zone, four distinct periods of relatively rapid subsidence are apparent: (1) a Middle Triassic period (Anisian-Ladinian; 241-235Ma), (2) a Late Triassic-Early Jurassic period (Norian-Hettangian; 223-203Ma), (3) a Middle-Late Jurassic period (Callovian-Tithonian; 161-146Ma), and (4) a Middle Cretaceous period (Cenomanian-Turonian; 97-89Ma). These periods represent rifting episodes along the southeastern Betic margin that can be correlated with the stepwise opening of the Central Atlantic and Ligurian oceans which induced transtensional movements between Africa and Iberia (Vegas & Banda, 1982; Lemoine & Trümpy, 1987). The subsidence patterns observed for each of these phases show an initial phase of rapid subsidence and a subsequent phase of decelerating subsidence which is typical for rifted margins, where the rapid subsidence is caused by the isostatic response of the lithosphere to crustal thinning and the slower subsidence is driven by thermal re-equilibration (McKenzie, 1978). The duration of these rifting events is in the order of 10 to 20Ma. The first and third rifting events resulted in an average tectonic subsidence rate of 3.5cm/1000 years whereas the second and fourth rifting events show tectonic subsidence rates in the order of 2cm/1000 years. These subsidence rates are relatively low compared to those of rift basins and other rifted margins,

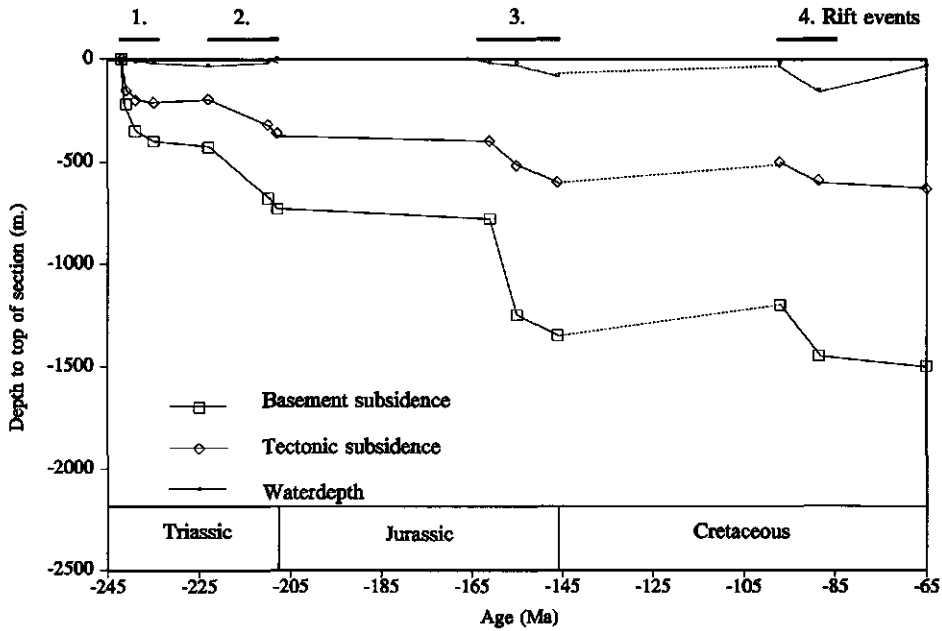


Fig. 2.12: Mesozoic subsidence curves for the southern Subbetic Zone near Ronda. Tectonic and basement subsidence derived from quantitative subsidence analysis incorporating paleowaterdepth and eustatic sealevel fluctuations.

but not abnormal. For comparison, the Sirte Basin of Libya shows tectonic subsidence rates exceeding 10cm/1000 years during active rifting (Van der Meer & Cloetingh, 1993a+b), and Kooi *et al.* (1989) found tectonic subsidence rates of 5cm/1000 years for the Central Graben of the North-Sea Basin. Comparable tectonic subsidence rates have been calculated for rifted margins (e.g. the U.S. Atlantic continental margin, 5cm/1000 years; Heller *et al.*, 1982, the eastern margin of Canada, 4cm/1000 years, Cloetingh *et al.*, 1990, Levant margin, 5cm/1000 years, Tibor *et al.*, 1992) although subsidence at the Gulf of Lions margin clearly exceeds these values (18cm/1000 years during an Oligocene to Early Miocene rifting event; Burrus *et al.*, 1987).

The Middle Triassic and the Late Triassic-Early Jurassic rifting phases (Fig. 2.12, rift events 1 and 2) coincide with a period of distensive wrench tectonics throughout the Atlantic realm (Ziegler, 1988; 1990). Volcanic detritus of Middle Triassic age in the Malaguide Complex (Roep, 1972; Mäkel, 1985) and metatuffaceous rocks in the Mulhacen Complex demonstrate rifting (De Jong & Bakker, 1991).



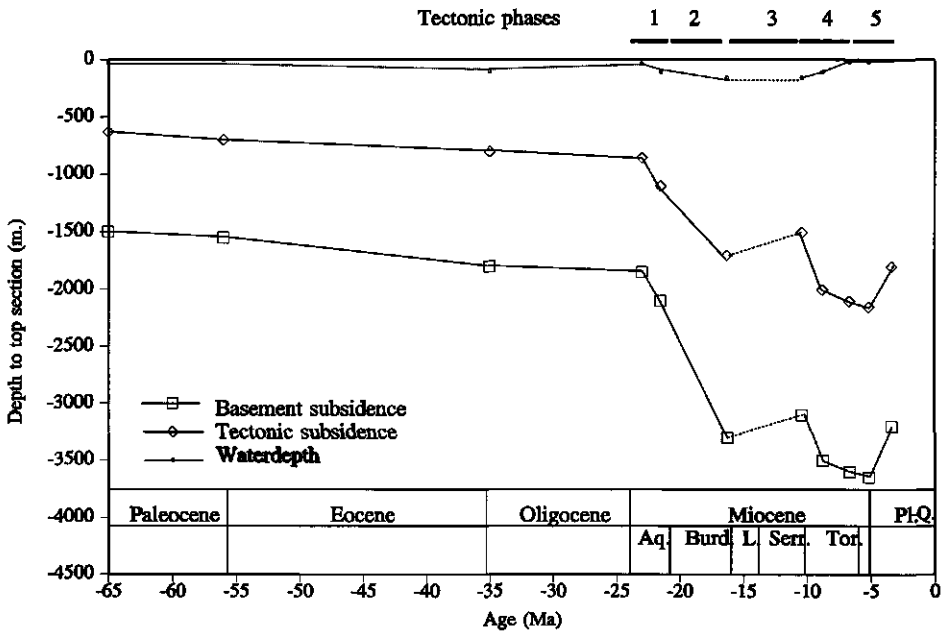


Fig. 2.13: Tertiary subsidence curves for the southern Subbetic Zone near Ronda. Tectonic and basement subsidence derived from quantitative subsidence analysis incorporating paleowaterdepth and eustatic sealevel fluctuations.

Dercourt *et al.* (1986), Savostin *et al.* (1986), and Srivastava *et al.* (1990) showed that a sinistral transtensional zone developed after the Late Triassic-Early Jurassic rifting, which separated Iberia from North Africa. This strike-slip zone connected the Jurassic Central Atlantic basin with the Ligurian basin east of Iberia (Dercourt *et al.*, 1986). Movement on this strike-slip system and simultaneous initiation of the Central and South Atlantic rifts (Savostin *et al.*, 1986) coincides with Middle-Late Jurassic rifting (Fig. 2.12, rift event 3). North Atlantic rift propagation between Iberia and Newfoundland commenced after the Bathonian-Callovian, contemporaneously with crustal separation in the South Atlantic and Ligurian oceans (Dercourt *et al.*, 1986; Lemoine & Trümpy, 1987; Srivastava *et al.*, 1990). At the same time, the Subbetic Zone experienced strong subsidence and mafic volcanism related to rifting (Puga *et al.*, 1989a); in the Mulhacen Complex the widespread occurrence of olivine-bearing gabbros (De Jong & Bakker, 1991) and pillow lavas (Puga *et al.*, 1989b) evidence crustal extension.

The Middle Cretaceous extension period of Fig. 2.12 (rift event 4) is not commonly recognized in basin studies of the Betic Cordilleras. Peper & Cloetingh (1992) recognized a

Middle Triassic, an Early Jurassic, and a Late Jurassic-Early Cretaceous rifting phase. However, Cenomanian extensional fault activity is well known from the Prebetic Zone (De Ruig, 1992) and olistostromes of Middle and Late Cretaceous age have been reported by various authors (e.g. Paquet, 1967; Vera *et al.*, 1982). There are no clear indications to relate this extensional phase to plate-tectonic movements. Sea floor spreading patterns in the Central Atlantic Ocean suggest that Iberia moved independently from Africa and Eurasia (Srivastava *et al.*, 1990) and rotated clockwise triggering transtensional movements in the Bay of Biscay (Puigdefàbregas & Souquet, 1986; De Jong, 1991). De Jong (1991) argues that these transtensional movements were compensated by subduction and continental thrusting in the Internal Betics, east of Iberia. This interpretation, however, is not consistent with the observed extension in both the Prebetic and Subbetic Zones.

The Coniacian-Late Oligocene subsidence history of the southern Subbetic Zone (Figs 12, 13) shows relatively low and decelerating subsidence rates indicating that rifting activity ceased and stable conditions prevailed. However, both the Internal and External Zones of the Betic Cordilleras record tectonic phases which can be correlated with collision in the Pyrenean domain (De Ruig *et al.*, 1991). Maastrichtian-Danian and Middle Eocene uplift was found by Kenter *et al.* (1990) in the External Zone. De Ruig (1992) pointed out that a regression 60Ma ago accompanied by slope faulting and associated olistostromes marked a phase of Middle Paleocene compression. He suggested that uplift of basin flanks and subsidence of the basin centre indicate a continental margin under compression causing a magnification of the peripheral bulge and subsequent seaward migration of the shoreline (see Cloetingh *et al.*, 1985). The Paleocene sediment record of the southern Subbetic Zone of the Ronda-Málaga region that has been investigated here shows widespread occurrence of in-situ *Microcodium* which indicates subaerial exposure (Klappa, 1978) reflecting a shallowing rather than a deepening of this part of the basin.

The Eocene sedimentary record of the southern Subbetic Zone shows an initial influx of non-calcareous detritus in the Early Eocene, associated with sandy turbidites. This seems to correspond to the Eocene compression interpreted by Geel (1973). In the subsidence record, the Eocene tectonic events are not resolved, possibly because the magnitude of these events is too small to trigger a significant uplift in the central part of the basin. Eocene compression can be directly related to the collision in the Pyrenees which began 59Ma ago and culminated in the Middle Eocene as a result of northward movement of Africa and Iberia (Srivastava *et al.*, 1990). This movement gradually ceased in the Late Oligocene as Iberia became part of the Eurasian plate. Simultaneously, compressive deformation concentrated on the Iberian continental margin.

A phase of Late Oligocene-Aquitania extension is well known throughout the western Mediterranean (Rehault *et al.*, 1984; De Ruig, 1992; De Jong, 1991). Renewed subsidence

during the Aquitanian (Fig. 2.13, tectonic phase 1) indicates this extension in our subsidence record. Extension in the Betic Cordilleras was immediately followed by thrust emplacement of the Internal Betic Zone onto the southern Iberian margin. De Jong (1991) argued that thrust emplacement occurred between 21.5 and 19Ma. This corresponds to a Burdigalian peak of subsidence in Fig. 2.13 (tectonic phase 2).

Following the thrusting of the Internal Zone onto the Iberian margin, a period of strike-slip related tectonics (Bon *et al.*, 1989) affected the Betic Cordilleras during the Late Langhian and Serravallian (Fig. 2.13, tectonic phase 3). Recent investigations showed that strike-slip related tectonics continued until the Pliocene (e.g. Kleverlaan, 1989; Van der Straaten, 1993). Dextral wrench movement resulted in the formation of N70°E and N100°E strike-slip faults and associated intramontane pull-apart basins in the eastern Betic Cordilleras (Montenat *et al.*, 1987), as for example the Abáran basin described by Van der Straaten (1990, 1993). Simultaneously, basins developed in the western Betic Cordilleras, like the Neogene basin north of Ronda. The subsidence curve shows that the southern Subbetic Zone emerged contemporaneously with this wrenching. Many authors have suggested that the westward movement of the Alboran microplate relative to the Iberian margin along the Crevillente and North Betic fault zones was the principal cause of this strike-slip related deformation (Le Blanc & Olivier, 1984; Andrieux *et al.*, 1971). More recently, these wrench fault zones were interpreted as major tear faults accommodating westward overthrusting of the Internal or Betic nappe pile over the External Zone (e.g. Frizon de Lamotte *et al.*, 1991).

Renewed extension during the Tortonian and Messinian (Fig. 2.13, tectonic phase 4) is indicated by coarse terrigenous influx of detritus and rapid subsidence of the basin. Post-dating this event is a compressional phase in the Pliocene (Fig. 2.13, tectonic phase 5) causing the observed N-S trending folds in the Tortonian and Messinian sediments. The Tortonian-Pliocene sedimentary and tectonic history of the Ronda-Málaga region is interpreted as resulting from strike-slip related deformation. The Neogene basins opening during the Late Miocene are considered pull-apart basins related to NE-SW trending strike-slip faults.

## 2.5 CONCLUSIONS

The Ronda-Málaga region, forming part of the southern Subbetic Zone of the Betic Cordilleras, has been the site of polyphase tectonism resulting in rapidly changing sedimentary environments throughout the Tertiary.

Throughout the Triassic the Ronda-Málaga region was the scene of continental conditions and supratidal environments in the north and intertidal and shallow marine environments to the south. During the Jurassic and Cretaceous the area formed part of the

slope of the Iberian continent as shallow marine shelf conditions prevailed with environments deepening southward. The onset of the Tertiary marked a period of increased tectonic activity resulting in the development of a submarine fan complex fed by large quantities of clastics shed in from the north. A reversal of facies patterns is observed in the Burdigalian during which detritus supply was dominantly from the south. The entire area emerged during the Serravallian and Langhian. After this, deposition resumed and continued throughout the Late Miocene in a number of narrow basins.

Quantitative subsidence analysis of stratigraphic data from the southern Subbetic Zone exposed near Ronda revealed a number of phases of accelerated subsidence which can be correlated with tectonic events in the Central Atlantic Ocean and with the deformation history of the western Mediterranean and the Betic Cordilleras. The Mesozoic subsidence history is characterized by four periods of rifting: (1) a Middle Triassic period (Anisian-Ladinian; 241-235Ma), (2) a Late Triassic-Early Jurassic period (Norian-Hettangian; 223-203Ma), (3) a Middle-Late Jurassic period (Callovian-Tithonian; 161-146Ma), and (4) a Middle Cretaceous period (Cenomanian-Turonian; 97-89Ma). The stress regime changed from extensional to mainly compressional in the Paleocene, related to the onset of the Pyrenean collision. The end of this collision in the Late Oligocene marks the beginning of accelerated but localized subsidence related to a period of NNE-SSW extension during the Aquitanian. The rapid local subsidence during the Burdigalian is related to NW-SE thrusting of the Internal Zone over the External Zone and subsequent emplacement of the Subbetic Zone over the Prebetic Zone. During the Late Langhian and Serravallian, the area emerged; northward directed movement was blocked and a system of wrench faults developed of which the North Betic fault zone and the Crevillente fault zone were the most important. During the Tortonian, local extension basins developed as pull-apart corridors within a period of wrench-related deformation which continued throughout the Late Miocene and Pliocene. Late-stage compression during the Pliocene is evidenced by N-S to NNE-SSW trending folds in Tortonian and Messinian sediments.

## CHAPTER 3:

### *A review of the tectonic evolution of the Ronda peridotite massif*

#### ABSTRACT

Ultramafic rocks belonging to the Alpujarride complex of the Betic Cordilleras crop out in the Sierra Alpujata and Sierra Bermeja west of Málaga. These show a progressive reduction of grain size toward the boundary with the underlying crustal rocks. A sharp downward increase of metamorphic grade in the units overlying the peridotites may be caused by extension-induced mantle upwarping. From the systematic analysis of quartz *c*-axes, olivine lattice preferred orientation fabrics, and other shear sense indicators, ductile thrusting of the hot peridotites in northeastern direction is inferred by several authors. Paleostress analysis carried out on limestones of the Subbetic zone exposed east of Ronda yield three main paleostress directions: ( 1 ) a stress tensor with a nearly vertical  $\sigma_1$  direction and horizontal  $\sigma_2$  and  $\sigma_3$  directions where the average  $\sigma_3$  orientation is N45°W (indicating normal faulting), ( 2 ) a stress tensor with  $\sigma_3$  nearly vertical and  $\sigma_1$  and  $\sigma_2$  nearly horizontal where the average  $\sigma_1$  orientation is N20°W (indicating reversed and thrust faulting), and ( 3 ) a stress tensor with  $\sigma_2$  nearly vertical and  $\sigma_1$  and  $\sigma_3$  nearly horizontal where  $\sigma_1$  varies with maxima at N30°E and N80°W directions (indicating strike-slip faulting). Microstructural evidence shows that the extensional stress tensors represent an older phase of deformation followed by compression. Since small-scale faults were measured in rocks of late Cretaceous age, the extension cannot be attributed to Jurassic rifting events. It is thus concluded that the fault surfaces measured developed under an extensional stress regime during late Oligocene-Aquitainian (see Chapter 2). The compressive stress tensor is consequently related to Burdigalian compression and the stress tensors indicating strike-slip tectonics are related to the late Langhian-Serravalian wrenching tectonics. Paleostress analysis carried out on fault surfaces and striations within the peridotites (resulting from serpentine crystallization) also revealed three predominant stress tensors. A tensor indicating N10°W directed extension, a tensor indicating N50°W directed compression, and a tensor related to N80°E directed wrenching. It is suggested that the Ronda peridotites have undergone at least three phases of late stage brittle deformation related to their final emplacement at crustal levels. The final emplacement took place after a period of late Langhian-Serravalian strike-slip related tectonics during which the peridotites were transplaced eastward along a dextral strike-slip corridor which developed along the former thrust contact.

### 3.1 INTRODUCTION

Peridotite massifs crop out on both sides of the Alboran Sea, at Beni Bouchera in Africa and near Ronda (southern Spain; Fig. 3.1) where they are generally regarded as belonging to the Alpujarride complex. Mafic layers enclosed in the peridotites show evidence of recrystallization along a decreasing P-T gradient and are considered to be partial fusion products resulting from the adiabatic rise of hot masses of peridotite (Dickey, 1970). From isotopic (Obata, 1980; Reisberg *et al.* 1989, 1991) and elemental studies (Frey *et al.* 1985; Suen & Frey, 1987) it was concluded that these ultramafic masses equilibrated at upper mantle temperatures and pressures (Suen & Frey, 1987) and must therefore have undergone considerable diapiric uprise. In addition, the presence of graphite pseudomorphs in both the Beni Bousera peridotite (Pearson *et al.*, 1989; Tabit *et al.*, 1990) and the Ronda peridotites (Davies *et al.*, 1993) indicate a deep origin at lithospheric or asthenospheric levels.

There is a still ongoing debate concerning the mode and timing of emplacement of the Ronda peridotites. Most authors agree on a first "hot" stage of emplacement related to diapiric uprise of these mantle bodies. A second "cold" phase of thrusting is recognized by some authors (e.g. Lundeen, 1978; Tubía, 1988a; Tubía & Cuevas, 1986; Westerhof, 1977; Obata, 1980) and debated by others (e.g. Loomis, 1972a+b; Bonini *et al.*, 1973; Doblas & Oyarzun, 1989). One more question related to the mode of emplacement of the Ronda peridotites is the direction of thrusting during the second "cold" deformation phase. Kornprobst (1976), Westerhof (1977), Lundeen (1978), and Obata (1980) favour a westward thrusting, others (Balanya & Garcia-Dueñas, 1987; Tubía & Cuevas, 1986; 1987) favour an east-northeast directed phase of thrusting followed by a northwest directed phase of thrusting.

Radiometric dating has constrained the emplacement of the peridotites as  $22 \pm 4$  Ma (Priem *et al.*, 1979; Zindler *et al.*, 1983; Reisberg *et al.*, 1989). Priem *et al.* (1979) from biotite analysis dated the cooling of the peridotites as 19.5Ma.

In this Chapter, it is demonstrated that the Ronda peridotites record evidence of three major phases of deformation: extensional tectonics, and compressional tectonics developing into wrenching type of tectonic deformation.

### 3.2 REGIONAL GEOLOGIC SETTING

The Ronda Peridotites form three large bodies ( $\pm 300\text{km}^2$ ) cropping out in the western part of the Alpine Betic Cordilleras in the Sierra Bermeja, the Sierra Alpujata, and near Carratraca. Structurally, these ultramafic masses are part of the Higher Alpujarride nappe units (Westerhof, 1975; Tubía *et al.*, 1992; Fig. 3.2). They form the base of the Los Reales nappe

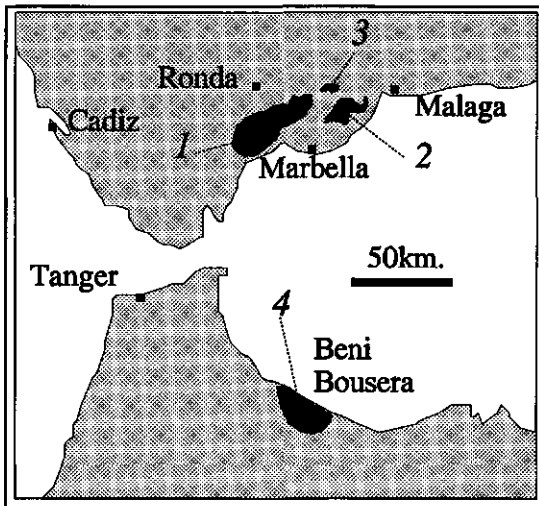


Fig. 3.1: Location of the ultramafic bodies in southern Spain and northern Morocco (1 = Sierra Bermeja peridotite body studied in this Chapter, 2 = Sierra Alpujata peridotite body, 3 = Sierra Ojén peridotite body, 4 = Beni Bousera peridotite body).

(Navarro-Vila & Tubía, 1983) of which the top corresponds to a metamorphic series (see Fig. 3.3). The Los Reales nappe is overlying the Ojén nappe, a metapelitic sequence overlain by a thick series of dolomitic marbles. The Ojén nappe is part of the Blanca unit referred to by Didon *et al.* (1973) and Mollat (1965, 1968), whereas Loomis (1972a) refers to it as the "Hornfels series". Within 500m. of the contact of Los Reales and Ojén nappe in the Sierra Alpujata, coarse-grained migmatites containing K-feldspar, plagioclase, cordierite, and quartz crop out which belong to the Ojén nappe. In the vicinity of the contact with the peridotites, these rocks display a intense mylonitic texture and contain biotite, sillimanite, and garnet (Tubía & Cuevas, 1986). The peridotites of the Los Reales nappe are composed mainly of lherzolites, with minor dunites and harzburgites (Obata, 1980). The contact between the peridotites of the Los Reales nappe and the migmatites of the Ojén nappe is an undulating surface with dips ranging from less than 5° to a maximum of 15° (Lundeen, 1978). Overlying the peridotites is a series of schists, gneisses and kinzigites showing metamorphic grades from greenschist facies to high-grade granulite facies (Dürr, 1967; Loomis, 1972a).

Van der Wal (1993) and Van der Wal & Vissers (1993) mapped the Ronda peridotites exposed in the Sierra Bermeja showing three main structural domains: ( 1 ) porphyroclastic spinel peridotites and mylonitic garnet-spinel peridotites in the northwestern part of the massif, ( 2 ) undeformed coarse-grained granular peridotites in the central part, and ( 3 ) porphyroclastic plagioclase peridotites in the southeastern part of the massif. Obata (1980) interpreted the garnet-spinel-plagioclase zonation of the peridotite massif as representing the uprise and subsequent cooling of hot mantle material. Van der Wal & Vissers (1993) present a new tectonic scenario based on inferred pressure-temperature trajectories (Van der Wal, 1993). These authors propose five phases of uplift and emplacement: ( 1 ) a Jurassic-Early

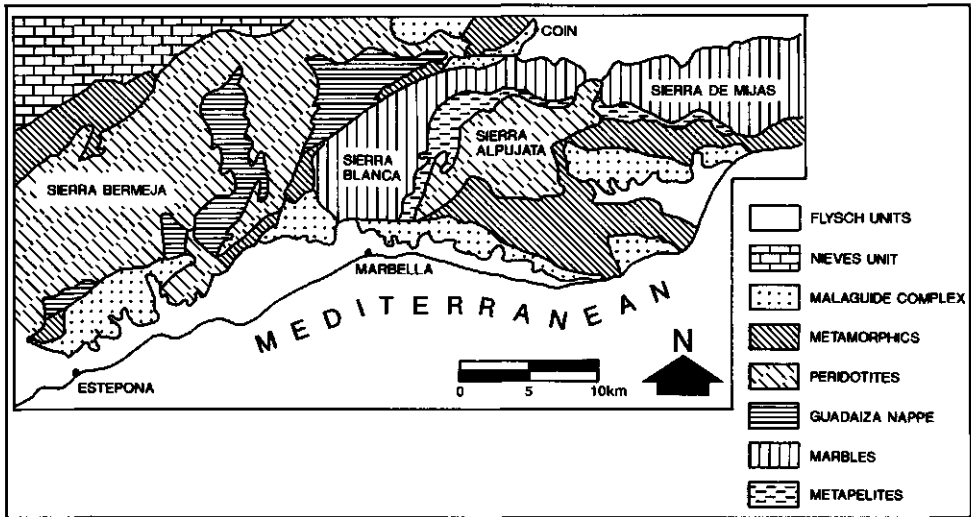


Fig. 3.2: Generalized geologic map of the southern Betic Cordilleras (Modified after Tubía, 1988b).

Cretaceous (?) early uplift from depths of 150km (represented by the diamond stability field; Davies *et al.*, 1993) into the spinel peridotite stability field, ( 2 ) Early Cretaceous and Paleocene cooling due to subduction and underthrusting, ( 3 ) subsequent slab detachment in Oligocene (Blanco & Spakman, 1993) triggering asthenospheric flows leading to the ascent of the asthenospheric mantle and resulting in uplift and heating, ( 4 ) Oligocene-Miocene extensional collapse leading to the emplacement of mantle fragments in the crust, and ( 5 ) thermal subsidence since middle Miocene. Data from Zeck *et al.* (1992) also indicate high and variable magnitudes and rates of cooling and uplift during a period ranging from 22 to 15.5 Ma.

### 3.3 A REVIEW OF FIELD AND MICROSTRUCTURES

In this section, a review of field and microstructures is presented indicating shear sense observed in the Ronda peridotites of both the Sierra Alpujata and the Sierra Bermeja. The data on the Sierra Alpujata peridotites mainly comes from Tubía (1985; 1988b) and Tubía & Cuevas (1986, 1987), whereas the data on the Sierra Bermeja peridotites mainly comes from Van der Wal (1993) and Van der Wal & Vissers (1993).



- the Ronda peridotite massif -

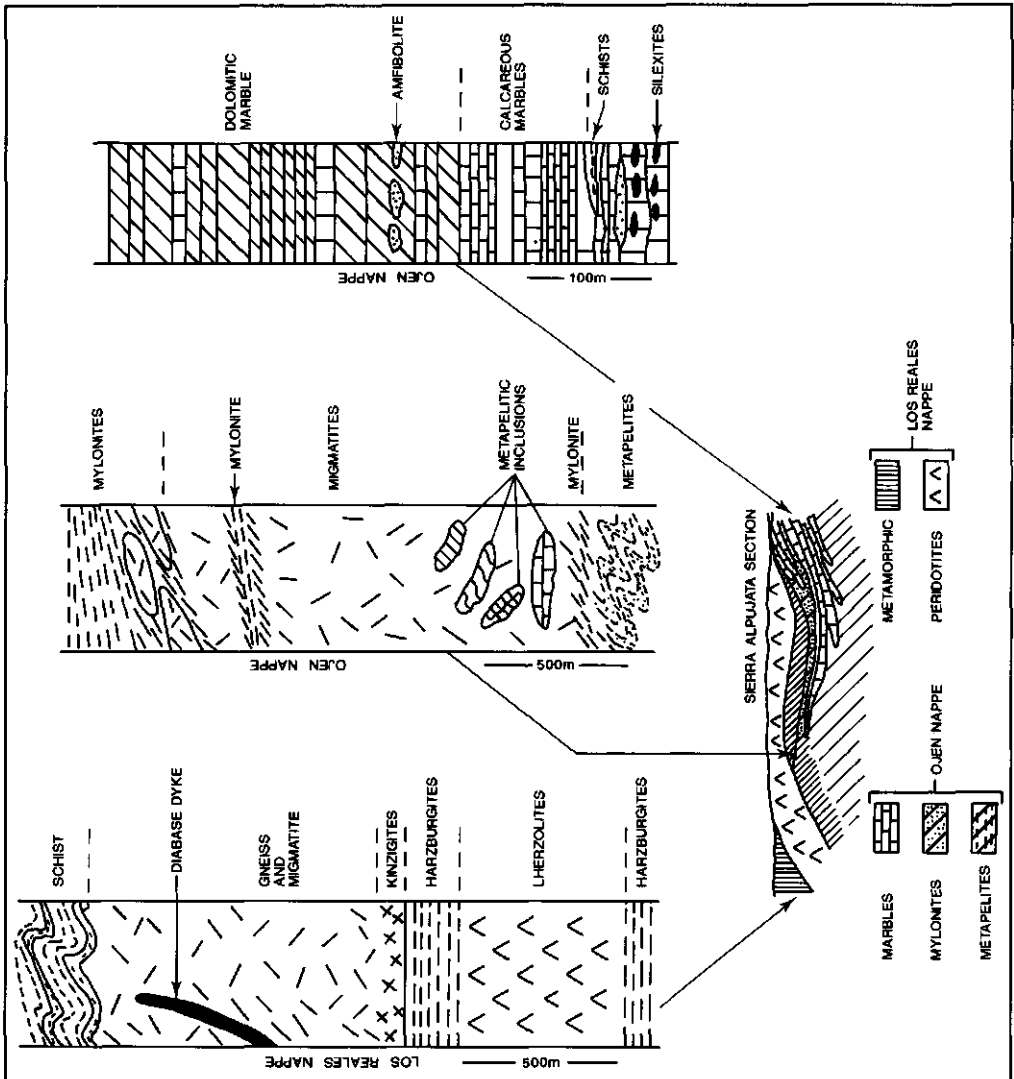


Fig. 3.3: Synthetic cross section through the Sierra Alpujata showing lithological and structural variation near the contact between the Ojén and Los Reales nappes (partly after Tubía & Cuevas, 1986; 1987).

### 3.3.1 the Sierra Alpujata

A mylonitic foliation is found in rocks of both the Los Reales nappe and the Ojén nappe developing parallel to the contact striking N110°E on average and dipping moderately south (Fig. 3.4). This foliation is defined by the shape and orientation of quartz and feldspar in the Ojén nappe and by olivine and enstatite in the Los Reales nappe. Associated with the foliation, a strongly defined penetrative stretching lineation appears with an azimuth of N70°E on the average. In the migmatites of the Ojén nappe it is marked by the elongation of biotite and sillimanite aggregates, in the peridotites enstatite porphyroclasts define the lineation.

Both the peridotites and migmatites show a progressive reduction in grain-size and a variation in grain-shape toward the contact. The core of the peridotite massif shows coarse-grained porphyroclastic and granular textures with mainly olivine and pyroxenes which are reduced to fine-grained mylonitic textures of mainly olivine including enstatite porphyroclasts in a zone of 300m. from the contact. In the migmatites of the Ojén nappe, quartz-feldspar mylonites are common with minor olivine and enstatite. Quartz *c*-axis orientations have been investigated using XZ sections (Tubía & Cuevas, 1986) of samples (Fig. 3.4); that is parallel to the stretching lineation and perpendicular to the foliation. Thus it is assumed that the foliation defined in part by flattened quartz grains is representing the XY plane of the finite strain ellipsoid (Behrmann & Platt, 1982). The quartz diagrams have in common important concentrations of the *c*-axes in the area of the Y-axis of the finite strain ellipsoid frequently attributed to the activity of prismatic {*m*} slip planes along the  $\langle a \rangle$  slip direction (Wilson, 1975; Bouchez, 1977). The diagrams show a pattern composed of a unique girdle and a strong maximum of *c*-axes perpendicular to the girdle considered as a particular case of the high-angle crossed-girdle pattern described by Lister & Dornsiepen (1982) and Lister & Williams (1979).

In the peridotites of the Sierra Alpujata, the enstatite crystallographic orientations have the [001] and [100] axes respectively at a small and a large angle to the lineation, and the [010] contained in the XY plane indicating plastic deformation occurring according to the (100)[001] slip system (Nicolas & Poirier, 1976; Fig. 3.5). From the distribution of olivine [100] and [010] axes (Fig. 3.5) Tubía & Cuevas (1986) deduced a deformation regime in the flattening domain at low temperatures ( $T^{\circ} < 950^{\circ}\text{C}$ ).

### 3.3.2 the Sierra Bermeja

Foliation in the peridotite dips steeply to the NW and SE and is defined by preferred orientation of elongated olivines. Stretching lineations in the foliation plane are dominantly

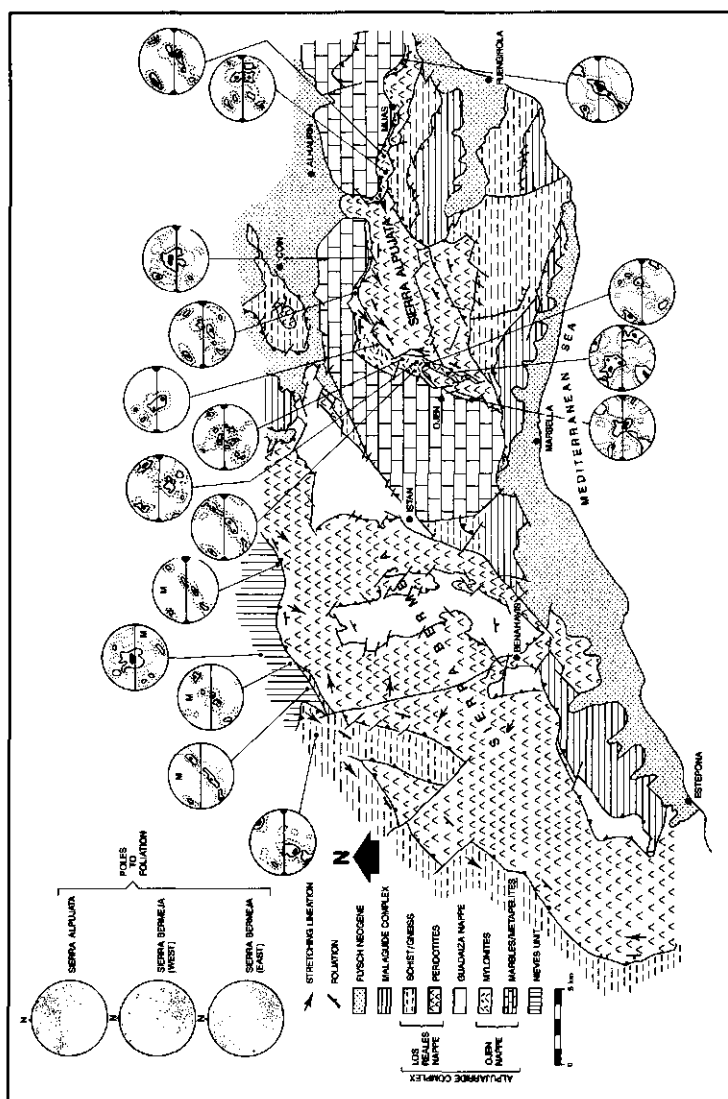


**Fig. 3.4:** Geologic map of the Sierra Bermeja and Sierra Alpujata peridotites and adjacent units. Orientation of poles of the mylonitic foliation measured in the Western and eastern Sierra Bermeja and the Sierra Alpujata, respectively, are given in the diagrams of the upper left corner of the figure. Other diagrams are quartz c-axis orientation diagrams showing XZ sections; X is the stretching lineation, and Y is the foliation (solid line in diagram). Those indicated with M are derived from long axes of calcite in marbles. The orientation fabrics indicate top-to-the-northeast shear sense. (Contour levels are 1, 3, 5%). Data are after Tubía & Cuevas (1986), Tubía (1988a+b) and Van der Wal (1993).

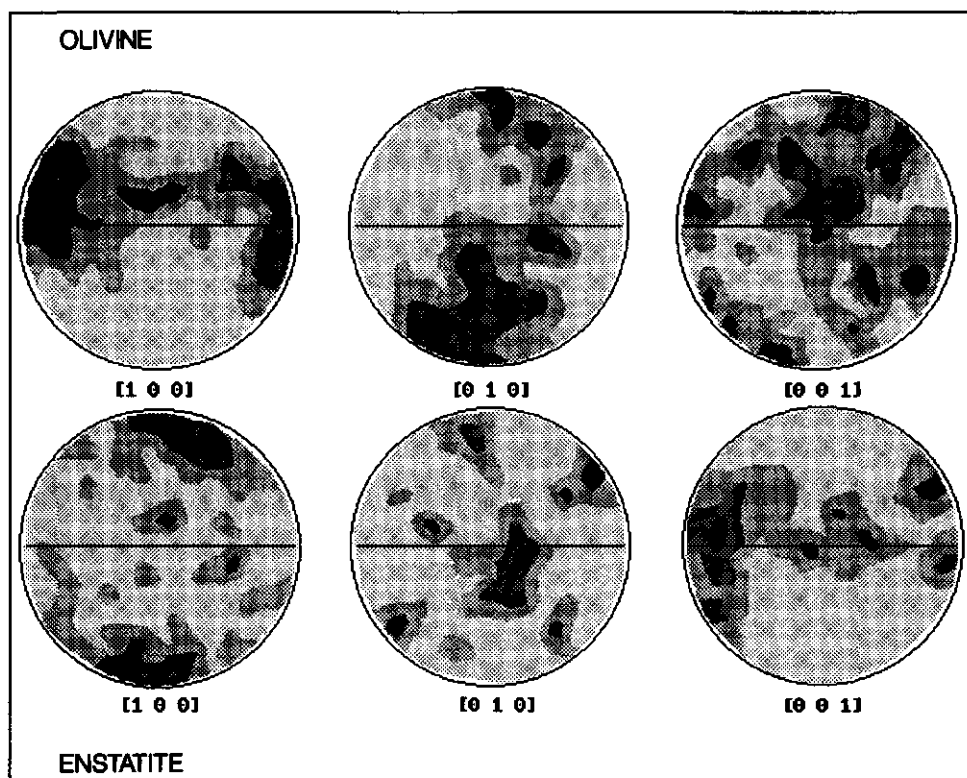
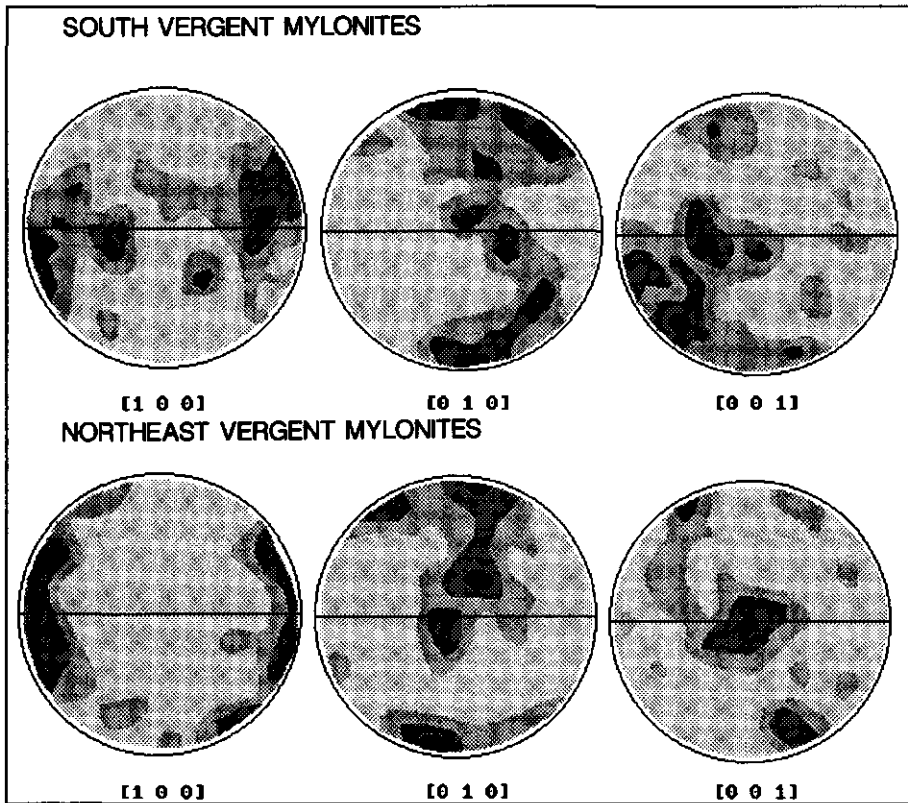


Fig. 3.5: Olivine (top) and Enstatite (bottom) preferred orientations in the peridotites from the Sierra Alpujata. XY sections; X is the stretching lineation, Y is the foliation (solid line in diagrams). The obliquity of [100] of olivine, and [001] and [100] of enstatite relative to the shape fabric indicate dextral shear sense (Contour levels are 1, 3, 5%). Data from Tubía & Cuevas (1986).

subhorizontal or dip moderately towards the SW (Fig. 3.4). Quartz *c*-axes orientations and preferred orientation of calcite *c*-axes examined in quartz-feldspar mylonites and marbles, respectively, forming the northern contact with the peridotites in the eastern Sierra Bermeja, show similar patterns as those described above from the Sierra Alpujata (Fig. 3.4). Van der Wal (1993) discusses olivine lattice preferred orientations from the western Sierra Bermeja. These show olivine [100] concentrated in a point maximum at small angles to the foliation plane, olivine [010] concentrated in a point maximum perpendicular to the foliation, and olivine [001] showing a maximum at large angles to the stretching lineation in the foliation plane. This fabric suggests intracrystalline slip on the olivine [100](0kl) slip-systems (Bouchez *et al.*, 1983; Van der Wal, 1993). In addition, Van der Wal (1993) shows S-vergent mylonites overprinted by N/E vergent mylonites both showing essentially similar olivine



**Fig. 3.6:** Olivine lattice preferred orientation fabrics of south- (top) and northeast (bottom) vergent mylonites from the Sierra Bermeja peridotites indicating top-to-the-north and top-to-the-southwest shear sense respectively. (Contour levels 1, 3, 5%). Data after Van der Wal (1993).

patterns with olivine [100] concentrated at small angles to the lineation, olivine [010] distributed along a partial girdle perpendicular to the foliation and lineation, and olivine [001] distributed along a girdle with a point maximum in the foliation plane (Fig. 3.6). This demonstrates crystal plastic slip on the olivine [100]{0kl} slip system during non-coaxial flow (Ave Lallemant & Carter, 1970; Van der Wal, 1993).

C-S structures as described by Berthé *et al.* (1979) are common in mylonitic gneisses bordering the peridotite to the north. These structures often develop into shear bands (Fig. 3.7a) where a late, weakly penetrative foliation develops at low angle to the mylonitic foliation (Berthé *et al.*, 1979; White *et al.*, 1980) indicating high strains (Simpson & Schmid, 1983). In quartz-feldspar mylonites, K-Feldspar appearing as porphyroclast often shows microfractures, having opposite sense of shear to the over-all shear sense in the rock, oriented

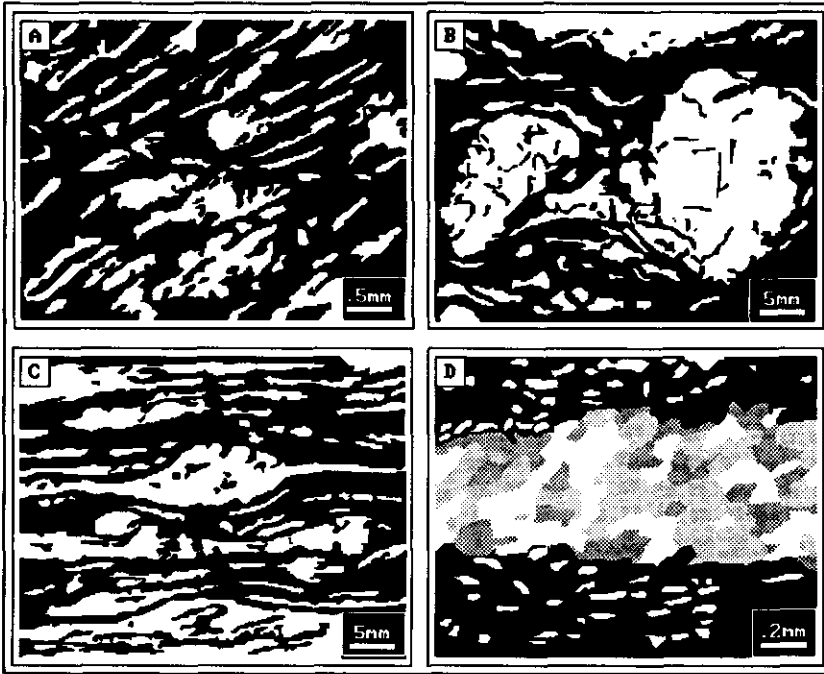


**Fig. 3.7:** Microstructures indicating dextral shear. (A) shear band in mica-rich mylonites in the Sierra Bermeja, (B) broken and displaced K-feldspar porphyroclast with asymmetric pressure shadow in a ductile matrix (after Tubía & Cuevas, 1986), (C) asymmetric K-feldspar augen in a mylonitic gneiss, (D) quartz subgrains and recrystallized grains with flattening plane oblique to the foliation plane (foliation parallel to the long axis of the drawing).

oblique to the foliation planes. Such displaced grains have also been reported in the mylonites of the Ojén nappe in the Sierra Alpujata by Tubía & Cuevas (1986; their Figure 4c). Asymmetric augen structures in quartz-feldspar mylonites are common shear sense indicators (Fig. 3.7c). Finally, subgrains and recrystallized grains with their flattening plane oblique to the foliation plane (Fig. 3.7d) often indicate dextral shear in mylonitic gneisses forming the contact with the peridotites in the Eastern Sierra Bermeja. The obliquity of elongate grain shapes to the foliation plane may be explained by the fact that the observed recrystallized grains and subgrains form relatively late during progressive shearing deformation (Schmid *et al.*, 1981; Brunel, 1980).

### 3.4 NEW PALEOSTRESS DATA

#### 3.4.1 Theory

Paleostress tensors were derived from the analysis of small-scale fault slip data using striated fault planes.

Fault slip data collected (i.e. a set of fault planes and associated lineations derived from striations) were processed using a computer program (Smid & Heijke, 1987) based on the method of Michael (1984; see also Angelier, 1984; 1989). This method assumes that all measured slip events are independent, that the stress tensor is homogeneous for a given phase, and that the magnitude of the tangential traction is similar on different fault planes. The program of Smid & Heijke (1987) allows to stepwise calculate several stress tensors from a given population of fault planes measured at a particular location. During each iteration, the angle between the measured and calculated shear stress (the tolerance angle of angular deviation;  $\Delta$ ), can be lowered such that a number of strongly deviating observations are eliminated prior to calculating the stress tensor. Stepwise decrease of the tolerance angle finally results in a stable stress tensor derived from a small number of measurements out of the total population of fault planes. Simultaneously, the stress-ratio,  $\Phi = (\sigma_2 - \sigma_3) / (\sigma_1 - \sigma_3)$ , is computed giving a measure for the relative sizes of the principal stresses (Angelier, 1984; 1989). A value of  $\Phi$  smaller than 0.3 indicates that the size of  $\sigma_2$  and  $\sigma_3$  is similar, if  $\Phi$  is higher than 0.6,  $\sigma_1$  and  $\sigma_2$  are similar in size and permutation of these stress axes may occur. With the remaining data, the process can be repeated to examine the data for other stress tensors occurring.

Other sources of paleostress data are tectonic stylolites, extension veins, and small-scale conjugate fault sets (De Charpal *et al.*, 1974). Stylolites often occur in carbonate rocks. These stylolites are composed of thin layers rich in clay minerals, opaque minerals, and fine quartz grains which represent insoluble residual material. They are often sharp peaked or show columnar cross-sections in which the caps of the columns contain thick seams of residue, and the sides of the columns are striated and have less residue. This is thought to indicate pressure solution across the caps and slip parallel to the column axis (Park & Schot, 1968). Two types of stylolites are generally recognized: ( 1 ) bedding-parallel stylolites formed due to compaction, and ( 2 ) tectonic stylolites forming an stylolitic cleavage as a result of compression. The tectonic stylolites mainly form in argillaceous limestones of the late Cretaceous "Capas Rojas" units (K2) and the middle-late Jurassic limestones (J3-J4) which have a low content of coarse terrigenous detritus. The orientation of the tectonic stylolite columns is interpreted as being parallel to the maximum compressive stress,  $\sigma_1$ ,

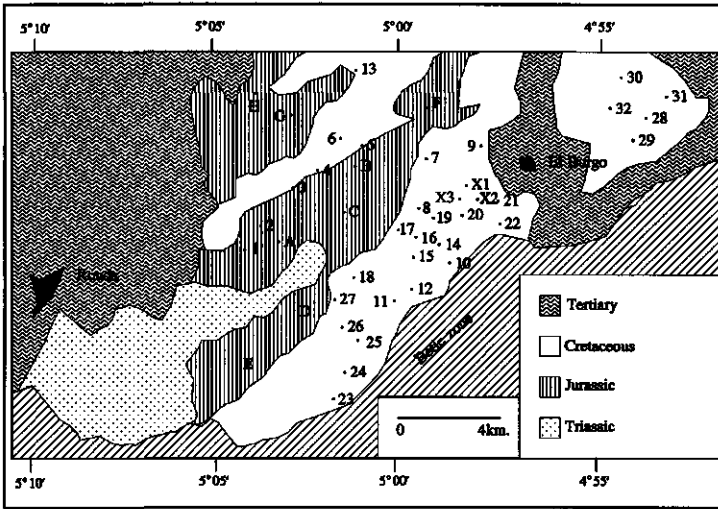


Fig. 3.8: Stress tensors (A) location of stations (numbers refer to Table 3.1), (B) tensors indicating extension (Table 3.1a), (C) tensors indicating compression (Table 3.1b), and (D) tensors indicating wrenching (Table 3.1c). Stress tensors derived from stylolites, extension veins and conjugate fault sets are shown in Table 3.1d.

(Choukroune, 1969; Arthaud & Choukroune, 1972; Geiser & Sansone, 1981) and can therefore yield a paleostress tensor. Associated with tectonic stylolites, calcite-filled co-genetic extension veins occur which record the orientation of  $\sigma_3$ . Conjugate sets of sigmoidal calcite-filled veins related to small-scale shear zones were also incorporated in the paleostress analysis.

### 3.4.2 Results and interpretation

Paleostress analysis was carried out on limestones of the Subbetic zone exposed east of Ronda and on the peridotites and adjacent marbles. Three main paleostress directions that can be distinguished from the analysis of the Subbetic limestones (Fig. 3.8) are: ( 1 ) a stress tensor with a nearly vertical  $\sigma_1$  direction and horizontal  $\sigma_2$  and  $\sigma_3$  directions where the average  $\sigma_3$  orientation is N45°W (indicating normal faulting), ( 2 ) a stress tensor with  $\sigma_3$  nearly vertical and  $\sigma_1$  and  $\sigma_2$  nearly horizontal where the average  $\sigma_1$  orientation is N20°W (indicating reversed and thrust faulting), and ( 3 ) a stress tensor with  $\sigma_2$  nearly vertical and  $\sigma_1$  and  $\sigma_3$  nearly horizontal where  $\sigma_1$  varies with maxima at N30°E and N80°W directions (indicating strike-slip faulting). In Table 3.1, the orientation and characteristics of computed stress tensors are given. Dating of these stress tensors is done using overprinting relations in the field at two different scales: regional scale and microstructural scale. On a regional scale (see also the discussion and interpretation of the subsidence record presented in Chapter 2), the oldest structures found in rocks of the Subbetic zone near Ronda are a set of NNW-SSE and NNE-



- the Ronda peridotite massif -

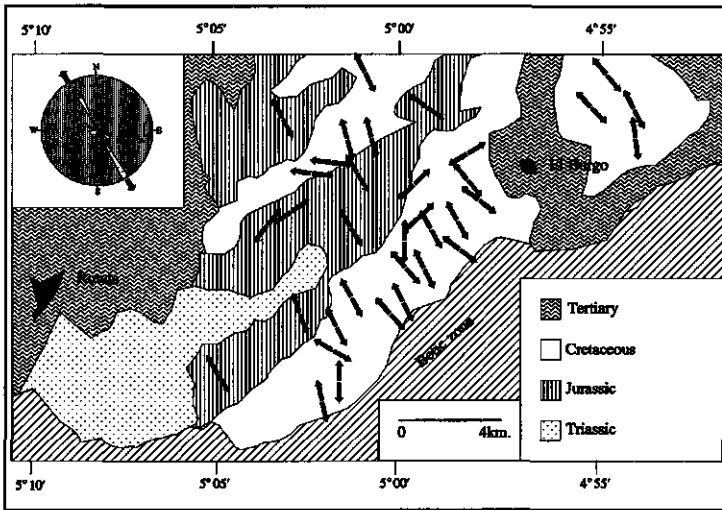


Fig. 3.8b

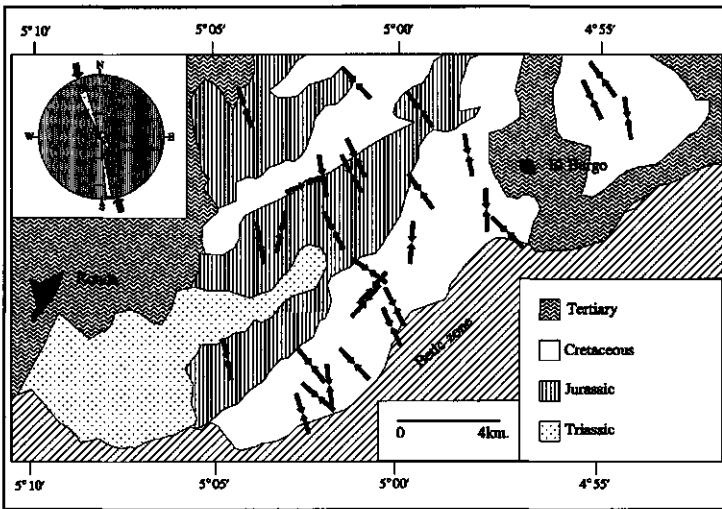


Fig. 3.8c

SSW trending normal faults. These terminate at Miocene formations indicating that they formed prior to the Miocene. An older set of normal faults trending NE-SW are found along the mountain ranges. These follow the so-called "Betic Trend" which according to some authors represents the trend of basement faults (Rodríguez-Estrella, 1977; Azéma *et al.*, 1979). These basement faults are thought to have controlled the paleogeographic differentiation during the Mesozoic-Paleogene passive marginal setting for the External Betic Zone, and were used as fold-thrust ramps during Neogene shortening. The variation of the thickness of the

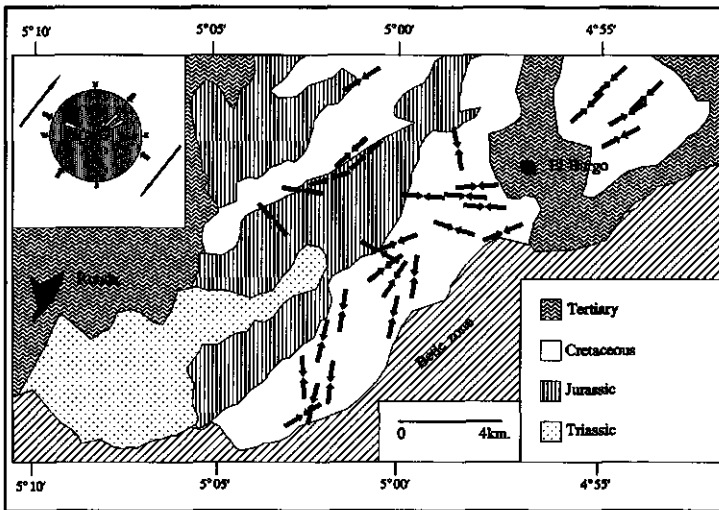
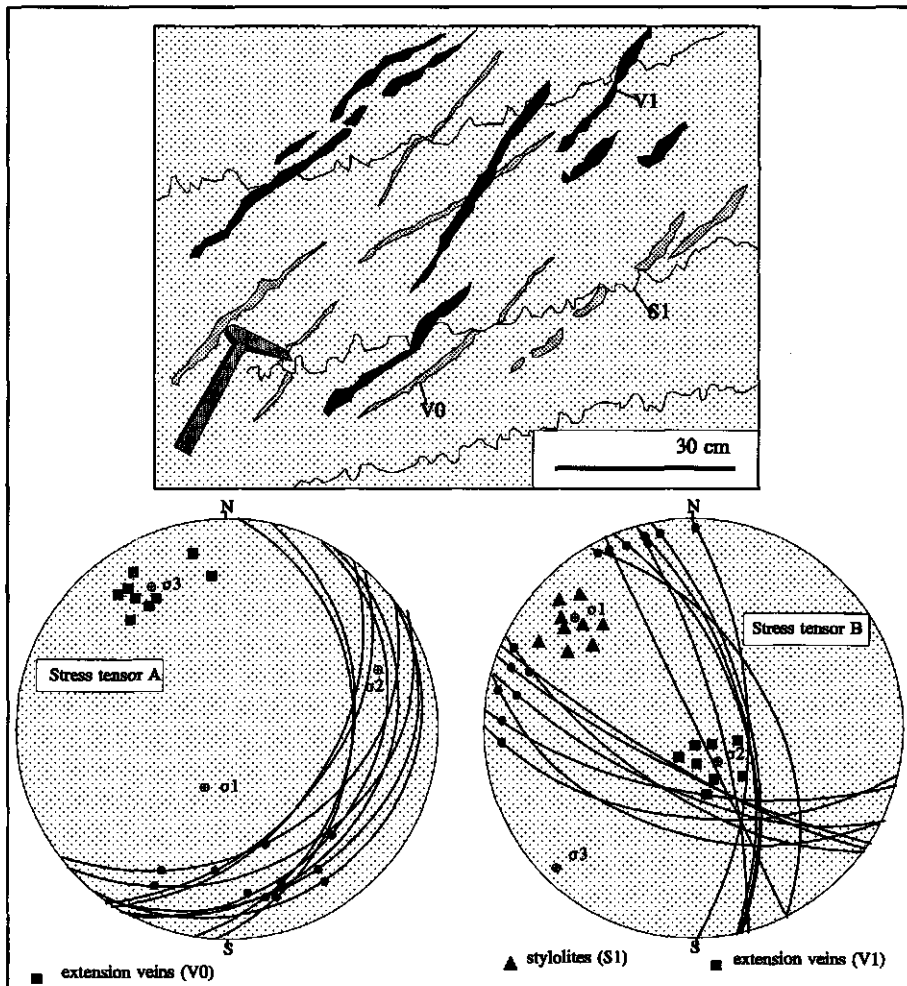


Fig. 3.8d

Capas Rojas unit over the Sierra Blanquilla from less than 100m to the north to more than 250m to the south of this mountain range, strongly suggests a deeper origin of the observed normal faults and supports the idea that folds nucleated on the pre-existing topography formed by these faults. This suggests that this fold trend was determined by the Mesozoic extensional structures. Due to the rheological differences between the resistant Jurassic limestone sequences and the incompetent Cretaceous rocks, two different folds styles developed. The Cretaceous units show intense deformation by flexural slip fold with a width not larger than 20m. The Jurassic rocks, forming the mountain ranges, are folded into box folds characterized by low to horizontal dips on the crest which steepen abruptly toward the limbs. Associated thrust and back-thrusts develop at the outer parts of the folds. These folds are in a successive deformation phase passively rotated towards a N-S direction as a result of wrenching along N70°E trending strike-slip faults. These induce N30°E folds to develop and contemporaneous N40°W trending antithetic shears and N50°E trending synthetic shears (Christie-Blick & Biddle, 1985). A last compressional deformation phase is seen in the Pliocene inducing N20°E trending folds in Tortonian sediments.

On the basis of overprinting relations of associated microstructures, the relative ages of the deformation phases represented by the stress tensors can be deduced. At location 5, tectonic stylolites with associated extension veins ( $S_1$  and  $V_1$  in Fig. 3.9 respectively) are found on a slightly inclined bedding plane. A stereographic plot of these tectonic stylolites and extension veins shows that their maxima correspond to the  $\sigma_1$  and  $\sigma_2$  directions, respectively, of stress tensor B (Fig. 3.9) derived from small-scale fault plane analysis. The  $\sigma_2$  and  $\sigma_3$  directions have changed position which is due to the low  $\Phi$ -value. These stylolites



**Fig. 3.9:** Pattern of stylolites and extension veins looking on a subhorizontal bedding plane. A set of stylolites ( $S_1$ ) and veins ( $V_1$ ) formed by NW-SE compression (stress tensor A) offset older extension veins ( $V_0$ ) formed by NW-SE extension (stress tensor B). See text for discussion.

offset older extension veins (denoted  $V_0$  in Fig. 3.9) formed by a stress tensor which corresponds to stress tensor A in Fig. 3.9. Therefore the extensional stress tensors represent an older phase of deformation than the compressional stress tensors. Since the small-scale faults were measured in rocks of late Cretaceous age, they cannot be attributed to the Jurassic rifting events. It is thus concluded that they developed under an extensional stress regime during late Oligocene-Aquitainian. The compressive stress tensors are consequently related to

Table 3.1a: Stress tensors (extension).

stat. no.	faults	PHASE I					
		EXTENSION					
		$\sigma_1$	$\sigma_2$	$\sigma_3$	$\Phi$	$\Omega$	n
1	23	291/76	127/73	036/4	0.88	28.9	6
2	15	322/52	138/38	229/2	0.59	10.6	7
3	63	025/78	181/11	272/05	0.42	6.9	18
4	62	019/77	188/13	279/02	0.57	9.5	13
5	38	199/64	068/18	332/18	0.59	16.2	12
6	22	199/64	068/18	332/18	0.72	15.8	10
7	32	120/69	308/20	217/03	0.20	8.9	10
8	59	327/90	162/1	072/1	0.1	3.5	10
9	44	074/76	326/04	235/14	0.33	32.6	15
10	12						
11	27	327/63	220/08	126/25	0.36	23.6	8
12	33	242/75	047/15	138/04	0.58	9.5	15
13	38	233/61	054/22	331/11	0.28	8.6	9
14	40	184/83	061/04	330/06	0.61	13.8	9
15	36	129/86	037/00	307/04	0.35	34.1	17
16	31						
17	39	105/79	289/11	199/01	0.66	15.1	13
18	19	038/55	225/35	132/03	0.55	16.5	9
19	12	178/63	051/17	314/20	0.82	23.2	10
20	21	328/74	233/01	142/16	0.51	8.7	9
21	25	320/82	214/02	124/07	0.45	16.6	8
22	33	146/65	034/10	299/22	0.40	16.1	14
23	33	326/76	078/05	169/13	0.46	21.1	8
24	33	061/67	277/19	183/12	0.75	14.8	8
25	27						
26	31	083/67	280/22	108/06	0.27	16.4	7
27	15	131/66	225/02	315/24	0.58	11.5	8
28	35	349/82	229/04	138/07	0.43	10.2	6
29	15	138/58	263/21	002/23	0.35	21.1	7
30	30	351/80	232/07	140/08	0.41	11.3	7
31	24						
32	36	351/85	221/06	141/08	0.31	10.1	9

Table 3.1b: Stress tensors (Compression).

stat. no.	faults	PHASE II					
		COMPRESSION					
		$\sigma_1$	$\sigma_2$	$\sigma_3$	$\Phi$	$\Omega$	n
1	23	170/01	263/18	078/77	0.20	26.0	11
2	15						
3	63	271/09	180/02	078/81	0.69	27.7	15
4	62	007/01	097/01	256/89	0.29	5.2	10
5	38	316/14	130/76	226/01	0.17	4.8	15
6	22						
7	32	296/08	030/31	198/58	0.68	10.1	11
8	59	169/01	259/15	077/75	0.20	26.0	24
9	44	168/13	258/00	350/77	0.59	10.1	12
10	12	331/19	063/05	166/70	0.43	35.5	6
11	27						
12	33	313/05	222/09	070/80	0.52	25.4	13
13	38	331/20	065/07	169/75	0.51	8.9	12
14	40	326/26	061/10	170/62	0.36	16.4	11
15	36	042/00	312/11	134/79	0.11	11.5	12
16	31	020/09	289/05	160/80	0.29	23.1	15
17	39	304/26	037/06	138/63	0.24	13.7	8
18	19						
19	12						
20	21						
21	25	186/04	095/07	291/73	0.52	7.9	8
22	33	307/18	215/07	105/71	0.64	13.7	11
23	33	174/13	081/13	305/72	0.24	10.1	7
24	33	140/32	049/02	315/58	0.25	9.6	11
25	27	359/18	090/04	192/72	0.69	11.8	7
26	31	320/02	229/30	053/59	0.53	24.1	11
27	15						
28	35	168/31	075/05	337/58	0.24	15.1	11
29	15						
30	30	345/10	077/10	211/76	0.45	11.3	8
31	24	143/13	050/11	280/73	0.56	4.5	7
32	36	346/11	081/09	210/81	0.41	11.1	10

- the Ronda peridotite massif -

Table 3.1c: Stress tensors (wrenching)

stat.	no. faults	PHASE III					
		WRENCHING					
		$\sigma_1$	$\sigma_2$	$\sigma_3$	$\Phi$	$\Delta$	n
1	23						
2	15	138/16	311/73	048/02	0.68	5.4	6
3	63	271/09	078/81	180/02	0.59	27.7	11
4	62	035/29	232/55	115/18	0.67	9.2	17
5	38	229/19	051/71	319/01	0.34	45.9	8
6	22	225/25	073/62	320/12	0.63	3.3	8
7	32	280/08	064/80	190/06	0.32	9.4	9
8	59	232/18	041/71	141/04	0.45	18.3	10
9	44	157/08	010/81	248/05	0.12	6.9	10
10	12						
11	27	024/06	209/84	114/01	0.30	13.9	15
12	33						
13	38	220/21	077/58	310/10	0.81	5.6	10
14	40	191/04	094/61	284/29	0.47	54.1	20
15	36	053/18	171/56	314/28	0.31	8.4	7
16	31	256/02	156/80	347/10	0.59	8.4	8
17	39	286/07	172/74	018/14	0.45	11.8	10
18	19	035/33	197/56	300/08	0.37	7.6	8
19	12						
20	21	109/10	346/72	202/15	0.25	31.3	10
21	25	265/18	111/70	357/08	0.33	35.1	9
22	33	058/05	157/58	325/31	0.35	18.1	7
23	33	042/21	163/54	300/28	0.56	10.9	8
24	33	010/12	167/77	279/05	0.36	10.2	11
25	27	007/12	156/75	276/07	0.32	8.0	9
26	31	189/01	335/88	099/01	0.46	6.9	6
27	15	038/01	307/62	128/28	0.31	29.8	7
28	35	058/02	352/58	149/32	0.58	8.0	13
29	15	037/02	263/87	122/03	0.56	12.6	8
30	30	216/09	020/80	125/03	0.46	21.9	9
31	24	052/04	309/70	143/19	0.56	15.0	8
32	36	033/04	270/88	121/04	0.71	12.8	9

Burdigalian compression and the stress tensors indicating strike-slip are related to the late Langhian-Serravalian wrenching tectonics.

Paleostress analysis carried out on fault surfaces and striations within the peridotites (resulting from serpentine crystallization) also revealed three predominant stress tensors (Fig. 3.10). A tensor indicating N10°W directed extension, a tensor indicating N50°W directed compression, and a tensor related to N80°E directed wrenching. The relative ages of these deformation events cannot be directly constrained from field evidence but will be discussed in the next section incorporating the results of stress analysis of the limestones and the subsidence record of the limestones.

Table 3.1d: Stress tensors from stylolites and extension veins.

stat.	STRESS TENSORS											
	PHASE I: EXTENSION				PHASE II: COMPRESSION				PHASE III: WRENCHING			
	$\sigma_1$	$\sigma_2$	$\sigma_3$	n	$\sigma_1$	$\sigma_2$	$\sigma_3$	n	$\sigma_1$	$\sigma_2$	$\sigma_3$	n
A					007/02		260/88	25-20				
B			330/12	15	325/10			21				
C			335/68	17	345/08		220/78	20-15				
D			359/11	20								
E			340/06	22	168/18		340/62	10-11				
F			145/08	21	143/15		281/82	11-8				
G			141/14	15								
H					348/08		210/81	7-10				
PALEOSTRESS TENSORS FROM CONJUGATE FAULT SETS												
X1									258/09	047/72	196/15	10
X2	164/74	043/06	312/14	8								
X3									276/31	084/58	184/04	9

### 3.5 DISCUSSION AND CONCLUSIONS

The sharp downward increase in metamorphic grade in the migmatite/gneiss series of the Los Reales unit (Westerhof, 1977; Tubía & Cuevas, 1986) toward the underlying peridotites points to mantle upwarping (Loomis, 1972a; Bakker *et al.*, 1989; De Jong, 1991; Van Wees *et al.*, 1992) and emplacement of the of the ultramafic bodies at crustal levels during a phase of extension. The coarse-grained peridotites forming the core of the massif also record evidence for mantle deformation. In the Sierra Alpujata, Tubía (1985) describes olivine fabrics and olivine neoblasts which record a phase of ductile deformation at high temperature and low deviatoric stress (Tubía *et al.*, 1992). Olivine lattice preferred orientation patterns from the Sierra Bermeja peridotites show similar fabrics suggesting crystal-plastic deformation accommodated by intracrystalline slip under mantle conditions.

In the Ojén nappe underlying the peridotites, an upward increase in metamorphic grade is apparent (Tubía & Cuevas, 1986; Blanca unit, Westerhof, 1977), resulting from thrusting of hot ultramafic rocks. Deformation structures in the mylonite zone separating the peridotites from the underlying migmatites as well as deformation structures in the peridotites, record this thrusting deformation. The quartz c-axes patterns presented in Fig. 3.4 indicate a northeast sense of transport similar to the directions which can be deduced from olivine and enstatite lattice preferred orientation fabrics. Microstructures found in mylonitic gneisses underlying the peridotites generally indicate a dextral shear-sense (Fig. 3.7) consistent with the top-to-the-northeast sense of shear from preferred mineral orientations. Flat-lying foliations that steepen toward the contact zone of the peridotites also support a final tectonic emplacement of the

- the Ronda peridotite massif -

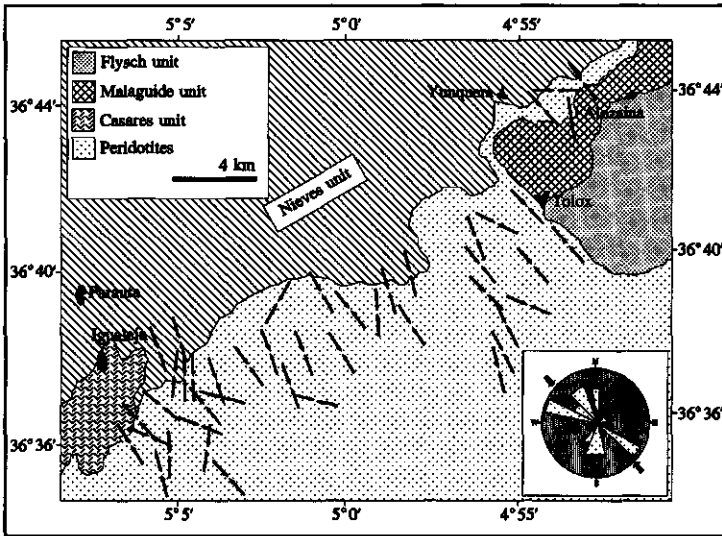


Fig. 3.10: Stress tensors measured in the Ronda peridotites indicating (A) compression, (B) strike-slip tectonics, and (C) extension.

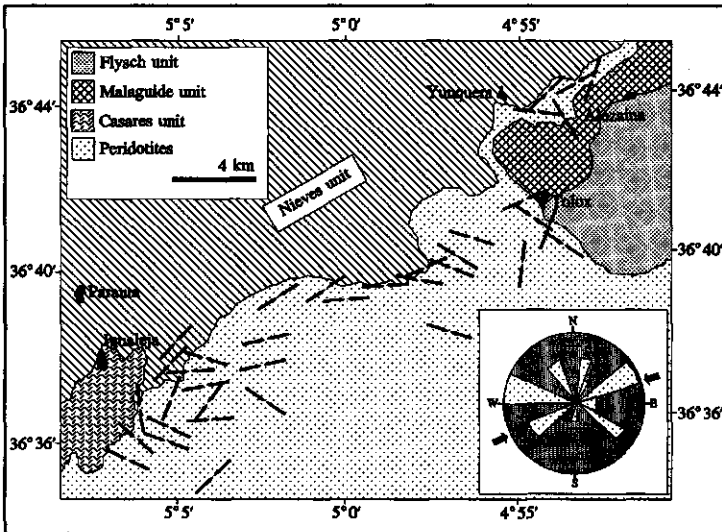


Fig. 3.10b

ultramafic masses (Lundeen, 1978; Westerhof, 1977; Tubía, 1988a+b).

Gravimetric data from Bonini *et al.* (1973) shows a positive Bouger anomaly of approximately 100mgal occurring in between Málaga and Marbella which forms part of a positive zone extending into the Alboran Sea more or less parallel to the present coastline. Careful inspection shows that this positive anomaly does not overly the ultramafic bodies themselves but that the outcrop of the peridotites is located some 50km northwest of the

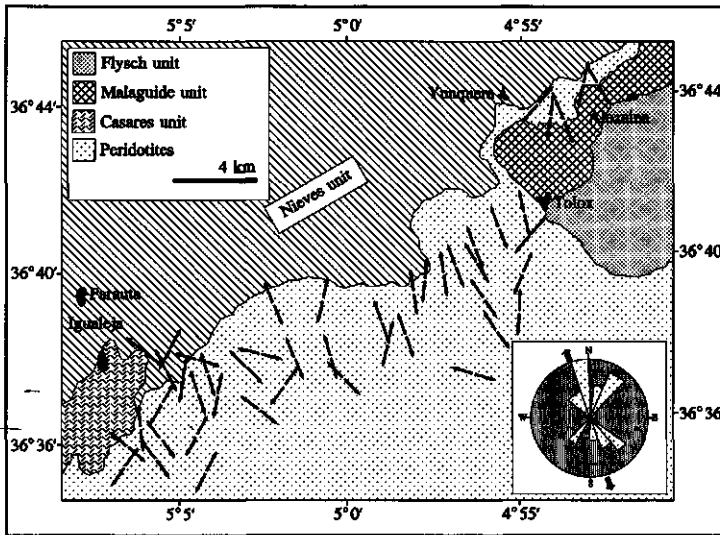


Fig. 3.10c

observed anomaly. Therefore the occurrence of the gravity anomaly favours a northwestward thrusting of the peridotite masses from the an area in the present day Alboran sea off the coast of southern Spain where the peridotites might have originated. Supporting evidence can be found in the seismic refraction analysis carried out by Barranco *et al.* (1990) who showed that the peridotites form a 5 to 10km thick sheet dipping south to southeast. Recent tomography analysis by Blanco & Spakman (1993) following on earlier seismic work by Spakman (1990), Chung & Kanamori (1976), Udias *et al.* (1976), and Bufo *et al.* (1988), indicates the presence of a northeast-striking, roughly vertical detached lithospheric fragment at a depth of 200-700km. in the mantle of the Betic-Alboran region interpreted by Zeck *et al.* (1992) as a remnant of an earlier active northwestward dipping subduction zone. Paleomagnetic data from the Betic-Rif chain has revealed opposite senses of up to 60° rotation of Mesozoic limestones sequences across the Alboran sea, i.e. dominantly clockwise rotations in southern Spain and dominantly anti-clockwise rotations in northern Morocco (Osete *et al.*, 1988; Platzman, 1992; Platzman *et al.*, 1993).

Radiometric dating of the emplacement of the peridotites resulted in 81Ma (Loomis, 1975). Priem *et al.* (1979) obtained a  $22 \pm 4$  Ma whole rock Rb/Sr age from an anatectic granite intruded into the peridotite. Rb/Sr and K/Ar dating obtained from biotite analysis resulted in a 19.5Ma age from the country rocks (Priem *et al.*, 1979). Zindler *et al.* (1983) dated the emplacement at  $21.5 \pm 1.8$  Ma from a garnet-clinopyroxenite mafic layer within the massif. This date is in good agreement with recent dating by Reisberg *et al.* (1989) who used Sr and Nd isotopic compositions to date the emplacement of the Ronda peridotite masses from the mantle into the crust as 22Ma. A phase of late Oligocene-Aquitania extension is



- the Ronda peridotite massif -

well known throughout the Western Mediterranean (Rehault *et al.*, 1984; De Ruig, 1992; De Jong, 1991). However, major phases of rifting in the Alboran domain are also known during the Mesozoic (see Chapter 2). It is suggested that ductile emplacement of the peridotites into the crust took place during these extension phases with a culmination in late Oligocene. After the cooling, subsequent brittle deformation events further structured the peridotites.

Extension in the Betic Cordilleras was immediately followed by thrust emplacement of the Internal Betic zone onto the southern Iberian margin. De Jong (1991) argued that the thrust emplacement (Lonergan *et al.*, 1994) took place between 21.5 Ma and 19 Ma (Burdigalian-Langhian; see Chapter 2). Following this period of compression, is a period of wrench related tectonics affecting the Betic Cordilleras during late Langhian-Serravalian (Montenat *et al.*, 1987; Le Blanc and Olivier, 1984; Andrieux *et al.*, 1971; De Smet, 1984; Van der Straaten, 1990, 1993; Allerton *et al.*, 1994). More recently, wrench faults were interpreted as major tear faults accommodating westward overthrusting of the Betic nappe pile over the External zone (e.g. Frizon de Lamotte *et al.*, 1991). Jabaloy *et al.* (1993) discuss metamorphism and deformation of the Alpujarride and Nevado-Filabride complexes in terms of a sinistral shear regime related to Early Miocene extension.

Our paleostress analysis carried out on fault surfaces and striations revealed three predominant stress tensors. A tensor indicating N10°W directed extension, a tensor indicating N50°W directed compression, and a tensor related to N80°E directed wrenching. The relative ages of these deformation events cannot be directly constrained from field evidence.

Based on the discussion above, it is suggested that the Ronda peridotites have undergone at least a three phases of late stage brittle deformation related to their final emplacement at crustal levels. Despite the fact that these phases cannot be dated directly from field evidence in the peridotites themselves, the following scenario is proposed. During the Burdigalian collisional events the peridotites are thrust northwestwards. The final emplacement takes place after a period of late Langhian-Serravalian strike-slip related tectonics during which the peridotites are transplaced eastward along a dextral strike-slip corridor which developed along the former thrust contact. Extension in Tortonian provides the third stress tensor computed.

## CHAPTER 4:

### *Spectral reflectance of carbonate mineral mixtures and bidirectional reflectance theory<sup>2</sup>*

#### ABSTRACT

Visible and near-infrared (0.4-2.5 $\mu$ m) reflectance spectra of carbonates are discussed in this Chapter. Electronic processes in cations and vibrational processes involving the crystal lattice produce the main spectral absorption features in such spectra. Subsequently, mineral impurities cause additional complications in carbonate reflectance spectra. A simple semi-empirical model is presented for the determination of artificial spectral reflectance of mineral mixtures based on their single-component reflectivity. This model, in conjunction with spectral measurements of well constrained mineral mixtures, is used to explain the effect of particle size and distribution, iron, water bounded by clay minerals, and organic material on the reflectivity of carbonate minerals. Similarly, reflectance spectra of calcite-dolomite mixtures are modelled and compared with spectra measured from well mixed samples. This analysis yields a semi-linear relationship for the position of the strongest carbonate absorption band and the calcite-dolomite ratio of the sample. This relationship theoretically allows for the mapping of dolomitization patterns from remote sensing data. The practical consequences of such an application in imaging spectrometry are further discussed in Chapter 9 of this thesis. The theoretical results from modelling are compared with reflectance spectra measured for 44 rock samples.

---

<sup>2</sup>Parts of this Chapter have been published as:

Van der Meer, F. 1994. Spectral reflectance of carbonate mineral mixtures and bidirectional reflectance theory: quantitative analysis techniques for application in remote sensing. *Remote Sensing Reviews*, In press.

Van der Meer, F. 1994. Sequential Indicator Conditional Simulation and Indicator Kriging applied to discrimination of dolomitization in GER 63 channel imaging spectrometer data. *Nonrenewable Resources*, 3(2): 146-164.

## 4.1 INTRODUCTION

When light interacts with a mineral or rock, light of a certain wavelengths is preferentially absorbed while at other wavelengths light is transmitted in the substance. Reflectance, defined as the ratio of the intensity of light reflected from a sample to the intensity of the light incident on it, is measured by reflection spectrophotometers which are composed of a light source and a prism to separate light into different wavelengths. This light beam interacts with the sample and the intensity of reflected light at various wavelengths is measured by a detector relative to a reference standard of known reflectance. Thus a continuous reflectance spectrum of the sample is obtained in the visible- and near-infrared wavelength region.

Reflectance spectra have been studied for many years to obtain compositional information of the earth's surface. Electronic transition and charge transfer processes (e.g., changes in energy states of electrons bound to atoms or molecules) associated with transition metal ions such as Fe, Ti, Cr, etc., determine largely the position of diagnostic absorption features in the visible- and near-infrared wavelength region of the spectra of minerals (Burns, 1970; Adams, 1974, 1975). In addition, vibrational processes in  $H_2O$  and  $OH^-$  (e.g., small displacements of the atoms about their resting positions) produce fundamental overtone absorptions (Hunt, 1977; Hunt & Salisbury, 1970). Electronic transitions produce broad absorption features that require higher energy levels than do vibrational processes, and therefore take place at shorter wavelengths (Hunt, 1977; Goetz, 1992). The position, shape, depth, width, and asymmetry of these absorption features are controlled by the particular crystal structure in which the absorbing species is contained and by the chemical structure of the mineral. Thus, parameters characterizing absorption features can be directly related to the mineralogy of the sample.

Reflectance spectra of minerals are well known (Hunt, 1977; Hunt & Salisbury, 1970; 1971; Hunt *et al.*, 1971a+b; 1972; 1973a; Clark *et al.*, 1990; Crowley, 1991; Grove *et al.*, 1992) and several studies have been conducted to determine reflectance spectra of rocks (Hunt *et al.*, 1973b+c; 1974; 1975; 1976a+b). Reflectance characteristics of rocks can be accurately simulated by studying the compound effect of reflectances of minerals in a spectral mixture forming the rock. Reflectance spectra of mineral mixtures are a systematic combination of the reflectances of the pure mineral components or end-members in the mixtures. Several investigators have examined the systematics of mixing theoretically and empirically, and found that if the scale of mixing is large, or macroscopic, the spectral systematics of mixing different materials are linear (Singer & McCord, 1979), while for microscopic or intimate mixtures the systematics are nonlinear (Nash & Conel, 1974; Singer, 1981). Mathematical models for the analysis of reflectance spectra of mineral mixtures have been presented by many workers. These theories in general model the reflectance of a particulate surface as a

function of variables related to (1) the physical state of the surface, (2) properties of the individual components comprising the surface, and (3) viewing geometry or type of reflectance measured. Emslie & Aronson (1973) treated a model based on radiative transfer, relating spectral reflectance of a particulate surface to microscopic properties of its components. Experimental verification of their model showed that gross features in the infrared emittance spectra of several types of powders could be reasonably reproduced (Aronson & Emslie, 1973). A comprehensive work on the solution of the radiative transfer problem for a particulate medium, deriving first-order analytic expressions relating reflectances of mineral mixtures, has been presented by Hapke (1981) and tested by Hapke & Wells (1981). The method presented by Hapke is by far the most used in literature because of its simplicity and straightforward approach, and has been applied successfully in many studies (e.g., Johnson *et al.*, 1983; Clark, 1983; Clark & Roush, 1984; Cloutis *et al.*, 1986; Mustard & Pieters, 1987).

In this Chapter, reflectance spectra of carbonate minerals and rocks are discussed with emphasis on the spectral effects of mineral impurities. Due to the difficulty in some cases to prepare realistic mineral mixtures resembling rock properties, the analysis relies partly on the results obtained from bidirectional reflectance models. When possible, mineral mixtures of known composition were prepared in the laboratory and analyzed spectrally. First, the application of scattering theory to reflectance spectroscopy is discussed yielding quantitative mixing models for simulating spectral properties of multimineral samples. Next, spectra of mineral mixtures are treated focusing on the spectral effects of particle size, sorting, impurities, and calcite-dolomite ratio. Finally, the results are compared to observations of reflectance spectra of rock samples.

## 4.2 BIDIRECTIONAL REFLECTANCE THEORY

Hapke (1981, 1984, 1987) presented a treatment of scattering theory as applied to reflectance spectroscopy. According to his method, the diffuse reflectance,  $r$ , of a particulate medium can be related to the mean single-scattering albedo,  $w$ , of an individual grain through the Kubelka-Munk equation (Kubelka, 1948; Wendtland & Hecht, 1966; Kortum, 1969; Hapke, 1981) as

$$\sqrt{(1 - w)} = (1 - r)/(1 + r) \quad (1)$$

which can be rearranged to give

$$w = 4r/(1 + r)^2 \quad (2)$$

where  $r$  and  $w$  are a function of wavelength. For a mineral having a measured bihemispherical reflectance spectrum,  $r(\lambda)$  (e.g., the ratio of the radiant power scattered from a surface in all directions to the uncollimated light incident on the surface), the single-scattering albedo spectrum can be derived directly from Eq.(1). From Hapke's (1981) Eq.(17), it can be seen that the mean single-scattering albedo,  $w(\lambda)$ , of a multi-component particulate mineral mixture is a linear combination of the single-scattering albedos of each of the components, weighted by their mean effective cross-sectional area. Thus, according to Hapke (1981), single-scattering albedo can be expressed as a function of the individual reflectance properties of the mineral phases as

$$w(\lambda) = \frac{\sum \{M_i w_i(\lambda)\} / \{\rho_i d_i\}}{\sum M_i / \{\rho_i d_i\}} \quad (3)$$

where  $i$  refers to the  $i$ th component in the mineral mixture,  $M$  is the mass fraction of the individual mineral phase,  $\rho$  is the particle density, and  $d$  is the effective particle diameter. This equation assumes that the particles are homogeneously distributed, and that one particle does not coat another particle type. By inverting Eq.(1), the bihemispherical reflectance of the resulting mixture can be obtained as

$$r(\lambda) = \frac{1 - \sqrt{1 - w(\lambda)}}{1 + \sqrt{1 - w(\lambda)}} \quad (4)$$

Hapke (1981) further developed the mineral mixing model incorporating also the phase function and the backscatter function of the surface. Johnson *et al.* (1983) also present equations to derive directional-hemispherical reflectance (e.g., the ratio of the radiant power scattered from a surface to the collimated light incident on the surface with a certain angle of incidence) from the mean single-scattering albedo of a particulate mineral. However, these parameters add several unknowns to the equations and it has been shown that the difference between bidirectional and directional hemispherical reflectance is only a few percent in the derived reflectance level and depth of absorption features (Gradie & Veverda, 1982). Taking this in consideration, therefore, the scattering theory presented in Eq.(1)-(4) will be used in this Chapter. However, where possible mineral mixtures prepared in the laboratory are preferred over the results obtained by modelling although it will be shown that model results do not deviate significantly from laboratory results.

- Reflectance spectra of carbonate minerals and rocks -

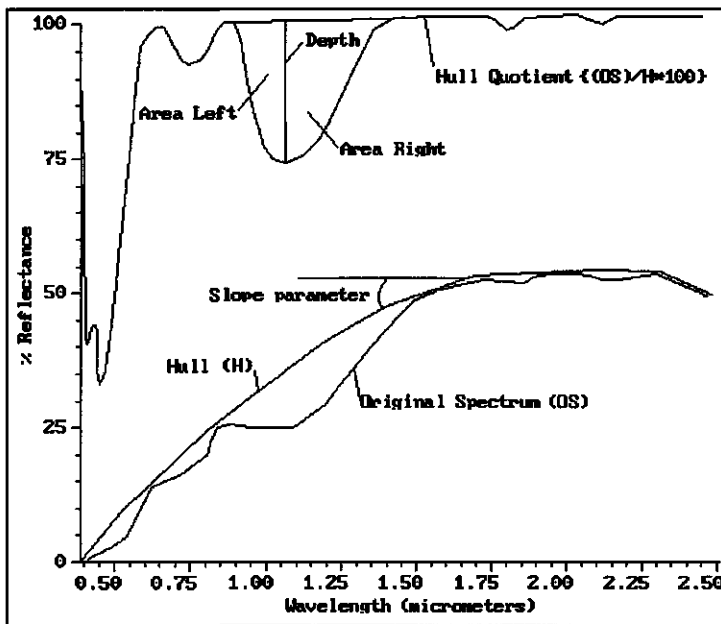


Fig. 4.1: Schematic diagram of parameters characterizing mineral absorption features in a goethite spectrum.

## 4.3 REFLECTANCE SPECTRA OF CARBONATE MINERALS AND ROCKS

### 4.3.1 Laboratory methods

Mineral samples were pulverized with a steel percussion mortar and sieved into different size fractions after grounding with mortar and pestle. Rock samples described later, were collected from the field and sawed to prepare thin sections. Reflectance spectra of rocks were recorded from these sawed surfaces. Diffuse hemispherical reflectance measurements in the visible and near-infrared wavelength region (0.4-2.5 $\mu$ m) of the electromagnetic spectrum presented in this and a later Chapter, were made using the Beckman UV5240 spectrometer fitted with an integrating sphere (Price, 1977).

The Beckman UV5240 spectrophotometer measures hemispherical reflectance in the visible and short wavelength infrared region (0.4-2.5 $\mu$ m). The NASA-JPL Beckman instrument used in this study, has been modified by rotating the integrating sphere 90 degrees, allowing the sample holder to remain in a horizontal position throughout the measurement. The Beckman UV5240 uses a single pass monochromator with a diffraction grating as its dispersing element. Sampling interval is approximately 1nm from 0.4 to 0.8 $\mu$ m, and

- Chapter 4 -

approximately 4nm from 0.8 to 2.5 $\mu$ m. Bandwidths range from approximately 1nm at 0.4 $\mu$ m to 40nm at 2.5 $\mu$ m with a spectral resolution (defined as bandwidth/wavelength) better than 2 percent at all wavelengths. A high intensity tungsten-halogen source lamp and a Halon reference are used for the measurements. Halon (a tradename for polytetrafluoroethylene powder; Venable *et al.*, 1976) has been shown to be a diffuse reflector whose reflectance has been measured by Weidner & Hsia (1981). However, Halon does have a small absorption feature over the spectral range near 2.14 $\mu$ m which manifests in spectra that have a high reflectance and are spectrally flat in the 2.0-2.5 $\mu$ m region. To correct for this Halon artefact, the spectra were multiplied by the reflectance of Halon versus a perfect diffuser given in Weidner & Hsia (1981) thus removing to a large extent the influence of the Halon absorption feature. A spectrum is obtained from an area of approximately 45mm<sup>2</sup> (3mm x 15mm) and spectra are subsequently digitized to 12 bit format. The spectra are stored in digital format on a VAX 11/750 for further manipulation. The Beckman UV5240 is described in more detail in an appendix to a publication of Lang *et al.* (1990) provided by the author.

Absorption features in reflectance spectra, were characterized by their wavelength position, depth, width, and asymmetry (Fig. 4.1). The absorption wavelength is defined as the wavelength of minimum reflectance of an absorption feature. Instead of directly inferring the width of an absorption feature from its starting point (left shoulder wavelength band) and ending point (right shoulder wavelength band), the width, *Width*, of an absorption feature was defined as

$$Width = \frac{(A_{left} + A_{right})}{2D} \quad (5)$$

where *D* is the depth of the feature relative to the Hull (Green & Graig, 1985; see Fig. 4.1). The upper convex Hull (denoted by H in Fig. 4.1) is an envelope curve fitted over the original reflectance spectrum (denoted by OS in Fig. 4.1) having no absorption features. The absorption spectrum known as hull-quotient is given by taking the ratio between the reflectance spectrum and the enveloping curve. The result is that the reflectance spectra are rescaled to 100% if no absorption features occur. The asymmetry of an absorption feature, *S*, is derived as the ratio of the area left (*A<sub>left</sub>*) of the absorption center to the area right (*A<sub>right</sub>*) of the absorption center (Fig. 4.1) as

$$S = A_{left} / A_{right} \quad (6)$$

- Reflectance spectra of carbonate minerals and rocks -

Table 4.1: Position and widths of carbonate bands for calcite and dolomite (after: Gaffey, 1986).

Carbonate Band	CALCITE		DOLOMITE	
	Position ( $\mu\text{m}$ )	Width ( $\mu\text{m}^{-1}$ )	Position ( $\mu\text{m}$ )	Width ( $\mu\text{m}^{-1}$ )
1	2.530-2.541	0.0223-0.0255	2.503-2.518	0.0208-0.0228
2	2.333-2.340	0.0154-0.0168	2.312-2.322	0.0173-0.0201
3	2.254-2.720	0.0121-0.0149	2.234-2.248	0.0099-0.0138
4	2.167-2.179	0.0170-0.0288	2.150-2.170	0.0188-0.0310
5	1.974-1.995	0.0183-0.0330	1.971-1.979	0.0206-0.0341
6	1.871-1.885	0.0190-0.0246	1.853-1.882	0.0188-0.0261
7	1.753-1.885	0.0256-0.0430	1.735-1.740	0.0178-0.0395

#### 4.3.2 Controls of carbonate absorption band positions

Light interacting with a carbonate mineral or rock is absorbed by vibrational processes of the carbonate ion ( $\text{CO}_3^{2-}$ ) and water, and by electronic processes related to the presence of metal cations in the unfilled d-shells. Vibrational processes produce a number of overtone bands in the infrared wavelength region. The two strongest bands are positioned near 2.50-2.55 $\mu\text{m}$  and 2.30-2.35 $\mu\text{m}$ , and three weaker bands occur near 2.12-2.16 $\mu\text{m}$ , 1.97-2.00 $\mu\text{m}$ , and 1.85-1.87 $\mu\text{m}$  (Hunt & Salisbury, 1971; Clark *et al.*, 1990). Gaffey (1986, 1987) identified two additional absorption bands centered at 2.23-2.27 $\mu\text{m}$  and 1.75-1.80 $\mu\text{m}$  (Table 4.1). Vibrational absorption bands due to  $\text{OH}^-$  stretching occurring in the 2.0-2.5 $\mu\text{m}$  produce absorption bands at 2.2 $\mu\text{m}$  (caused by  $\text{AlOH}$ ), 2.3 $\mu\text{m}$  (caused by  $\text{MgOH}$ ), and 2.29 $\mu\text{m}$  (caused by  $\text{FeOH}$ ). The position of the absorption bands are controlled mainly by: (1) the valences of the cation and anion, (2) the coordination number of the cation, (3) the mass of the cation, (4) the degree of covalency of the bond, (5) interatomic distances between cation and anion, and (6) site symmetry (Povarennykh, 1978; Lazarev, 1974). Cation mass is the most important of these factors, and cation radius is the second most important (Gaffey, 1984). The absolute intensities of carbonate bands (absorption depth) is dependent on the particle size, sorting, porosity, and mineral impurities, as will be discussed in the following sections.

The crystal structure and mineralogy of carbonate minerals is not further treated in this Chapter. The interested reader is referred to discussions by Goldsmith (1983), Reeder (1983), and Speer (1983).



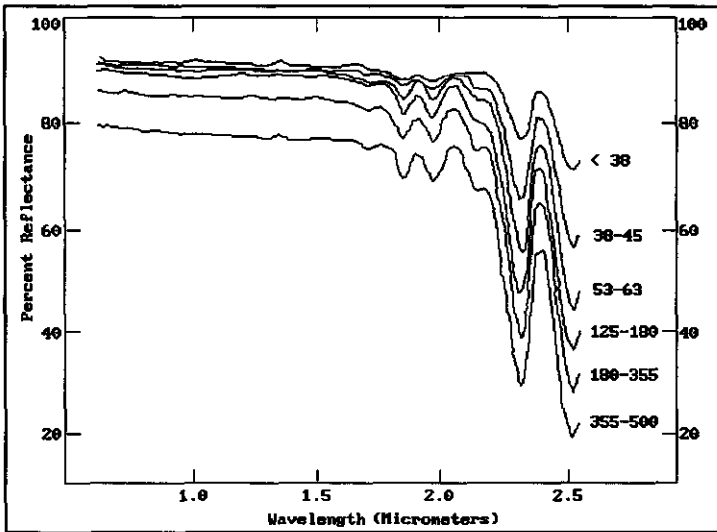


Fig. 4.2: Calcite powder spectra of different grain size (data after: Gaffey, 1986).

#### 4.3.3 Effects of particle size

Fig. 4.2 shows spectra Iceland spar samples (from Gaffey, 1986) of different grain size fractions. These spectra show that the only spectral parameters that vary with grain size are the overall brightness and depth of absorption bands, whereas the width and asymmetry of absorption features, and the number of absorption bands are invariant with grain size. This is also shown in Fig. 4.3 where the depth,  $D$ , of the characteristic carbonate absorption features at 2.3 and 1.98  $\mu\text{m}$  are measured in each of the spectra of Fig. 4.2 as well as the percent reflectance at 1.6  $\mu\text{m}$ , and indication for the overall brightness of the sample. In general, fine-grained samples are relatively bright and show weak absorption features compared to coarse samples that are darker and show deeper, more prominent absorption features. The relative band intensity, expressed as the ratio of the intensity of a given absorption feature to that of the other features in the spectrum, is constant and independent of the grain size. Techniques for the automatic calculation of grain-shape and grain-size parameters from digital thin section images have been discussed in Van der Meer (1994e).

#### 4.3.4 Effects of sorting

Crowley (1986) investigated effects of petrographic texture by statistically examining

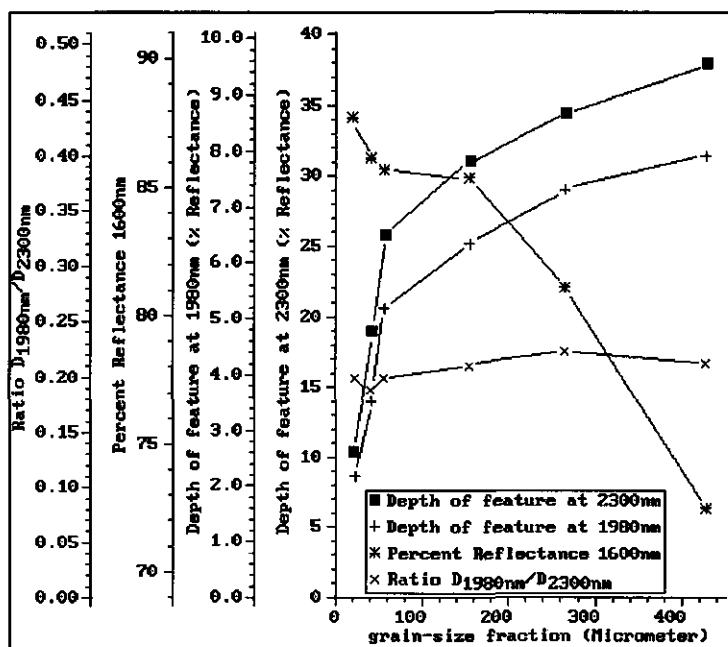


Fig. 4.3: Depth of absorption features at 2.3 $\mu$ m, 1.98 $\mu$ m, and 1.6 $\mu$ m as a function of grain size for reflectance spectra shown in Fig. 4.2.

reflectance spectra of carbonate rocks. He distinguished three groups of particle textures: unimodal, skewed, and bimodal. No relation was found between grain size and overall brightness or albedo of the samples. However, the unimodal group was characterized by bright spectra with moderately deep carbonate absorption features, the skewed group showed bright spectra with a low contrast in the carbonate absorption bands, and the bimodal group were found to exhibit relatively dark spectra with very deep carbonate features. Thus a qualitative classification of carbonate petrographic texture seems possible on basis of spectral reflectance characteristics.

In an attempt to predict spectral reflectance characteristics of carbonate rocks in relation to petrographic texture, mineral mixtures of various grain size fractions were modelled using Hapke's bidirectional reflectance theory discussed earlier (Fig. 4.4). The two end-members, a fine and a coarse sample, are spectrum A and F in Fig. 4.4, respectively. The fine-grained sample is relatively bright (reflectance at 1.6 $\mu$ m is 85%) and has weak absorption features, on the contrary, the coarse-grained end-member has very deep absorption features and is much darker (reflectance at 1.6 $\mu$ m is 65%). However, the relative contribution of the coarse-grained sample to the overall reflectance characteristics of the mixtures is limited. Spectrum B and C are nearly identical although the first spectrum represents a bimodal carbonate texture and the second spectrum represents a unimodal spectrum from a sample of

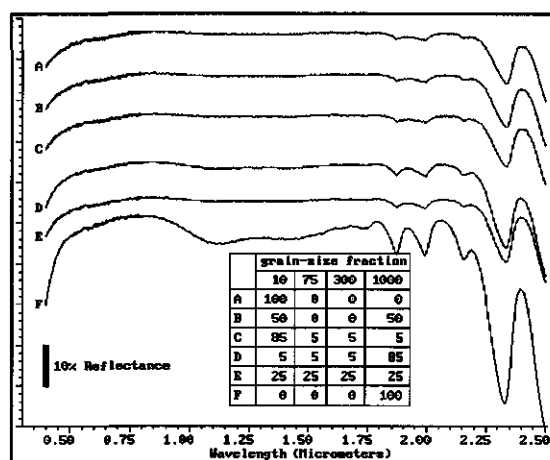


Fig. 4.4: Spectra of mixtures of different grain size. The percentage of each grain size fraction is listed in the table. Spectra are vertically offset for clarity.

predominantly finer grains. The unimodal spectrum with 85% coarse carbonate grains (spectrum D in Fig. 4.4) can be distinguished from the other mixtures on basis of the depth of the absorption features. A well sorted sample (spectrum E in Fig. 4.4) produces a spectrum which is similar to that of the fine-grained end-member. Thus, on basis of model predictions from the bidirectional reflectance theory, the effects of petrographic texture on reflectance characteristics are obscured by the predominant effect of spectral quenching produced by scattering among very fine grains.

#### 4.3.5 Calcite-Dolomite mixtures

Discriminating calcite from dolomite in laboratory reflectance spectra or by means of using remote sensing data is theoretically possible because both minerals show absorption features in the near-infrared which are slightly displaced (e.g., Windeler & Lyon, 1991). The center of the calcite absorption feature is found at a few nanometers higher wavelength than that of dolomite. Although this phenomena is known for a number of years, the exact position of the calcite absorption band has been reported at different wavelengths by various groups of workers (e.g., 2.35 $\mu\text{m}$  Hunt & Salisbury, 1971; 2.37 $\mu\text{m}$ , Schroeder *et al.*, 1962; 2.33 $\mu\text{m}$ , Matossi, 1928; 2.33-2.34, Gaffey, 1986). In Fig. 4.5, calculated reflectance spectra using Eq.(4) of mixtures of calcite and dolomite are shown (specific gravity used is 2.7 and 2.85 g/cm<sup>3</sup> for calcite and dolomite respectively; Frye, 1981). Fig. 4.6 shows the depth, asymmetry, and position of the carbonate feature in the reflectance spectra of the binary mixtures of Fig. 4.5 as a function of the weight percent of calcite in the sample. Pure calcite has an absorption feature centered at 2.332 $\mu\text{m}$  with a depth of 31% reflectance, whereas dolomite has an absorption feature centered at 2.304 $\mu\text{m}$  with a depth of 24.9% reflectance. The position,  $\lambda_{\text{CO}_3}$ ,

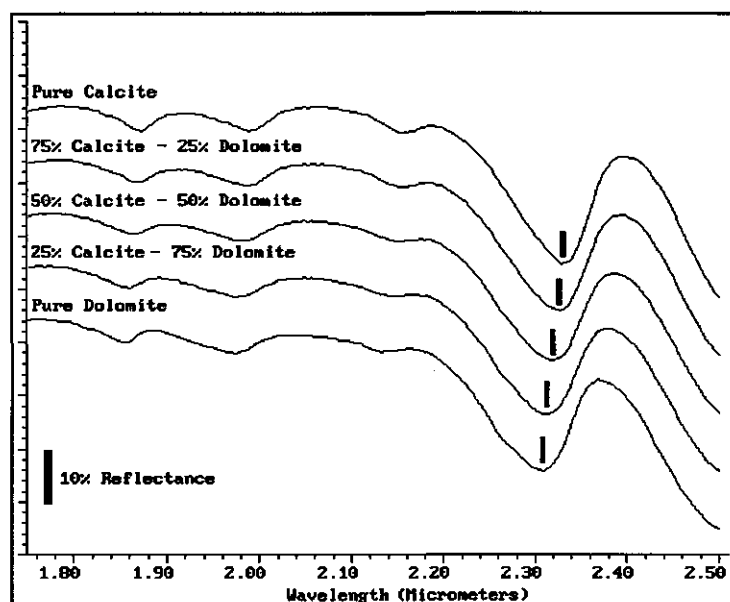


Fig. 4.5: Modelled spectra of mineral calcite-dolomite mixtures (45 $\mu$ m. grain size). Bars indicate the center of the carbonate absorption band. Spectra are vertically offset for clarity.

and depth,  $D_{CO_3}$ , of the carbonate absorption feature are linearly related to the percent calcite (or dolomite) in the sample can be deduced from data presented in Fig. 4.6 as

$$\lambda_{CO_3} = 0.0028 M_{calcite} + 2.3040$$

(7)

$$D_{CO_3} = 0.0670 M_{calcite} + 24.900$$

where  $M_{calcite}$  is the mass fraction calcite in the sample.

Mineral mixtures of calcite and dolomite with known abundances were prepared in the laboratory in order to verify the theoretical model results. Samples of pure calcite and dolomite used in this study were obtained from the NASA-JPL in-house collection which in turn consists of samples from Ward's Natural Science Establishment, Rochester, New York (Grove *et al.*, 1992). Mineral samples were pulverized with an alumina mortar and pestle and impurities were removed by hand-picking and by using a magnet. The pulverized samples were separated into different size fractions by wet-sieving. In the spectral analysis described below, relatively coarse samples with a 45-125 $\mu$ m size fraction (corresponding to coarse silt to very fine sand) were used. The rationale for using coarse-grained samples is that the absorption-band depth increases with increasing grain-size. Although the overall brightness decreases with increasing grain-size (e.g., Gaffey, 1985; 1986; 1987; Crowley, 1986),

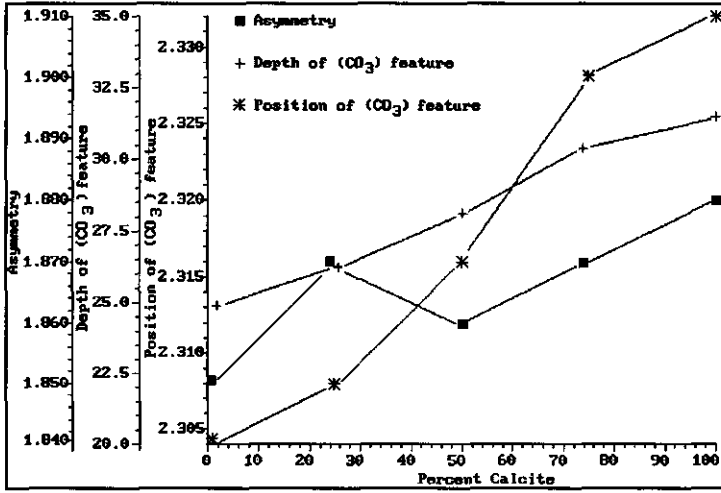


Fig. 4.6: Depth, position, and asymmetry of the carbonate absorption feature versus the calcite content of the sample for mineral mixtures of calcite and dolomite shown in Fig. 4.5.

absorption-band parameters can be better estimated from coarse samples (Clark & Roush, 1984). The position of an absorption band, however, is invariant with grain-size (Gaffey, 1985). The purity of each sample was evaluated using standard X ray diffraction (XRD) and X ray fluorescence (XRF) methods indicating that the dolomite and calcite sample used were spectrally pure (see Table 4.2). Next, well-controlled samples were prepared with known weight percentages of calcite and dolomite (ranging from the pure calcite to the pure dolomite sample with increments of 10 weight % dolomite added). Reflectance spectra of these samples in the visible and near-infrared wavelength region (0.4-2.5 $\mu$ m) were measured on a Beckman UV5470 spectrometer described in detail in Clark *et al.* (1990).

In Fig. 4.7, the near-infrared region of 0.4-2.5 $\mu$ m reflectance spectra of some of the powdered mineral mixtures of calcite and dolomite are shown. In total, 11 such samples of calcite-dolomite mineral mixtures were prepared and for each of these samples a spectrum was measured 10 times for different portions of the sample. The absorption-band depth and center of the carbonate absorption-band near 2.3 $\mu$ m was estimated after fitting and subtracting a continuum over the reflectance spectra (Clark & Roush, 1984). A continuum is a mathematical function used to isolate particular absorption features in a spectrum from the overall decrease in reflectivity toward the infrared and the visible part of the spectrum. The technique is analogous to fitting a rubber band over a spectrum to form a continuum which is removed, thus providing a more consistent definition of band-depth and center. This step is particularly important because wavelength dependent scattering may impart a slope to the spectrum causing apparent shifts in the absorption-band minima. Removing the slope thus corrects the band minimum to that of the true band center (Clark & Roush, 1984). The absorption-band depth ( $D_b$ ) for the carbonate absorption feature was calculated following the

- Reflectance spectra of carbonate minerals and rocks -

Table 4.2: Major element composition of calcite and dolomite sample used.

Element	Calcite		Dolomite	
	Weight %	Std. Error	Weight %	Std. Error
MgO	0.39	0.02	18.0	0.2
SiO <sub>2</sub>	0.102	0.008	0.13	0.01
P <sub>2</sub> O <sub>5</sub>	0.044	0.004	0.012	0.005
SO <sub>3</sub>	0.076	0.006	---	---
Cl	0.010	0.001	0.009	0.001
Ar	---	---	0.005	0.001
K <sub>2</sub> O	0.0101	0.0009	0.012	0.001
CaO	44.0	0.3	26.4	0.3
MnO	0.008	0.001	---	---
Fe <sub>2</sub> O <sub>3</sub>	0.035	0.003	0.027	0.002
CuO	0.013	0.001	---	---
ZnO	0.0064	0.0007	---	---
SrO	0.014	0.001	0.014	0.001
Cs <sub>2</sub> O	0.006	0.002	0.007	0.002
BaO	0.011	0.002	0.012	0.002
Rest CO <sub>2</sub>	55.24	---	55.31	---

definition by Clark & Roush (1984):

$$D_h \equiv \frac{R_c - R_b}{R_c} \quad (8)$$

where  $R_b$  is the reflectance at the band center, and  $R_c$  is the reflectance of the continuum at the band center. More details on the continuum removal technique are given in Clark & Roush (1984) and Green & Graig (1985).

Fig. 4.8 shows the calculated absorption-band depth and position of the center of the carbonate absorption feature in the reflectance spectra of the 11 mineral mixtures described earlier. These parameters were calculated 10 times for each sample to insure a unbiased result. The range of results are shown in Table 4.3 indicating that the band center can be estimated within a range of approximately 0.0016 $\mu$ m. The pure calcite end-member has an absorption feature centered at 2.346 $\mu$ m with a absorption-band depth of 24.9% reflectance, whereas the pure dolomite end-member has an absorption feature centered at 2.304 $\mu$ m with an absorption-band depth of 31.6% reflectance. These measures agree well with absorption-band positions reported by others in recent studies (e.g., Gaffey, 1985, 1986, 1987; Clark *et al.*, 1990; Grove *et al.*, 1992). The center of the carbonate absorption-band for the intermediate mineral

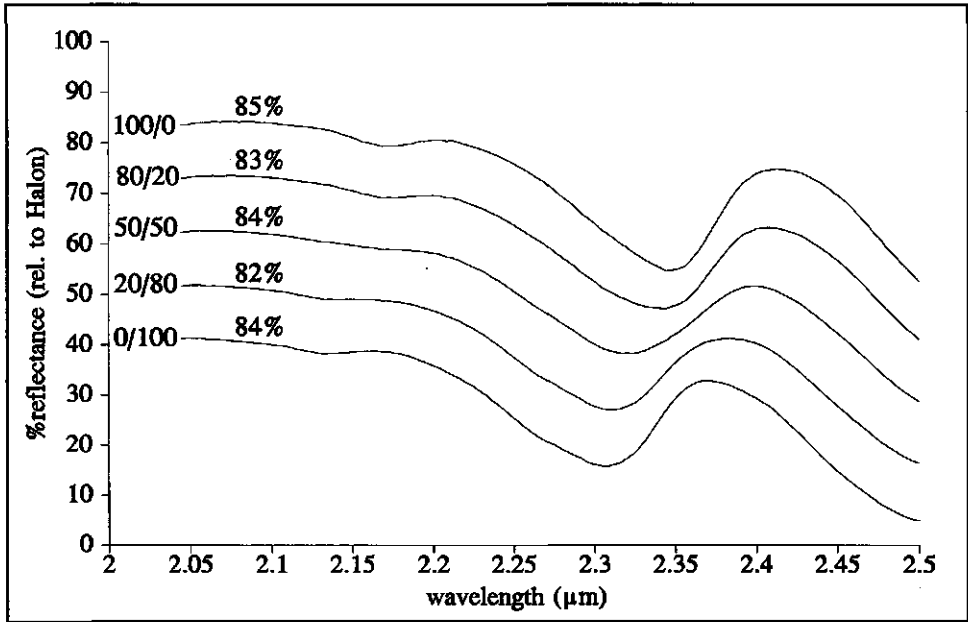


Fig. 4.7: Spectra for some calcite-dolomite mixtures in various mass fractions. Calcite/dolomite fraction is indicated near 2.0 $\mu$ m (e.g., 80 weight % calcite plus 20 weight % dolomite is indicated by 80/20). Brightness of the samples is indicated above the spectra at 2.1 $\mu$ m. Note that each spectrum is offset vertically for clarity (except for the pure calcite spectrum at the top) by 10% reflectance relative to the spectrum above it.

mixtures lies between the values measured for the two pure end-members. The actual position is semi-linearly related to the weight % calcite of the sample as can be deduced from Fig. 4.8. This linear relation is used in Chapter 9 to map calcite/dolomite mineral mixtures from GER 63-channel imaging spectrometer data (Van der Meer, 1994f).

#### 4.3.6 Effects of impurities

In this section, the effects of mineral impurities on spectral reflectance characteristics of carbonates are evaluated. Carbonate rocks contain organic matter, water, clay, silica, iron oxides, sulfides, and sulfates as impurities. Although carbonate rocks may contain up to 50% of quartz grains, the effect of quartz on the spectral reflectance characteristics of carbonate rocks is limited since quartz is spectrally flat in the visible and near-infrared wavelength region (Hunt & Salisbury, 1970; Grove *et al.*, 1992). Crowley (1986) investigated 51

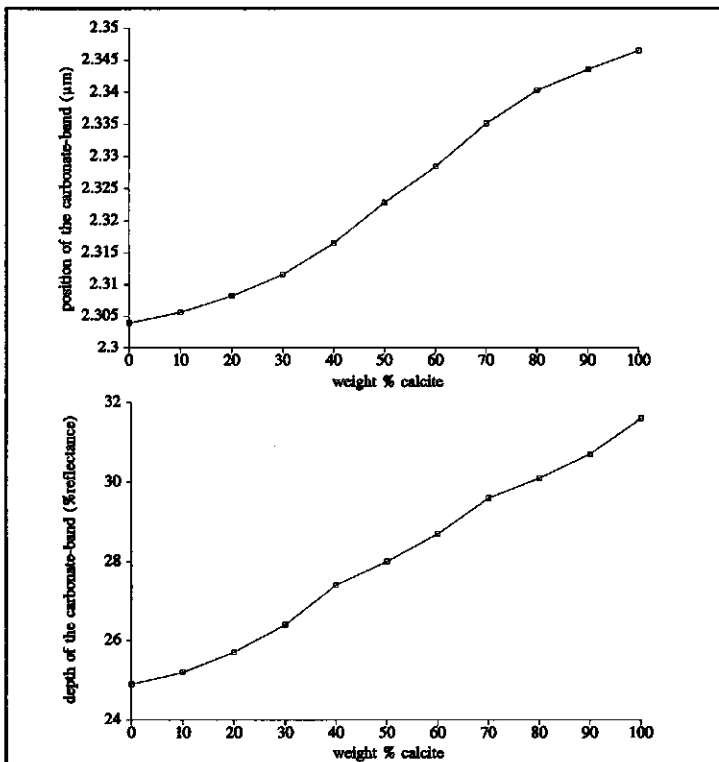


Fig. 4.8: Position (top) and depth (bottom) of the carbonate absorption-band versus the calcite content of the sample (expressed in weight %). See also Table 4.3.

reflectance spectra of various types of carbonate rocks and found that the mineralogical impurities contributing most to the reflectance of these rocks were (1) aqueous fluid inclusions, (2) transition metal cations, and (3) organic material.

**Aqueous fluid inclusions** - Reflectance spectra of carbonate rocks and minerals are extremely sensitive to the presence of water. Water can be recognized in minerals either as fluid inclusions or as isolated molecules (Aines & Rossman, 1984) producing strong absorption features in the near-infrared at 1.4μm and 1.9μm (Clark, 1981; Clark & Lucey, 1984). Weaker water absorption bands occur centered at 1.80, 1.20, 0.97, and 0.76μm (Hunt, 1977; Hunt & Salisbury, 1970). In addition, there are two strong fundamentals, the symmetric and asymmetric stretches that occur at about 2.90μm. Although this feature occurs outside the visible and near-infrared spectral region of reflectance spectra studied in this Chapter, this band is generally so strong that it influences the reflectance characteristics in the 2.00-2.50μm region. Fluid inclusions are nearly ubiquitous in carbonate rocks containing abundant skeletal material, however, diagenetic processes alter the fluid-inclusion content of skeletal material.



Table 4.3: Absorption-band depth and position of synthetic calcite/dolomite mineral mixtures.

weight% calcite	carbonate-band position ( $\mu\text{m}$ )			carbonate-band depth(%refl.)		
	minimum	average	maximum	minimum	average	maximum
0	2.3031	2.3039	2.3049	31.4	31.6	31.8
10	2.3049	2.3056	2.3066	30.4	30.7	30.9
20	2.3079	2.3082	2.3089	29.7	30.1	30.5
30	2.3101	2.3116	2.3125	29.2	29.6	30.0
40	2.3151	2.3165	2.3176	28.4	28.7	28.9
50	2.3219	2.3228	2.3239	27.9	28.0	28.4
60	2.3271	2.3284	2.3291	27.0	27.4	27.6
70	2.3340	2.3351	2.3360	26.2	26.4	26.8
80	2.3390	2.3403	2.3415	25.5	25.7	26.0
90	2.3436	2.3445	2.3453	25.0	25.2	25.5
100	2.3451	2.3465	2.3473	24.7	24.9	25.2

Studies by Conger *et al.* (1977) and Green *et al.* (1980) of electrontransparent foils of coral skeletons, and a study by Gaffey (1985) on spectra of planktonic foraminifers, have shown that these contain fluid inclusions of 1000Å or less in diameter.

Many carbonate rocks contain minor traces of water bearing clay minerals, typically kaolinite, montmorillonite, and smectite which produce  $\text{H}_2\text{O}$  and  $\text{OH}^-$  absorption features. Bands due to water bound by clay minerals are narrower and occur at shorter wavelengths because of the  $\text{OH}^-$  modes. Kaolinite  $\{\text{Al}_2\text{Si}_2\text{O}_5(\text{OH})_4\}$  has a strong absorption feature at 1.4 $\mu\text{m}$  and a double absorption feature centered at 2.16 and 2.2 $\mu\text{m}$ . Due to the lack of  $\text{H}_2\text{O}$ , the feature at 1.9 $\mu\text{m}$  is weakly developed or missing (Hunt & Salisbury, 1970; Clark *et al.*, 1990). Montmorillonite  $\{(\text{Na,Ca})_{0.33}(\text{Al,Mg})_2\text{Si}_4\text{O}_{10}(\text{OH})_2\cdot\text{H}_2\text{O}\}$  has strong  $\text{OH}^-$  and  $\text{H}_2\text{O}$  absorption features at 1.4, 1.9, and 2.2 $\mu\text{m}$  (Hunt & Salisbury, 1970; Clark *et al.*, 1990). Thus kaolinite trace abundances can be differentiated from fluid inclusions and other clay minerals from the absence of the 1.9 $\mu\text{m}$  feature.

In Fig. 4.9, reflectance spectra of mineral mixtures of kaolinite and calcite prepared in the laboratory are shown as measured on the laboratory reflectance spectrometer. Trace amounts of less than 1% kaolinite are not noticeable. A clear absorption feature at 1.4 $\mu\text{m}$  is visible for spectra with more than 2% kaolinite. When more than 5% kaolinite is mixed, the double absorption feature at 2.2 $\mu\text{m}$  becomes very pronounced. Simultaneously, the spectra tend to be "pulled down" at longer wavelengths due to the rapid decrease of reflectance values of kaolinite in the 2.0-2.5 $\mu\text{m}$  wavelength region. Note that the 1.9 $\mu\text{m}$  water absorption feature, which is characteristic for other clay minerals occurring as impurities in carbonates, is absent in these spectra.

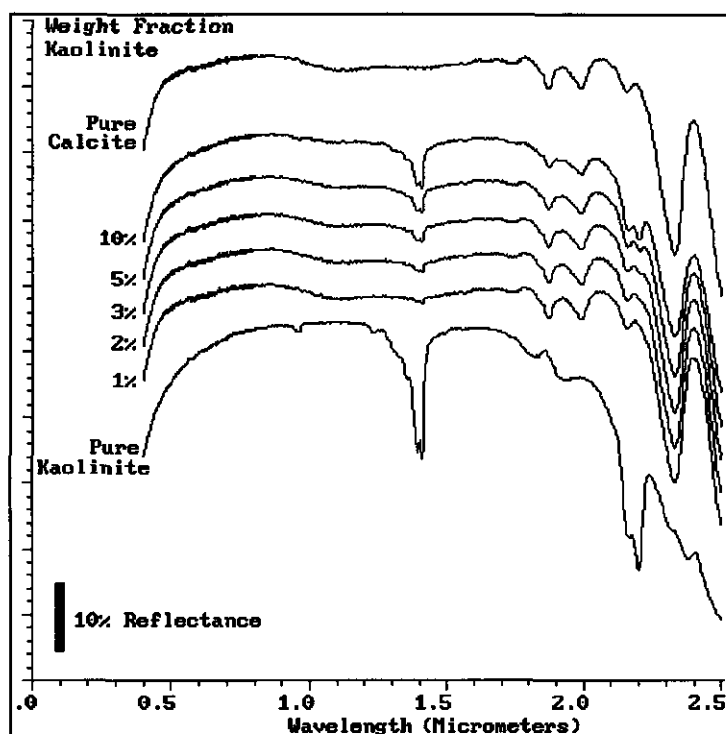


Fig. 4.9: Spectra of mixtures of calcite (grain size of  $45\mu\text{m}$ ) and kaolinite (grain size  $5\mu\text{m}$ ). Spectra are vertically offset for clarity.

**Transition metal ions** - Iron in the form of  $\text{Fe}^{2+}$  substitutes  $\text{Ca}^{2+}$  and  $\text{Mg}^{2+}$  in calcite and dolomite (Deer *et al.*, 1962; Reeder, 1983) producing broad absorption bands near  $1.2\text{--}1.3\mu\text{m}$ .  $\text{Fe}^{2+}$  absorption bands in calcite and dolomite spectra differ in position and shape. In the calcite spectrum, a broad double band is centered near  $1.3\mu\text{m}$ , while in dolomite this feature occurs at  $1.2\mu\text{m}$  and the splitting is less pronounced. The metal-ligand distance in calcite is generally larger than in dolomite, therefore it requires higher energies to produce an absorption feature in dolomite which thus occurs at shorter wavelength than in calcite (Reeder, 1983; Burns, 1970). The intensity of iron absorption bands have been shown to be positively correlated with the concentrations of  $\text{Fe}^{2+}$  in the sample (Gaffey, 1986).

In addition, carbonates often contain  $\text{Fe}^{3+}$  due to Fe oxides formed by weathering. Iron oxides have intense absorption features at wavelengths less than  $1\mu\text{m}$  but are relatively transparent at longer wavelengths (Hunt & Salisbury, 1970). Typically, the ferrous ion produces a broad absorption band near  $1.0\mu\text{m}$  and smaller bands centered near  $0.55\mu\text{m}$ ,  $0.51\mu\text{m}$ ,  $0.45\mu\text{m}$ , and  $0.43\mu\text{m}$ , and the ferric ion produces bands at  $0.87\mu\text{m}$ ,  $0.7\mu\text{m}$ , and  $0.4\mu\text{m}$  (Hunt *et al.*, 1971a). Strong iron absorption features at short wavelengths outside the spectral range of  $0.4\text{--}2.55\mu\text{m}$  may account for the strong decrease of reflectance from  $1.0\mu\text{m}$  to shorter

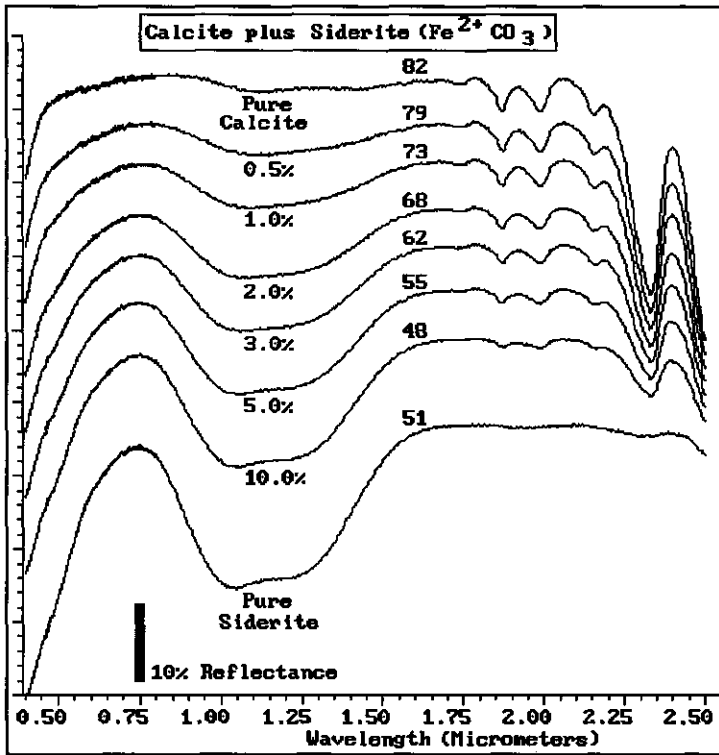


Fig. 4.10: Spectra of mixtures of calcite (grain size 45 $\mu$ m.) and siderite (grain size 5 $\mu$ m.). Spectra are vertically offset for clarity.

wavelengths.

To predict the effects of iron on carbonate reflectance spectra, mixtures of calcite with goethite and siderite were prepared. Reflectance spectra of these mineral mixtures were measured in the laboratory. As discussed above,  $\text{Fe}^{2+}$  occurs in carbonates as a replacement for Ca and Mg rather than in the mineral form. However, the effect of siderite on the spectral reflectance characteristics of carbonates is nearly similar to that of  $\text{Fe}^{2+}$ . Spectra of siderite and calcite mixtures are shown in Fig. 4.10. Siderite ( $\text{Fe}^{2+}\text{CO}_3$ ) has a very strong, broad iron absorption feature in the 1.0-1.25 $\mu$ m wavelength region and is spectrally flat in the 1.7-2.5 $\mu$ m wavelength region. Small amounts of siderite (more than 0.3%) can account for a weak, broad absorption in carbonate reflectance spectra. With increasing iron content, this feature becomes more pronounced and simultaneously the other characteristics of the calcite spectrum disappear. Iron content may considerably darken the sample and obscure carbonate absorption features. From Fig. 4.10, it can be seen that large quantities of iron may reduce overall brightness by more than 25% and considerably reduce the depth of the carbonate absorption feature at 2.34 $\mu$ m. The reduction of brightness is in good agreement with data presented by Gaffey (1985; her Figure 6), however, the masking effect of iron on the carbonate bands has

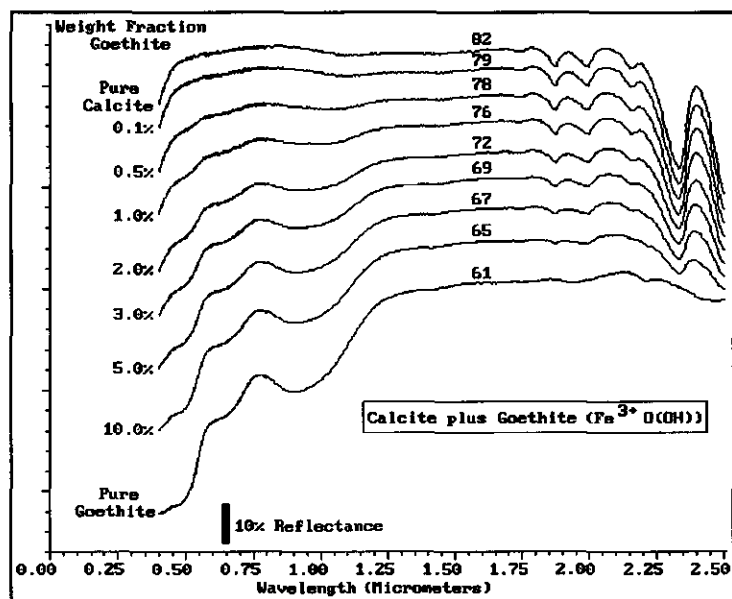


Fig. 4.11: Spectra of mineral mixtures of calcite (grain size 45μm.) and goethite (grain size 5μm.) showing the effect of Fe<sup>3+</sup> on carbonate reflectance spectra. The percent reflectance at 1.6μm is indicated above each spectrum. Spectra are vertically offset for clarity.

not yet been reported.

Goethite (Fe<sup>3+</sup>HO<sub>2</sub>) is formed under oxidizing conditions as a weathering product of iron-bearing minerals and often occurs in combination with hematite (Fe<sub>2</sub>O<sub>3</sub>). Together, these minerals impart the reddish or brownish color of weathered rocks and are often abundant in carbonate samples. Their spectra are rather similar and show strong, broad absorption features near 0.9μm due to Fe, and two additional smaller features at 0.65μm and 0.5μm. The fall-off short of 0.55μm is a result of a conduction band with a well-resolved absorption edge typical for iron oxides (Hunt *et al.*, 1971a). The net effect of Fe<sup>3+</sup> on carbonate reflectance spectra is demonstrated in Fig. 4.11, where reflectance spectra of calcite and goethite mineral mixtures are shown with varying amounts of goethite. The iron oxides give rise to a broad absorption feature centered at 0.9μm in carbonate spectra and a gradual decreasing reflectance from approximately 1.25μm toward shorter wavelengths. This in contrast to the fall-off noticed in the siderite-calcite spectra (Fig. 4.10) which is more apparent and occurs from 0.75μm. Goethite reduces the overall brightness of the sample and masks carbonate absorption features, however, this effect is less pronounced than in the siderite spectra. The strengths of the iron features not only depends on the amount of iron, but a smaller grain size will produce a stronger effect than larger grain sizes.

**Organic material** - Plant rests are likely to be preserved in carbonate rocks in some form of organic material. Organic material may be present in carbonate rocks in the form of hydrogen,

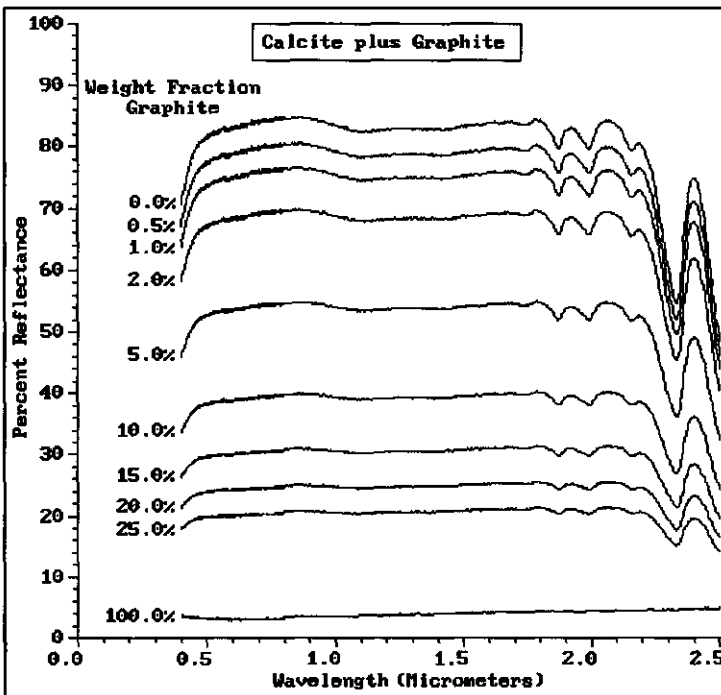
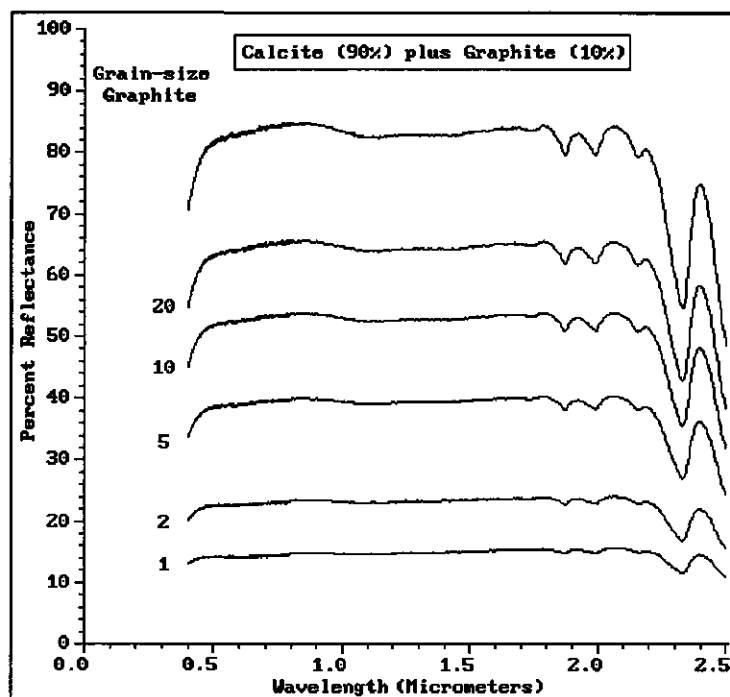


Fig. 4.12: Spectra of mixtures of calcite and graphite demonstrating the spectral quenching effect of organic material. Spectra are not offset vertically.

carbon, and kerogen. Kerogen, organic matter that is insoluble in organic solvents, usually constitutes most of the organic matter in carbonate rocks. Very small amounts of organic matter are known to substantially darken samples. Organic quenching not only reduces the overall sample brightness, but also masks carbonate features making them less pronounced such that the resulting reflectance spectrum resembles a coarse sample in terms of its brightness and has band intensity characteristics of a very fine-grained sample. This effect is related to the opacity of organic matter. Opacity of organic matter increases in response to thermal alteration (Staplin, 1969; Long *et al.*, 1968). Other factors influencing the spectral quenching effect are the amount of organic material and the grain size of this material (Clark, 1983). Clark (1983) showed that the various water absorption bands in montmorillonite are suppressed differently with different amounts of dark opaque charcoal grains mixed. Thus, the ratio of overtone band depths vary as a function of opaque content and can be used to estimate these contents.

To demonstrate the spectral quenching by organic material, spectra for mixtures of calcite with various amounts of graphite of variable grain size were measured in the laboratory. Graphite is essentially pure carbon and has a very dark reflectance spectrum lacking any absorption features. Fig. 4.12 shows mixtures of calcite (45 $\mu$ m) with variable



**Fig. 4.13:** Effect of grain size of organic impurities on spectral reflectance characteristics. Spectra are not offset vertically.

weight fraction of graphite ( $5\mu\text{m.}$ ) added. Note that the spectra in this figure are not offset vertically. Clearly, from Fig. 4.12 it can be seen that small amounts of graphite substantially darken a sample reducing the overall reflectance and masking the prominent carbonate absorption features. However, for amounts up to 25% of graphite, the  $2.34\mu\text{m}$  carbonate absorption feature is still detectable. In many cases, organic matter forms a coating on carbonate grains producing more radical effects in reducing the depth of the carbonate features. The spectral quenching effect of organic matter is highly dependent on the grain size of the organic material as can be deduced from Fig. 4.13. In case the carbon grains are relatively large compared to the carbonate material, the spectral quenching effect is minor. With decreasing grain size of the impurity, the effect becomes increasingly more pronounced while very finely disseminated organic material in small quantities may mask even the strongest carbonate absorption features. Finely disseminated organic material is known from studies of chondrites (Johnson & Fanale, 1973) and the spectral effects discussed above agree well with results presented by Clark (1983) on montmorillonite/carbon black mixtures and form a justification of work presented by Crowley (1986).

- Chapter 4 -

Table 4.4: Description of polished thin sections.

sample	grain-size ( $\mu\text{m}$ )	classification	components	XRF	remarks
b3	210	grainstone	foraminifers	yes	
b3a	305	grainstone	algae	yes	
b4	25	grainstone	lithoclasts		opaque, qtz.
b7	144	sparite	lithoclasts		recrystallized
b8	11	wackstone	lithoclasts		porous
b9	295	sparite	lithoclasts		recrystallized
b11	27	sparite	lithoclasts		recrystallized
b12	300	sparite	lithoclasts		iron stains
b14	20	sparite	lithoclasts		porous
b15	80	grainstone	lithoclasts		porous
b17	50	packstone			
b19	30	crystalline			recrystallized
b20	55	crystalline			recrystallized
b21	100	mudstone			laminated
b22	53	mudstone			
b23	110	wackstone	lithoclasts		
b25	156	grainstone			
b26	115	sparite			
b27	88	packstone			
b28	101	wackstone	lithoclasts		quartz?
b30	43	grainstone	lithoclasts		
b31	110	mudstone	lithoclasts		
b33	95	wackstone		yes	iron stains
b34	89	wackstone			iron stains
m9206	21	grainstone	pellets/ooliths	yes	shell fragments
m9210	35	wackstone	ostracods	yes	
m9213	65	packstone	onkoids		
m9215	25	micrite			
m9216	20	mudstone	foraminifera		
m9220	70	mudstone	ooliths		
m9221	248	mudstone	globigerinen	yes	gastropods
m9223	75	mudstone	ostracods		
m9226	60	wackstone	pellets		shell fragments
m9227	32	grainstone	pellets/ooliths	yes	
m9249	130	sparite		yes	dark opaques
m9250	206	sparite			
m9254	60	sparite			
m9256	150	sparite			
m9269	30	sparite		yes	
m9275	55	sparite		yes	
m9278	30	sparite		yes	recrystallized
m9293	250	sparite		yes	iron stains
m92112	175	sparite			

- Reflectance spectra of carbonate minerals and rocks -

**Table 4.5:** Major element composition of rock samples from XRF analysis.

sample number	Na <sub>2</sub> O	MgO	Al <sub>2</sub> O <sub>3</sub>	SiO <sub>2</sub>	K <sub>2</sub> O	CaO	Fe <sub>2</sub> O <sub>3</sub>	Other traces
m9206	0.288	0.575	8.057	---	---	84.772	6.308	MnO, NiO
m9210	---	0.879	0.266	1.758	0.180	96.69	0.158	P <sub>2</sub> O <sub>5</sub> , SO <sub>3</sub> , TiO <sub>2</sub>
m9221	0.168	0.842	3.136	11.785	0.358	82.702	1.010	P <sub>2</sub> O <sub>5</sub> , Cl, TiO <sub>2</sub> , MnO
m9227	---	0.876	---	0.229	0.022	98.794	0.079	SO <sub>3</sub> , MnO, SrO
m9249	---	22.247	0.271	1.715	0.072	75.547	0.148	SO <sub>3</sub> , Cl
m9269	---	40.387	---	0.292	0.027	59.234	0.061	P <sub>2</sub> O <sub>5</sub> , Cl, Ar
m9275	---	39.366	---	0.588	---	59.953	0.093	P <sub>2</sub> O <sub>5</sub> , MnO, SrO
m9278	0.041	37.408	---	4.585	---	57.938	0.027	Cl
m9293	0.199	1.019	0.069	0.598	0.029	97.889	0.197	TiO <sub>2</sub> , Cl
b3	0.062	1.972	2.300	9.242	0.472	78.866	7.086	P <sub>2</sub> O <sub>5</sub> , S, Cl, Ar, ZnO
b3a	---	1.120	0.594	3.704	0.153	93.971	0.457	SO <sub>3</sub> , TiO <sub>2</sub> , MnO
b33	0.109	1.357	0.394	2.582	0.197	95.186	0.175	TiO <sub>2</sub> , Cl, SO <sub>3</sub>

#### 4.4 REFLECTANCE SPECTRA OF ROCK SAMPLES

Visible and near-infrared reflectance spectra of 44 polished sections of carbonate rocks were studied to evaluate the effects of particle size, sorting, texture, and impurities on reflectance as concluded from the theoretical investigations discussed above. The rock texture was quantified using the grain size statistics and carbonates were named using the Dunham (1962) classification scheme. Grain boundaries of a few hundred grains in each thin section were identified by crystal extinction resulting from rotating the microscope table. The mean grain size for each sample was determined as well as the kind of cement and type of components (Table 4.4). For some samples, major and trace element composition was determined by X-ray fluorescence (XRF) analysis of powdered samples (Table 4.5).

Fig. 4.14 shows a scatter plot of mean grain size versus percent reflectance measured at 1.6 $\mu$ m for 44 spectra of rock samples. Although the plot exhibits some scatter, reflectivity seems to be decreasing with increasing mean grain size. This contradicts earlier results presented by Crowley (1986) who found no correlation between sample grain size and overall brightness of samples.

In Fig. 4.15 seven spectra of rock samples are displayed. Samples m9275 and m9278 are partly dolomitized limestones as can be deduced from the results of the XRF analysis in Table 4.4. The lowest value of the 2.3 $\mu$ m absorption feature is shifted to smaller wavelengths



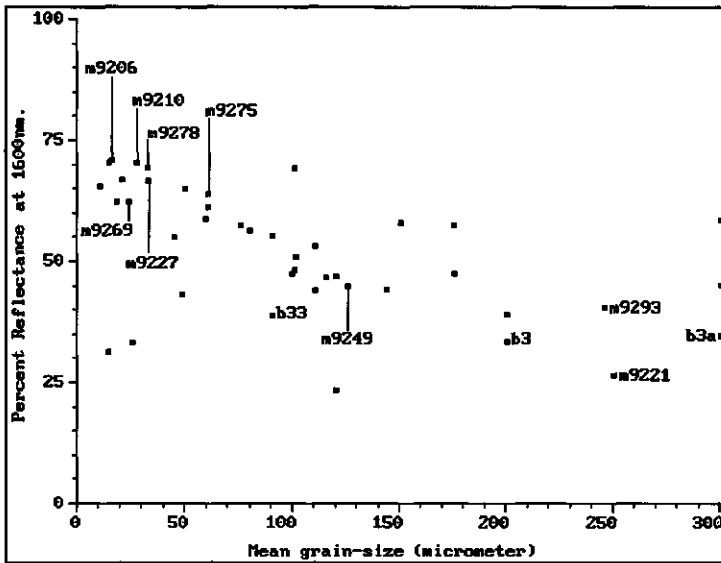


Fig. 4.14: Mean grain size versus brightness for 44 rock samples showing a decrease in overall brightness with increasing grain size.

in comparison with sample m9210, a pure calcite. This shift was discussed previously for theoretical mixtures of calcite and dolomite. A small amount of  $Al_2O_3$  was detected in sample m9210 which indicates the presence of clay minerals in the sample causing the weak hydroxyl absorption feature at  $1.4\mu m$ . This absorption feature becomes more pronounced in the spectrum of sample m9206 which also shows a strong absorption band at  $1.6\mu m$  indicating that water bonded by clay minerals is present. The lowermost three samples in Fig. 4.15 are relatively dark and absorption features are obscured. XRF analysis (Table 4.4) showed that these samples contain large amounts of  $SiO_2$  possibly in the form of radiolarian and other organisms which have a siliceous skeleton. No analysis for organic material was undertaken because of the complexity of such analytical work and the numerous errors which may arise from it (Forsman, 1963; Durand & Monin, 1980). However, in sample m9221 and other samples, dark opaque material was seen under the microscope which may represent organic material, whereas in most cases dark reflectance spectra correlated with thin sections showing a uniform dark, brownish color attributed to the presence of finely disseminated organic material.

Fig. 4.16 shows a scatter plot of the reflectivity measured at  $1.6\mu m$  versus the depth of the carbonate absorption band (centered near  $2.34\mu m$ ). In this figure, five groups of carbonate rocks with different textures can be recognized on basis of their reflectance characteristics. Group I carbonates (indicated by the box symbol in Fig. 4.16) have relatively strong carbonate absorption features and a bright continuum. These are mainly poorly sorted biosparites with pellets and intraclasts as the main components. Group II carbonates (indicated

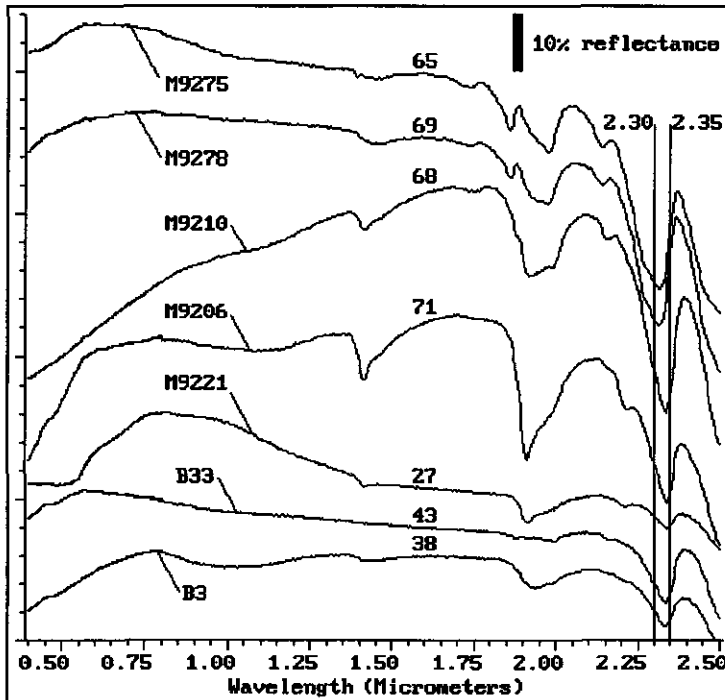


Fig. 4.15: Reflectance spectra of rock samples discussed in the text (Van der Meer, 1994g).

by the circle symbol in Fig. 4.16) have moderate to weak carbonate absorption features and a high overall reflectivity. This group represents the pure sparites which were found to be well sorted. The reflectance and depth of carbonate feature for these sparites is dominated by the overall grain size of the sample; the fine-grained samples being brighter with weaker absorption features than their coarse-grained counterparts. Group III carbonates (indicated by the delta symbol in Fig. 4.16) have a moderately high reflectivity and weak carbonate absorption features. These limestones were either medium- to coarse-grained bioclastic grainstones or wackestones containing fragmented shells or skeletons of gastropods, pelecypods, foraminifers, algae, etc. Group IV carbonates (indicated by the plus symbol in Fig. 4.16) have weak carbonate absorption features and are characterized by rather dark spectra. This group typically represents limestones containing organic material or clay mineral impurities. Their petrographic texture and composition is variable and the reflectance characteristics are altered as a result of high amounts of impurities. Some of these contain high amounts of silica in the form of skeletal remains of radiolarian and other siliceous organisms of which the effect on the reflectance spectrum was discussed earlier.

Group V carbonates (indicated by the cross symbol in Fig. 4.16) have a moderate overall brightness with relatively strong carbonate absorption features. These carbonates were

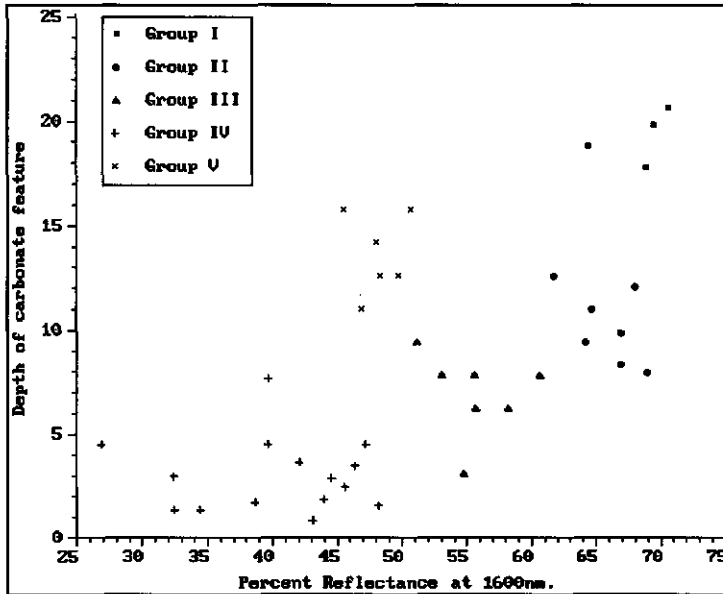


Fig. 4.16: Brightness versus spectral contrast in absorption features for the five groups of carbonate rocks which are discussed in the text.

found to be predominantly wackestones and some mudstones with pellets, and ooliths as their main components.

## 4.5 CONCLUSIONS

Reflectance spectra of carbonate minerals exhibit seven absorption bands in the 0.4-2.5 $\mu$ m wavelength region. From the results presented, the following conclusions arise:

- (1) The overall brightness of a sample as expressed as the reflectance measured at 1.6 $\mu$ m decreases almost linearly with increasing grain size of the sample.
- (2) The depth of individual carbonate absorption features increases non-linearly with increasing grain size of the sample.
- (3) The ratio of the intensity of a given band versus another band is invariant with grain size. This relation can be used to deduce a measure for the grain size of a sample from the bidirectional reflectance theory presented by Hapke (1981, 1984, 1987).
- (4) The theoretical effect of petrographic texture and sorting on the spectral reflectance

*- Reflectance spectra of carbonate minerals and rocks -*

characteristics of a mineral assemblage is difficult to address due to the pronounced effect of fine material on the overall reflectance characteristics of a mixture.

(5) Calcite/dolomite mixtures form the two end-members in a continuous series of mixtures where the depth and position of the carbonate absorption feature in the 2.3-2.4 $\mu\text{m}$  wavelength region can be expressed as a linear combination of calcite (or dolomite) content. This can be shown theoretically using mixing models and was verified in laboratory measurements of samples with known composition.

(6) Fluid inclusions, which are nearly ubiquitous in carbonate rocks containing abundant skeletal material, produce strong absorption features in the near-infrared at 1.4 $\mu\text{m}$  and 1.9 $\mu\text{m}$ , and weaker water absorption bands centered at 1.80, 1.20, 0.97, and 0.76 $\mu\text{m}$ .

(7) Water bearing clay minerals, typically kaolinite, montmorillonite, and smectite, are often present as impurities in carbonates. Kaolinite results in an absorption feature at 1.4 $\mu\text{m}$  and a double absorption feature centered at 2.16 and 2.2 $\mu\text{m}$ . Due to the lack of  $\text{H}_2\text{O}$ , the feature at 1.9 $\mu\text{m}$  is missing. Montmorillonite gives rise to absorption features at 1.4, 1.9, and 2.2 $\mu\text{m}$ .

(8) Iron in the form of  $\text{Fe}^{2+}$  substitutes  $\text{Ca}^{2+}$  and  $\text{Mg}^{2+}$  in calcite and dolomite producing broad absorption bands near 1.2-1.3 $\mu\text{m}$  and a rapid fall-off of reflectance at very short wavelengths.  $\text{Fe}^{3+}$  in carbonates result from oxidation of iron by weathering producing absorption bands at 0.87 $\mu\text{m}$ , 0.7 $\mu\text{m}$ , and 0.4 $\mu\text{m}$ . Strong iron absorption features at short wavelengths outside the spectral range of 0.4-2.55 $\mu\text{m}$  may account for the strong decrease of reflectance from 1.0 $\mu\text{m}$  to shorter wavelengths.

(9) Very small amounts of organic matter substantially darken samples thus reducing the overall reflectance and band intensities of carbonate absorption bands. The spectral quenching effect of organic material is highly dependent on the size fraction of the impurity.

## CHAPTER 5:

### *Spectral reflectance of ultramafic rocks and the effect of serpentinization<sup>3</sup>*

#### ABSTRACT

Visible- and near-infrared (0.4-2.5 $\mu$ m) reflectance spectra of ultramafic rocks are discussed in this Chapter in relation to their mineralogy. The reflectance spectra are dominated by ferrous and ferric ion absorption bands. The wavelength position of these bands depends on the presence and relative amounts of primary minerals such as olivine and orthopyroxenes. As a result of hydrothermal alteration, several samples contain secondary hydrous-serpentine group minerals as a replacement for primary magnesium silicate minerals. Serpentinization results in a decrease in contrast of olivine-pyroxene iron absorption features and an appearance and increase in OH-absorption features near 1.4 $\mu$ m and 2.3 $\mu$ m characteristic for serpentine minerals. The degree of serpentinization is expressed as a function of the brightness of the sample and the depth of the 2.3 $\mu$ m absorption feature. This relation can also be derived from semi-empirical mixing models. However, the presence of small amounts of magnetite in a sample obscures the spectral contrast and decreases the overall brightness of the sample.

---

<sup>3</sup>Parts of this Chapter have been published as:

Van der Meer, F. 1994. Mapping the degree of serpentinization within ultramafic rock bodies using imaging spectrometer data. *International Journal of Remote Sensing*, 15(18): 3851-3857.

## 5.1 INTRODUCTION

Ultramafic rocks are dark colored rocks containing less than 45 percent silica. Predominant minerals are olivine, orthopyroxene (typically enstatite), clinopyroxene (augite, diopside, wollastonite), hornblende, sometimes biotite, and often small amounts of garnet and spinel. They are subdivided into peridotites and pyroxenites, the first containing more than 40% olivine, the latter containing less than 40% olivine. Further classification is based on the relative abundances of olivine, pyroxene and hornblende using the diagrams of Fig. 5.1 published by Streckeisen (1973, his Figures 2a and 2b; 1976).

Peridotites are ultramafic rocks containing more than 40% olivine, and orthopyroxene (typically enstatite), clinopyroxene (augite, diopside, wollastonite), hornblende, sometimes biotite, and often small amounts of garnet and spinel. Reflectance spectra of these minerals are well known (Hunt & Salisbury, 1970; Hunt *et al.*, 1973; Clark *et al.*, 1990; Grove *et al.*, 1992) and several studies have been conducted to determine reflectance spectra of ultramafic rocks (e.g. Hunt *et al.*, 1974). Olivine reflectance spectra in the 0.4-2.5 $\mu\text{m}$  wavelength region show a broad asymmetric absorption feature near 1 $\mu\text{m}$  (Burns, 1970) resulting from electronic transitions in  $\text{Fe}^{2+}$  cations. Cloutis *et al.* (1990) showed that this band minimum shifts toward longer wavelengths with increasing iron content (see also King & Ridley, 1987). At wavelengths shorter than 0.55 $\mu\text{m}$  a steep drop-off in reflectance occurs due to various charge transfer absorptions (Burns, 1970). Orthopyroxenes exhibit two main absorption features near 1 $\mu\text{m}$  and 2 $\mu\text{m}$  due to crystal field transitions in ferrous iron (Burns, 1970) whose positions shift to longer wavelengths with increasing iron content (Cloutis *et al.*, 1990; Adams, 1974). Clinopyroxenes such as augite and diopside, display two broad absorption bands at 0.77 $\mu\text{m}$  and 1.1 $\mu\text{m}$  due to ferrous iron and a rapid fall-off of reflectance toward the blue (Hunt & Salisbury, 1970; Adams, 1974).

Spectra of serpentine-group minerals are bright (except for the magnetite spectrum), and display sharp intense doubled or multiple absorption bands near 1.4 $\mu\text{m}$  and 2.3 $\mu\text{m}$  with supplementary broader and weaker features near 1.95 $\mu\text{m}$  and 2.1 $\mu\text{m}$  (Hunt *et al.*, 1971; King & Clark, 1989). These features can be attributed to vibrational overtone and combination tones involving  $\text{OH}^-$  stretching modes. The 2.3 $\mu\text{m}$  feature in these minerals is due to a combination of the  $\text{OH}^-$  stretching fundamental with the  $\text{MgOH}$  bending mode whereas the  $\text{AlOH}$  bending mode results in a feature near 2.2 $\mu\text{m}$  (Boutin & Basset, 1963).

Hunt & Evarts (1981) provided the first qualitative estimates of the degree of serpentinization based on reflectance spectroscopy. These authors showed that increasing serpentinization is indicated by the decrease in contrast of absorption features of primary magnesian silicate minerals, and the appearance and increase in contrast of the 1.4 $\mu\text{m}$  and 2.3 $\mu\text{m}$  absorption features of serpentine-group minerals. Hunt & Evarts (1981) conclude that

- Reflectance spectra of ultramafic rocks -

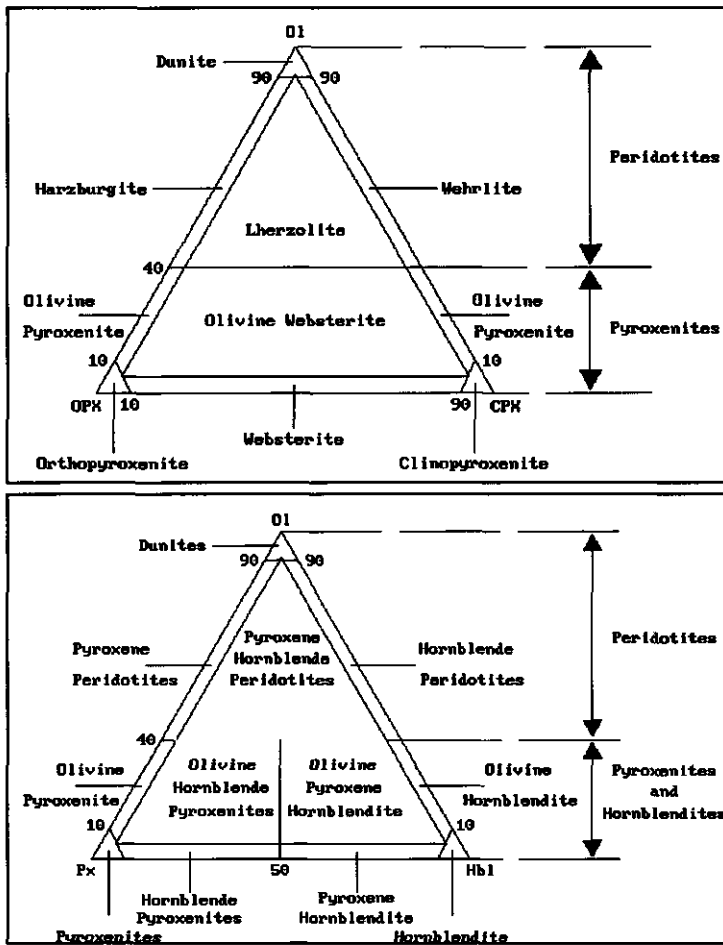


Fig. 5.1: Classification and nomenclature of ultramafic rocks based on the proportions of olivine (Ol), orthopyroxene (OPX), clinopyroxene (CPX), pyroxene (Px), and hornblende (Hbl)(after Streckeisen, 1973).

small amounts of magnetite lowers the overall reflectance of the sample and decreases the contrast of absorption features thus complicating the estimation of the degree of serpentinization from reflectance spectra.

Only few studies describe reflectance spectra of ultramafic rocks, probably because their reflectivity is relatively low over the visible and near-infrared wavelength range thus producing dark spectra which are relatively featureless. In this Chapter, reflectance spectra of a variety of ultramafic rocks are discussed which were collected from the Ronda peridotite body. An attempt is made to evaluate their spectral characteristics in relation to their mineralogy. Furthermore, the effect of serpentinization on the reflectance characteristics is investigated and its implications for remote sensing (Van der Meer, 1994i+j).

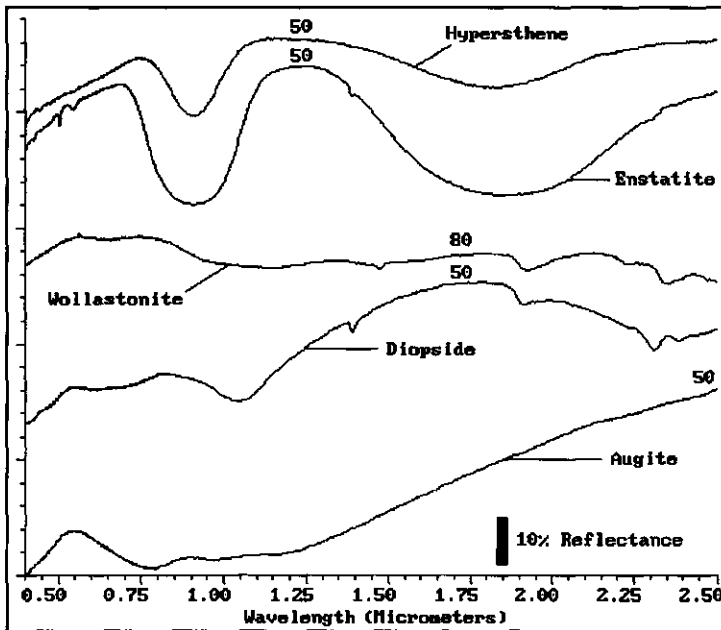


Fig. 5.2: Reflectance spectra of ortho- and clinopyroxenes that occur as primary minerals in ultramafic rocks. Spectra are vertically offset for clarity. Reflectance values at various wavelengths are denoted above the curves.

## 5.2 REFLECTANCE SPECTRA OF ULTRAMAFIC ROCKS

### 5.2.1 Laboratory method

For the spectral analysis, part of the hand specimen was sawed off for the preparation of a thin section from which the bulk mineralogy was determined. Identification of the serpentine species and their relative proportions was done by X-ray diffractometry from powders. Hemispherical reflectance measurements in the visible and near-infrared wavelength region (0.4-2.5μm) of the electromagnetic spectrum presented in this Chapter, were made using the Beckman UV5240 spectrometer described in detail in Chapter 4.

### 5.2.2 Mineral spectra

Mineral reflectance spectra of ortho- and clinopyroxenes constituting ultramafic rocks are shown in Fig. 5.2. Augite  $\{(Ca, Na)(Mg, Fe, Al, Ti)(Si, Al)_2O_6\}$ , a monoclinic pyroxene, displays two broad absorption bands at 0.77μm, due to ferric iron, and at 1.1μm, due to ferrous iron.



- Reflectance spectra of ultramafic rocks -

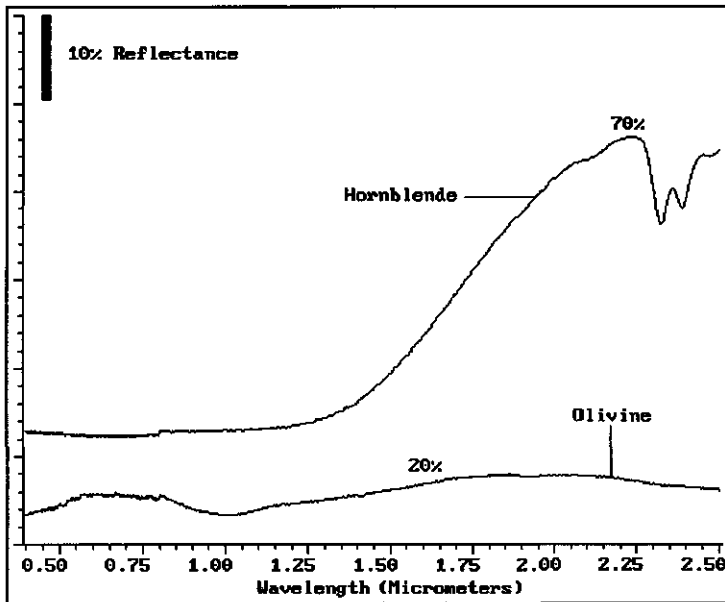


Fig. 5.3: Reflectance spectra of olivine and hornblende. Spectra are vertically offset for clarity. Reflectance values at 1.6 $\mu$ m are denoted above the curves.

Diopside  $\{(Na, Ca) (Mg, Fe, Al) Si_2O_6\}$  shows an intense ferrous iron absorption band at 1.05 $\mu$ m and minor ferric iron absorption features at 0.7 and 0.8 $\mu$ m. A small amount of water in fluid inclusions is indicated by the weak water band. Wollastonite  $[CaSiO_3]$  shows a weak iron absorption feature at 1.1 $\mu$ m and an additional feature at 2.23 $\mu$ m due to the presence of calcium. Enstatite  $[Mg SiO_3]$  and Hypersthene  $\{(Mg, Fe)_2 Si_2O_6\}$  are typical orthopyroxenes occurring in ultramafic rocks. They have broad and intense pairs of absorption bands centered at 0.9 $\mu$ m and 1.8 $\mu$ m due to ferrous iron. The olivines form an isomorphous mineral series varying from fosterite,  $[Mg_2 SiO_4]$ , to fayalite,  $[Fe_2 SiO_4]$ . Commonly, olivine has a  $(Mg, Fe)_2 SiO_4$  composition and the pure ferrous or magnesian end-members are rare. Pure fosterite has a relatively flat spectrum whereas pure fayalite shows strong iron absorption bands centered near 0.45 $\mu$ m and 1.0 $\mu$ m. Fig. 5.3 shows a typical sample of olivine which is spectrally dark and exhibits a iron band near 1.05 $\mu$ m. Hornblende  $\{(Ca, Na, K)_{2-3} (Mg, Fe^{2+}, Fe^{3+}, Al)_5 (Si_6(Si, Al)_2 O_{22}) (OH, F)_2\}$  is the name given to a complex series of amphiboles which varies with respect to at least ten major components. The spectrum shown in Fig. 5.3 is typical of a hornblende spectrum, which displays a rapid fall off in intensity from 2.0 $\mu$ m to the blue due to broad  $Fe^{2+}$  and  $Fe^{3+}$  absorption features near 0.7 $\mu$ m and 1.0 $\mu$ m. The features at 2.33 $\mu$ m and 2.4 $\mu$ m are due to OH.

In addition to the main minerals constituting ultramafic rocks, various amounts of spinel, biotite and garnet may occur. Biotite is a potassium, magnesian, iron, aluminium silicate, essentially  $K(Mg, Fe)_3 AlSi_3O_{10}(OH)_2$  which has a similar spectrum to hornblende

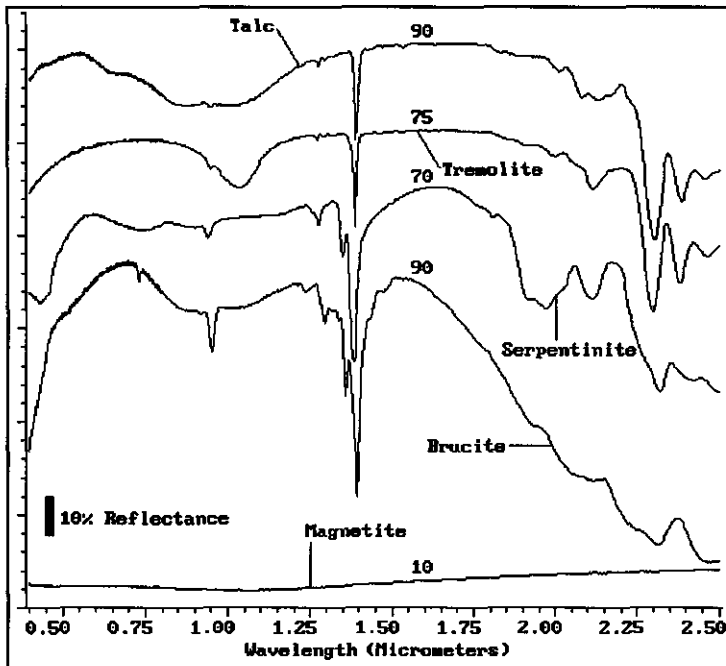


Fig. 5.4: Spectra of secondary minerals formed as a result of serpentinization. Spectra are vertically offset for clarity. Reflectance values at 1.6 $\mu$ m are denoted above the curves.

showing a rapid fall-off of reflectivity from 2.0 $\mu$ m to the blue due to broad ferric iron bands in the 0.6-1.5 $\mu$ m wavelength region. The OH overtones at higher wavelengths are generally obscured. The spinel spectrum is almost featureless (Hunt & Salisbury, 1970). Garnet spectra have been studied extensively (e.g. Moore & White, 1971; Dowty, 1971). Most garnets contain iron which thus produce strong absorption bands in the 0.4-1.0 $\mu$ m wavelengths region. In addition, often diagnostic absorption features are observed at 1.28 $\mu$ m and 1.7 $\mu$ m.

As a result of the hydrothermal serpentinization process, magnesian silicate minerals (especially olivines and pyroxenes) in ultramafic rocks are often replaced by hydrous minerals of the serpentine group composed mainly of flaky antigorite and fibrous chrysotile plus lesser amounts of brucite, talc, tremolite and magnetite. The green color of serpentine minerals and serpentinites (e.g. rocks composed mainly of serpentine-group minerals) is principally determined by the iron content, becoming deeper as it increases. Spectra of serpentine minerals  $\{Mg_3(Si_2O_5)(OH)_4\}$  are shown in Fig. 5.4 (see also Hunt & Evarts, 1981). Except for the magnetite spectrum, these are bright spectra displaying sharp intense doubled or multiple absorption bands near 1.4 $\mu$ m and 2.3 $\mu$ m, with supplementary broader and weaker features near 1.95 $\mu$ m and 2.1 $\mu$ m. These features can be attributed to vibrational overtone and combination tones involving OH-stretching modes. The 2.3 $\mu$ m feature in these minerals is due to a combination of the OH-stretching fundamental with the MgOH-bending mode whereas

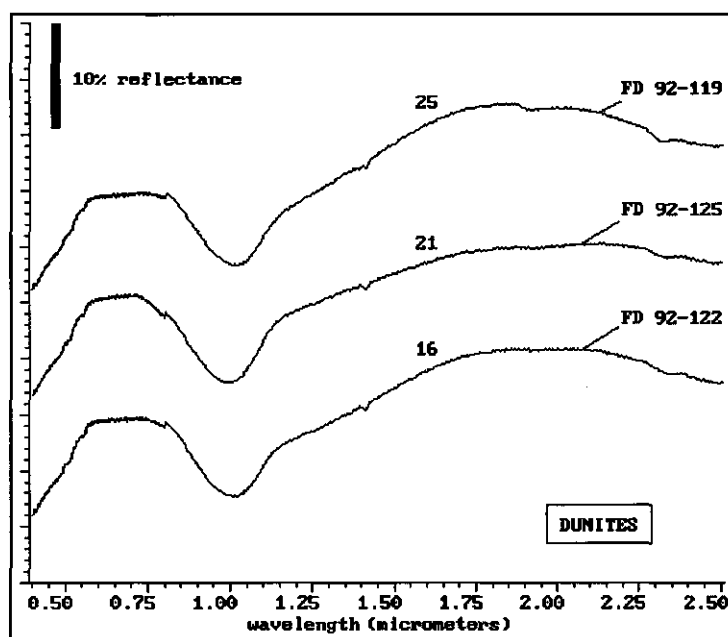


Fig. 5.5: Reflectance spectra of dunite samples. Mineralogy of the samples is listed in Table 5.1. Spectra are vertically offset for clarity. Reflectance values at 1.6 $\mu$ m are denoted above the curves.

the ALOH-bending mode results in a feature near 2.2 $\mu$ m (Boutin & Basset, 1963). Magnetite ( $\text{Fe}_3\text{O}_4$ ) is an opaque mineral with a dark featureless spectrum.

### 5.2.3 Rock spectra

Spectra of three samples of dunites are shown in Fig. 5.5. Their mineralogy, as determined from mineral counts in thin sections, is shown in Table 5.1. Samples FD 92-119, -125, and -122 consist respectively of 99%, 95%, and 91% olivine. Their spectra are typical for those of dunites, having strong ferrous ion olivine bands centered near 1.05 $\mu$ m, a rapid fall-off to the blue that is associated with prominent iron bands in the infrared, and an overall low reflectivity producing a dark spectrum. Weak hydroxyl bands near 2.3 $\mu$ m and 1.4 $\mu$ m show that olivine is slightly altered to serpentine.

Reflectance spectra of five harzburgite samples are shown in Fig. 5.6. They consist of olivine and orthopyroxene with a small amount of clinopyroxene. The pyroxene dominates the spectra yielding ferrous ion bands near 0.95 $\mu$ m and 1.85 $\mu$ m as well as the fall-off to the blue in the visible part of the spectra. The depth of the iron feature at 1.85 $\mu$ m depends on the amount of orthopyroxene relative to olivine. Sample FD 92-109, -110, and -115 have more orthopyroxene than olivine (see Table 5.1) and therefore show this broad feature more

- Chapter 5 -

Table 5.1: Percent mineral contents of rock samples (Ol. = Olivine, Opx. = Orthopyroxene, Cpx. = Clinopyroxene, Hbl. = Hornblende, Mag. = Magnetite, Serp. = serpentine, D = Dunite, H = Harzburgite, L = Lherzolite, W = Websterite, P = Pyroxenite, S = Serpentinite).

sample	Mineralogy						Rock
	Ol.	Opx.	Cpx.	Hbl.	Mag.	Serp.	
FD 92-122	99	---	---	---	---	1	D
FD 92-125	95	3	---	---	---	2	D
FD 92-119	91	---	6	---	1	2	D
FD 92-111	75	20	4	---	---	1	H
FD 92-109	42	50	5	---	---	3	H
FD 92-110	41	58	1	---	---	---	H
FD 92-115	52	47	1	---	---	---	H
FD 92-118	80	14	1	---	---	5	H
FD 92-131	61	18	21	---	---	---	L
FD 92-133	42	28	27	---	---	3	L
FD 92-136	55	26	14	---	---	5	L
FD 92-139	16	41	42	---	---	---	Ol.W.
FD 92-141	36	51	---	13	---	---	Ol.P.
FD 92-142	23	16	---	61	---	---	Ol.P.
FD 92-143	1	---	---	---	---	99	S
FD 92-99	8	4	3	---	---	83	S
FD 92-123	28	4	---	---	---	68	S
FD 92-146	34	14	4	1	---	47	S
FD 92-117	42	18	5	---	---	35	S
FD 92-121	44	4	---	---	---	52	S
FD 92-108	74	8	4	---	---	14	D.S.
FD 92-147	33	9	---	---	8	50	S
FD 92-151	5	2	---	---	7	86	S

prominently than do samples FD 92-111, and -118. The position of the ferrous iron band near 1.0 $\mu$ m shifts to smaller wavelengths with decreasing olivine content of the sample. Sample FD 92-118 shows a weak hydroxyl band at 1.4 $\mu$ m due to the presence of some serpentine minerals.

- Reflectance spectra of ultramafic rocks -

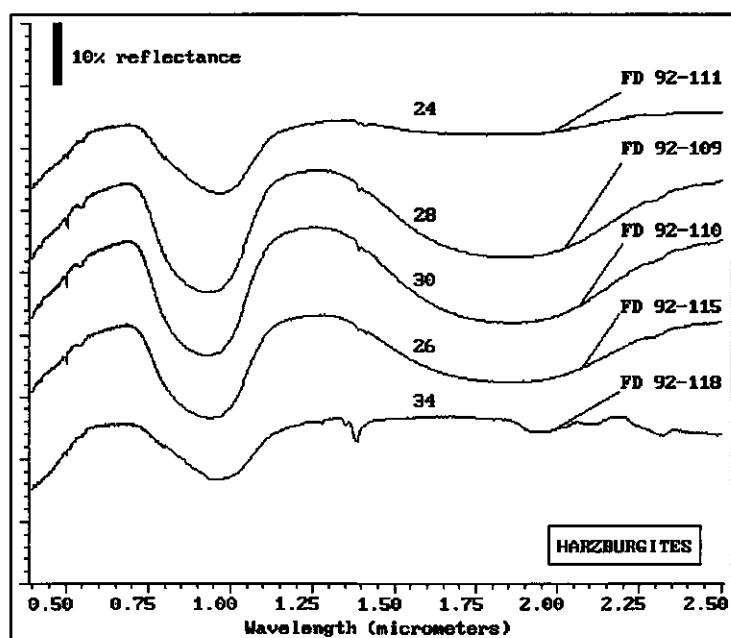


Fig. 5.6: Reflectance spectra of harzburgite samples. Mineralogy of the samples is listed in Table 5.1. Spectra are vertically offset for clarity. Reflectance values at 1.6 $\mu$ m are denoted above the curves.

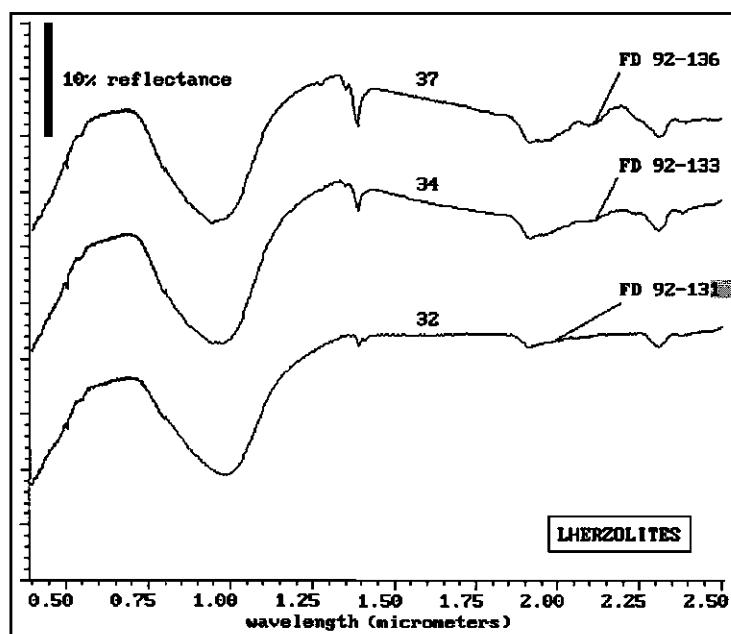


Fig. 5.7: Reflectance spectra of lherzolite samples. Mineralogy of the samples is listed in Table 5.1. Spectra are vertically offset for clarity.

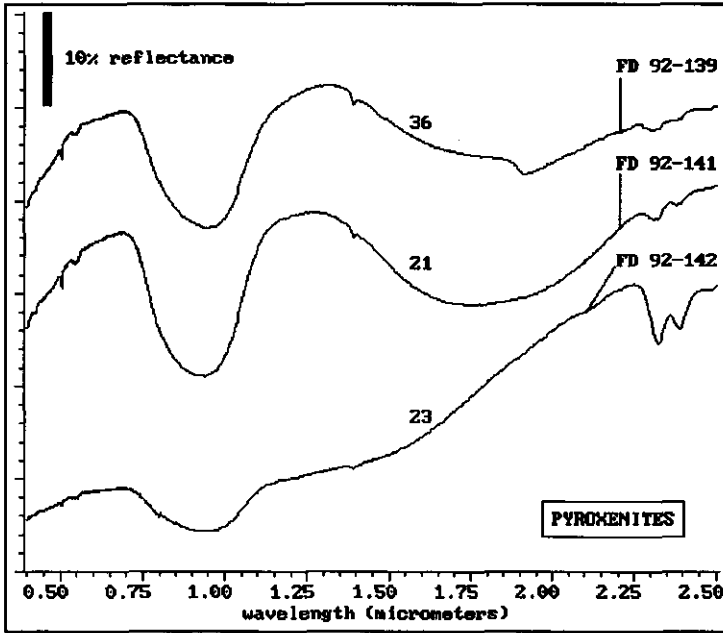


Fig. 5.8: Reflectance spectra of pyroxenite samples. Mineralogy of the samples is listed in Table 5.1. Spectra are vertically offset for clarity. Reflectance values at 1.6 $\mu$ m are denoted above the curves.

Reflectance spectra of three lherzolite samples are shown in Fig. 5.7. Mineralogically, these samples consist of olivine with various amounts of clino- and orthopyroxenes and some accessory minerals (e.g. magnetite, serpentine minerals). Their spectra show broad ferrous ion olivine bands centered at 1.0 $\mu$ m and additional hydroxyl bands at 2.2-2.5 $\mu$ m. The water bands at 1.4 $\mu$ m and 1.9 $\mu$ m may be due to the presence of fluid inclusions or to a slight alteration of pyroxenes to amphiboles.

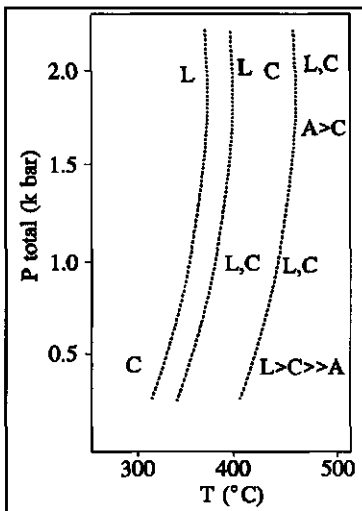
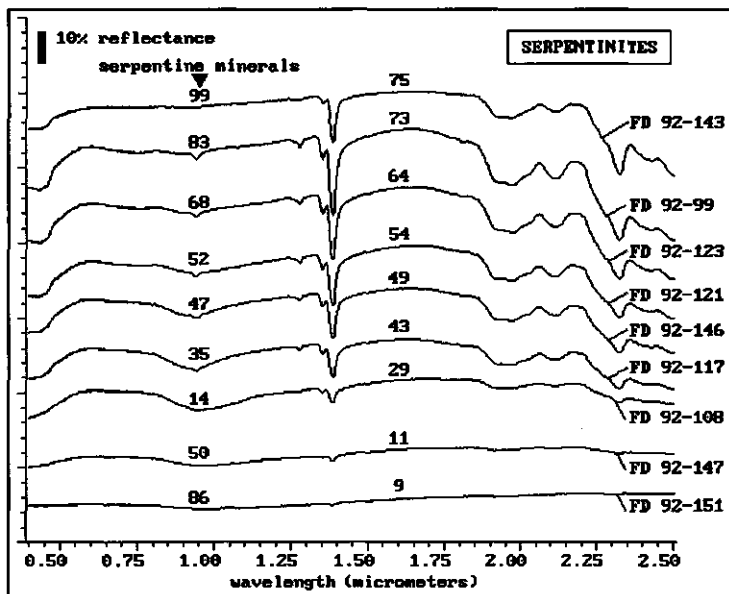


Fig. 5.9: Stability of serpentine polymorphs resulting from reversed bracketing experiments (after: Moody, 1976; L = Lizardite, C = Chrysotile, A = Antigorite).



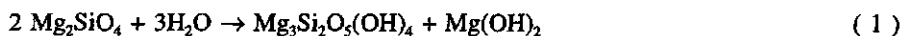
**Fig. 5.10:** Spectra of serpentized peridotites offset vertically for clarity. Reflectance values at 1.6 $\mu$ m are denoted above the curves. The percent serpentine minerals present is indicated near 0.9 $\mu$ m above the curve. Mineralogy of the samples is listed in Table 5.1.

Three reflectance spectra of pyroxenites are shown in Fig. 5.8. Samples FD 92-139 and FD 92-141, a olivine-websterite and a olivine-hornblende pyroxenite respectively, show similar spectra to that of the above discussed harzburgites. The olivine-pyroxene hornblendite (sample FD 92-142 shown in Fig. 5.8) shows a rather different spectrum dominated by the presence of hornblende producing a rapid fall-off toward the visible due to broad  $\text{Fe}^{2+}$  and  $\text{Fe}^{3+}$  absorption features near  $0.7\mu\text{m}$  and  $1.0\mu\text{m}$ .

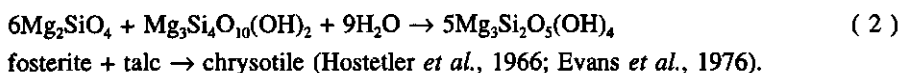
### 5.3 EFFECT OF SERPENTINIZATION ON REFLECTANCE SPECTRA

### 5.3.1 Theory

The formation of serpentinite by the hydration of peridotite results in a 20% decrease of the density of the rock from 3.3g/cm<sup>3</sup> for peridotite to 2.65g/cm<sup>3</sup> for serpentinite. Two reaction describing the hydration of olivine to produce serpentine-group minerals are proposed:

fosterite + water  $\rightarrow$  chrysotile + brucite (Johannes, 1969; Chernosky, 1973)

and



The process of serpentinization has been discussed by many authors indicating that the geochemistry of the parent material and the temperature and pressure conditions at which the hydration takes place control the mineralogy of the serpentinites (Wicks & O'Hanley, 1988; O'Hanley *et al.*, 1989). Hostetler *et al.* (1966) demonstrated that brucite is missing from serpentinites derived from peridotites having high (>40%) amounts of pyroxene. Iron present in olivine, is generally redistributed in the form of magnetite during serpentinization (Ashley, 1975). Temperature/pressure experiments by Moody (1976) indicated that at low pressures and temperatures of hydration chrysotile forms, whereas increasing temperature results in a replacement of chrysotile by lizardite and finally also antigorite. Serpentinization at high pressure and temperature yields almost entirely lizardite (Fig. 5.9).

Finally, the problem of constancy of volume during serpentinization has long been debated. Thayer (1966) argued for constant-volume serpentinization, Hostetler *et al.* (1966) argued for an increase in volume and Gresens (1967) argued for a decrease in volume during serpentinization. In a recent publication, O'Hanley (1992) shows that serpentinization leads to an increase in volume. An excellent review of serpentinization processes is given by Malpas (1992).

### 5.3.2 Reflectance spectra of serpentinites

As discussed previously, serpentine minerals are products of hydrothermal alteration of magnesium-rich silicate minerals such as olivine and pyroxene. The effect of serpentinization on the spectral reflectance characteristics of peridotites is shown in Fig. 5.10 where nine spectra of rock samples of serpentinized dunites and harzburgites differing in amount of serpentine minerals are displayed. The expected spectral changes, the gradual disappearance of the major iron absorption feature near 1.0 $\mu\text{m}$  due to primary ultramafic rock-forming minerals, and the gradual appearance of features due to the secondary minerals, are indeed realized as can be seen in Fig. 5.10. In this figure, the percent reflectance at 1.6 $\mu\text{m}$  is shown near 1.6 $\mu\text{m}$  and the percent serpentine minerals is indicated near 0.9 $\mu\text{m}$ . Progressing from the fresh dunite sample (FD 92-108) in the bottom of Fig. 5.10 to the almost entirely serpentinized sample (FD 92-143) sample in the top, simultaneously an increase in reflectivity from 29% to 75% respectively can be observed. In contrast, spectra of samples FD 92-147



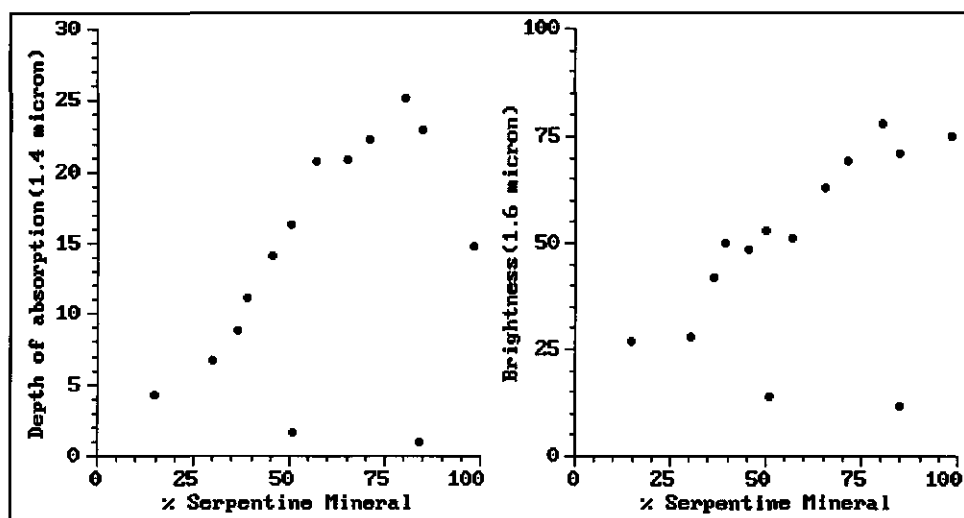


Fig. 5.11: Plot of overall brightness of a sample (expressed as the percent reflectance at 1.6 $\mu$ m) and the depth of the 1.4 $\mu$ m absorption feature versus the percent serpentine minerals: a quantitative measure for the degree of serpentinization.

and FD 92-151 are spectrally flat, mineral absorption features are reduced, and the reflectivity over the entire wavelength region is much less than would be expected from the mineral content. This flattening and loss of contrast is caused by the presence of finely disseminated magnetite. Extremely fine-grained magnetite, derived from iron in the original olivine and pyroxene, is invariably present in serpentinized peridotites, its amount dependent on the iron content of the original minerals (Page, 1967). Magnetite is an opaque mineral which does not transmit light. The effect of the presence of very small amounts of opaques on the reflectivity of particulate substances is to reduce the overall brightness of the sample and the contrast of absorption features. Hunt & Evarts (1981) showed that adding 1% magnetite to a sample of talc reduces the reflectivity from 96% to 38% as a result of this "magnetite effect".

In Fig. 5.11 the reflectance measured at 1.6 $\mu$ m (e.g. the overall brightness of the sample) and the depth of the serpentine hydroxyl feature at 1.4 $\mu$ m are plotted as a function of the percent serpentine minerals in the sample. A nearly linear relation exists between the degree of serpentinization (expressed in terms of percent serpentine minerals) and both the brightness of the sample as well as the depth of the serpentine OH-absorption feature at 1.4 $\mu$ m. However, samples which were serpentinized to an extent of 75% or more have almost similar reflectivity.

In an attempt to model the observed increase in reflectivity due to serpentinization, spectra of mineral mixtures were calculated using the scattering theory presented by Hapke

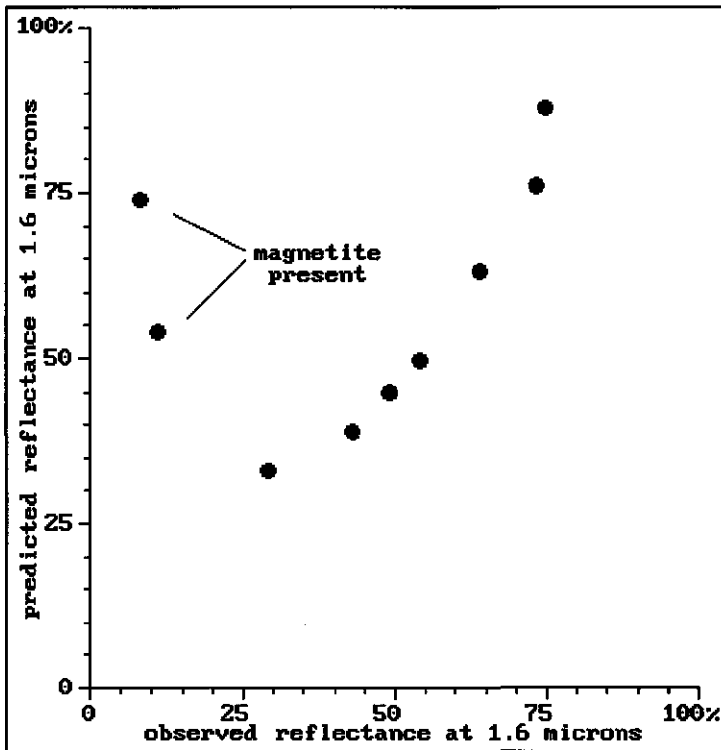


Fig. 5.12: Comparison between observed brightness values and calculated brightness values using Hapke's (1981; 1984; 1987) mineral mixing models for samples of different degree of serpentinization.

(1981, 1984, 1987) and described in detail in Chapter 4. Considering the mineralogy of the serpentine samples from Table 5.1, reflectance spectra were modelled using the Hapke model and the calculated brightness was compared with the observed brightness from Fig. 5.11 (using 2.55, 3.3, and 4.3 g/cm<sup>3</sup> for the density of serpentine minerals, pyroxenes, and olivine, respectively). The results of this comparison are shown in Fig. 5.12. From this figure it can be concluded that the observed increase in overall sample brightness due to serpentinization can be predicted from model results.

In order to simulate the effect of magnetite on the spectral reflectance characteristics of serpentinites, olivine-serpentine-magnetite powder mixtures were prepared in the laboratory with well constraint weight percentages of these minerals. In Fig. 5.13, spectral reflectance curves in the 0.4-2.5 $\mu$ m wavelength region are shown for these mixtures. Relative abundances of serpentine-group minerals and olivine are indicated in the figure (e.g., 60 wt % serpentine plus 35 weight % olivine is indicated as 60/35). A constant amount of 5 weight % magnetite was added to the sample. In Fig. 5.14 the depth of the absorption feature occurring near 2.3 $\mu$ m is plotted against the weight percent serpentine minerals of the sample. This plot shows

- Reflectance spectra of ultramafic rocks -

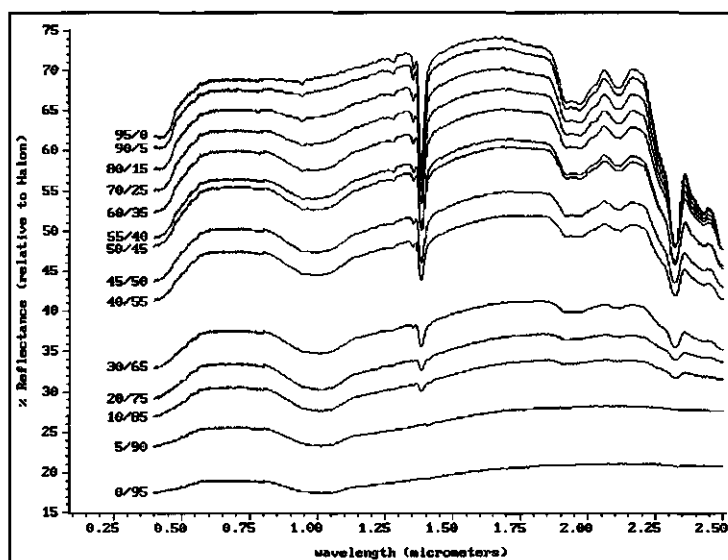


Fig. 5.13: Reflectance spectra (not offset) of olivine-serpentine mixtures with 5 weight % magnetite added. The numbers indicate the olivine and serpentine weight percentages (e.g., 60 weight % serpentine and 35 weight % olivine is indicated as 60/35). Grain-size fraction for olivine and serpentine are 45-125 $\mu$ m whereas magnetite is <45 $\mu$ m.

that a nearly linear relation exists between the band depth of the serpentine-absorption band and the abundance of serpentine-group minerals for samples with approximately 55 weight % or more serpentine minerals. The effect of magnetite on the contrast of the absorption feature becomes noticeable below 55 weight % serpentine, thus reducing the band-depth of the 2.3 $\mu$ m absorption band. Our analysis also shows that this turnover point shifts to higher weight percent serpentine for coarser samples. As was expected, the overall contrast of the absorption feature increases with increasing grain-size of the sample. The "magnetite effect" is dependent also on the grain-size of the magnetite added, becoming stronger with decreasing grain-size fraction. However, our analysis shows that the effect of magnetite is most apparent in weakly serpentinized samples and hardly influences the spectral characteristics of highly serpentinized samples.

## 5.4 CONCLUSIONS

The investigation of visible and near-infrared (0.4-2.5 $\mu$ m) reflectance spectra of ultramafic rocks yields the following conclusions:

- (1) Dunite spectra are relatively dark and dominated by ferrous ion absorption bands of olivine centered at 1.05 $\mu$ m.

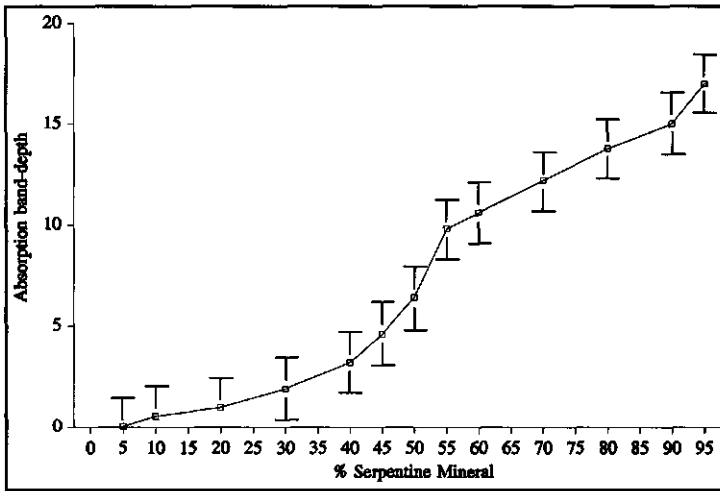


Fig. 5.14: Plot of depth of the 2.3 $\mu$ m absorption feature versus the amount of serpentine mineral of the mixture showing a linear relation for highly serpentinized samples which is obscured by the contrast masking caused by magnetite in weakly serpentinized samples.

(2) Harzburgite spectra from samples with relative high amounts of orthopyroxenes show strong ferrous ion bands near 0.95 $\mu$ m and 1.85 $\mu$ m as well as the fall-off to the blue in the visible part of the spectra. Harzburgites with predominantly olivine have iron absorption features at slightly higher wavelengths (around 1.0 $\mu$ m) which are weaker with respect to the orthopyroxene dominated harzburgites, and they lack the broad iron band at 1.85 $\mu$ m.

(3) Lherzolites spectra show broad ferrous ion olivine bands centered at 1.0 $\mu$ m and additional hydroxyl bands in the 2.2-2.5 $\mu$ m wavelength region due to the presence of clinopyroxenes.

(4) Increasing degree of serpentinization results in the decrease in contrast of features due to primary magnesian silicate minerals and simultaneously to the increase in contrast of features of serpentine-group minerals. Characteristic absorption features of serpentine minerals occur at 1.4 $\mu$ m and 2.3 $\mu$ m.

(5) The overall brightness of the sample, expressed as the reflectivity at 1.6 $\mu$ m, and the depth of the OH-absorption feature at 1.4 $\mu$ m and 2.3 $\mu$ m are an nearly linear function of the percent serpentine minerals which in turn is a measure for the degree of serpentinization. This relation can be modelled using semi-empirical mixing models.

(6) Small amounts (typically less than 1%) of finely disseminated magnetite lowers the overall reflectivity of the sample and decreases the contrast of specific absorption features.

## CHAPTER 6:

### *Reflectance spectra of weathered rock samples, soil, vegetation and field reflectance spectra<sup>4</sup>*

#### ABSTRACT

Visible and short-wave infrared spectra of weathered rock samples, soil samples, and vegetation samples are presented in this Chapter. Weathered carbonate samples indicate that the overall reflectivity of the sample is hardly affected by the weathering and that many small carbonate absorption features are obscured due to weathering. The position of the strong carbonate absorption band is clearly observed and its position is the same in both the weathered and fresh sample. Weathering of ultramafic rocks decreases the overall albedo. Due to the complexity of the chemistry of ultramafic rocks, no straightforward conclusions can be drawn from the analysis of weathered rock surfaces. Soil reflectance is determined by a combination of inherent spectral behaviour of mineral and organic matter and soil water and is dependent on the underlying lithology. Reflectance spectra of vegetation samples established the importance of leaf pigments, leaf water, and internal scattering on the reflectance and transmittance properties of leaves. The pigments, in particular chlorophyll-a and chlorophyll-b, are primarily responsible for the reflectance characteristics in the visible wavelength region ranging from 0.4 $\mu$ m to 0.7 $\mu$ m. The steep increase in reflectance and the plateau in the near-infrared are due to cell wall-air interfaces within the leaf. The spectral reflectance characteristics of leaves in the near-infrared and short wave infrared region from 1.2 $\mu$ m to 2.5 $\mu$ m are controlled mainly by the absorption properties of water. Water has four overtone combination bands at 0.97 $\mu$ m, 1.19 $\mu$ m, 1.45 $\mu$ m, and 1.94 $\mu$ m. Finally, organic compounds such as protein, lignin, starch, and cellulose contribute to the reflectance characteristics of leaves in the middle infrared and ultraviolet regions. Spectral reflectance curves of vegetation in various states of decay are presented showing a gradual transition to spectra similar to those of soils. Spectral signatures of rocks on three sections across the peridotite-country rock boundary are described: The Ronda-San Pedro section, the Guaitara section, and the Jubrique section. Finally a case study is presented to relate field and laboratory spectra to image spectra: the Los Pedroches Batholith case study.

---

<sup>4</sup>Parts of this Chapter have been published as:

Van der Meer, F., Westerhof, A.B. & Van Dijk, P.M. 1994. Digital Classification of the contact metamorphic aureole along the Los Pedroches batholith, south-central Spain, using Landsat Thematic Mapper data. *International Journal of Remote Sensing*, in press.

## 6.1 INTRODUCTION

Visible and short-wave infrared spectra of weathered rock samples, soil samples, and vegetation samples are presented in this Chapter. These samples are more representative for the expected spectral signature of pixel spectra than the laboratory spectra of rock samples presented in the previous two Chapters. Furthermore, spectral signatures of rocks on three sections across the peridotite-country rock boundary are described: the Ronda-San Pedro section, the Guaitara section, and the Jubrique section. Finally a case study is presented to relate field and laboratory spectra to image spectra: the Los Pedroches Batholith case study (Van der Meer *et al.*, 1994). In this Case Study, visible and near-infrared laboratory reflectance spectra of soils sampled over the southern contact metamorphic aureole of the Los Pedroches granodiorite north of Cordoba in the southern-central part of the Iberian Peninsula are characterized in terms of relative albedo, and depth, width, asymmetry, and wavelength position of absorption features. A decrease in albedo and relative depth of the Al-OH absorption feature (near 2.2 $\mu$ m), the H<sub>2</sub>O feature (near 1.9 $\mu$ m), and the OH feature (near 1.4 $\mu$ m) is observed with distance to the contact metamorphic zone. This effect is attributed to spectral quenching related to the absorbing capacity of finely disseminated carbonaceous material in soils which opacity increases with increasing temperature related to metamorphism. Fe<sup>2+</sup> and Fe<sup>3+</sup> cause absorption features near 1.0 $\mu$ m, 0.55 $\mu$ m, and 0.46 $\mu$ m and also, a decrease of reflectivity in the 0.8-0.4 $\mu$ m wavelength region. These absorption features, however, are unaffected by the amount of carbonaceous material. Landsat TM images were used for mapping variation in iron, water, and hydroxyl absorption features over the contact zone using ratio and normalized difference images with TM 3:1 for Fe and TM 5:7 for H<sub>2</sub>O. TM 5 was added as blue component in a colour ratio component image mapping the effect of spectral quenching. Ratios enhanced the spectral variability between individual bands resulting in correlation coefficients in the order of (plus or minus) 0.2.

## 6.2 REFLECTANCE CHARACTERISTICS OF WEATHERED ROCK SAMPLES

### 6.2.1 Carbonates

The dominating weathering process for limestones is solution, a process of chemical weathering by which rock passes into solution. Limestones are resistant to solution in normal waters, however in the presence of dissolved carbon dioxide, calcium carbonate is replaced by calcium bicarbonate which is soluble in water.

- Weathered rock and soil reflectance spectra -

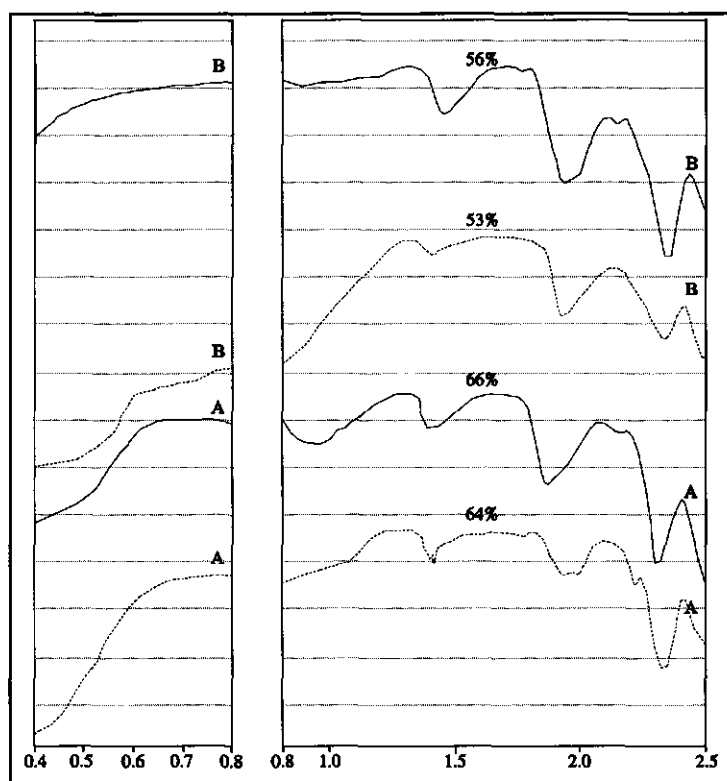


**Fig. 6.1a:** Reflectance spectra of fresh (solid lines) and weathered (broken lines) rock samples of carbonates with strong water absorption bands. The spectra are offset for clarity. The percentage above the curves at 1.6 $\mu\text{m}$  indicate the overall reflectivity of the sample. Each vertical line represents 10% reflectivity.

In the Ronda area, the limestones are relatively fresh. The freshest rock units are the blue-grey sugary calcite marbles. The dolomitic marbles and dolomites weather more easily and deeply. Often they disintegrate as a result of weathering and are varnished with a thin, dark grey sediment coating or varnish containing iron.

In Fig. 6.1, reflectance spectra of fresh and weathered surfaces of limestone samples are shown. Conclusions with respect to the effect of weathering on spectral characteristics which can be drawn from studying these spectra are the following:

- 1) weathering does not affect the overall reflectivity of the sample (measured as the reflectance at 1.6 $\mu\text{m}$ )
- 2) most of the smaller absorption features are not retained in the weathered reflectance spectra
- 3) the absorption bands near 1.4 $\mu\text{m}$  and 1.9-2.0 $\mu\text{m}$  are of the same depth in both fresh and weathered rock spectra
- 4) the depth of the carbonate absorption band between 2.3-2.35 $\mu\text{m}$  decreases in weathered spectra

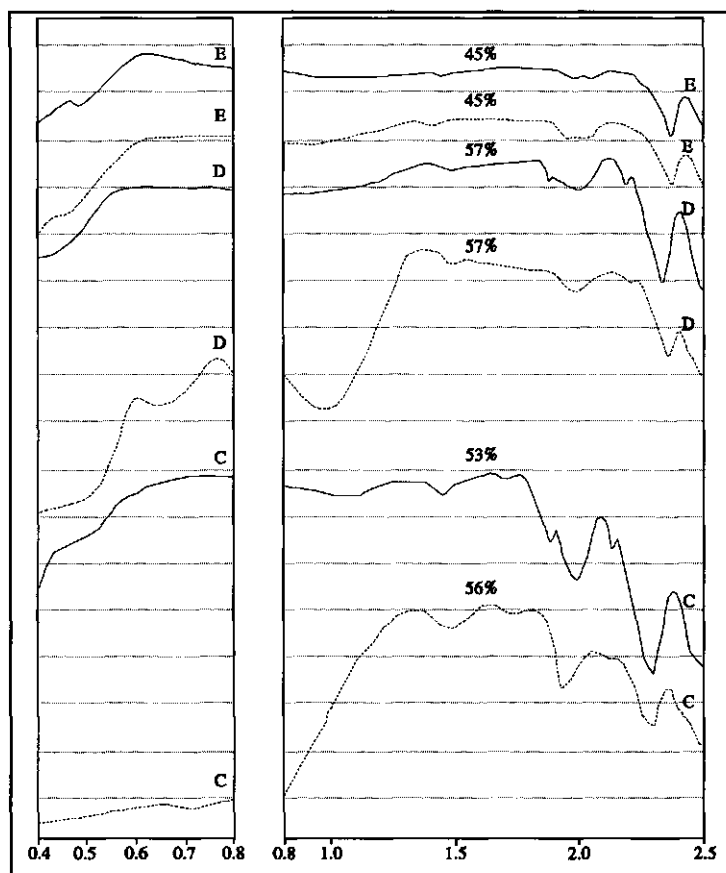


**Fig. 6.1b:** Reflectance spectra of fresh (solid lines) and weathered (broken lines) rock samples of carbonates. The spectra are offset for clarity. The percentage above the curves at  $1.6\mu\text{m}$  indicate the overall reflectivity of the sample. Each vertical line represents 10% reflectivity.

- 5) the position of the carbonate absorption band between  $2.3\text{--}2.35\mu\text{m}$  remains the same in fresh and weathered rock samples
- 6) The reflectivity of weathered samples decreases strongly from  $1.3\mu\text{m}$  toward the visible part of the spectrum
- 7) weathered rock spectra show pronounced iron absorption features with mainly ferrous absorption bands near  $1.1\mu\text{m}$ ,  $0.55\mu\text{m}$ ,  $0.51\mu\text{m}$ ,  $0.45\mu\text{m}$ ,  $0.43\mu\text{m}$  and some ferric iron bands at  $0.87\mu\text{m}$ ,  $0.7\mu\text{m}$ , and  $0.4\mu\text{m}$ .

Conclusion 1 follows directly from Fig. 6.1. In total 11 weathered and fresh rock samples were measured (of which only five are shown in Fig. 6.1) all indicating that the reflectivity of weathered and fresh sample is similar in the SWIR wavelength region. Spectrum C in Fig. 6.1 gives the best example of a spectrum in which small (doublet) absorption features are lost. Note the absorption features at  $1.88\mu\text{m}$  and  $2.16\mu\text{m}$  which are obscured in the weathered rock spectrum. Absorption bands near  $1.4\mu\text{m}$  and  $1.9\mu\text{m}$  seen in the weathered and less in the fresh



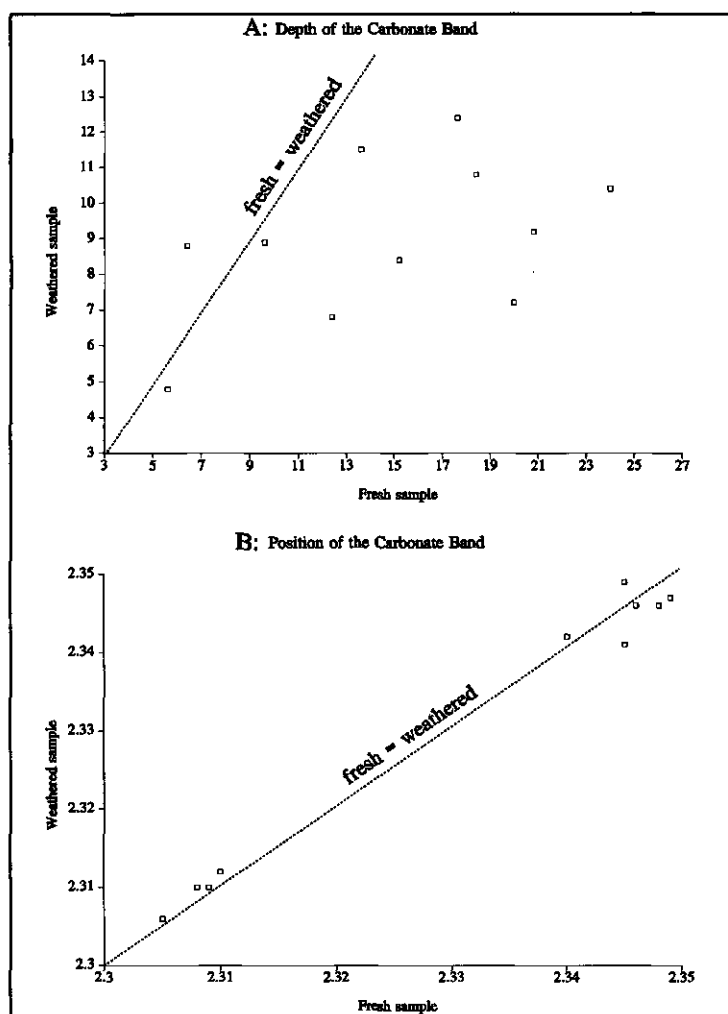


Fig. 6.2: (A) depth of the carbonate absorption feature centered at  $2.35\mu\text{m}$  for weathered and fresh rock samples, and (B) position of the carbonate absorption feature centered at  $2.35\mu\text{m}$  for weathered and fresh rock samples.

rock reflectance spectra are water and hydroxyl features which may be attributed to the presence of clay minerals. Spectrum A reveals as double absorption band near  $1.4\mu\text{m}$  which may be attributed to the presence of kaolinite. The band-depth of the carbonate absorption band decreases in the weathered spectra, however the position of this feature is unaffected by the weathering (Fig. 6.2). The decrease in reflectivity from  $1.3\mu\text{m}$  toward the visible part of the spectrum seems characteristic for weathered carbonate spectra. Additional absorption features near  $0.375\mu\text{m}$ ,  $0.7\mu\text{m}$  and the broad minimum near  $0.87\mu\text{m}$  are due to ferric iron coatings associated with the clay. The  $1.1\mu\text{m}$  and the  $0.5\mu\text{m}$  absorption bands can be

attributed to the ferrous ion intrinsic to the clay structure.

### 6.2.2 Ultramafics

The weathering characteristics of ultramafic rock types are highly variable and dependent on rock texture and mineralogy. Most of the common minerals forming ultramafic rocks weather easily. Olivine alteration is very rapid and may result in chlorite and iron oxide. Pyroxenes and amphiboles weather to kaolinite and free iron and magnesium. Feldspars alter to kaolinite, but alteration to secondary micas such as sericite is also common. Garnet and spinel-type minerals are resistant to weathering. Garnet-pyroxene rocks weather to a brown or dark red-brown color suggesting coating by goethite. Sometimes reddish-brown coatings are observed on garnet indicating hematite.

In general, weathering results in the decrease of the average albedo and an steepening of the slope of the spectrum shorter than  $0.7\mu\text{m}$  for ultramafic samples. Iron and magnesium often occur as secondary weathering products yielding characteristic absorption features short of  $1.1\mu\text{m}$ .

In Fig. 6.3, five examples are shown of visible and short wave infrared ( $0.4\text{--}2.5\mu\text{m}$ ) reflectance spectra of weathered and fresh rock samples of various types of ultramafics. Spectrum A shows a peridotite containing much plagioclase. The fresh sample shows water absorption bands near  $1.4\mu\text{m}$  and  $1.9\mu\text{m}$  typical of plagioclase and lacks the broad absorption band near  $1.0\mu\text{m}$  characteristic of olivine. Its weathered counterpart shows absorption bands characteristic of montmorillonite with strong band near  $1.4\mu\text{m}$  and  $1.9\mu\text{m}$  and a weaker feature near  $2.25\mu\text{m}$ . Spectrum B (in Fig. 6.3) shows a harzburgite consisting of orthopyroxene and olivine. Pyroxene dominates the spectrum yielding ferrous ion bands near  $0.95\mu\text{m}$  and  $1.85\mu\text{m}$  and a falloff to the blue in the visible. Weathering did not affect the reflectance characteristics of this sample. Spectrum C is from a peridotite (hornblendite ?) consisting of an altered olivine matrix with veins of amphibole (in this case hornblende). The weathered as well as the fresh spectrum typically display a rapid falloff in intensity from  $2.0\mu\text{m}$  to the blue due to broad ferric and ferrous ion absorption bands near  $0.7\mu\text{m}$  and  $1.0\mu\text{m}$ . The  $2.33\mu\text{m}$  and  $2.4\mu\text{m}$  double absorption bands are due to OH. Spectrum D is a peridotite containing garnet. The spectrum is dominated by the intense absorption at  $1.28\mu\text{m}$  and  $1.7\mu\text{m}$  due to ferrous ion and the rapid falloff to the blue caused by both ferrous and ferric ion absorptions. Other characteristic bands near  $0.7\mu\text{m}$  and  $0.85\mu\text{m}$  and a series of absorption features in the visible, are not resolved. Spectrum E is a peridotite containing mainly augite. The spectrum is dominated by both ferrous and ferric absorptions which produce a very general broad band centered near  $1.0\mu\text{m}$ . A faint  $2.3\mu\text{m}$  band due to hydroxyl combinations

- Weathered rock and soil reflectance spectra -

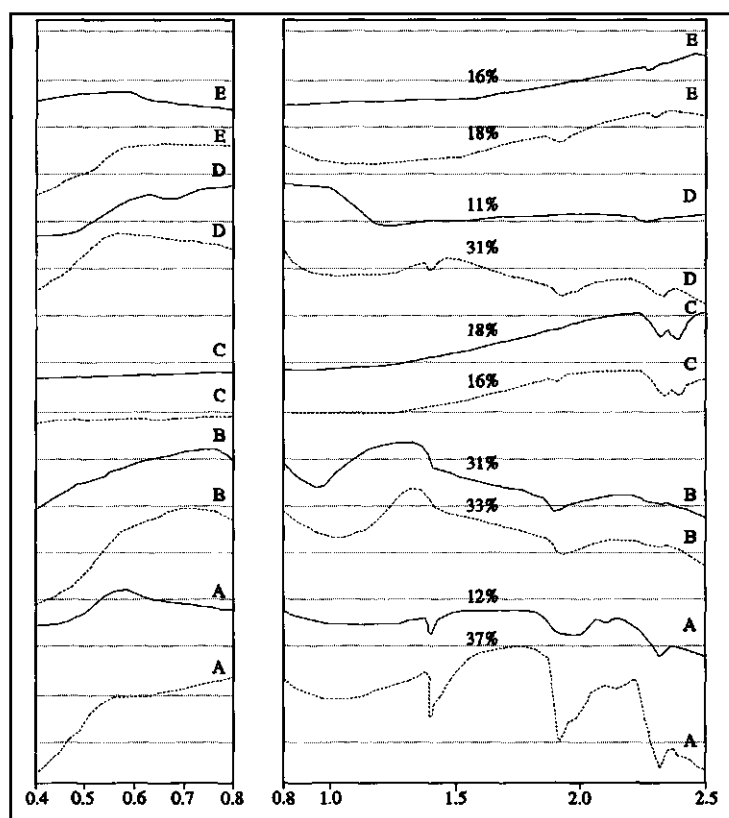


**Fig. 6.3:** Reflectance spectra of fresh (solid lines) and weathered (broken lines) rock samples of peridotites. The spectra are offset for clarity. The percentage above the curves at 1.6 $\mu$ m indicate the overall reflectivity of the sample. Each vertical line represents 10% reflectivity.

is discernible. In the weathered sample, the spectrum is obscured due to a water absorption band at 1.9 $\mu$ m and minor iron bands reducing the reflectivity at wavelengths shorter than 0.6 $\mu$ m.

### 6.3 SOIL REFLECTANCE CHARACTERISTICS

The rocks of the Ronda area are not deeply weathered. Outcrops are plentiful and parts not directly outcropping are covered with a surface layer of residual rock fragments reflecting the underlying lithology. Samples in this section referred to as 'soil samples' were scrapped off from the topmost land surface. In total 14 such soil samples were collected from the most important lithologic units in the area covered by the GER data (Fig. 6.4). These were 3 soils developing on marbles, four soils developing on peridotites, 5 soils at the peridotite-marble contact, 1 soil developing on gneiss and 1 soil developing on limestone (indicated by the

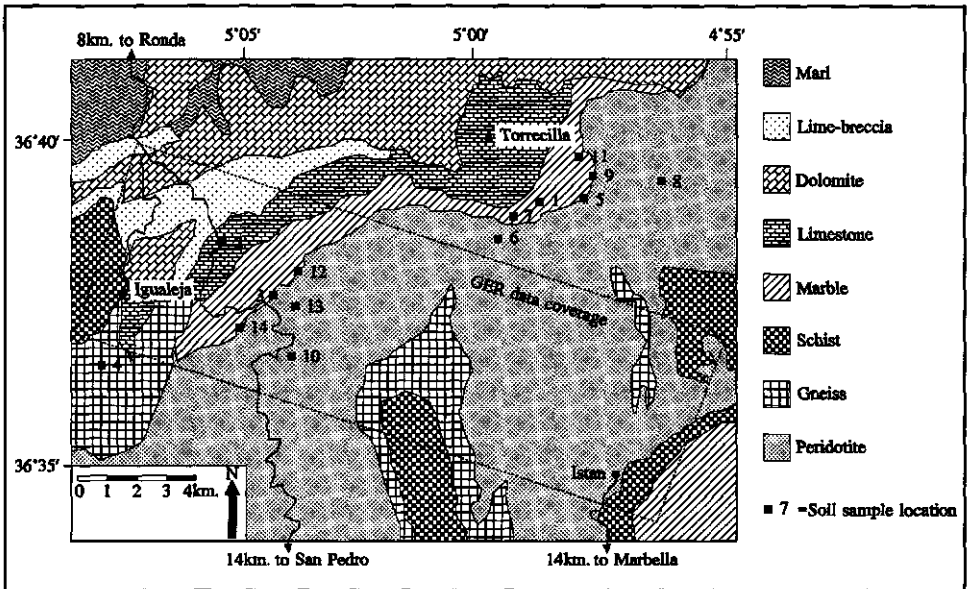


Fig. 6.4: Location of the 14 soil samples.

block and star in the figures).

Soil reflectance is determined by a combination of inherent spectral behaviour of mineral and organic matter and soil water (Mulders, 1987). Baumgardner *et al.* (1985) described the relative contributions of various sources of spectral discrimination of which organic matter, soil moisture, particle size distribution, soil structure, iron oxide content, soil mineralogy, and parent material are the most important factors (Coulson & Reynolds, 1971). De Jong's (1992) correspondence analysis of spectral characteristics of soils revealed lime, clay, iron and organic matter as the important variables and pH, bulk density, silt content, and hue as minor contributing variables. Fig. 6.5 shows reflectance spectra of the soil samples measured on a Beckman UV5240 spectrometer. Table 6.1 shows the absorption-band depths of the main spectral absorption features derived using the continuum removal technique discussed by Clark & Roush (1984). Chemical analysis results measuring free iron, moisture content, organic carbon, and soil mineralogy are given in Table 6.2. From this table it can be seen that organic carbon content is very high for soil samples taken near the contact between the peridotite and marbles except for soil sample 3 which is anomalous in this respect. There is no straightforward correlation between free iron and any of the lithologies although the iron content in peridotite soils is generally higher than that of the other soil types. When plotting the percent organic carbon versus the albedo of the sample (expressed as the percent reflectivity measured at  $1.6\mu\text{m}$ ), the expected decrease in reflectivity with increasing organic

- Weathered rock and soil reflectance spectra -

*Table 6.1:* Spectral characteristics of soil samples. Depth of absorption features and albedo are given (in % reflectance).

soil	albedo	2.3 $\mu$ m	2.2 $\mu$ m	1.9 $\mu$ m	1.4 $\mu$ m	0.9 $\mu$ m	0.65 $\mu$ m	0.55 $\mu$ m
1	51	8.4	--	8.0	2.0	0.4	0.2	1.6
2	48	0.8	3.2	7.9	3.4	2.4	--	4.0
3	18	2.4	--	5.6	2.0	1.6	0.4	1.4
4	37	--	3.9	5.2	4.0	2.8	--	3.2
5	34	1.6	--	2.8	0.4	3.0	--	4.4
6	26	0.1	4.0	10.4	4.4	2.4	0.8	1.5
7	21	3.2	--	4.6	3.2	0.7	0.2	0.1
8	27	0.2	3.6	8.4	3.0	2.4	0.1	2.5
9	5	--	--	0.1	0.1	--	--	--
10	24	2.0	--	5.2	1.6	2.3	--	2.1
11	37	5.1	--	4.4	0.9	--	0.3	0.6
12	25	0.1	0.1	2.1	0.6	4.4	--	3.2
13	26	0.3	1.2	1.4	1.0	4.6	--	3.6
14	25	0.8	--	2.8	0.6	0.7	--	1.5

carbon content is not very well resolved perhaps due to the fact that organic matter is present in form of larger plant remains instead of in the form of finely disseminated material. However, it is apparent that the peridotite soils have relatively low reflectivity and low organic carbon contents compared to the marble samples. The contact soils show relatively high organic carbon and low reflectivity. The absorption band-depths of both the 1.4 $\mu$ m and 1.9 $\mu$ m absorption band are plotted against the organic carbon content of the soil in Fig. 6.6. These show clearly a decrease in absorption band contrast (e.g. absorption band-depth) with increasing organic matter. If the absorption band-depth of the 2.3 $\mu$ m and 2.2 $\mu$ m absorption bands are plotted, the marble soils cluster because of relatively deep carbonate absorption bands whereas the 2.2 $\mu$ m hydroxyl band is mostly absent. On the contrary, the peridotites have deep 2.2 $\mu$ m absorption bands and weak 2.3 $\mu$ m features. The contact soils show moderate carbonate absorption bands and no 2.2 $\mu$ m feature. A nearly linear relation can be established between the depth of the 1.4 $\mu$ m absorption band and the depth of the 1.9 $\mu$ m absorption band. Contact soils have weak absorptions in both the 1.4 $\mu$ m as well as in the 1.9 $\mu$ m absorption band.

- Chapter 6 -

**Table 6.2:** Mineralogy and chemical composition of soil samples.

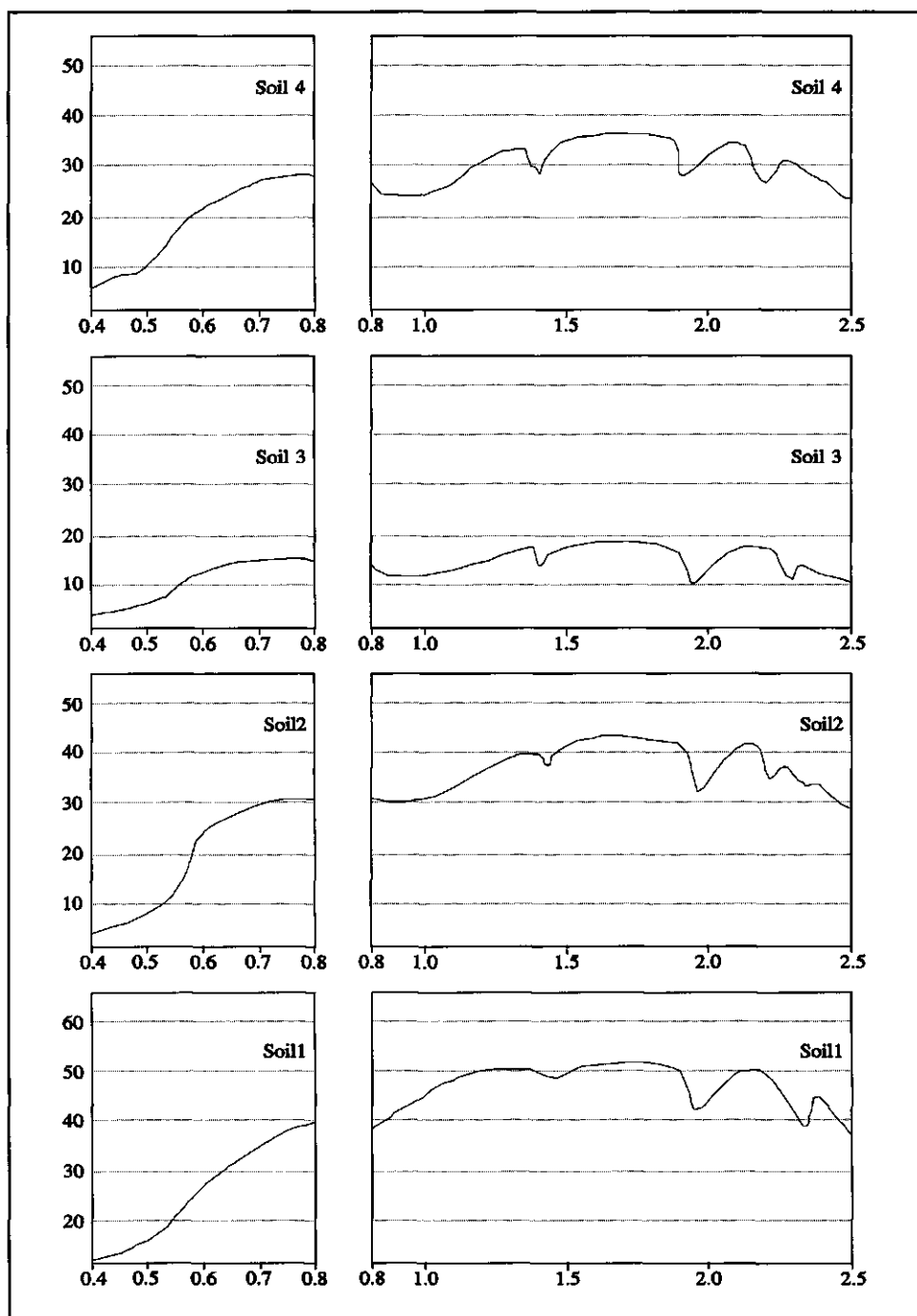
soil sample	lithology	moisture content (%)	organic carbon (%)	Free Fe (%)	Mineralogy
1	Marble	0.0	0.68	0.2	HIV*
2	Limestone	<0.1	0.80	2.0	HIV*
3	Contact	<0.1	0.02	0.5	Smectite
4	Gneiss	<0.1	0.17	1.2	Kaolinite
5	Contact	<0.1	2.31	4.6	Serpentine
6	Peridotite	<0.1	0.20	1.7	Smectite
7	Marble	<0.1	0.04	0.3	Smectite
8	Peridotite	<0.1	0.61	3.3	Smectite
9	Contact	0.1	0.91	1.3	Smectite
10	Peridotite	<0.1	0.21	1.8	Smectite
11	Marble	<0.1	5.11	0.2	Kaolinite, Smectite, Illite, Chlorite
12	Contact	<0.1	2.76	1.0	Chlorite
13	Peridotite	<0.1	0.29	14.4	Chlorite
14	Contact	<0.1	4.13	4.4	Serpentine

\*HIV = Hydroxy Interlayered Vermiculite

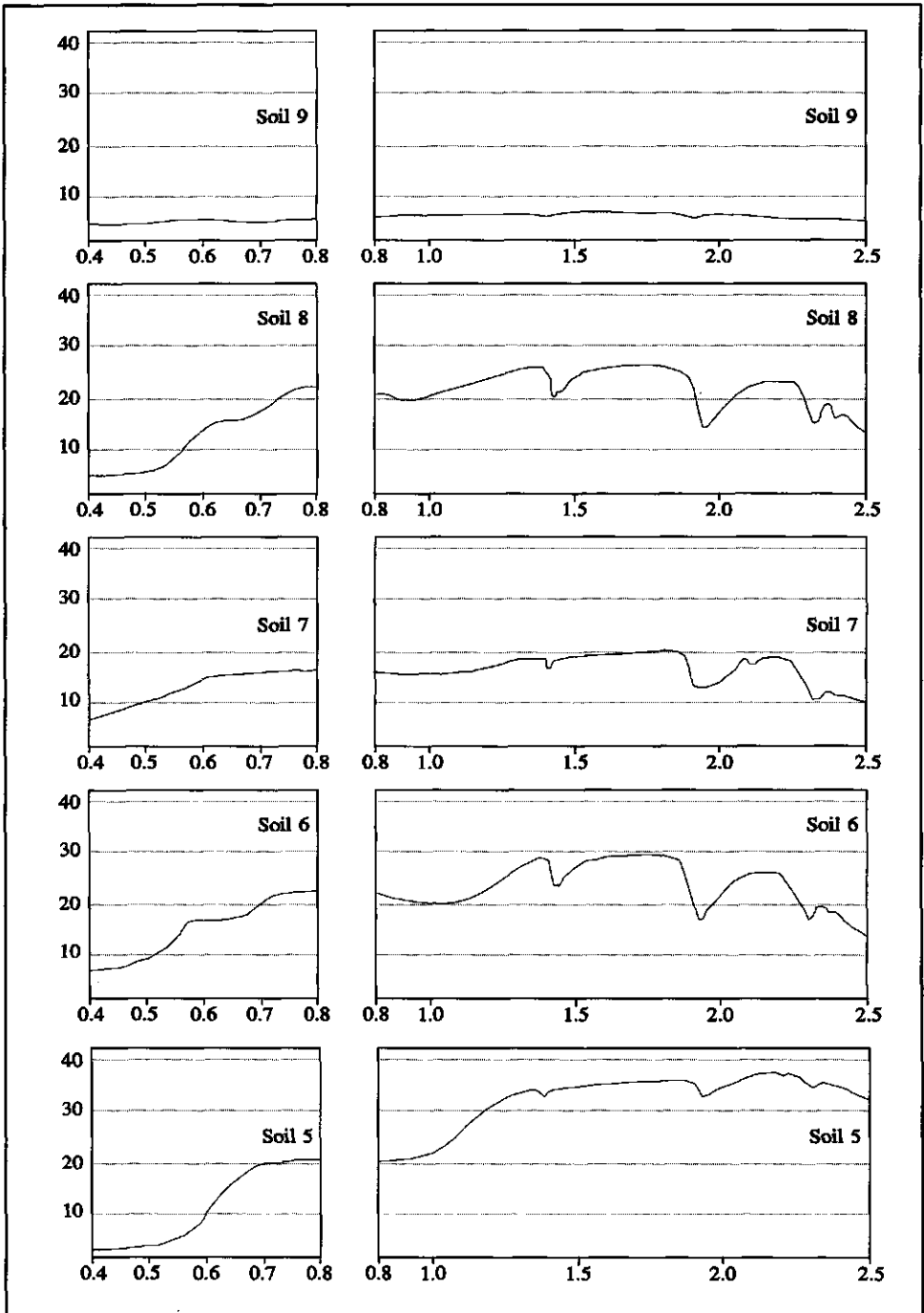
On page 127 to 129 Fig. 6.5 is displayed:

**Fig. 6.5:** Visible and near-infrared (0.4-2.5 $\mu$ m) reflectance spectra of the soil samples.

- Weathered rock and soil reflectance spectra -

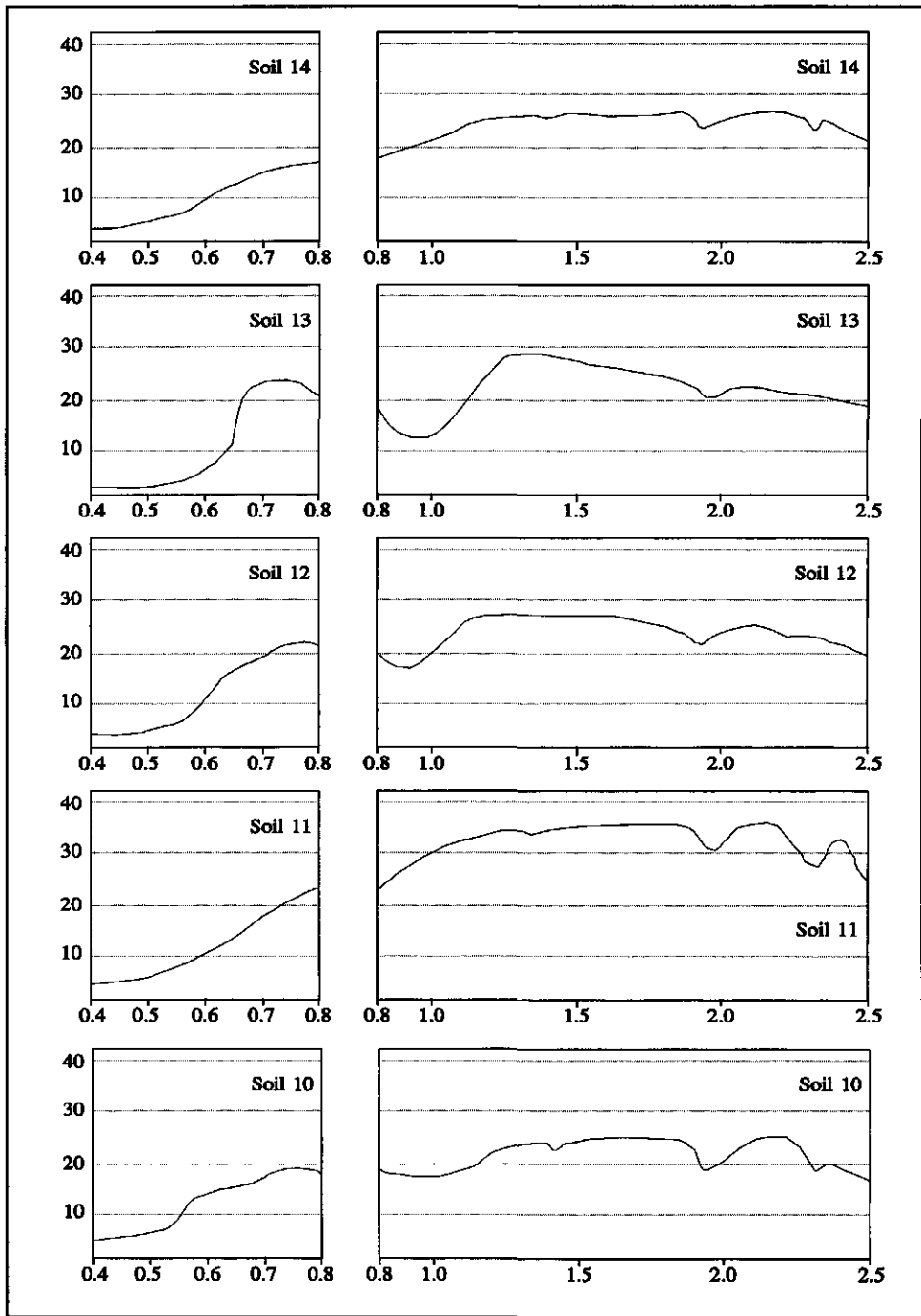


- Chapter 6 -





- Weathered rock and soil reflectance spectra -



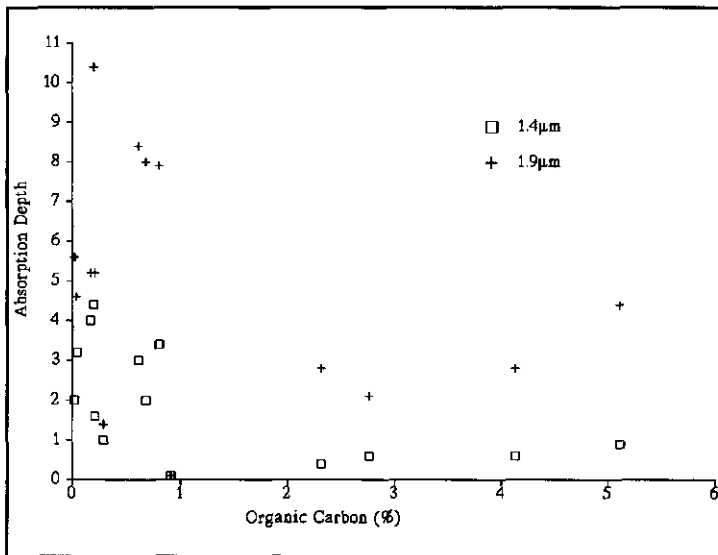


**Fig. 6.6:** Organic carbon versus absorption band-depth of the 1.4μm (square) and 1.9μm (plus) absorption band showing an overall decrease in contrast with increasing organic carbon content.

#### 6.4 VEGETATION REFLECTANCE SPECTRA

Gates *et al.* (1965), Ferns *et al.* (1984) and Gausman *et al.* (1969) first studied leaf reflectance spectra and established the importance of leaf pigments, leaf water, and internal scattering on the reflectance and transmittance properties of leaves (Sellers, 1989; Gausman, 1974; Baret, 1994). The pigments, in particular chlorophyll-a and chlorophyll-b, are primarily responsible for the reflectance characteristics in the visible wavelength region ranging from 0.4μm to 0.7μm (Curran & Milton, 1983). The steep increase in reflectance and the plateau in the near-infrared are due to cell wall-air interfaces within the leaf (Gausman *et al.*, 1970). The spectral reflectance characteristics of leaves in the near-infrared and short wave infrared region from 1.2μm to 2.5μm are controlled mainly by the absorption properties of water. Water has four overtone combination bands at 0.97μm, 1.19μm, 1.45μm, and 1.94μm. Finally, organic compounds such as protein, lignin, starch, and cellulose contribute to the reflectance characteristics of leaves in the middle infrared and ultraviolet regions. Cellulose is a polysaccharide found in the cells walls of plants where it acts to strengthen and protect plant structures. The main absorption bands caused by cellulose are at 1.22, 1.48, 1.93, 2.10, 2.28, 2.34, and 2.48μm (Guyot *et al.*, 1992; Basset *et al.*, 1963). Lignin is a complex polymer which encrusts and penetrates cellulosic materials. Lignin has an intense absorption feature in the ultraviolet centered at 0.28μm (Schubert, 1965), a broad absorption feature between 2.05 and 2.14μm, and additional smaller absorption bands near 1.45, 1.68, 1.93, 2.27, 2.33,

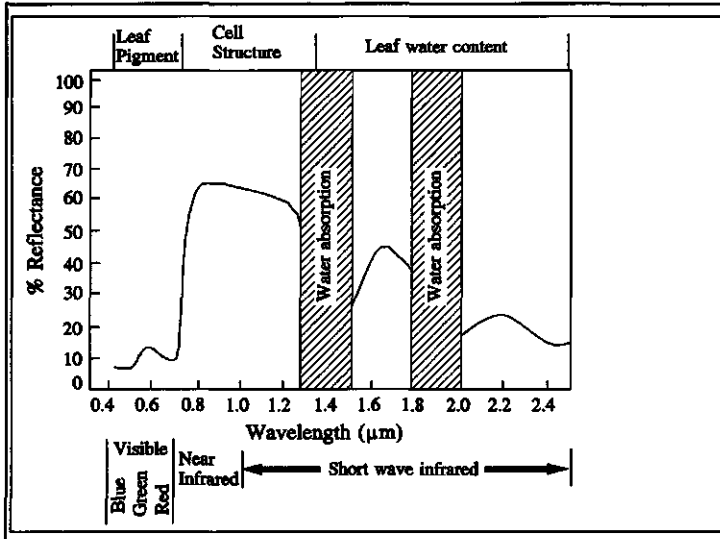
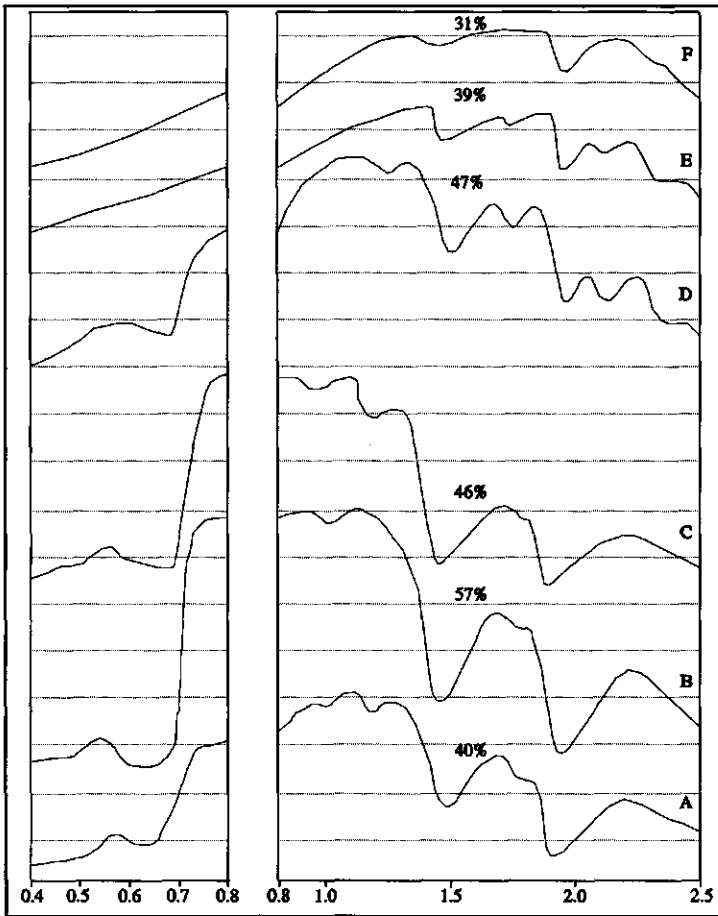


Fig. 6.7: Spectral reflectance of a green leaf (from: Goetz, 1992).

2.38, and 2.50μm. Starch is a polysaccharide having characteristic absorption features at 0.99, 1.22, 1.45, 1.56, 1.70, 1.77, 1.93, 2.10, 2.32, and 2.48μm (Elvidge, 1990). Protein is the most abundant nitrogen bearing compound of green leaves having absorption bands at 1.50, 1.68, 1.74, 1.94, 2.05, 2.17, 2.29, and 2.47μm (Elvidge, 1990).

Fig. 6.7 shows a typical spectral reflectance curve of a green leaf indicating the dominant factors controlling the leaf reflectance. The vegetation type did not differ significantly between the limestones and the peridotites. Therefore samples of vegetation on both lithologies were measured at various stages of senescence. In total six spectra were measured shown in Fig. 6.8: green grass (spectrum A, Fig. 6.8), healthy leaf growing on marble (spectrum B, Fig. 6.8), healthy leaf growing on peridotite (spectrum C, Fig. 6.8), senescent leaf (spectrum D, Fig. 6.8), decayed leaf (spectrum E, Fig. 6.8), and brown wood (spectrum F, Fig. 6.8).

The reflectance spectra of green grass and healthy vegetation on both marble and peridotite (spectra A-C, Fig. 6.8) show very strong near infrared plateau reflectance. The spectra are dominated by water absorption on both the plateau and the plateau lobes, and absorption features caused by organic compounds are absent. Note the strong pigment absorptions in the blue and red portion of the visible wavelength region and the relatively high reflectance in the green giving the plant its colour. Distinct changes occur in the reflectance characteristics of leaves as they senesce (spectrum D, Fig. 6.8). Intense pigment absorption are retained in the blue and green and red reflectance increase causing leaves to colour brown. The red-edge of the near infrared plateau shifts to shorter wavelengths



**Fig. 6.8:** Reflectance spectra of (A) green grass, (B) healthy vegetation on marble, (C) healthy vegetation on peridotite, (D) senesced vegetation, (E) decayed vegetation, and (F) brown wood. Spectra are vertically offset for clarity. Percent reflectance indicated defines the height of the near infrared plateau.

and the near infrared plateau becomes more rounded in appearance. Water absorption features still dominate the reflectance characteristics, however absorption features of lignin and cellulose are weakly visible. The decayed vegetation spectrum (spectrum E in Fig. 6.8) lacks the intense chlorophyll and water absorptions and exhibits a monotonous rise from 0.4  $\mu\text{m}$  to 1.85  $\mu\text{m}$  with a weak water absorption band at 1.4  $\mu\text{m}$ . Beyond 1.0  $\mu\text{m}$ , lignin and cellulose absorptions dominate the spectrum. Note the broad absorption feature between 2.05  $\mu\text{m}$  and 2.14  $\mu\text{m}$  caused by lignin. In the brown wood sample (spectrum F, Fig. 6.8) cellulose dominates the spectral reflectance with a sharp feature at 2.3  $\mu\text{m}$ .

## 6.5 REFLECTANCE SPECTRA CHARACTERIZING THE PERIDOTITE-METAMORPHICS CONTACT

In this section, three transects are described across the contact between peridotites and the bordering metamorphic sequences: the Ronda-San Pedro section along the C-339 road some 14 km. south of Ronda, the Guaitara section just east of Pujerra, and the Jubrique section just south of Jubrique. Emphasis will be on the spectral characteristics of the contrasting rock types rather than on the geologic and tectonic implications which will be discussed later.

### 6.5.1 The Ronda-San Pedro contact

The Ronda-San Pedro section follows the C-339 road from Ronda to San Pedro starting some 14km. south of Ronda in an essentially non-metamorphic sequence of bedded and crystalline limestones. To the south these grade into white crystalline marbles which near the contact with the peridotites develop into banded marbles. Along the contact, tremolite and diopside are found in the marbles. The contact between the marbles and the peridotites is formed by a 3m. thick mylonitic zone bordered by relatively fresh dunites. Some 2km. northeast of the contact zone, garnet peridotites were found. Following the C-339 we first encounter hornblende peridotites and finally plagioclase-rich peridotites. The locations of samples for which reflectance spectra were measured are shown in Fig. 6.9. The corresponding reflectance spectra are given in Fig. 6.10.

Spectrum A is that of a crystalline limestone characterized by strong molecular vibration bands near  $2.3\mu\text{m}$  and just beyond  $2.5\mu\text{m}$  and weaker combination tones near  $2.0\mu\text{m}$ . The combination tones are lost in the spectra due to the strong water and hydroxyl bands at  $1.4\mu\text{m}$  and  $1.9\mu\text{m}$  due to the clay component of the rock. A spectrum of a bedded limestone is shown in Fig. 6.10 as spectrum B. This dark grey limestone contains abundant ( $>10\%$ ) finely disseminated carbonaceous material. This carbonaceous material is opaque and masks all but the strongest carbonate bands. Spectra C and D represent a massive crystalline white marble and a white marble with faint banding, respectively. Both spectra show very strong carbonate bands near  $1.88\mu\text{m}$ ,  $2.16\mu\text{m}$ ,  $2.35\mu\text{m}$ , and  $2.50\mu\text{m}$  due to the calcite and relatively strong  $1.4\mu\text{m}$  and  $1.9\mu\text{m}$  bands indicating the presence of some clay fraction. The fall-off to the blue in the visible portion of Spectrum D is probably due to minor substitution of iron for calcium in the calcite. Spectra E and F represent samples of banded marbles. Both spectra are nearly featureless due to spectra quenching caused by the presence of small quantities of organic impurities. The masking of the carbonate absorption bands increases when approaching the contact with the peridotites (compare spectra E and F). This may be

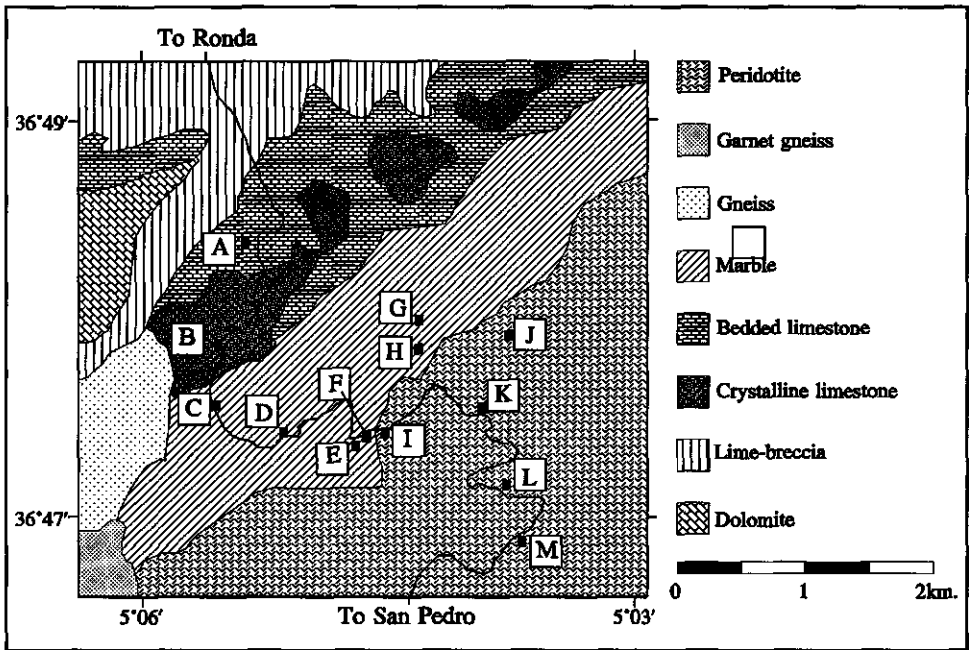


Fig. 6.9: Location of the samples of the Ronda-San Pedro section (Legend: A = crystalline limestone, B = bedded limestone, C = massive white crystalline marble, D = white marble, E = banded marble, F = banded marble, G = marble with tremolite, H = marble with diopside, I = mylonite, J = garnet bearing peridotite, K = dunite, L = hornblendite, and M = plagioclase bearing peridotite).

attributed to the fact that heating increases the opacity of organic material thus increasing the spectral masking effect of the opaque material (see also Crowley, 1986; Rowan *et al.*, 1990). The spectrum of Tremolite found near the contact of the peridotites and the marbles is shown as spectrum G in Fig. 6.10. Tremolite displays a sharp band near  $1.4\mu\text{m}$  and less sharp bands between  $2.0\mu\text{m}$  and  $2.5\mu\text{m}$  due to the overtone and combination tones of the OH stretch. The  $1.9\mu\text{m}$  band may be attributed to  $\text{H}_2\text{O}$  and the strong band near  $1.0\mu\text{m}$  indicates the presence of ferrous iron. Spectrum H is that of diopside, a clinopyroxene often found in metamorphic limestones. The spectrum displays a strong iron absorption band at  $1.05\mu\text{m}$  which together with a band centered at  $0.8\mu\text{m}$  and the fall-off toward the blue produces a peak in the visible near  $0.55\mu\text{m}$ . The contact between the peridotites and the marbles is formed by a three meter thick mylonitic interval. The material is very fine-grained and dark coloured. Its spectrum is dark and completely featureless. Spectrum J is that of a harzburgite containing abundant garnet. The spectral features of olivine and pyroxenes are completely overprinted by the characteristic features of the garnet. The most prominent absorption band is centered near

- Weathered rock and soil reflectance spectra -

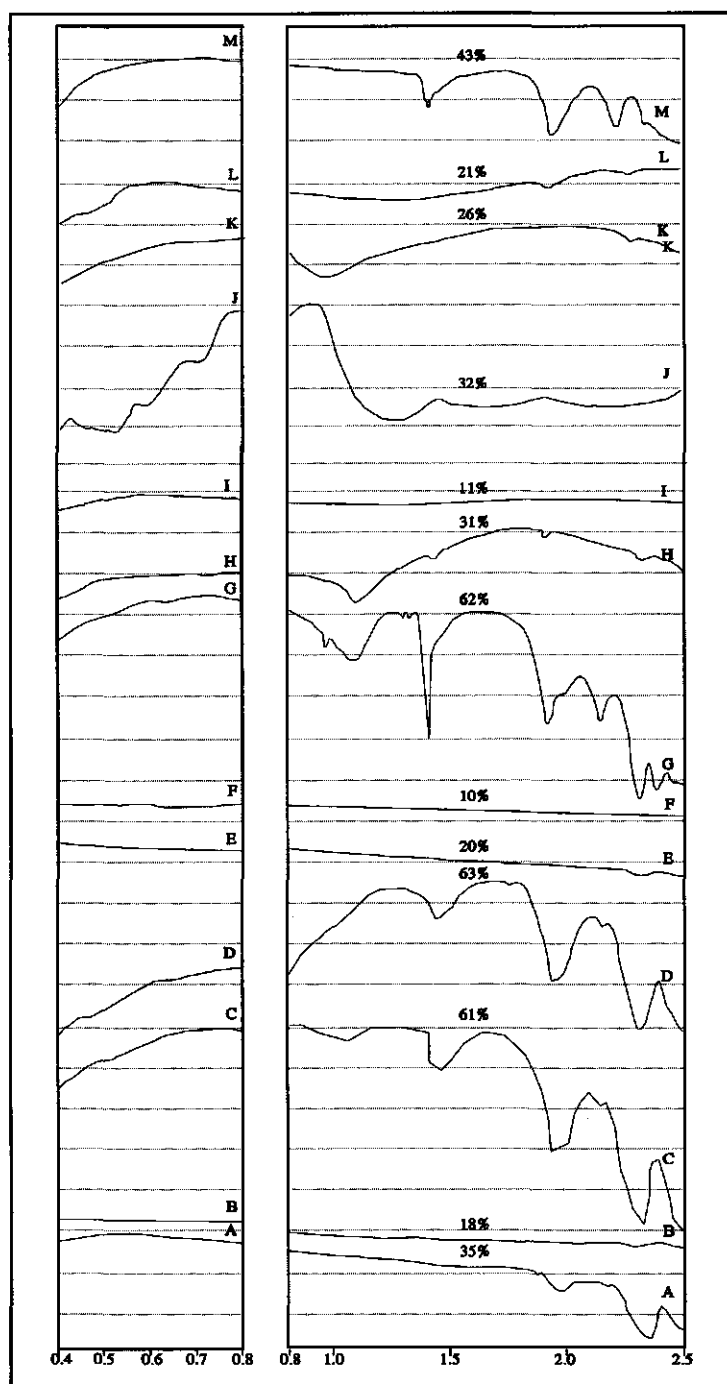


Fig. 6.10: Spectra of rock samples over the contact of peridotites and marbles along the C-339 road stretching from Ronda to San Pedro. Letters refer to location in Fig. 6.9.

1.28 $\mu\text{m}$  and a weaker band at 1.7 $\mu\text{m}$  due to ferrous iron. The visible and near-infrared part of the spectrum are dominated by a rapid fall-off from 1.0 $\mu\text{m}$  toward shorter wavelengths due to both ferric and ferrous iron. These ions are responsible for the observed absorption bands at 0.85 $\mu\text{m}$ , 0.7 $\mu\text{m}$ , 0.57 $\mu\text{m}$ , 0.51 $\mu\text{m}$ , and 0.43 $\mu\text{m}$ . The spectrum of a dunite sample is shown as spectrum K in Fig. 6.10. This sample is almost entirely composed of olivine displaying the ferrous iron band at 1.05 $\mu\text{m}$  with weaker features near 1.25 $\mu\text{m}$  and 0.85 $\mu\text{m}$ . The weak 2.3 $\mu\text{m}$  band indicates the presence of hydroxyl groups and suggests that olivine is slightly altered to serpentine. Spectrum L represents a hornblendite consisting almost entirely of hornblende with minor olivine. The rapid fall-off from 0.7 $\mu\text{m}$  toward shorter wavelengths is characteristic for hornblende and caused by broad ferrous and ferric iron bands. The double hydroxyl absorption band near 2.2 $\mu\text{m}$  and 2.3 $\mu\text{m}$  is not well resolved. The last spectrum is that of a plagioclase bearing peridotite sample (spectrum M in Fig. 6.10). The most prominent bands are the 1.4 $\mu\text{m}$  and 1.9 $\mu\text{m}$  absorptions bands due to water in fluid inclusions. The presence of an absorption feature near 2.3 $\mu\text{m}$  suggest alteration of the olivine to serpentine. The characteristic iron absorption band near 1.05 $\mu\text{m}$  of olivine is almost completely lost in the strong water bands.

### 6.5.2 The Guaitara section

The Guaitara section just east of Pujerra, stretches through a gneiss-schist-phyllite sequence affected by contact metamorphism. The lowest degree of metamorphism is found in a series of phyllites exposed some 5km. northwest of the peridotite contact. These phyllites contain quartz, muscovite, biotite, and some chlorite. Approaching the peridotite contact, we find first mica-schists, followed by banded gneisses and finally garnet bearing gneisses in contact with the peridotite. The mica-schists are characterized by a mineral assemblage of quartz, muscovite, biotite, staurolite, andalusite, sillimanite, and plagioclase. The banded gneisses contain quartz, plagioclase, biotite and sillimanite, whereas the gneisses most closed to the peridotite contact are composed of quartz, plagioclase, biotite, cordierite, sillimanite, tourmaline, spinel, and garnet. The garnet may reach an maximum diameter of 1cm.

Chlorite displays two broad absorption bands between 0.7 $\mu\text{m}$  and 1.1 $\mu\text{m}$  which primarily cause the marked decrease of reflectivity from 2.0 $\mu\text{m}$  toward shorter wavelengths. Furthermore, chlorite is characterized by sharp hydroxyl features between 2.0 $\mu\text{m}$  and 2.6 $\mu\text{m}$ . Muscovite displays prominent hydroxyl bands at 1.4 $\mu\text{m}$  and between 2.0 $\mu\text{m}$  and 2.6 $\mu\text{m}$ . Quartz has strong water absorption bands at 1.4 $\mu\text{m}$  and 1.9 $\mu\text{m}$ . Feldspars have relatively flat spectra with features at 1.4 $\mu\text{m}$ , 1.9 $\mu\text{m}$ , and 2.2 $\mu\text{m}$  depending on the chemical composition and type of feldspar. Often replacement by iron occurs yielding iron absorption bands in the



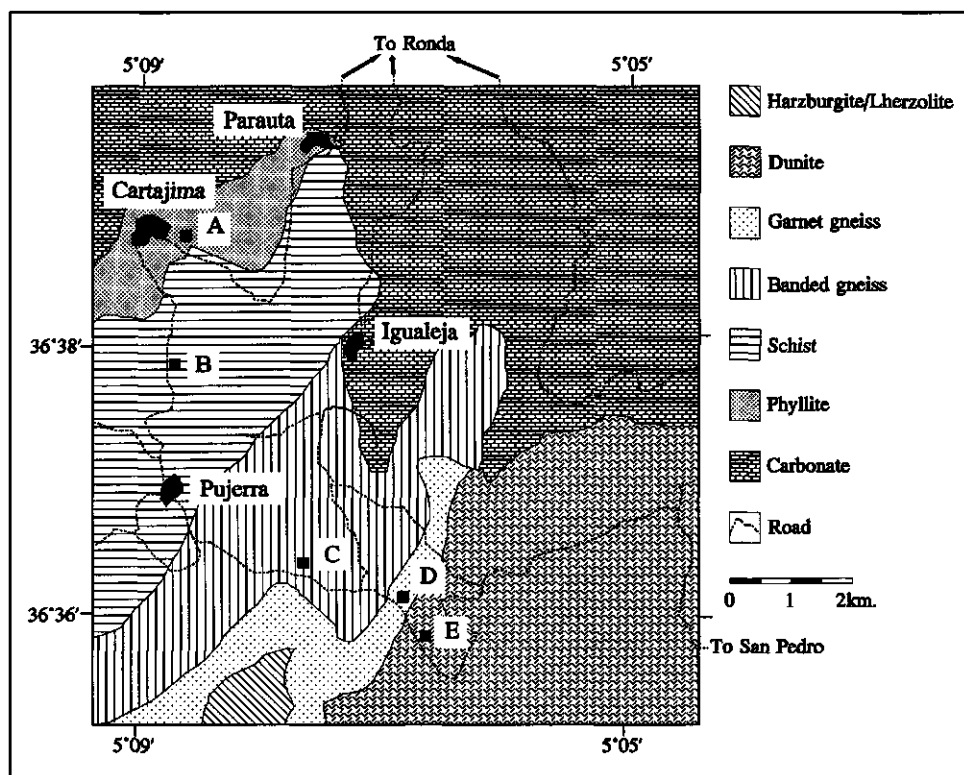
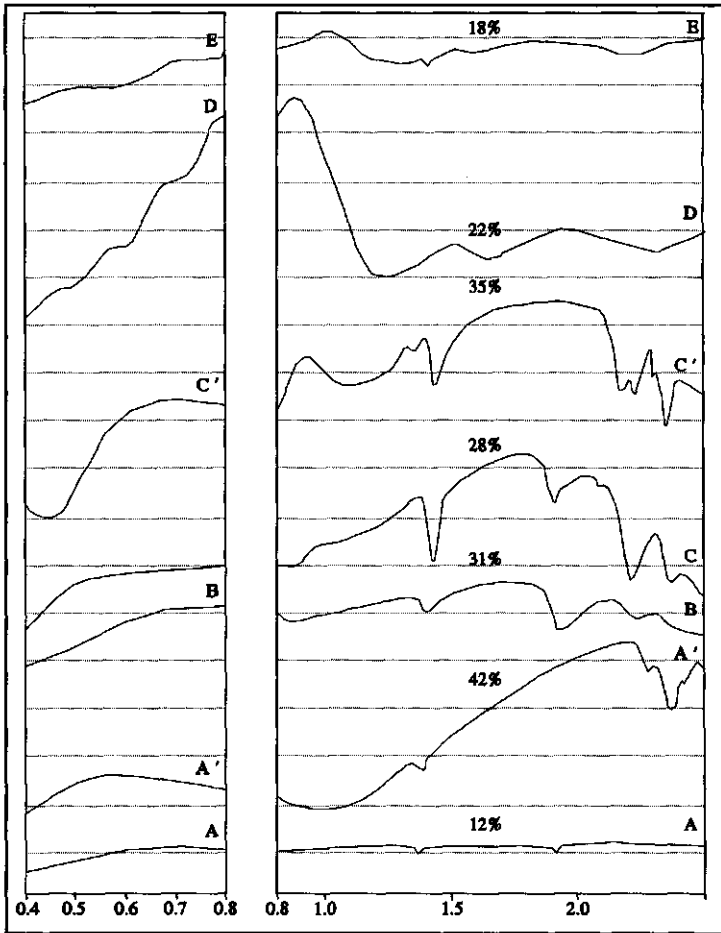


Fig. 6.11: Location of the samples of the Guaitara section (Legend: A = Grey phyllite and chlorite bearing phyllite, B = Schist, C = Banded quartz-plagioclase-biotite-sillimanite gneiss, D = Garnet-quartz-plagioclase-cordierite-sillimanite-spinel gneiss, E = Garnet peridotite).

visible and near infrared portion of the spectrum. Staurolite shows strong absorption to both long and short wavelengths which produces an apparent reflection maximum at  $1.05\mu\text{m}$ . Sillimanite is characterized by strong hydroxyl ( $1.4\mu\text{m}$  and  $2.2\mu\text{m}$ ) bands and a flat spectrum. Cordierite also shows hydroxyl and water bands and often weak iron absorption features. Tourmaline has a spectrum similar to that of chlorite in that its reflectivity decreases from  $2.0\mu\text{m}$  toward shorter wavelengths. Furthermore, tourmaline has a number of hydroxyl bands between  $2.2\mu\text{m}$  and  $2.4\mu\text{m}$ , intense features near  $0.75\mu\text{m}$  and  $1.1\mu\text{m}$  and a fall-off toward the blue in the visible. The garnet spectrum is characterized by a peak reflectivity near  $0.95\mu\text{m}$  and several iron absorption bands in the visible and intense absorptions near  $1.28\mu\text{m}$  and  $1.7\mu\text{m}$  due to iron.

From the above discussion it is apparent that reflectance spectra of phyllite, schists, and gneisses are dominated by water and hydroxyl bands from the quartz, feldspars, and



**Fig. 6.12:** Spectra of rock samples over the contact of peridotites and adjacent gneiss-schist-phyllite series in the Guaitara section. Letters refer to locations on Fig. 6.11.

micas. These features are often overprinted completely by the spectra of accessory minerals such as garnet, chlorite, and tourmaline.

In Fig. 6.11 the location of samples of which spectra are given in Fig. 6.12 are shown. Spectrum A and A' are spectra of a grey phyllite and a chlorite bearing phyllite, respectively. The spectrum of the phyllite is dark and relatively featureless due to the fine-grained nature of the rock specimen. The chlorite phyllite spectrum is dominated by the chlorite absorption features such as the distinctive chlorite hydroxyl bands centered at  $2.34\mu\text{m}$  and the weaker feature at  $1.4\mu\text{m}$ . Spectrum B represents that of a schist characterized by absorption features near  $1.4\mu\text{m}$ ,  $1.9\mu\text{m}$ , and  $2.2\mu\text{m}$ . Spectrum C is a spectrum measured for a banded gneiss sample containing quartz, plagioclase, biotite, and sillimanite. The spectrum is dominated by intense water and hydroxyl bands near  $1.4\mu\text{m}$  and  $1.9\mu\text{m}$ , however the sillimanite probably

contributes the 2.2 $\mu$ m band. Spectrum C' in Fig. 6.12 is that of a banded gneiss containing tourmaline as accessory mineral. The spectrum is completely overprinted by the features of tourmaline, e.g. the iron bands near 0.75 $\mu$ m and 1.1 $\mu$ m, the 1.4 $\mu$ m feature, and the characteristic hydroxyl bands between 2.2 $\mu$ m and 2.4 $\mu$ m. The spectrum of a garnet gneiss consisting of quartz, plagioclase, cordierite, sillimanite, spinel and garnet is shown as spectrum D in Fig. 6.12. The features of most minerals are obscured by the strong bands of the garnet. The spectrum is dominated by the 1.28 $\mu$ m and 1.7 $\mu$ m iron absorption feature and several iron absorption bands in the visible and near infrared yielding a peak reflectivity just short of 0.95 $\mu$ m. Spectrum E represents the garnet bearing peridotite bordering the garnet gneisses. The spectrum is essentially similar to that of the garnet gneiss however the features are less pronounced and the overall reflectivity is much lower.

### 6.5.3 The Jubrique section

The Jubrique section follows the road running from Jubrique southeast toward Estepona. A series of phyllites, schists, and gneisses borders the peridotites. The peridotites are developed in the classical way as described by Obata (1980) from the garnet lherzolite facies near the gneiss-peridotite contact to the plagioclase lherzolite facies some ten kilometers from the contact. The location of the samples taken is shown in Fig. 6.13, whereas the reflectance spectra are shown in Fig. 6.14.

Spectrum A is that of a grey phyllite/schist displaying weak water absorption bands. Spectra B and C represent gneisses of slightly different mineralogy. Sample B contains biotite and sillimanite and sample C contains biotite, sillimanite, and garnet. The sillimanite of sample B probably contributes to the 2.2 $\mu$ m hydroxyl band whereas the garnet of sample C determines the shape of the spectrum in the visible and near infrared yielding a peak reflectivity at 0.95 $\mu$ m. This feature is however subdued most likely due to the presence of finely disseminated graphite. Sample D contains cordierite and garnet. The garnet features are not very dominant, and the spectrum of this gneiss is mainly characterized by water and hydroxyl bands which may be attributed to the cordierite. The contact between garnet bearing gneisses opposing garnet lherzolites south of Jubrique is marked by a felsic intrusion of granitic composition (spectrum E). Its spectrum shows strong water absorption bands near 1.4 $\mu$ m, 1.9 $\mu$ m, and 2.5 $\mu$ m. The double absorption band near 2.2 $\mu$ m is probably due to hydroxyl in sericite produced during late stage alteration of the feldspar. The garnet lherzolite spectra shown as spectrum F and G, respectively in Fig. 6.14 are dominated by the garnet absorption bands. Spectrum F represents a sample with coarse (>3mm.) garnets whereas the sample of spectrum G is finer grained. The most prominent absorption band is centered near

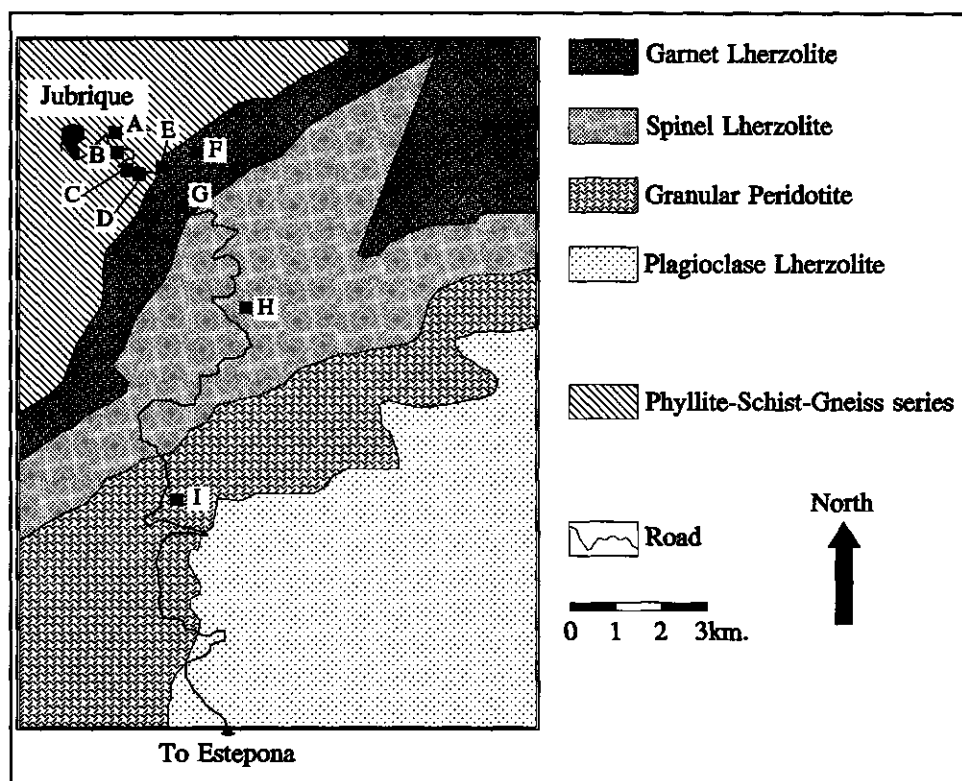


**Fig. 6.13:** Location of the samples in the Jubrique section of which spectra (Legend: A = Grey phyllite/schist, B = Biotite-sillimanite gneiss, C = biotite-garnet-sillimanite-graphite gneiss, D = Biotite-garnet-sillimanite-cordierite, E = granitic intrusion, F = Coarse-grained garnet lherzolite, G = Fine-grained garnet lherzolite, H = Spinel lherzolite, I = Granular harzburgite).

1.28 $\mu$ m and a weaker band at 1.7 $\mu$ m due to ferrous iron. The visible and near-infrared part of the spectrum are dominated by a rapid fall-off from 1.0 $\mu$ m toward shorter wavelengths due to both ferric and ferrous iron. These ions are responsible for the observed absorption bands at 0.85 $\mu$ m, 0.7 $\mu$ m, 0.57 $\mu$ m, 0.51 $\mu$ m, and 0.43 $\mu$ m. Spectrum H is that of a spinel lherzolite. This sample weak absorption bands, most bands are masked due to the presence of magnetite. Sample I is a granular peridotite which is a coarse grained harzburgite consisting of olivine and orthopyroxene (enstatite). The strong absorption band near 0.91 $\mu$ m is due to ferrous iron in the pyroxene thus overprinting the olivine ferrous iron band which would occur near 1.1 $\mu$ m. The additional water and hydroxyl features are due to vibrational transitions in the OH groups indicating minor alteration of olivine to serpentine.

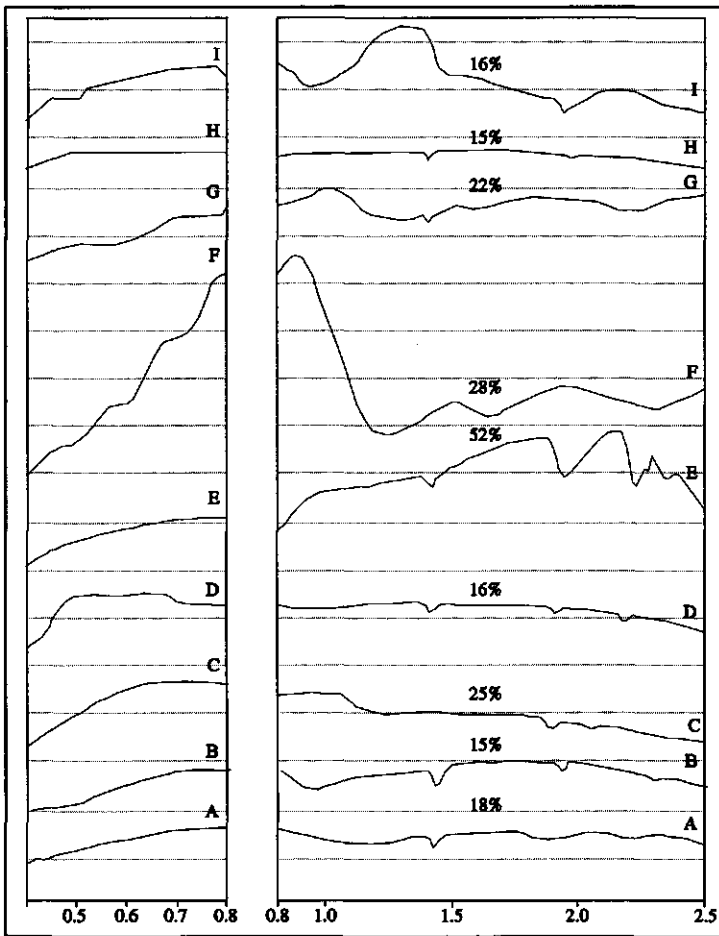


**Fig. 6.14:** Reflectance spectra of samples in the Jubrique section. Letters refer to locations on Fig. 6.13.

## **6.6 RELATION BETWEEN LABORATORY, FIELD, AND IMAGE SPECTRA: A CASE STUDY FROM THE LOS PEDROCHES BATHOLITH**

The aim of this Case Study is to relate spectral information obtained from laboratory analysis with spectral signature of pixel spectra through the use of field spectroscopy. A study carried out on the Los Pedroches batholith (near Almadén, Fig. 6.15) and its surrounding contact metamorphic aureole is presented. The aureole stands out clearly on Landsat Thematic Mapper (TM) and Landsat Multispectral Scanner (MSS) imagery. Soils on the contact-metamorphic aureoles are dark, reddish-brown in colour, contrasting with lighter coloured

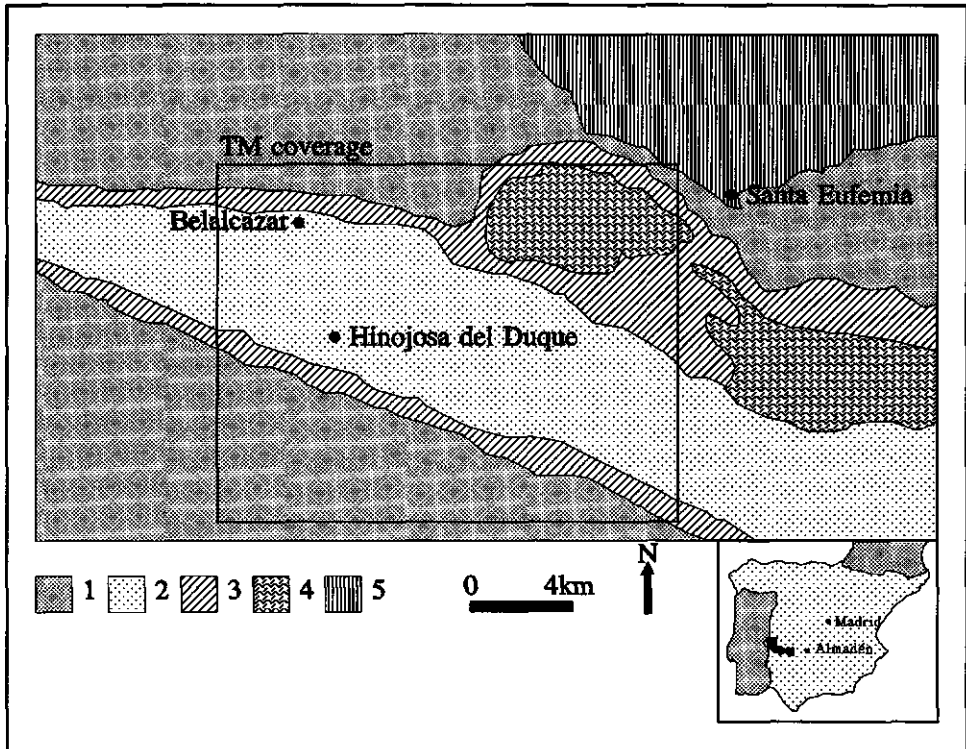


**Fig. 6.15:** Location and generalized geologic map of the Hinojosa del Duque area. TM coverage discussed in this paper is indicated by the box (Legend: 1 = Shale and greywackes (Culm, Carboniferous), 2 = Biotite Granodiorite (Los Pedroches Batholith), 3 = Hornfelses and 'spotted' slates (Contact metamorphic aureole), 4 = Porphyritic granite (Santa Eufemia stock), 5 = Sandstones and quartzites (Ordovician-Devonian units)).

soils developing on granitic rocks of the plutons and country rock outside the aureole. This difference is caused by the combined effects of a number of parameters such as  $H_2O$  and  $OH$  content, total Fe,  $Fe^{2+}/Fe^{3+}$  ratio and amount and form of carbon as reflected by the soil mineralogy.

Due to its metal potential (e.g. the huge mercury deposits of Almadén and lead-silver deposits of the Linares district; Ortega-Gironés & Hernandez-Sobrino, 1992; Saupé, 1990; Eichmann *et al.*, 1977; Maucher & Saupé, 1967), the southern margin of the Central Iberian domain, at which the Los Pedroches batholith is located, has been relatively well studied (e.g. Almela *et al.*, 1962; Puschmann, 1967a+b). The Los Pedroches batholith is a calc-alkaline igneous intrusion emplaced into slates and greywackes of Middle Carboniferous age (Saupé, 1973, 1990; Saupé *et al.*, 1977). The major part of the Los Pedroches batholith consists of

biotite  $\pm$  amphibole granodiorite and aluminous porphyritic biotite  $\pm$  amphibole  $\pm$  cordierite monzogranite. The latter is exposed in the southeastern part of the Los Pedroches batholith and also in satellite bodies as the Santa Eufemia pluton (Fig. 6.15). This pluton also contains enclaves of leucogranite with aplitic affinity and numerous dikes of aplitic, pegmatitic or monzogranitic composition and thick quartz veins (Garcia-Casco, 1986; Garcia-Casco & Pascual, 1987). Medium-grade contact metamorphism has transformed the Culm slates and greywackes into hornfels and spotted slate with neoformation of cordierite, andalusite, and biotite.

### 6.6.1 Chemical composition of soils

A total of 13 soil samples were analyzed which were taken from a transect along the C-420 road that leads from the village of Hinojosa del Duque to Belmez in the north of the Province of Cordoba (Fig. 6.16). This section crosses the southern contact-metamorphic aureole of the Los Pedroches batholith almost perpendicularly. At every sample station a composite soil sample was taken from recently ploughed fields. This improved the representativity of the sample and also largely eliminated the presence of vegetation (see also Richardson & Wiegand, 1977; Roberts *et al.*, 1993). Rock samples were collected from the nearest outcrop or from float in the field.

The composition of these soils was determined through X-ray diffraction (XRD) analysis. Generally, soils are composed of a mixture of new-formed clay minerals and iron (hydr)oxides and minerals inherited from the underlying bedrock. These minerals show strong variations in their resistance against chemical weathering. Examination of X-ray diffraction patterns of soil samples taken along a profile over the contact metamorphic aureole indicate variable proportions of the following minerals: quartz, feldspar, muscovite, chlorite, biotite, montmorillonite (smectite group), illite and/or phengite (illite group), kaolinite (kaolinite group), goethite and hematite (Table 6.3). From the above, the following parameters can be summarized as being instrumental to the reflectance characteristics of the soils: total iron, ferro/ferri ratio, the hydroxyl feature, the Al-hydroxyl feature, the water absorption feature, the carbon content, and the bulk mineralogical composition. Soil mineralogy is a function of climatic conditions, soil drainage, and mineralogy of the underlying bedrock. The igneous rocks of the Los Pedroches granodiorite are mainly composed of K-feldspar, quartz, plagioclase, and biotite. Plagioclase is in the weathering zone largely replaced by sericite: a microcrystalline mixture of muscovite, hydromuscovite, and phengite. Biotite is almost completely altered to chlorite and rutile. Hornfelds and their soils, forming the inner contact aureole, are composed of quartz, muscovite, chlorite, feldspar and locally cordierite and

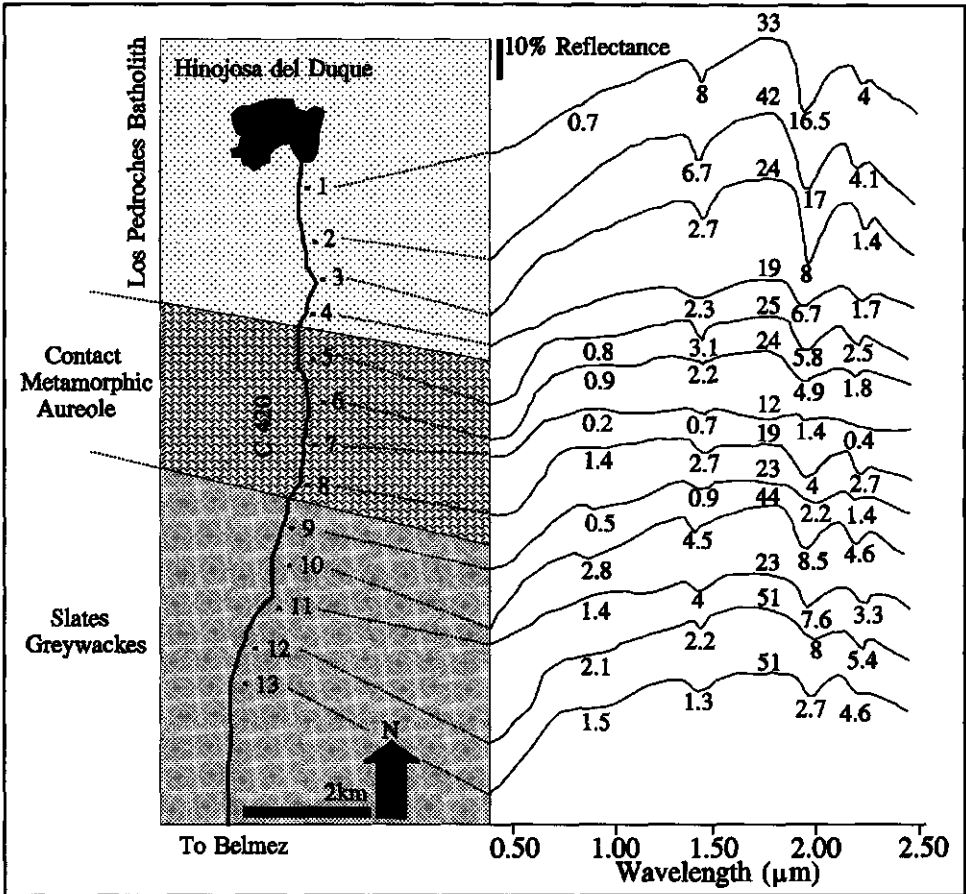


Fig. 6.16: Visible and near-infrared reflectance spectra of soils sampled along the C-420 road from Hinojosa del Duque to Belmez perpendicular to the contact aureole of the Los Pedroches batholith. The reflectivity at 1.6  $\mu\text{m}$  is indicated above the curve, underneath each absorption feature the depth (in percent reflectance) relative to Hull is indicated.

andalusite. 'Spotted' slates in the outer contact aureole and their soils are composed of fine-grained phyllite with green-yellow spots of poikilitic mica (biotite or chamosite) and cordierite, containing quartz some feldspar and 5% by volume of microcrystalline opaque matter. Greywackes and slates of the Culm facies are mainly composed of quartz, feldspar, and variable (3-25 vol. %) amounts of limonite.



## 6.6.2 Spectra of minerals contributing to soil reflectance

Minerals contributing to the spectral reflectance of the soils sampled over the contact metamorphic aureole are essentially biotite, muscovite, chlorite, smectite (mainly montmorillonite), illite and kaolinite. Their spectra are shown in Fig. 6.17. These are phyllosilicates whose structure is that of indefinitely extended silicon-oxygen sheets formed by sharing of three of the four oxygens in each  $\text{SiO}_4$  tetrahedron with the neighbouring tetrahedra. Phyllosilicates are hydroxyl-bearing, and Si is often substituted for aluminum.

Biotite is a potassium magnesium-iron-aluminum silicate, essentially  $\text{K}(\text{Mg,Fe})_3\text{AlSi}_3\text{O}_{10}(\text{OH})_2$ . Ferrous and ferric ions cause a very broad band in the 0.6-1.5  $\mu\text{m}$  region, and a drop-off in the blue. As in the sample shown in Fig. 6.17, very often hydroxyl bands are barely observable.

Muscovite is essentially  $\text{KAl}_3\text{Si}_3\text{O}_{10}(\text{OH})_2$ , but frequently contains small amounts of  $\text{Fe}^{2+}$  or  $\text{Fe}^{3+}$  resulting in a broad iron absorption band near 0.95  $\mu\text{m}$  and a sharp absorption feature near 0.44  $\mu\text{m}$ . Hydroxyl bands centered at 1.4 and 2.2  $\mu\text{m}$  are rather deep and sharp. An additional double absorption feature attributed to hydroxyl can be observed at 2.34 and 2.42  $\mu\text{m}$  (Hunt *et al.*, 1973).

Chlorite,  $(\text{Mg, Fe}^{2+}, \text{Fe}^{3+})_6\text{AlSi}_3\text{O}_{10}(\text{OH})_8$ , is a monoclinic, platy mineral which forms as a result of alteration of ferromagnesian silicates such as pyroxenes, amphiboles, and biotite. The chlorite spectrum shows three broad bands between 0.7 and 1.1  $\mu\text{m}$ . The bands at 0.7  $\mu\text{m}$  and at 0.9  $\mu\text{m}$  are due to  $\text{Fe}^{3+}$  whereas the band at 1.1  $\mu\text{m}$  is due to  $\text{Fe}^{2+}$  (Fig. 6.17). Additional hydroxyl bands occur at 1.4  $\mu\text{m}$  and between 2.0 and 2.5  $\mu\text{m}$ .

Smectite is a group of expanding-lattice clay minerals characterized by a three-layer lattice (one sheet of aluminum and hydroxyl between two layers of silicon and oxygen). Montmorillonite, the high-alumina end-member of the smectite group, is the most common smectite in the study area. Montmorillonite is  $\text{Na}_{0.33}\text{Al}_{1.67}\text{Mg}_{0.33}\text{Si}_4\text{O}_{10}(\text{OH})_2 \cdot n\text{H}_2\text{O}$ , where water molecules are absorbed between the sheets of the structure. The spectrum of montmorillonite is typical for a water-rich mineral showing strong absorption bands near 1.4 and 1.9  $\mu\text{m}$  and an additional band near 2.2  $\mu\text{m}$ .

Absorption features of illite are generally broader and less well defined compared to those of muscovite, nevertheless, the illite, muscovite and montmorillonite spectra have similar absorption bands. Illite  $\{(\text{K,H}_3\text{O})(\text{Al,Mg,Fe})_2(\text{Si,Al})_4\text{O}_{10}[(\text{OH})_2,\text{H}_2\text{O}]\}$  shows broad water absorption features near 1.4 and 1.9  $\mu\text{m}$  and additional Al-hydroxyl features at 2.2, 2.3, and 2.4  $\mu\text{m}$ . Illite and muscovite have absorption bands near 2.35 and 2.45  $\mu\text{m}$  which are lacking in the montmorillonite spectrum.

The kaolinite  $(\text{Al}_2\text{Si}_2\text{O}_5(\text{OH})_4)$  spectrum of Fig. 6.17 shows the well-known doublet absorption near 2.2  $\mu\text{m}$  and an additional hydroxyl feature at 1.4  $\mu\text{m}$ . Kaolinite occurs in soils

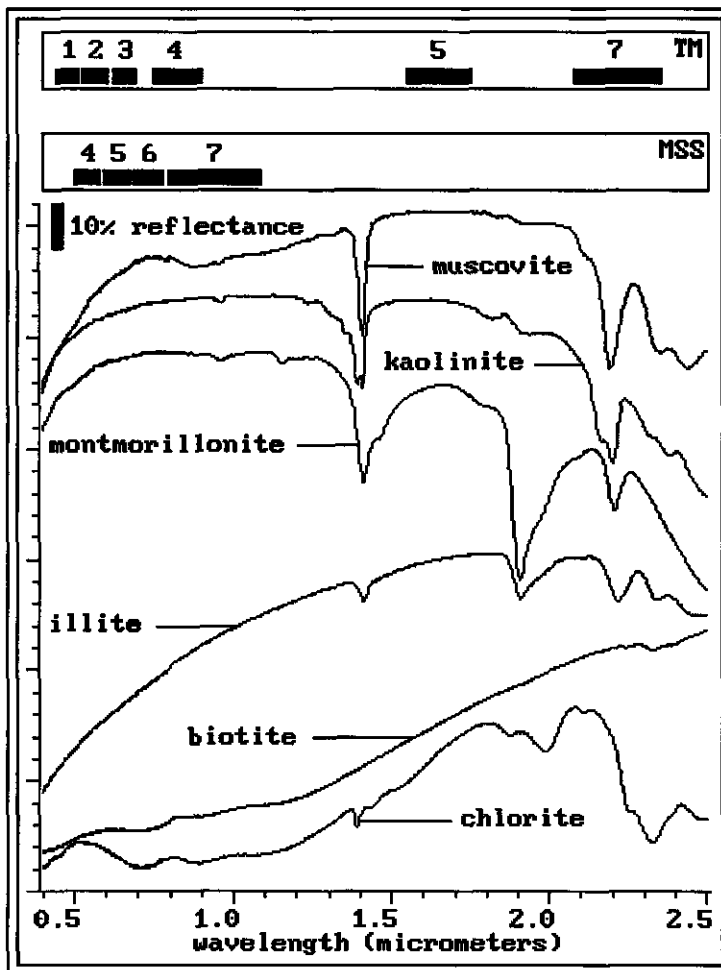


Fig. 6.17: Spectra of minerals contributing to the spectral properties of the investigated soil samples. Landsat MSS and TM channel positions are indicated as reference.

as an alteration product of aluminum silicates, particularly feldspar.

Thin-section examination of rock samples and laboratory analysis of soil samples indicated the presence of limonite in opaque form in the contact metamorphic soils. Limonite is an hydrous iron oxide, mainly  $2\text{Fe}_2\text{O}_3 \cdot 3\text{H}_2\text{O}$ , which often occurs in the form of goethite with some hematite. Its reflectivity over the entire wavelength region of the spectrum is very low in opaque form, but in transparent form it displays ferric absorption bands near 0.55 and 0.9 $\mu\text{m}$ .

- Weathered rock and soil reflectance spectra -

Table 6.3: Overview of sheet silicates showing properties relevant to their reflectance characteristics (modified from Deer *et al.*, 1967).

Mineral	Crystallographic positions			(OH) <sup>-</sup>	Al(OH)	H <sub>2</sub> O	Iron
	X	Y	Z				
Kaolinite		Al <sub>2</sub>	Si <sub>2</sub>	16	8		traces
Montmorillonite	( $\frac{1}{2}$ Ca,Na) <sub>0.66</sub>	Al <sub>1.34</sub> (Mg,Fe) <sub>0.66</sub>	Si <sub>2</sub>	4	3.34	~2	minor
Illite	K <sub>2-x</sub>	Al <sub>4</sub>	Si <sub>6-2x</sub> Al <sub>2-x</sub>	4	4		traces
Phengite	K <sub>2</sub>	Al <sub>6-x</sub> (Mg,Fe <sup>2+</sup> ) <sub>x</sub>	Si <sub>6-x</sub> Al <sub>2-x</sub>	4	4-x		minor
Hydromuscovite	(K,H <sub>3</sub> O) <sub>2</sub>	Al <sub>4</sub>	Si <sub>4</sub> Al <sub>2</sub>	4+x	4+x		traces
Muscovite	K <sub>2</sub>	Al <sub>4</sub>	Si <sub>6</sub> Al <sub>2</sub>	<4*	<4		minor
Chlorite		(Mg,Fe <sup>2+</sup> ) <sub>11-4</sub> (Al,Fe <sup>3+</sup> ) <sub>1-4</sub>	Si <sub>7-4</sub> Al <sub>1-4</sub>	16	1-4		substantial
Biotite	K <sub>2</sub>	(Mg,Fe <sup>2+</sup> ) <sub>6-4</sub> (Fe <sup>3+</sup> ,Al,Ti) <sub>0-2</sub>	Si <sub>6-3</sub> Al <sub>2-3</sub>	<1*	0-2		substantial

\*some (OH)<sup>-</sup> replaced by F<sup>-</sup>

### 6.6.3 Spectra of soil samples

Laboratory reflectance spectra of 13 soil samples, measured using the Beckman UV5240 spectrometer, are shown in Fig. 6.16. Soil samples 5-8 were collected on the hornfels series marking the contact aureole. In this Figure, the percent reflectance at 1.6μm (which is referred to as albedo) has been indicated above the spectrum. Beneath each absorption feature, the depth of the feature relative to Hull has been denoted (in percent reflectance). In order to further characterize absorption features in soil reflectance spectra, wavelength position, depth, width, asymmetry, and slope of the upper Hull was calculated for all absorption features. Laboratory spectra of soils are discussed in detail in Condit (1970, 1972).

The positions of various features is relatively constant as is the asymmetry, and the depth and width of a feature which are strongly correlated. The slope parameter is rather insignificant in comparison with the channel width of TM channels. Therefore focus is on the relative albedo and the position and depth of hydroxyl, iron, and water absorption features in the reflectance spectra. The relative albedo, measured as the reflectance at 1.6μm, is shown for each soil sample in Fig. 6.18. Soil samples 5-8 marking the contact metamorphic aureole are relatively dark. Albedo increases with distance from the contact metamorphic zone. The depth of both iron absorption features in soil spectra is shown in Fig. 6.19. Fe<sup>2+</sup> results in a broad feature near 1.0μm whereas Fe<sup>3+</sup> gives rise to a decrease in reflectance from 0.8 to

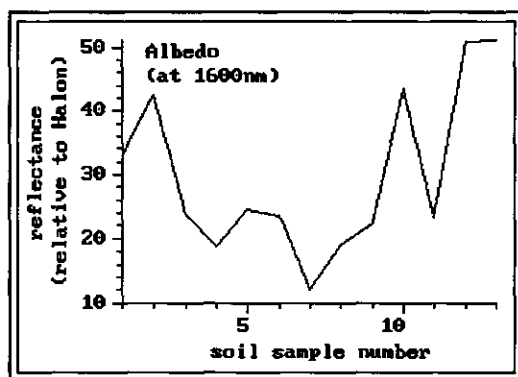


Fig. 6.18: Albedo expressed as reflectivity at 1.6 $\mu$ m for 13 soil samples.

0.4 $\mu$ m. The Fe<sup>3+</sup> absorption feature has been characterized as the difference between the reflectance at 0.8 $\mu$ m and the reflectance at 0.4 $\mu$ m. From Fig. 6.19 it can be seen that soils developing on the contact-metamorphic aureole have relatively weak Fe<sup>3+</sup> features and moderate Fe<sup>2+</sup> features. The soils characterized by weak iron features, however, constitute a broad zone surrounding the contact metamorphic aureole on both sides. At larger distance from the hornfels series, iron content in the soil increases as indicated by intense absorption features in soil samples 9-13. The depth of the Al-hydroxyl feature centered near 2.2 $\mu$ m, the depth of the water absorption band at 1.9 $\mu$ m, and the depth of the hydroxyl feature at 1.4 $\mu$ m are shown in Fig. 6.20. These three features appear to be highly correlated. The contact metamorphic soils show relatively weak water and hydroxyl features which increase in depth with distance from the contact zone. Soil sample 11 should perhaps be regarded as displaying a reflectance spectrum differing from the surrounding samples in that it has relatively low albedo and weak iron features. This decreased albedo, which is also characteristic of the contact metamorphic soils, may be caused by the presence of carbonaceous material instead of mineralogic differences. The opacity of carbonaceous material increases with increasing temperature associated with contact metamorphism (Long *et al.*, 1968; Staplin, 1969; Rowan *et al.*, 1987). Various authors noted the spectral quenching effect of small amounts (<0.1 percent) of finely disseminated carbonaceous material thus reducing the overall reflectance and subduing the intensity of absorption bands (Johnson & Fanale, 1973; Clark, 1983; Crowley, 1986). Hunt & Salisbury (1976) and Clark (1983) attribute these characteristics to the high absorption coefficient of the carbonaceous material. Clearly, from Fig. 6.16 it can be seen that this spectral quenching effect affects the relative albedo and the depth of water and hydroxyl bands in the soil spectra but has little effect on the iron absorption features. An extreme example of spectral quenching is soil sample 7 which has a high (>4%) content of opaque material masking all but the strongest absorption bands.

- Weathered rock and soil reflectance spectra -

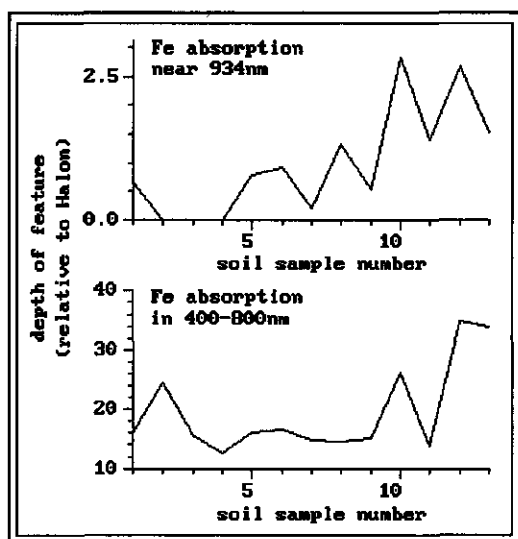


Fig. 6.19: Depth of the  $\text{Fe}^{2+}$  feature near  $1.0\mu\text{m}$  expressed in percent reflectance relative to Hull and the depth of the  $\text{Fe}^{3+}$  feature expressed as the difference in reflectance at  $0.8$  and  $0.4\mu\text{m}$ .

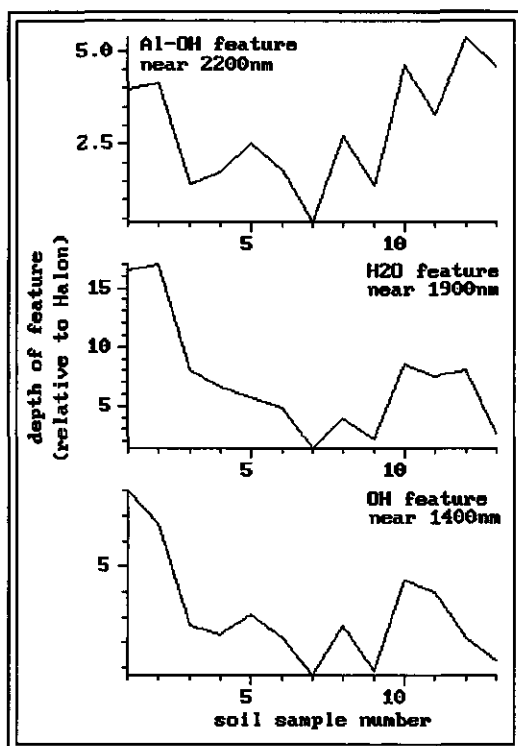


Fig. 6.20: Depth of hydroxyl bands centered at  $1.4$  and  $2.2\mu\text{m}$  and the water absorption band centered at  $1.9\mu\text{m}$ .

#### 6.6.4. Image processing and analysis

Studies by Rowan *et al.* (1987) and Marconnet *et al.* (1984) indicated that Landsat MSS band 7 images could be used to detect contact metamorphosed pelitic rocks and soils around and in aureoles. In the present study, laboratory and field spectra of soils are documented and linked with image data for geologic mapping of a contact metamorphic aureole.

The study area was covered by Landsat MSS and TM scenes. In order to evaluate whether the spectral absorption features characterizing the soil samples would be represented also in the digital products, 0.5-by-0.5m sized soil samples were spectrally analyzed using a field spectrometer covering the four MSS wavelength bands. For comparison, the laboratory reflectance spectra were re-sampled to the width of the Landsat MSS channels by averaging the reflectance over the wavelength region covered by each of the channels. The resulting scatter plots for each individual channel are shown in Fig. 6.21. These indicate that a good correlation exists between laboratory spectra and image spectra.

*Reduction of image correlation using ratio images* - Table 6.4 shows the correlation matrix between individual Landsat TM bands. The channels are highly correlated indicating that they are spectrally similar. Thus, colour additive component images generated from three band combinations of such channels would display a limited range of colours. Contrast enhancement of three highly correlated image channels displayed as red, green, and blue will serve mainly to expand the dark-light range of intensities; it does little to expand the range of colours displayed. Several techniques have been proposed for exaggeration of the colour saturation independent of the brightness such as stretching of decorrelated images, stretching of hue-saturation-intensity transformed images, and the use of ratio images and normalized difference images (Mather, 1987; Jensen, 1986). Decorrelation stretch (Soha & Schwartz, 1978; Gillespie *et al.*, 1986) is based on principal component (PC) transformation. The highly correlated bands are first transformed to their three principal components which are independently stretched in the PC-space and subsequently retransformed to the original coordinate system for display. The Hue-Saturation-Intensity (HSI) transformation is a technique for numerically describing colour in the image domain using spherical coordinates which are analogous to the conventional perceptual attributes: Hue, Saturation and Lightness (or Intensity; Gillespie, 1980; Gillespie *et al.*, 1986).

Both ratio and normalized difference images have been used as input for three band colour composites. Ratio images are created by calculating, on a pixel by pixel basis, ratios of DN (representing intensity) values from two TM band images as

$$RDN_{ij} = DN_i / DN_j \quad (1)$$

where DN is the intensity in the  $i^{\text{th}}$  or  $j^{\text{th}}$  channel of the TM images and RDN is the ratio

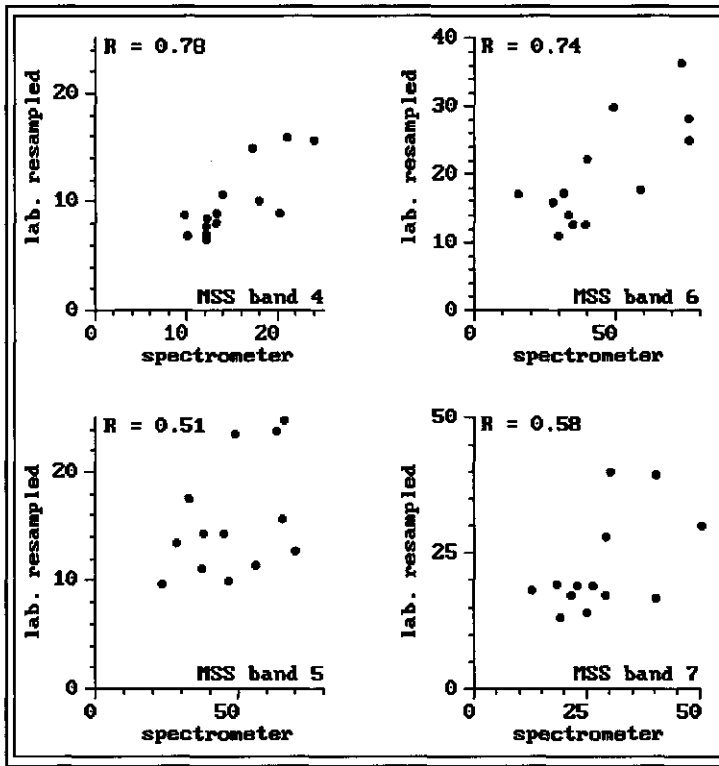


Fig. 6.21: Scatter plots of reflectance in Landsat MSS bands 4, 5, 6, and 7 as measured by a field spectrometer using 0.5-by-0.5m. samples and resampled reflectance in these channels from laboratory spectra.

value in the ratio image. This ratio ranges from 0 to 1 (negative radiance ratio) and from 1 to infinity (positive radiance ratio). The correlation among ratio images is lower than the correlations among the original TM band images resulting from the reduction of a wide range of  $(DN_i, DN_j)$  to a single  $RDN_{ij}$ . The source of variation which can be attributed to illumination differences in a scene, is reduced after ratioing, which means that the spectral shape becomes proportionally more important. However, reducing variance due to illumination also implies that additive noise as well as effects of multiple reflections and atmospheric scattering will be exaggerated in ratio images. Fig. 6.22 shows a colour ratio component image displaying TM 5:7 in red, TM 3:1 in green, and TM band 5 in blue. A correction was not applied to remove atmospheric scattering which is largest in TM channel 1. Atmospheric scattered light will decrease the TM 3:1 values of the dark contact metamorphic soil and increase the TM 3:1 over the high albedo objects, thus increasing the separability of these features. In the TM bands 5 and 7 the effects of atmospheric scattering are minimal and will only have a minor effect on the interpretation of the colour ratio component image. The rationale for using a combination of TM 5:7, TM 3:1, and TM 5 is the following. TM 5:7

Table 6.4: Correlation matrix for Landsat TM bands of the Hinojosa del Duque image.

	TM-1	TM-2	TM-3	TM-4	TM-5	TM-7
TM-1	1.000					
TM-2	0.943	1.000				
TM-3	0.898	0.973	1.000			
TM-4	0.764	0.822	0.850	1.000		
TM-5	0.718	0.755	0.792	0.832	1.000	
TM-7	0.719	0.789	0.793	0.689	0.883	1.000

measures the decrease in reflectance from  $1.6\mu\text{m}$  to  $2.3\mu\text{m}$  related to a strong  $\text{H}_2\text{O}$  absorption feature. Since TM-5 is centered on the  $2.2\mu\text{m}$  hydroxyl feature, the ratio TM 5:7 gives an indication of the relative depth of this feature. In all observed soil spectra the reflectance value in TM-5 is higher than the reflectance value in TM-7 thus resulting in  $\text{RDN}_{57}$  values ranging from 1 to infinity. The ratio of TM 3 over TM 1 (TM 3:1) maps the decrease in reflectance from  $0.7$  to  $0.4\mu\text{m}$  that is an indication for  $\text{Fe}^{3+}$  related absorption. In general, reflectance in TM 3 is higher than reflectance in TM 1 thus resulting in ratios,  $\text{RDN}_{31}$ , that range from 1 to infinity. The choice of TM 5 as the blue component is related to the spectral quenching effect discussed in the previous section. TM 5 is an indication of the relative albedo which increases with distance from the contact metamorphic aureole. The correlation matrix of the bands used for the colour ratio component image are shown in Table 6.5, indicating that the individual images are relatively uncorrelated. The colour scheme of the colour ratio component image presented in Fig. 6.22 is explained in Table 6.6. The contact metamorphic soils show as light green and dark green colours, indicating very low DN values in TM 5:7 and TM 5. This is related to the weak  $\text{H}_2\text{O}$  absorption and hydroxyl feature and the relative low albedo of these soils related to spectral quenching. Therefore the weak  $\text{Fe}^{3+}$  absorption expressed in TM 3:1 (the green band) is dominating the colour in Fig. 6.22. In between the two prominent almost linear contact metamorphic zones is an highly cultivated area with dominantly light blue colour. These soils have a relative high albedo and strong  $\text{Fe}^{3+}$  features and relatively weak  $\text{H}_2\text{O}$  and OH features. Dark blue colours are towns and infrastructure. Towards the east, red and yellow colours prevail indicating strong  $\text{H}_2\text{O}$  absorption features and strong  $\text{H}_2\text{O}$  and  $\text{Fe}^{3+}$  features, respectively. North of the contact zone, the prevailing colour is magenta representing soils with high reflectivity and strong  $\text{H}_2\text{O}$  absorption features lacking  $\text{Fe}^{3+}$  features. Two plutons can be distinguished on the image: the first pluton (the Santa Eufemia granite) covers the northeastern corner of the image. The



- Weathered rock and soil reflectance spectra -

Table 6.5: Correlation matrix for Landsat TM ratios and bands used for the colour ratio component image of Fig. 6.22.

	TM 5:7	TM 3:1	TM 5
TM 5:7	1.000		
TM 3:1	-0.321	1.000	
TM 5	-0.180	-0.134	1.000

second pluton (the Los Pedroches batholith) is seen as the WNW-ESE striking wedge-shaped zone covering the central part of the image. Contact metamorphic zones border this pluton both to the northeast and the southwest. The Santa Eufemia granite is not so prominent probably because it is deeply buried. However, it is locally marked by a dark green contact zone and a core of yellow coloured pixels indicating strong  $\text{Fe}^{3+}$  and  $\text{H}_2\text{O}$  absorption features that decrease toward the boundary of the pluton.

*Reduction of image correlation using normalized difference images* - Instead of using ratio images for colour ratio component images, spectral gradients may be used. The gradient, expressed as a fraction of the average radiance, is given by the difference between intensities of two channels, normalized to their average value as

$$\text{DDN}_{ij} = [(\text{DN}_i - \text{DN}_j) / (\text{DN}_i + \text{DN}_j)] (2/\lambda_i - \lambda_j) \quad (2)$$

where  $\text{DDN}_{ij}$  is the value of the normalized intensity difference for channels  $i$  and  $j$  and  $\lambda_i$  and  $\lambda_j$  are their respective wavelengths (Gillespie *et al.*, 1987). Division by  $(\lambda_i - \lambda_j)$  is necessary if  $\text{DDN}_{ij}$  is to be interpreted as a spectral gradient, but makes no difference in image enhancements because the  $\text{DDN}_{ij}$  values will be stretched. Normalization reduces the effect of albedo and topographic shading on DDN. The DDN values range symmetrically around zero instead of from 0 to 1 for negative gradients and from 1 to infinity for positive gradients, as do ratio images. Enhancing difference images thus implies that positive and negative slopes are treated similarly. This implies that information concerning the slope direction (falloff to shorter or longer wavelength) of the spectral gradient is lost, but the relative spectral difference in the individual ratios are more enhanced. For example, the area north of the contact metamorphic zone is now characterized by several gradations of magenta related to the depth of the  $\text{H}_2\text{O}$  feature (see Fig. 6.23 and Table 6.7). The contact metamorphic zones themselves appear in yellow to brown colours with locally some reddish colours suggesting a variety of soil types characterized by relatively low albedo and variable  $\text{Fe}^{3+}$  and  $\text{H}_2\text{O}$  absorption features.

This figure is displayed as colour plate 1 on page 313

**Fig. 6.22:** Colour Ratio component image with TM 5:7 displayed in red, TM 3:1 displayed in green, and TM 5 displayed in blue (see text for discussion).

**Table 6.6:** Relation between relative RDN value, colour in the Colour Ratio Component image (Fig. 6.22), and main absorption feature. Relative ratio values are indicated by H=high, M=moderate, L=low.

TM 5:7 Red	TM 3:1 Green	TM 5 Blue	image colour	absorption features
H	L	L	Red	H <sub>2</sub> O, OH, low albedo
H	L	H	Magenta	H <sub>2</sub> O, high albedo
H	L	M	Pink	H <sub>2</sub> O, OH
L	M	L	Dark Green	weak Fe <sup>3+</sup> , low albedo
L	M-H	L-M	Light Green	weak Fe <sup>3+</sup> , OH, H <sub>2</sub> O, carbonaceous material
L	M-H	M-H	Cyan	Moderate albedo, strong Fe <sup>3+</sup> , low H <sub>2</sub> O
L	L	M	Dark Blue	moderate albedo
L	M	H	Light Blue	high albedo, moderate Fe <sup>3+</sup> , low H <sub>2</sub> O
M-H	M-H	L-M	Yellow	Moderate Fe <sup>3+</sup> and H <sub>2</sub> O
M	M	L	Brown	
H	H	H	White	
L	L	L	Black	

This figure is displayed as colour plate 2 on page 313

Fig. 6.23: Colour Ratio component image with TM 5:7 displayed in red, TM 3:1 displayed in green, and TM 5 displayed in blue. All ratios are normalized difference images (see text for discussion).

Table 6.7: Relation between relative DDN value, colour in the Colour Ratio Component image (Fig. 6.23), and main absorption feature. Relative ratio values are indicated by H=high, M=moderate, L=low.

TM 5:7 Red (normalized)	TM 3:1 Green (normalized)	TM 5 Blue	image colour	absorption features
M	L	M	Magenta	H <sub>2</sub> O
H	M-H	L	Yellow	weak H <sub>2</sub> O, OH, Fe <sup>3+</sup>
L	M	L	Dark Green	Fe <sup>3+</sup>
H	L	L	Red	H <sub>2</sub> O
L	M-H	M-H	Cyan	Fe <sup>3+</sup>
L	L-M	M	Dark Cyan	low Fe <sup>3+</sup>
M-H	L-M	L	Brown	Moderate H <sub>2</sub> O, low Fe <sub>3</sub>
H	H	H	White	

## 6.7 CONCLUSIONS

Weathered carbonate samples indicate that the overall reflectivity of the sample is hardly affected by the weathering and that many small carbonate absorption features are obscured due to weathering. The position of the strong carbonate absorption band is clearly observed and its position is the same in both the weathered and fresh sample. Due to the complexity of the chemistry of ultramafic rocks, no straightforward conclusions can be drawn from the analysis of weathered rock surfaces. Composition of soils reflect the lithology of the underlying bedrock and thus have similar spectral signature to their corresponding rock units. However, soil samples taken near and at the contact defined by the peridotites and metamorphic sequences, show weak absorption features and low overall reflectivity as a result of the presence of finely disseminated carbon. Spectral reflectance curves of vegetation in various states of decay show a gradual transition to spectra similar to those of soils. Spectral signatures of rocks on three sections across the peridotite-country rock boundary (e.g. the Ronda-San Pedro section, the Guaitara section, and the Jubrique section) show that spectral reflectance characteristics change when approaching the contact related to a change in mineral composition.

The Los Pedroches Case Study demonstrates that laboratory spectra can be linked with pixel spectra through field spectral analysis. Spectral analysis of 13 soil samples show that these soils are spectral end-members of illite, muscovite, and chlorite. Characteristic absorption features occur at  $2.2\mu\text{m}$  due to  $\text{Al-OH}$ , at  $1.9\mu\text{m}$  due to  $\text{H}_2\text{O}$ , and at  $1.4\mu\text{m}$  due to hydroxyl. Decreasing reflectivity from 0.8 down to  $0.4\mu\text{m}$  can be attributed to  $\text{Fe}^{3+}$  whereas several small absorption in the  $0.4\text{-}0.6\mu\text{m}$  wavelength range and a broad feature near  $1.0\mu\text{m}$  are related to  $\text{Fe}^{2+}$ . The depth and width of hydroxyl features and the  $\text{H}_2\text{O}$  feature at  $1.9\mu\text{m}$  increase with distance from the contact metamorphic zone related to the absorbing capacity of finely disseminated carbonaceous material. The opacity of carbonaceous material increases with increasing temperature due to metamorphism thus decreasing the overall reflectivity (albedo) and weakening the absorption features. Iron related absorption features seem to be unaffected by this process.

Several techniques have been proposed to decorrelate individual image channels, e.g. decorrelation stretch, HSI transformation, use of ratio images, and the use of normalized difference images. The analysis showed that ratios decrease the correlation from an average in the order of 0.8 for the individual TM channels to a value in the order of 0.2 for the two-channel ratios. Ratios subdue the effect of illumination differences and therefore enhance noise and atmospheric scattering. Furthermore, the values in ratio images range from 0 to 1 (negative ratio radiance) and 1 to infinity (positive ratio radiance) which makes them difficult to interpret after contrast enhancement. Normalized difference images result in values that are

*- Weathered rock and soil reflectance spectra -*

symmetric around zero. After contrast stretching, negative and positive spectral gradients are treated similarly which leads to more colour differences and less correlation among these normalized images than in the case of ordinary ratio images. More colour contrast could be obtained by using HSI transformation or decorrelation stretching on the ratio images, but the information content gained is relatively small compared to the usage of ratios only. Mapping of water and hydroxyl features, iron features, and albedo was done successfully using colour ratio component images constructed with TM 5:7, TM 3:1, and TM 5.

## CHAPTER 7:

### *Preprocessing of imaging spectrometer data and atmospheric calibration*<sup>5</sup>

#### ABSTRACT

Raw imaging spectrometer data from the AVIRIS and GERIS scanners used throughout this thesis are acquired in absolute radiance-mode and need to be preprocessed to obtain reflectance-mode data comparable to laboratory spectra. Such preprocessing is described in this Chapter using an AVIRIS data set from the Cuprite Mining district and a GERIS data set from southern Spain. In order to characterize the data properties, signal-to-noise ratios are estimated using three methods: (1) the "homogeneous area method", (2) the "local mean and local variances method", and the "geostatistical method". In general, GERIS data have higher signal-to-noise ratios than AVIRIS data, however, significant differences occur between estimates of different methods used. Next, wavelength calibration is discussed with emphasis on the GERIS data set. A one channel offset is found on the basis of the position of CO<sub>2</sub> absorption bands; an offset regularly encountered in such data. The major part of this Chapter is devoted to a critical review of the performance of a number of atmospheric calibration algorithms (e.g., the Flat-field method, the Empirical Line method, the Internal Average Relative Reflectance (IARR) method, and the Atmospheric Removal method (ATREM)).

---

<sup>5</sup>Parts of this Chapter have been published as:

Van der Meer, F. 1994. Calibration of Airborne Visible/Infrared Imaging Spectrometer data (AVIRIS) to reflectance and mineral mapping in hydrothermal alteration zones: an example from the "Cuprite Mining District". *Geocarto International*, 9(3): 23-37.

Van der Meer, F. 1994. Mineral identification and mapping of hydrothermal alteration zones using high-spectral resolution images (AVIRIS). *ITC-Journal*, 94(2): 145-154.

## 7.1 INTRODUCTION

"Raw" data from imaging spectrometers are acquired in two fundamentally different modes. Geoscan Advanced Multispectral Scanner Mark II (GEOSCAN) data, for example, are acquired in relative radiance-mode which is similar to reflectance-mode data. Data from NASA instruments (e.g. the Airborne Imaging Spectrometer, the Airborne Visible/Infrared Imaging Spectrometer) and data from the Geophysical Environmental Research Imaging Spectrometer (GERIS) are acquired in absolute radiance-mode and must be preprocessed to obtain reflectance-mode data. The "raw" imaging spectrometer data of such systems represents an atmospheric spectrum displaying a rapid falloff of reflectance toward longer wavelengths and a number of absorption bands which may be attributed to major gasses in the atmosphere.

In this Chapter, an overview is given of the sensors used and the data sets acquired in the study presented in this thesis. Their inherent performance characteristics are evaluated in terms of the signal-to-noise ratio achieved using three intrinsically different methods. Finally, wavelength and radiometric calibration is described and atmospheric calibration techniques currently available are critically reviewed. In this, I follow the preprocessing strategy outlined in detail by Rockwell (1991).

## 7.2 IMAGING SPECTROMETER SYSTEMS

### 7.2.1 The Airborne Visible/Infrared Imaging Spectrometer (AVIRIS)

The Airborne Visible/Infrared Imaging Spectrometer (AVIRIS; Vane *et al.*, 1993) was proposed in 1983 and first flown in 1987 as the first imaging system acquiring data in narrow, contiguous spectral bands across the solar reflected portion of the electromagnetic spectrum from 0.4 $\mu$ m to 2.5 $\mu$ m (Vane *et al.*, 1984). AVIRIS became operational in 1989 and has been flown since at many locations mainly in North and Central America and in Europe. The scanner consists of four spectrometers known as spectrometer A, B, C, and D covering the 0.40-0.70 $\mu$ m, 0.65-1.25 $\mu$ m, 1.20-1.82 $\mu$ m, and 1.78-2.40 $\mu$ m wavelength ranges respectively. The key performance parameters shown in Table 7.1 are the spectral coverage, 0.4-2.5 $\mu$ m, the instantaneous field of view, 1mRAD, which provides a 20m pixel, and the swath width, 10.5km, covering 614 pixels cross track. The AVIRIS is mounted on the U-2/ER-2 aircraft operating from an altitude of 20km. This platform was chosen because it is generally very stable, it has relatively low velocity-to-height ratio, and it has a long range of action. AVIRIS data are calibrated during the flight season both in the laboratory as during the flight. The laboratory and in-flight calibration is performed at the beginning and end of the season.

- Atmospheric calibration -

Table 7.1: Performance characteristics of the AVIRIS scanner (after: Vane *et al.*, 1988; 1993).

Wavelength Range	400-2500nm
Sampling Interval	10nm
Channel width	10nm
Platform	ER-2
Altitude	20km
Field of View	33 degrees
Image width (614 pixels)	10.5km
Maximum Image Length	1000km
Instantaneous FOV	1mRAD
Ground FOV	20m

Laboratory calibrations performed are primarily spectral and radiometric (see e.g., Vane *et al.*, 1988; Chrien *et al.*, 1990). The purpose of the spectral calibration is to map the center wavelength falling on each detector element, and to determine the wavelength bandwidth for the AVIRIS channels. Radiometric calibration provides a calibration file used to convert AVIRIS data numbers (DN's) to units of radiance. In-flight calibration procedures are described in detail in Green (1992a+b). Results of AVIRIS spectral and radiometric calibration accuracy are shown in Table 7.2.

Table 7.2: AVIRIS spectral and radiometric calibration accuracy (after: Green, 1992b).

Wavelength (nm)	Spectral (nm)	Radiometric (%)
400-700	1.7	3.24
700-1200	0.3	1.72
1200-1800	0.4	1.96
1800-2500	1.3	3.71



- Chapter 7 -

*Table 7.3: Specification of band number and position for the GER 63-channel imaging spectrometer data set flown on october 7th, 1991, over the Iguala-Istán area.*

Channel	Position (nm)	Channel	Position (nm)
1	464.12	34	1979.56
2	490.69	35	1996.57
3	517.26	36	2013.57
4	543.82	37	2030.57
5	570.39	38	2047.57
6	596.96	39	2064.57
7	623.52	40	2081.57
8	650.09	41	2098.58
9	676.65	42	2115.58
10	703.22	43	2132.58
11	729.79	44	2149.58
12	756.35	45	2166.58
13	782.92	46	2183.58
14	809.49	47	2200.59
15	836.05	48	2217.59
16	862.62	49	2234.59
17	889.19	50	2251.59
18	915.75	51	2268.59
19	942.32	52	2285.60
20	968.89	53	2302.60
21	995.45	54	2319.60
22	1022.02	55	2336.60
23	1048.59	56	2353.60
24	1075.15	57	2370.61
25	1165.90	58	2387.61
26	1274.70	59	2404.61
27	1383.50	60	2421.61
28	1492.30	61	2438.61
29	1601.10	62	2455.61
30	1709.90	63	2472.62
31	1818.70		
32	1945.56		
33	1962.56		

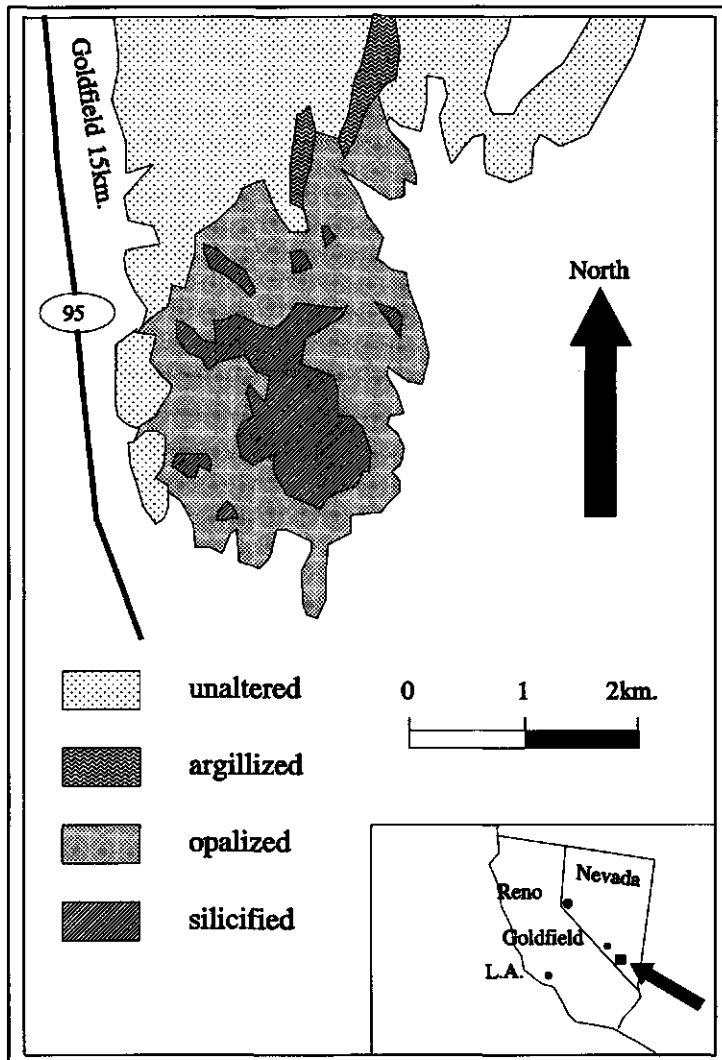


Fig. 7.1: Geology of the Cuprite Mining District. The map shows hydrothermal alteration zones after Ashley & Abrams (1980), Albers & Stewart (1972) and Abrams *et al.* (1977).

### 7.2.2 Geophysical Environmental Research Imaging Spectrometer (GERIS)

Data from the Geophysical Environmental Research Imaging Spectrometer (GERIS) are used in this study. This scanner uses an optoelectronic scanning device consisting of a rotating mirror to scan a line of 512 pixels perpendicular to the flight track with a scan angle of  $45^\circ$  to either side of the flight direction. The incoming radiation of a ground pixel is split and sent to three spectrometers each with a separate line detector array (Lehmann *et al.*, 1990). The



Fig. 7.2: AVIRIS spectral band 68 (1.013 $\mu$ m) from the Cuprite Mining District data set (A = Stonewall Playa, B = Kaolinite Hill, C = Alunite deposit, D = Buddingtonite deposit; after: Vane, 1989).

three grating spectrometers acquire 63 inherently co-registered data channels (Table 7.3) simultaneously in the 0.4-2.5 $\mu$ m wavelength region. The spectral bandwidths vary over the spectrum: the scanner has 24 channels of 23nm width in the 0.499-1.083 $\mu$ m wavelength region, 7 channels of 120nm width in the 1.080-1.800 $\mu$ m wavelength region, and 32 channels of 17nm width in the 1.980-2.494 $\mu$ m wavelength region (Collins & Chang, 1990). The scanner has three instantly changeable aperture sizes corresponding to 2.5, 3.3, and 4.6 mRAD IFOV. This yields a ground resolution of 18, 24, or 36 square meters, respectively, for an aircraft altitude of 20,000ft. The swath width at 20,000 ft. is approximately 12km. The data has a digital resolution of 12 bit and a 16 bit dynamic range and no gain or offset adjustments are necessary. Collins & Chang (1988) claim a signal-to-noise ratio as high as 5000 in the 0.4-1.1 $\mu$ m region and a signal-to-noise ratio of 500 in the 1.1-2.5 $\mu$ m region. However, Kaufman *et al.* (1991) for the GER data set of the Makhtesh Ramon (Negev, Israel) found signal-to-noise ratios varying between 10 and 45 for the same spectral regions. GER also claims radiometric calibration repeatability within 1 percent from flight to flight (Collins & Chang, 1990), however Hill (1991) measured significant differences between pre- and inflight instrument calibration but noted that these parameters differ from scene to scene. The GERIS is flown on a Piper Aztec twin engine aircraft at an altitude of 20,000 ft. The entire data set used in this study has a swath width of 512 pixels and 2400 pixels along-flightline and was flown at 15,000 ft. yielding a pixel size of approximately 12.44m (GER, pers. comm., 1991).

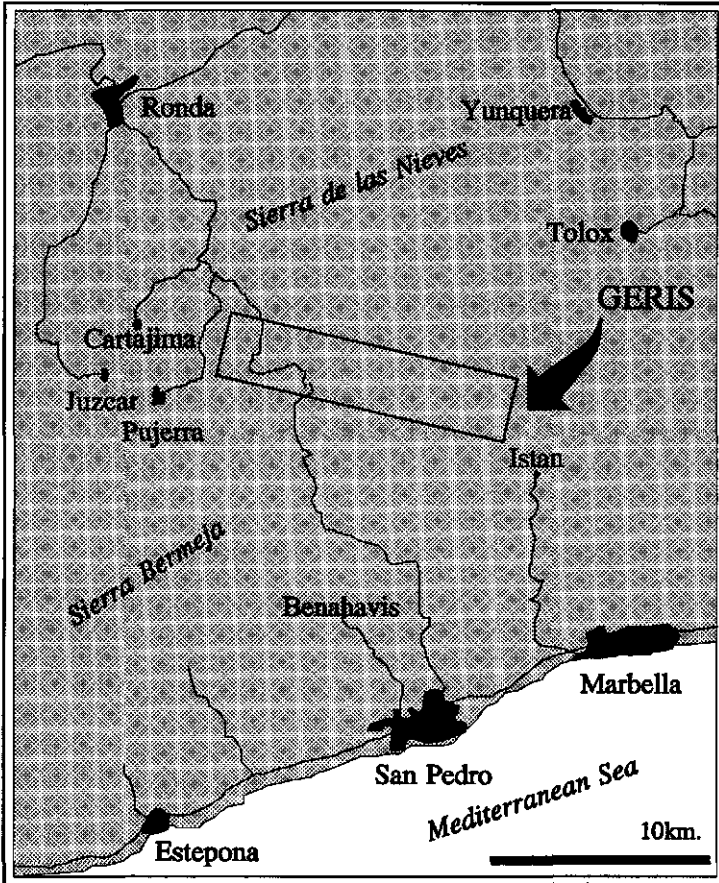


Fig. 7.3: Location of the GERIS data strip.

### 7.2.3 Imaging spectrometer data sets used

Throughout this thesis, two imaging spectrometer data sets are used: (1) the AVIRIS Cuprite Mining District data set, and (2) the GERIS Istán-Iqualeja data set.

The area of study, the Cuprite mining district (Fig. 7.1) is situated in western Nevada some 30km. south of Goldfield, and contains both hydrothermally altered and unaltered rocks. The eastern half of the district, which is discussed in this thesis, is an area of extensive hydrothermal alteration within a sequence of rhyolitic welded ash flow and air fall tuffs (Albers & Stewart, 1972). These altered rocks can be subdivided into three mappable units: silicified rocks, opalized rocks, and argillized rocks. Silicified rocks, containing abundant hydrothermal quartz, form a large irregular patch extending from the middle to the south end of the area. Opalized rocks contain abundant opal and as much as 30% Alunite and Kaolinite.

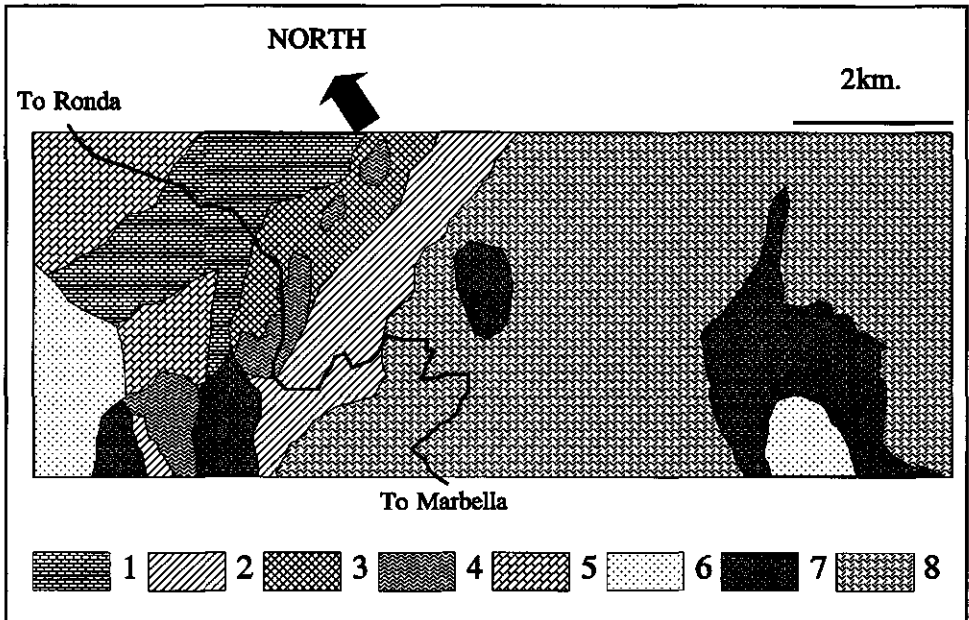


Fig. 7.4: Generalized lithologic map of the strip covered by the GER Imaging Spectrometer (1 = lime-breccia, 2 = marble, 3 = bedded limestone, 4 = massive limestone, 5 = dolomite, 6 = schist, 7 = gneiss, 8 = peridotite/serpentine; after: IGME, 1972).

Locally, an interval of soft, poorly exposed material mapped as argillized rock separates fresh rock from opalized rock. In the argillized rocks, plagioclase is altered to Kaolinite, and glass is altered to opal and varying amounts of montmorillonite and Kaolinite. The distribution of these alteration assemblages is characteristic for a fossilized hot-spring deposit (e.g., Buchanan, 1981) which often contain gold. The general geology of the Cuprite mining district is treated in more detail in Abrams *et al.* (1977). The AVIRIS data (see Fig. 7.2) used in this study were acquired on 29 september 1989 at 11:25 AM (local time).

The GERIS data from southern Spain were flown on october, 7, 1991 covering a strip stretching from the village of Istán in the southeast to the village of Igualaja in the northwest (Fig. 7.3). In the southeastern most part the data cover the marbles of the Blanca unit and the gneisses and schists of the Alpujarride nappe complex. Progressing towards the northwest, the Ronda peridotites and part of the schist and granitoid gneiss sequence of the Alpujarride nappe complex are covered. The contact between the peridotites and the marble-bedded and crystalline limestone-dolomite-lime breccia of the Nieves unit is seen in the northwestern most part of the scene. A small part of the garnet gneiss-schist-phyllite series of the Alpujarride nappe complex is covered which is exposed just south of the village of Igualaja (Fig. 7.4).

In total, the data set has 512 pixels along track over a flight-line of 2400 pixels amounting to an area of approximately 5 by 25 kilometres.

The AVIRIS Cuprite Mining District data set has been extensively studied by many authors (e.g. Hook *et al.*, 1991; Rast *et al.*, 1991), and many articles have been published on the use of remote sensing in the Cuprite Mining district by means of other image data types (e.g., Kruse *et al.* 1990; Okada & Iwashita, 1992; Kahle & Goetz, 1983). Since both the geology and the spectral signature of rocks in the Cuprite mining district have been characterized in detail, throughout this thesis the AVIRIS Cuprite Mining District data set is used mainly for testing of atmospheric calibration techniques and other pre-processing techniques and for the evaluation of newly developed algorithms for mineral mapping. These can then be applied to the GERIS data set from southern Spain which has not been reported in the literature.

### 7.3 ESTIMATION OF SIGNAL-TO-NOISE RATIO

Signal in imaging spectrometry is considered to be the quantity measured by an imaging spectrometer sensor, whereas noise describes the random variability of the signal. The quantification of the noise level alone is not a very useful measure for the quality of a imaging spectrometer data set since the effect is more severe when signal is low. Therefore, in most studies the signal-to-noise ratio is used estimated as the ratio of the signal's mean to its standard deviation.

Imaging spectrometer data sets contain both periodic (coherent) sensor noise that can be removed and random noise that cannot. The signal-to-noise calculation is done on data sets with periodic noise removed. Curran & Dungan (1989) used a notch filter on fast-fourier transformed data for this purpose. The remaining random noise can be additive noise, which is independent of the signal, and multiplicative noise which is proportional to the signal. The major part of the noise in imaging spectrometer data sets is additive and decreases sharply with both an increase in wavelength and atmospheric absorption. This random noise component consists of random sensor noise (which is image independent), intra-pixel variability (resulting from spatially heterogeneous pixel contents), and interpixel variability.

Several methods have been proposed to estimate the signal-to-noise ratio of imaging spectrometer data sets which can be separated into three classes: "laboratory methods", "dark current methods", and "image methods". A typical "laboratory method" uses the signal's mean ( $\bar{z}$ ) and its standard deviation ( $s$ ) of a bright surface to estimate the signal-to-noise ratio for a few spectral bands (Vane *et al.*, 1988). The estimated signal-to-noise ratio is in most cases too high since a very bright target is used. A typical "dark current method" uses variation in

the signal dark currents as a measure of noise (Carrere & Abrams, 1988; Green *et al.*, 1988; Green, 1992). One simple "image method" for estimating the signal-to-noise ratio of an image is to find a homogeneous area within the scene and compute the signal mean,  $z$ , and its standard deviation,  $s$ . The ratio of the mean to the standard deviation gives an estimate for the signal-to-noise ratio of the image (Fujimoto *et al.*, 1989; Duggin *et al.*, 1985). The method in most cases underestimates the signal-to-noise ratio since interpixel variability contributes to the noise component,  $s$ , thus suppressing the signal-to-noise ratio. Another shortcoming of the approach is the difficulty in finding an homogeneous area which is representative for the entire image. Lee & Hoppel (1989) developed a method for automatic estimation of signal-to-noise ratios for imaging spectrometer data. According to their method, the image is divided into small 4x4 or 8x8 pixel blocks and the signal's mean and standard deviation is calculated for each block. From this, a scatter plot is constructed plotting the squares of the means versus the variances defining a straight line representing the noise characteristics of the image. Meer *et al.* (1990) developed a parallel algorithm which allows to separate additive noise from multiplicative noise.

In this section, I will concentrate on three methods which will be referred to as the "homogeneous area method" (Fujimoto *et al.*, 1989), the "local means and local variances method" (Gao, 1993) and the "geostatistical method" (Curran & Dungan, 1989). The "homogeneous area method" has been outlined earlier. The two other methods will be outlined below.

### 7.3.1 The "local means and local variances method"

The "local means and local variances method" developed by Gao (1993) builds on the concept of Lee & Hoppel (1989) dividing an image into small blocks and computing local means and variances. An image is divided into small blocks of 4x4, 5x5, ..., 8x8 pixels. For each block, a local mean (denoted LM by Gao, 1993) is calculated according to

$$LM = \frac{1}{N} \sum_{i=1}^{i=N} S_i \quad (1)$$

where  $S_i$  is the signal value of the  $i$ th pixel in the block and  $N$  is the total number of pixels in the block. The local standard deviation (LSD) is calculated as

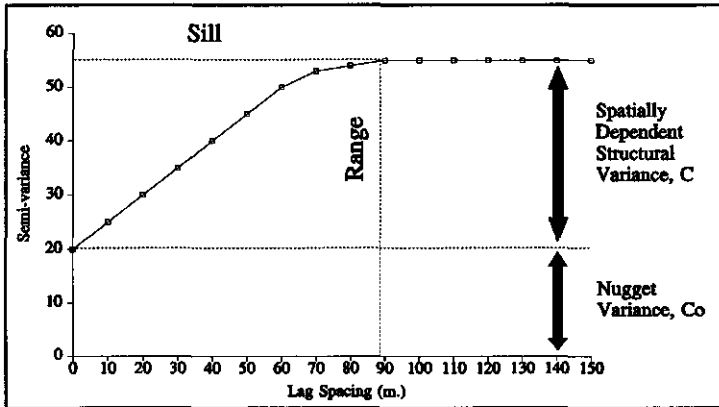


Fig. 7.5: Definition of variogram parameters.

$$LSD = \left[ \frac{1}{(N - 1)} \sum_{i=1}^{i=N} (S_i - LM)^2 \right]^{1/2} \quad (2)$$

Homogeneous blocks have small LSD values and therefore provide information on the noise of the image, while inhomogeneous blocks, such as those containing edges have large LSD values. The distribution of the LSD values is used to characterize the random noise. Gao (1993) proposes to set-up a number of classes of LSD values between the minimum and maximum values occurring. The LSD value corresponding to the most frequent class (e.g. that class containing most of the blocks) is the mean noise. The signal-to-noise ratio is found as the ratio of mean signal (i.e. the mean of the LM values found in Eq(1)) and the mean noise.

### 7.3.2 The "geostatistical method"

The "geostatistical method" proposed by Curran & Dungan (1989) allows to calculate the signal-to-noise ratio of a imaging spectrometer data set free of interpixel variability. The intrapixel variability and the random sensor noise are estimated using the semi-variogram produced from a transect of pixels. The semi-variogram,  $\gamma(h)$ , defines the variances of the differences between pairs of pixel signals,  $z(x_i) - z(x_i + h)$ , a distance  $h$  apart and can be estimated by



$$\gamma(h) = \frac{1}{2n} \sum_{i=1}^n [z(x_i) - z(x_i + h)]^2 \quad (3)$$

where  $n$  is the number of pairs of points used to calculate the lag  $h$ . The semi-variogram is characterized by three parameters: the range, the sill, and the nugget component (Fig. 7.5). The sill is the asymptotic upper bound value of  $\gamma(h)$  which is often equal to the variance of the data set. The range is the distance or lag-spacing at which the sill is reached defining the degree of spatial correlation of the data set. The nugget component is the non-zero y-intercept of the semi-variogram implying that measuring a point twice would yield different results. This variance does not have a spatial component and is composed almost entirely of random sensor noise. Curran & Dungan (1989) propose that the signal-to-noise ratio (SNR) is estimated from the signal's mean,  $z$ , and the nugget component  $C_0$  by

$$\text{SNR} = z / \sqrt{C_0} \quad (4)$$

Difficulties with the "geostatistical method" are the estimation of the nugget component from the variograms since the semi-variogram itself at a lag of 0 pixels is not defined. Furthermore, data sets are seldom isotropic and anisotropy may result in direction-dependent nugget components.

### 7.3.3 Results

Calculated signal-to-noise ratio's for the AVIRIS Cuprite data set are shown in Fig. 7.6 and Table 7.4. These show that the computed noise values for the "homogeneous area method" are slightly higher than those for the "local mean and standard deviation method". These two methods give values from 15:1 to 75:1 for spectrometer A, 25:1 to 125:1 for spectrometer B, 1:1 to 23:1 for spectrometer C, and 1:1 to 8:1 for spectrometer D. On the average, signal-to-noise ratio's for 30:1, 50:1, 15:1, and 10:1 are measured for spectrometers A-D respectively, which are in good agreement with results presented by Carrere & Abrams (1988). The "geostatistical method" produces in general higher signal-to-noise ratio's due to a lower estimate of the noise. The signal-to-noise values seem to correlate better with the range of wavelengths covered by the individual AVIRIS spectrometer. Gao (1993) presented signal-to-noise ratio's calculated using the "local mean and standard deviation method" for GERIS data from the Cuprite mining area. The signal-to-noise ratio's in the 0.5 and 0.95 $\mu$ m wavelength range are between 45:1 and 70:1, the few broad channels between 1.0 and 1.3 $\mu$ m show values

*- Atmospheric calibration -*

**Table 7.4:** Statistics of differences between noise and signal-to-noise ratio's estimated using the "homogeneous area method", and the "local mean and standard deviation method" and the "geostatistical method" (e.g.  $\text{snr}(\text{homogeneous area method}) - \text{snr}(\text{geostatistical method})$ ) for the AVIRIS Curpita data set.

	"local mean and standard deviation"		"geostatistical method"	
	noise	snr	noise	snr
mean	6.24	-7.39	8.97	-8.94
variance	33.62	88.74	154.86	180.25
std. dev.	5.79	9.42	12.44	13.43
skewness	2.75	-1.23	3.75	0.695
kurtosis	13.81	10.10	21.85	9.11
minimum	-3.0	-64.82	-18.0	-43.65
25%	+3.6	-10.27	+4.0	-14.87
median	+4.9	-3.71	+7.0	-5.21
75%	+7.0	-1.13	+10.1	-1.75
maximum	+40.0	+5.46	+99.04	+57.46

**Table 7.5:** Statistics of differences between noise and signal-to-noise ratio's estimated using the "homogeneous area method", and the "local mean and standard deviation method" and the "geostatistical method" (e.g.  $\text{snr}(\text{homogeneous area method}) - \text{snr}(\text{geostatistical method})$ ) for the GERIS dataset of southern Spain.

	"local mean and standard deviation"		"geostatistical method"	
	noise	snr	noise	snr
mean	10.12	-5.97	20.55	-23.83
variance	85.19	98.29	358.14	336.32
std. dev.	9.23	9.91	18.92	18.34
skewness	0.60	0.32	1.09	-0.25
kurtosis	4.53	3.75	4.72	5.15
minimum	-11.0	-27.05	-11.0	-82.26
25%	+5.0	-11.44	+7.0	-31.39
median	+8.2	-6.0	+19.0	-25.32
75%	+15.0	-0.38	+27.55	-12.22
maximum	+38.0	+23.39	+82.0	+34.74

of less than 5:1, and the signal-to-noise ratio's in the 2.0-2.5 $\mu$ m wavelength range are typically 25:1 to 35:1. Clearly, the signal-to-noise ratio's in the 2.0-2.5 $\mu$ m, which is a very important region for geological mapping, are significantly higher than those produced by AVIRIS over the same area. The results of calculating the signal-to-noise ratio for the GER data set over the Istan-Cartajima area of southern Spain are shown in Fig. 7.7 and Table 7.5. The "homogeneous area method" and the "local mean and standard deviation method" produce similar results, however the signal-to-noise ratio's calculated from the "homogeneous area method" are higher than those from the "local mean and standard deviation method". The "geostatistical method" again shows a different result from the other two methods.

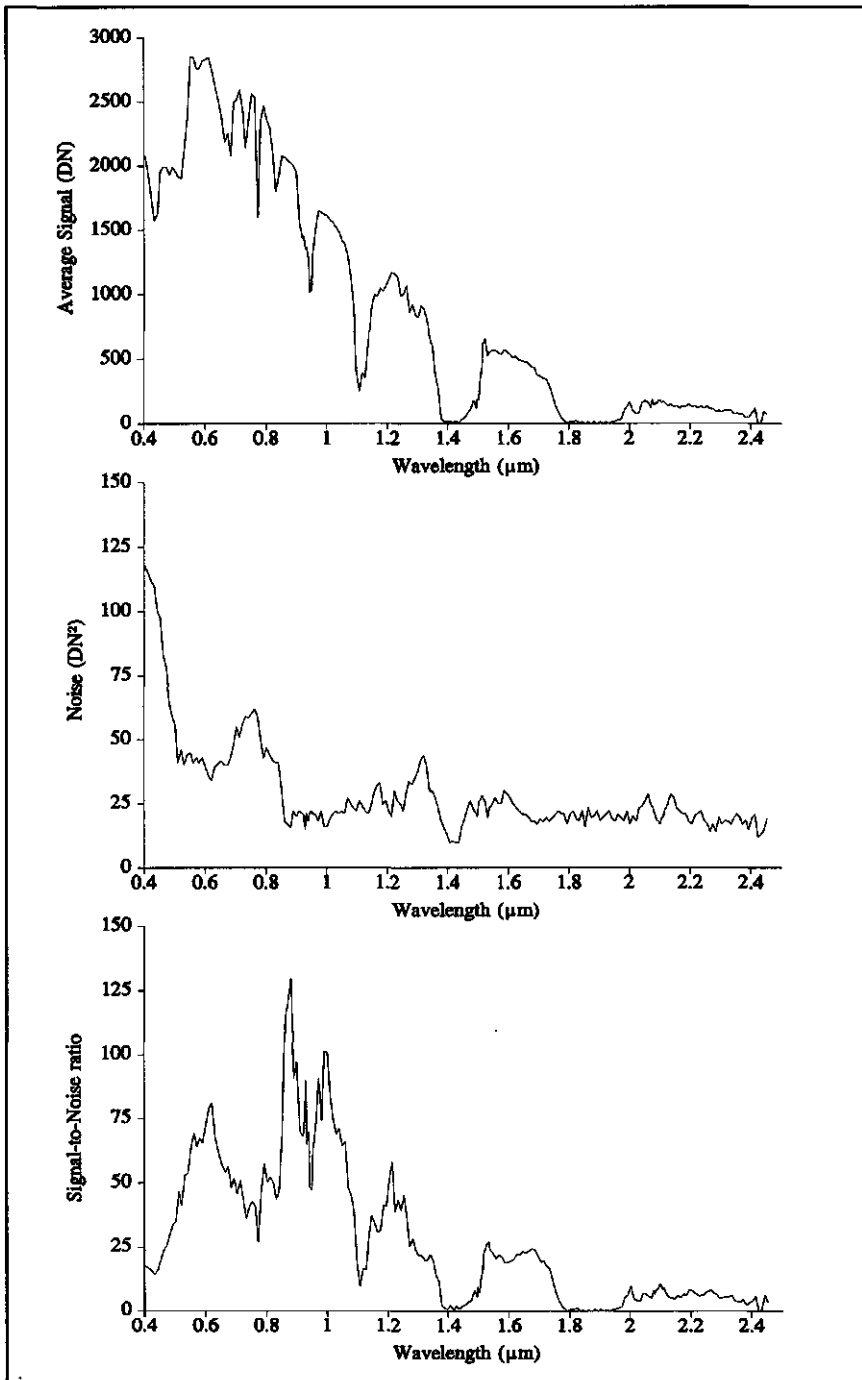
---

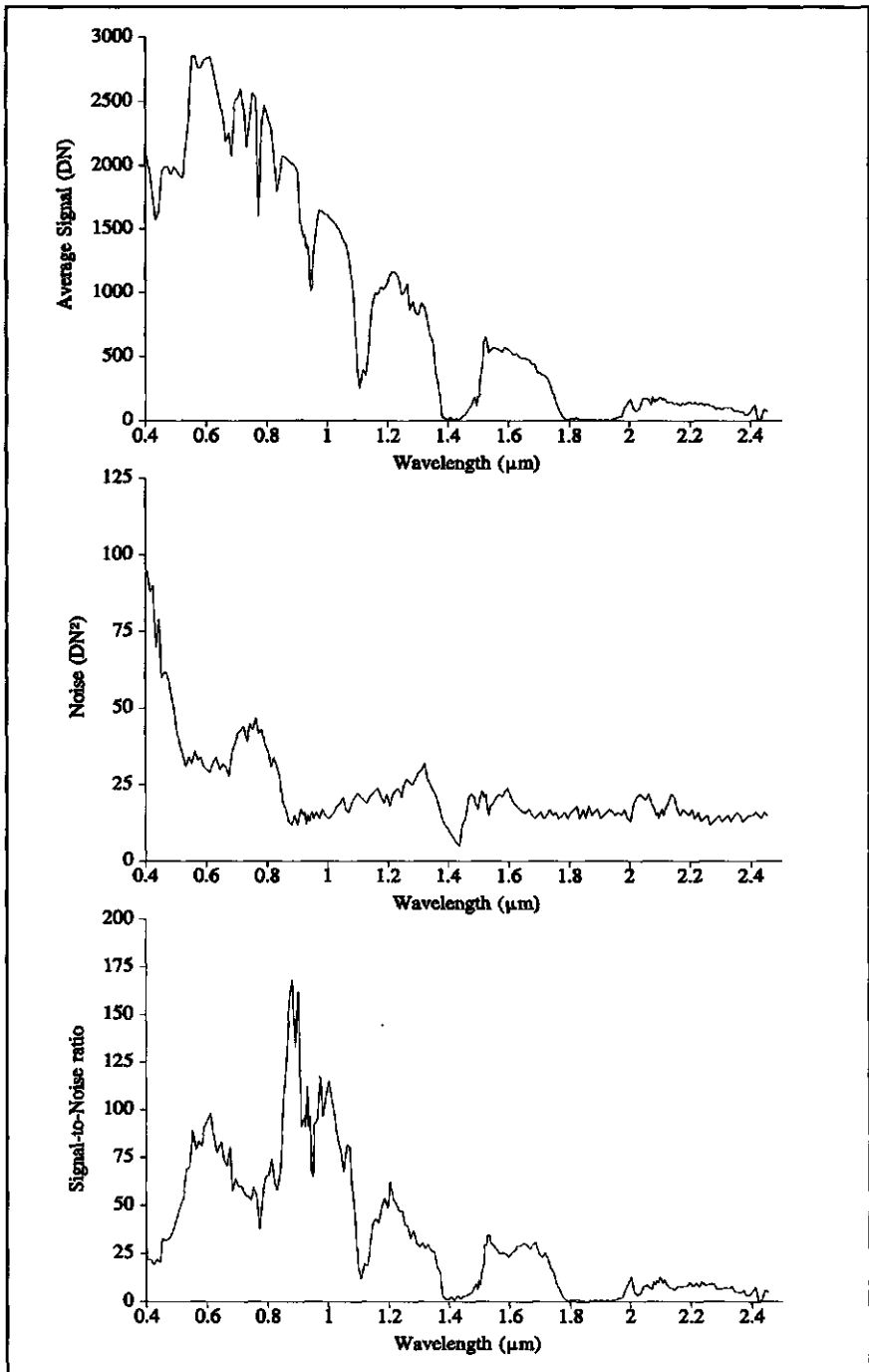
On page 173 to 178 Figs. 7.6 and 7.7 are displayed:

*Fig. 7.6: Average signal, noise, and signal-to-noise ratio calculated through (A) the "homogenous area method"(page 173), (B) the "local mean and standard deviation method" (page 174), and (C) the "geostatistical method" (page 175) for AVIRIS data from the Cuprite Mining area.*

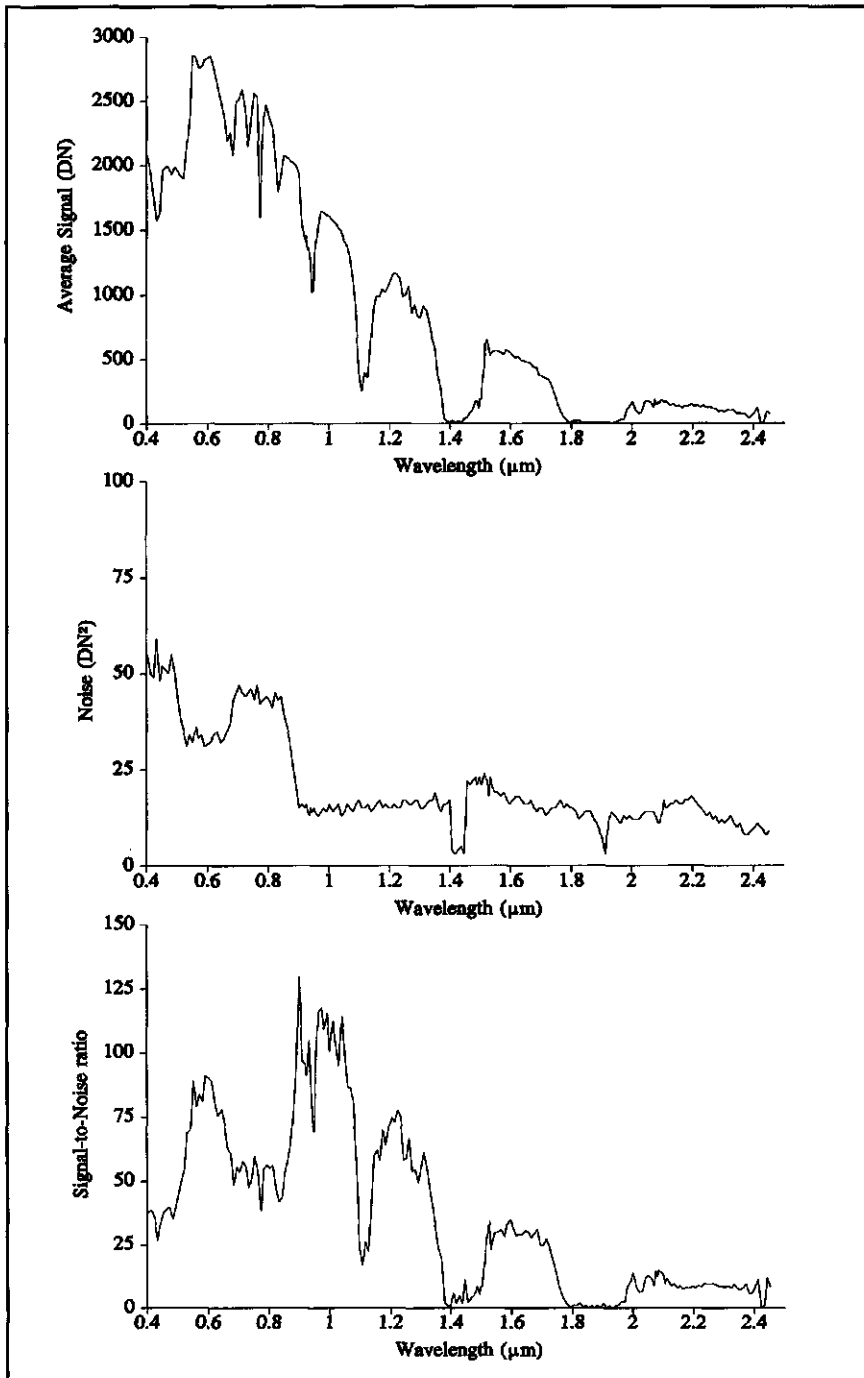
*Fig. 7.7: Average signal, noise, and signal-to-noise ratio calculated through (A) the "homogenous area method" (page 176), (B) the "local mean and standard deviation method" (page 177), and (C) the "geostatistical method" (page 178) for GERIS data from southern Spain.*

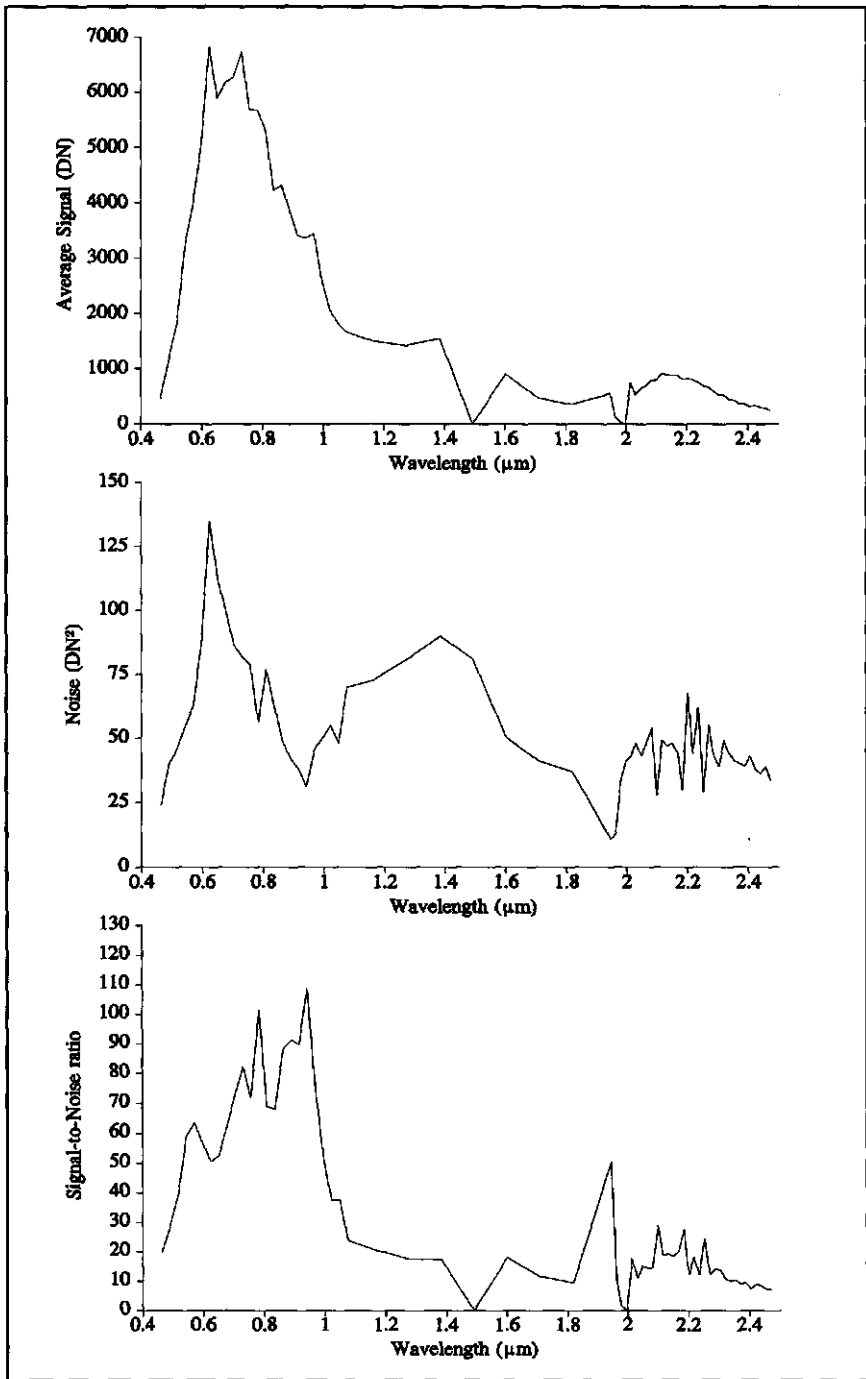
- Atmospheric calibration -



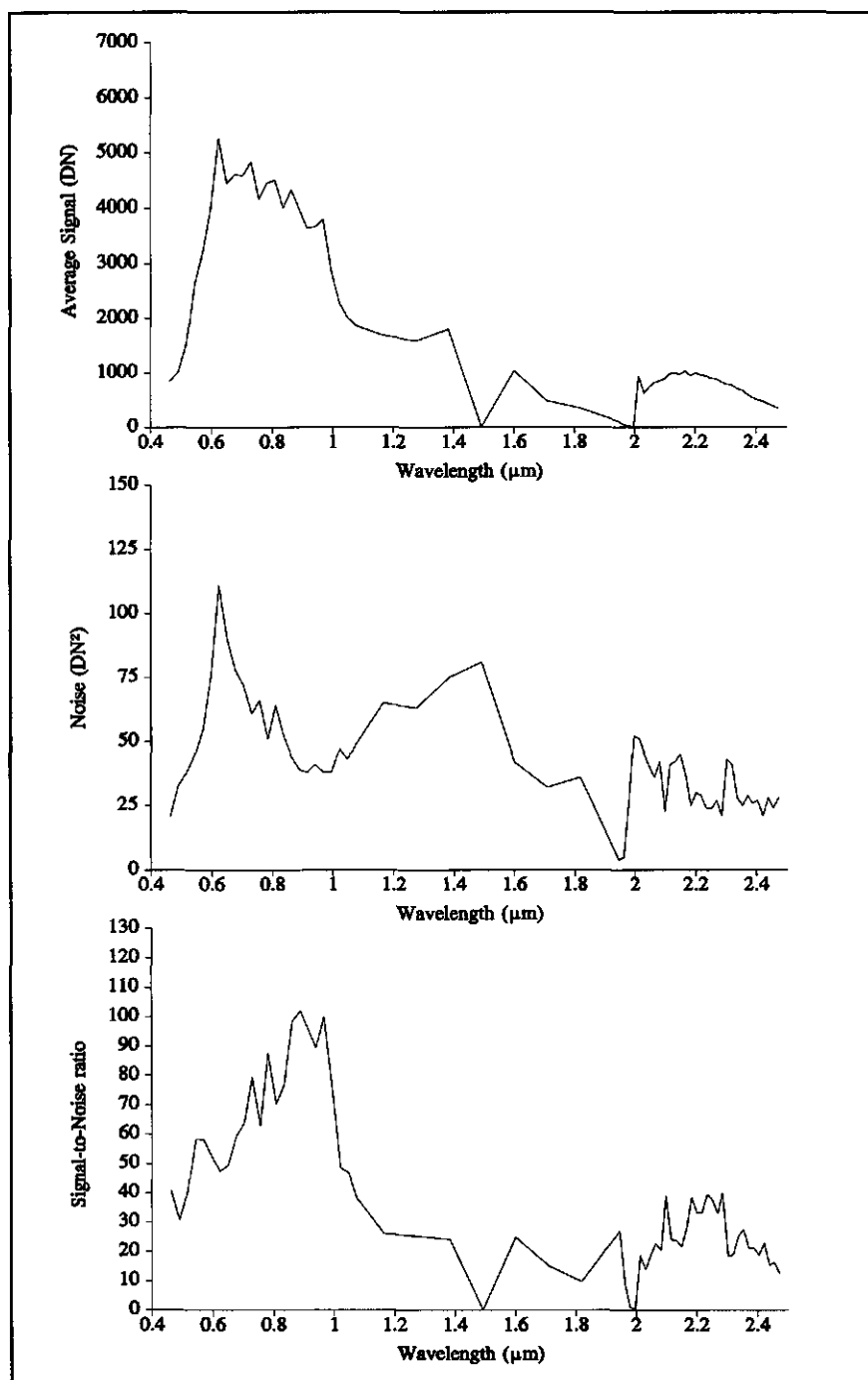


- Atmospheric calibration -



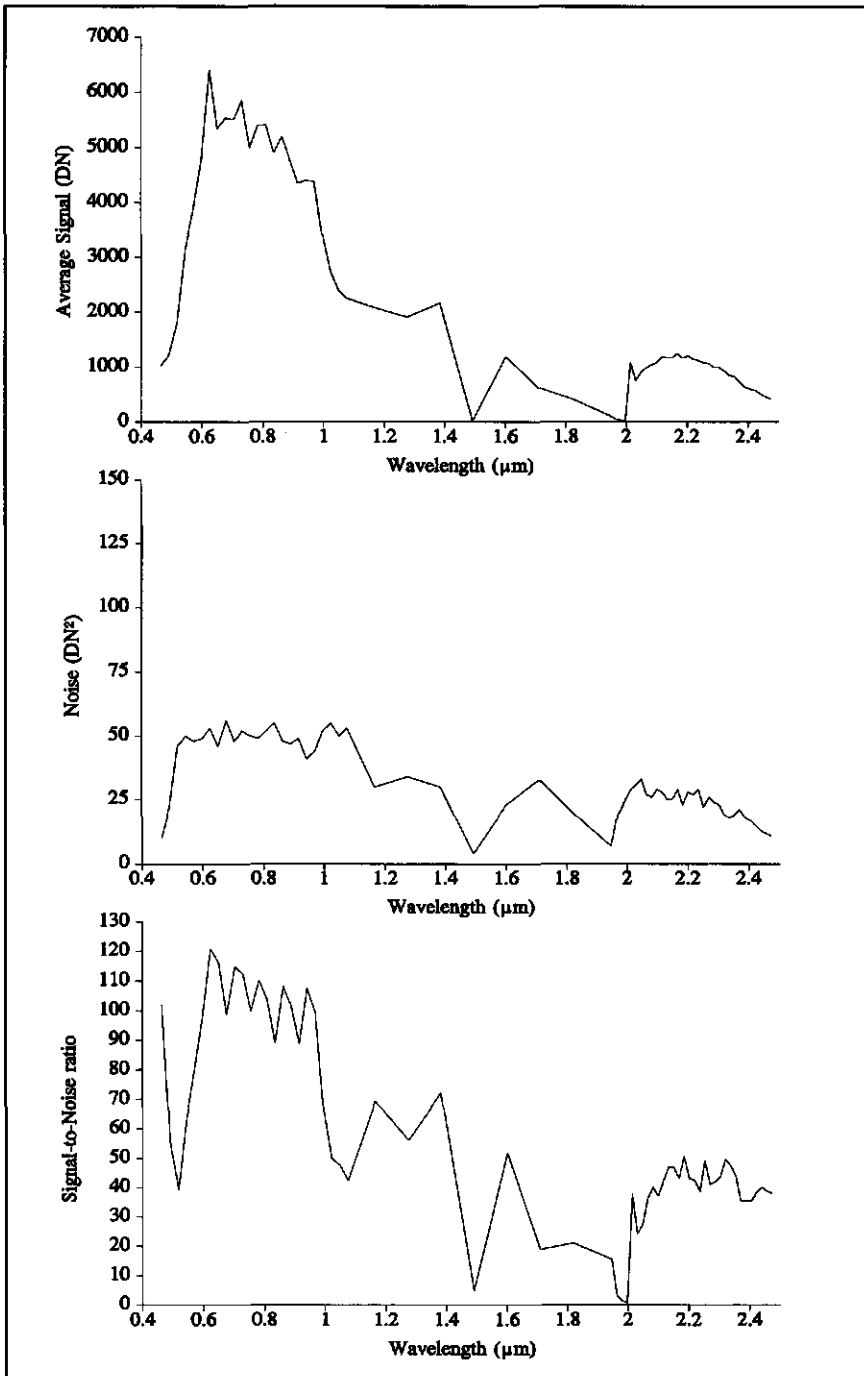


- Atmospheric calibration -





- Chapter 7 -



## 7.4 WAVELENGTH CALIBRATION

The AVIRIS data from the Cuprite Mining District used in this study was calibrated for wavelength shifts at the NASA Jet Propulsion Laboratory. Regular in-flight calibration experiments of AVIRIS data have shown that the channel positions in all four AVIRIS spectrometers closely agree with the corresponding parameters measured in the laboratory (Green, 1992b) or modelled using an advanced atmospheric model (Kneizys *et al.*, 1988).

Wavelength calibration of the southern Spain GERIS data was carried out by GER. An additional check on the wavelength calibration was made by comparing the positions of known atmospheric absorption features to their locations in "raw" GER pixel spectra following the procedure outlined by Kruse *et al.* (1990). Atmospheric carbon dioxide (CO<sub>2</sub>) absorption bands located at 2.005 $\mu$ m and 2.055 $\mu$ m were compared to their respective spectral position in a number of GER pixel spectra. The corresponding CO<sub>2</sub> absorption bands were observed at 2.0178 $\mu$ m and 2.0681 $\mu$ m, an offset of +0.0128 $\mu$ m and 0.0131 $\mu$ m, respectively, corresponding approximately to a one channel offset. Rubin (1993) found a similar one channel offset in GERIS data from the Yerington District, Nevada, Keirein-Young & Kruse (1989) and Kruse *et al.* (1990) found a similar one channel offset for GERIS data from the Cuprite Mining District. Accordingly, the wavelength positions were adjusted one channel in the last spectrometer to shift the CO<sub>2</sub> bands to their proper spectral positions. In the visible portion of the spectrum, the H<sub>2</sub>O absorption band centered at 0.94 $\mu$ m was used. Unfortunately, this band is much broader than the CO<sub>2</sub> absorption bands described above and could therefore not be exactly positioned. Since the location of the band did not deviate much from the predicted location, the GER band positions were used for spectrometers 1 and 2.

## 7.5 ATMOSPHERIC CALIBRATION TECHNIQUES

Raw imaging spectrometer data have the general appearance of the solar irradiance curve, with radiance decreasing towards longer wavelengths, and exhibit several absorption bands due to scattering and absorption by gasses in the atmosphere. The major atmospheric water vapour bands (H<sub>2</sub>O) are centered approximately at 0.94 $\mu$ m, 1.14 $\mu$ m, 1.38 $\mu$ m and 1.88 $\mu$ m, the oxygen (O<sub>2</sub>) band at 0.76 $\mu$ m, and carbon dioxide (CO<sub>2</sub>) bands near 2.01 $\mu$ m and 2.08 $\mu$ m. Additionally, other gasses including ozone (O<sub>3</sub>), carbon monoxide (CO), nitrous oxide (N<sub>2</sub>O), and methane (CH<sub>4</sub>), produce noticeable absorption features in the 0.4-2.5 $\mu$ m wavelength region.

The effect of atmospheric calibration algorithms is to re-scale the raw radiance data provided by imaging spectrometers to reflectance by correcting for atmospheric influence thus

shifting all spectra to nearly the same albedo. The result is a data set in which each pixel can be represented by a reflectance spectrum which can be directly compared to reflectance spectra of rocks and minerals acquired either in the field or in the laboratory. Techniques discussed here are the Flat-field correction, the Log-residual and Flat-field log-residual method, the Empirical Line Method, the Internal Average Relative Reflectance (IARR) Atmospheric correction technique, and the Atmospheric Removal Method (ATREM). The first three methods require pixel spectra for the calibration, whereas the other two rely on information derived solely from the data cube.

The pre-processing of the raw AVIRIS radiance data to produce the image product provided by NASA-JPL is described in Reimer *et al.* (1987) and Porter *et al.* (1990). Collins & Chang (1988) describe the pre-processing and in-flight calibration of the GERIS data set as is provided to the investigator.

### 7.5.1 the Flat-field correction

The purpose of the flat-field correction is to reduce the atmospheric influence in the raw imaging spectrometer data and eliminate the solar irradiance drop-off, as well as any residual instrument effects. This is achieved by dividing the whole data set by the mean value of an area within the scene which is spectrally and morphologically flat, and spectrally homogeneous. The flat-field chosen should have a high albedo to avoid decreasing the signal-to-noise ratio. This can also be achieved by increasing the number of pixel spectra used to produce the flat-field spectrum. In order to select properly an flat-field target area, ground truth data is necessary to ensure that the calibration target is indeed spectrally flat. In that case, the flat-field method removes the solar irradiance curve and major gaseous absorption features as well as system induced defects.

### 7.5.2 the Log-residual and Flat-field log-residual method

The Log-residual correction was developed by Green & Graig (1985) and modified by Lyon & Lanz (1985) in order to remove the solar irradiance drop-off, atmospheric effects, and topographic effects in the raw imaging spectrometer data set. In their approach, radiance measured by the sensor,  $L_{i\lambda}$ , is related to the corrected reflectance,  $R_{i\lambda}$ , in pixel  $i$  at wavelength  $\lambda$  as:

$$L_{i\lambda} = T_i R_{i\lambda} I_\lambda \quad (5)$$

where  $T_i$  is the topographic factor which is a constant factor for all wavelengths which varies with slope angle and orientation thus accounting for the brightness variations due to differences in angle and orientation of the topography. The illumination factor,  $I_\lambda$ , describes the solar irradiance curve and is constant for pixels at a given wavelength. The log-residual equation is given by Green & Graig (1985) as:

$$\log(\text{RES}_{ij}) = \log(\text{DN}_{ij}) - \log(\text{aveDN}_i) - \log(\text{aveDN}_j) + \log(\text{DN}_g) \quad (6)$$

where  $\text{RES}_{ij}$  is the residual value for pixel  $i$  and channel  $j$ ,  $\text{DN}_{ij}$  is the value of input pixel for pixel  $i$  and channel  $j$ ,  $\text{aveDN}_i$  is the average value of all channels for pixel  $i$ ,  $\text{aveDN}_j$  is the average value for all pixels for channel  $j$ , and  $\text{DN}_g$  is the global average of all pixels for all channels. Intrinsically this correction does not require ground truth knowledge. However, as can be seen from the above equation, log residual spectra are affected by the mean values of the scene. Thus if minerals with strong absorption features are present, the averages will reflect these features thus obscuring absorption bands after calibration or introducing artefacts such as small peaks on the corrected pixel spectra. To overcome this problem, the flat-field log-residual method was developed using average values from a spectrally flat portion of the scene in a similar fashion as the flat-field correction described earlier. The flat-field log-residual equation is given as (Hutsonpillier, 1988):

$$\log(\text{FFRes}_{ij}) = \log(\text{DN}_{ij}) - \log(\text{aveDN}_i) - \log(\text{aveDN}_{\text{FF}}) + \log(\text{DN}_{\text{FFg}}) \quad (7)$$

where  $\text{FFRes}_{ij}$  is the flat-field residual value for pixel  $i$  and channel  $j$ ,  $\text{aveDN}_{\text{FF}}$  the average value of all pixels in a spectrally flat area for channel  $j$ , and  $\text{DN}_{\text{FFg}}$  the global average of all pixels in the spectrally flat area for all channels.

### 7.5.3 the Empirical Line method

Conversion of raw imaging spectrometer data to reflectance data using the Empirical Line method (Kruse *et al.*, 1985; Kruse, 1988; Keirein-Young & Kruse, 1989; Kruse *et al.*, 1990) requires the selection and spectral characterization of two calibration targets (Roberts *et al.*, 1985), thus assuming a priori knowledge of each site. This empirical correction uses a constant gain and offset for each band to force a best fit between sets of field spectra and image spectra characterizing the same ground areas thus removing atmospheric effects, residual instrument artifacts, and viewing geometry effects. The correction requires four basic steps (Kruse *et al.*, 1990):

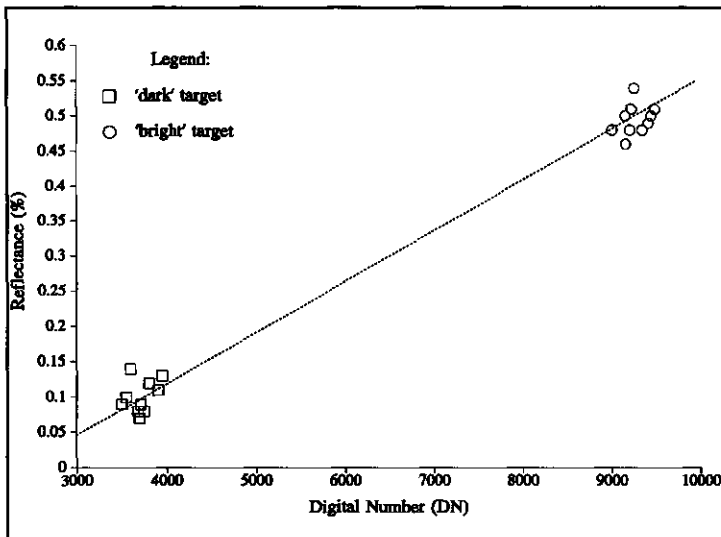


Fig. 7.8: Derivation of gain and offset values (after: Keirein-Young & Kruse, 1989, their Figure 4). The DN values extracted from image pixels are plotted against the corresponding field reflectance values for the two calibration targets at a certain wavelength channel. By means of least square fitting of a best-fit line the offset and gain value are found to be -0.24 and 0.000082, respectively. The reflectance for all image pixels in the channel is given by the relation,  $\text{Reflectance} = -0.24 + 0.000082(\text{DN})$ .

- 1) The first step is the choosing of two ground target regions of a wide albedo range (e.g., a dark and a bright target) and acquiring field spectra characterizing these targets.
- 2) Next, multiple pixels are selected that are associated with each of the two ground targets.
- 3) Then, an over determined system of linear equations may be constructed for each band in which the number of unknowns is two, the gain and offset values, and the number of knowns is equal to the total number of image pixels chosen. Solving these equations by means of least squares fitting provides gain and offset spectra and a standard error for these values for each parameter at each wavelength (Fig. 7.8). The gain spectrum is an inverse solar irradiance curve, whereas the offset spectrum is a negative correction factor that increases with wavelength.
- 4) The final step, the actual calibration of the data, is a multiplication of the instrument DN values by the proper gain factor adding corresponding offset value.

#### 7.5.4 the Internal Average Relative Reflectance (IARR) Atmospheric correction technique

The Internal Average Relative Reflectance (IARR) correction method (Kruse *et al.*, 1985; Kruse, 1988, Ben-Dor & Kruse, 1994) allows the calibration of raw imaging spectrometer data to reflectance data when no calibration information is available. This procedure uses an 'Average Reference Spectrum' (ARS) calculated as the average pixel spectrum of the entire scene. This spectrum is divided into each image radiance spectrum to produce a relative reflectance spectrum for each pixel. Care should be taken when cover types with strong absorption features are present in the scene. In such a case the IARR correction method may cause artifacts which may be wrongly interpreted as being spectral features.

#### 7.5.5 the Atmospheric Removal Method (ATREM)

As described earlier, seven gasses (e.g., atmospheric water vapour bands ( $H_2O$ ), oxygen ( $O_2$ ), carbon dioxide ( $CO_2$ ), ozone ( $O_3$ ), carbon monoxide ( $CO$ ), nitrous oxide ( $N_2O$ ), and methane ( $CH_4$ ), produce noticeable absorption features in the 0.4-2.5 $\mu m$  wavelength region of the spectrum. Additionally, atmospheric molecules and aerosols scatter solar radiation. The atmospheric removal method (ATREM) described by Gao *et al.* (1993) is a method for deriving surface reflectances from radiance data based on radiative transfer removing water vapour absorption features on a pixel by pixel basis and modelling scattering effects with the 5S radiative transfer code.

In the radiative transfer code called Simulation of the Satellite Signal in Solar Spectrum (5S) developed by Tanré *et al.* (1986), apparent reflectance,  $\rho^*(\theta_s, \phi_s, \theta_v, \phi_v, \lambda)$ , is defined as:

$$\rho^*(\theta_s, \phi_s, \theta_v, \phi_v, \lambda) = \frac{\pi L(\theta_s, \phi_s, \theta_v, \phi_v, \lambda)}{\mu_s E_s(\lambda)} \quad (8)$$

where  $\theta_s$  is the solar zenith angle,  $\phi_s$  is the solar azimuth angle,  $\theta_v$  is the sensor zenith angle,  $\phi_v$  is the sensor azimuth angle,  $\lambda$  is the wavelength,  $L$  is the radiance measured at the satellite,  $E_s$  is the solar flux measured at the top of the atmosphere, and  $\mu_s = \cos(\theta_s)$ . According to Tanré *et al.* (1986), for a horizontal surface of uniform Lambertian reflectance,  $\rho^*(\theta_s, \phi_s, \theta_v, \phi_v, \lambda)$  can be rewritten as:

$$\rho^*(\theta_s, \varphi_s, \theta_v, \varphi_v, \lambda) = \frac{T_g(\theta_s, \theta_v, \lambda) \{ \rho_a(\theta_s, \varphi_s, \theta_v, \varphi_v, \lambda) + \frac{T(\theta_s, \lambda)T(\theta_v, \lambda)\rho(\lambda)}{1 - \rho(\lambda)S(\lambda)} \}}{T_g(\theta_s, \theta_v, \lambda)} \quad (9)$$

where  $T_g$  is the total gaseous transmittance in the Sun-surface-sensor path,  $\rho_a$  is the atmospheric reflectance related to the path radiance resulting from atmospheric scattering,  $T(\theta_s)$  is the downward scattering transmittance,  $T(\theta_v)$  is the upward scattering transmittance,  $S$  is the spherical albedo of the atmosphere, and  $\rho$  is the surface reflectance.  $T_g$  is expressed as:

$$T_g(\theta_s, \theta_v, \lambda) = \prod_{i=1}^n T_{gi}(\theta_s, \theta_v, \lambda) \quad (10)$$

where  $T_{gi}$  is the transmittance of the  $i$ th gas in the Sun-surface-sensor path and  $n$  is the number of gasses assuming no atmospheric scattering.

The scattering terms,  $\rho_s$ ,  $T(\theta_s)$ ,  $T(\theta_v)$ , and  $S$  are calculated by assuming no atmospheric gaseous absorptions, and the expression for  $T_g(\theta_s, \theta_v, \lambda)$  only holds when there are no overlapping absorption with different gasses. Gao *et al.* (1993) give a modification of the 5S code for retrieving surface reflectance instead of simulated radiance values. Following Teillet (1989),  $\rho$  can be solved as:

$$\rho(\lambda) = \frac{\rho^*(\theta_s, \varphi_s, \theta_v, \lambda)}{T_g(\theta_s, \theta_v, \lambda)} - \rho_a(\theta_s, \varphi_s, \theta_v, \varphi_v, \lambda) \quad (11)$$

$$X \{ T(\theta_s, \lambda)T(\theta_v, \lambda) + S(\lambda) [ \frac{\rho^*(\theta_s, \varphi_s, \theta_v, \lambda)}{T_g(\theta_s, \theta_v, \lambda)} - \rho_a(\theta_s, \varphi_s, \theta_v, \varphi_v, \lambda) ] \}^{-1}$$

Gao *et al.* (1993) use a three-channel ratioing technique to derive the water vapour values from an AVIRIS pixel spectrum. Subsequent calibration of raw imaging spectrometer data to reflectance using ATREM requires six basic steps (Gao *et al.*, 1993):

- 1) Derivation of the solar zenith angle based on time of acquisition of the data.

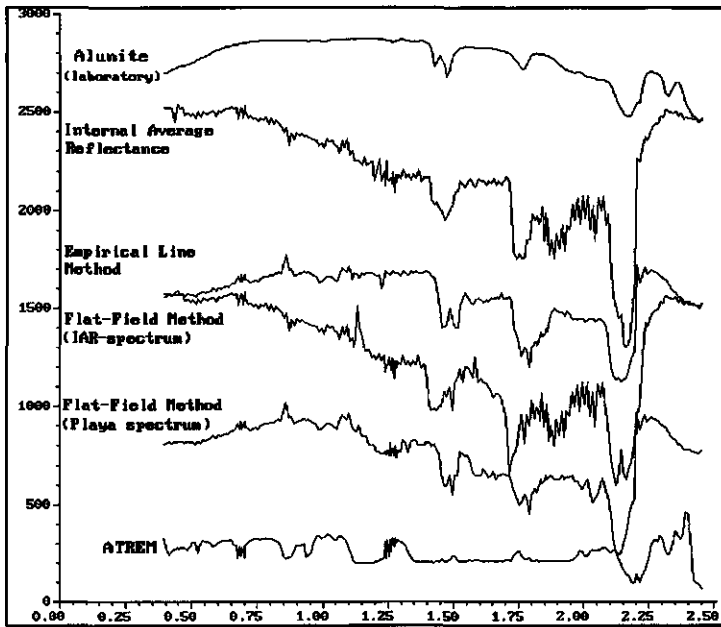


Fig. 7.9: Example of un-smoothed Alunite three-by-three pixel averaged spectra extracted from the calibrated AVIRIS data cube (see Fig. 7.2 for location) using IAR calibration, Flat-Field correction, Empirical Line Method, and ATREM. Spectra are offset vertically for clarity.

- 2) Calculation of the total atmospheric transmittance spectra,  $T_g$ , from the transmittance spectra of individual gasses. Transmittance spectra of  $O_2$ ,  $CO_2$ ,  $O_3$ ,  $CO$ ,  $N_2O$ ,  $CH_4$ , are based on solar and observational geometries and calculated using the Malkmus (1967) spectral model.
- 3) The scattering terms, albedo, and atmospheric reflectance (e.g.,  $\rho_a$ ,  $S$ ,  $T(\theta_s)$ ,  $T(\theta_v)$ ), are derived from the 5S radiative transfer model.
- 4) The AVIRIS pixel spectra are divided by the solar irradiance curve above the atmosphere (Kneizys *et al.*, 1988) to obtain apparent reflectance spectrum  $\rho^*(\theta_s, \phi_s, \theta_v, \phi_v, \lambda)$ .
- 5) Water vapour amounts for the  $0.94\mu m$  and  $1.14\mu m$  bands are calculated by means of the three-channel ratioing approach using the apparent reflectance spectrum.
- 6) Finally, the surface reflectance is derived from Eq.(11).

### 7.5.6 Performance of Atmospheric Calibration techniques

In order to evaluate the results of different calibration techniques, three-by-three pixel spectra (Fig. 7.9) have been extracted from the normalized data cubes for areas with known occurrences of kaolinite, alunite and buddingtonite (location B, C, and D respectively in Fig. 7.2) in the AVIRIS Cuprite Mining District data set. Four atmospheric calibration techniques



- Chapter 7 -

Table 7.6: Input file for ATREM for the AVIRIS Cuprite Mining District data set.

Input	Comment
07 23 1990 20 58 32	Date (mm dd yyyy) and time (hh mm ss)
37 30 08	Latitude (deg min s)
N	Hemisphere (N or S)
117 13 17	Longitude (deg min s)
W	Hemisphere (E or W)
/tmp/AVIRIS.wav	Wavelength file
10.	Resolution of input spectra (nm)
1	Indicator whether the band ratio parameters are provided (0=no, 1=yes)
0.8630 1.0550 3 3 0.9298 7	Band ratio parameters for the first atmospheric window
1.0550 1.2470 3 3 1.1414 7	Band ratio parameters for the second atmospheric window
2	Atmospheric model number
1 1 1 1 1 1	Gas selectors (0=don't include, 1=include)
0.34	Total amount of ozone (cm)
1 100	Aerosol type and visibility (km)
1.5	Average elevation (km)
/tmp/AVIRIS.cub	Input AVIRIS cube
0	Indicator of whether the cube dimensions are provided (0=no, 1=yes)
/tmp/AVIRIS_atm.cub	Output file for atmospherically reduced cube
10.	Resolution of the output spectra (nm)
/tmp/AVIRIS.vap	Output file for water vapor images

were used: the Flat-field correction, the Empirical Line method, the Internal Average Relative Reflectance method, and the atmospheric removal method (ATREM). For the Flat-field method a five-by-five spectrum over the Stonewall playa area was used as the calibration target (Fig. 7.2). The Stonewall playa spectrum and a varnished tuff spectrum were used as bright and dark targets, respectively, to reduce the raw AVIRIS data to reflectance with the Empirical Line method (Fig. 7.2). Field spectra to characterize these targets were obtained from Kruse *et al.* (1990). Input parameters used in ATREM are shown in Table 7.6.

The true merits of the calibration techniques can be best evaluated in terms of the

- Atmospheric calibration -

**Table 7.7:** Overall removal characteristics of calibration techniques for the AVIRIS Cuprite Mining District data set.

processing technique	removal of solar irradiance	removal of atmospheric absorption	noise	artefacts	spectral interpretability
Flat-Field Method	good	moderate	high	numerous	good
Empirical Line Method	excellent	good	high/low	moderate	good
Internal Average Reflectance (IAR)	poor	poor	high	numerous	moderate
ATREM	excellent	poor	low	moderate	poor

noise which is suppressed and introduced after calibration, the number of processing artifacts introduced, normalization of the solar irradiance, removal of atmospheric absorption features, and spectral interpretability (Table 7.7). The noise has been qualitatively evaluated by inspecting the spectra and quantitatively evaluated by calculating the coefficient of variation (standard deviation divided by the mean of the reflectance values) of the spectra. Since all spectra represent spectra of the same mineral, the observed variation in the reflectance values is ideally to be the same. All additional variation can be directly attributed to noise and to absorption features not related to the spectral properties of the investigated mineral. Then, the effective signal-to-noise ration was approximated by ratioing the mean value of the pixel spectra DN values (defined as the reflectivity) and the standard deviation of the pixel spectra DN values (defined as the noise; see also Kaufmann *et al.*, 1991). Furthermore, laboratory

**Table 7.8:** Statistics for removal techniques for the AVIRIS Cuprite Mining District data set.

processing technique	alunite			Kaolinite			Buddingtonite		
	CV% <sup>1</sup>	Corr. <sup>2</sup>	Diff. <sup>3</sup>	CV% <sup>1</sup>	Corr. <sup>2</sup>	Diff. <sup>3</sup>	CV% <sup>1</sup>	Corr. <sup>2</sup>	Diff. <sup>3</sup>
Flat-field method	27	0.46	37	17	0.46	2	10	0.89	4
Empirical Line method	10	0.57	15	24	0.49	1	14	0.82	2
Internal Average reflectance (IAR)	15	0.30	114	13	0.21	59	8	0.13	34
ATREM	20	0.23	24	23	0.31	81	25	0.42	46

<sup>1</sup>CV% is the Coefficient of variation (C.V.) equal to the standard deviation divided by the mean of the pixel spectra DN values expressed in percent.

<sup>2</sup>Corr. is the correlation between the pixel and laboratory spectrum.

<sup>3</sup>Diff. is the mean absolute difference between the pixel and laboratory spectrum (in DN).

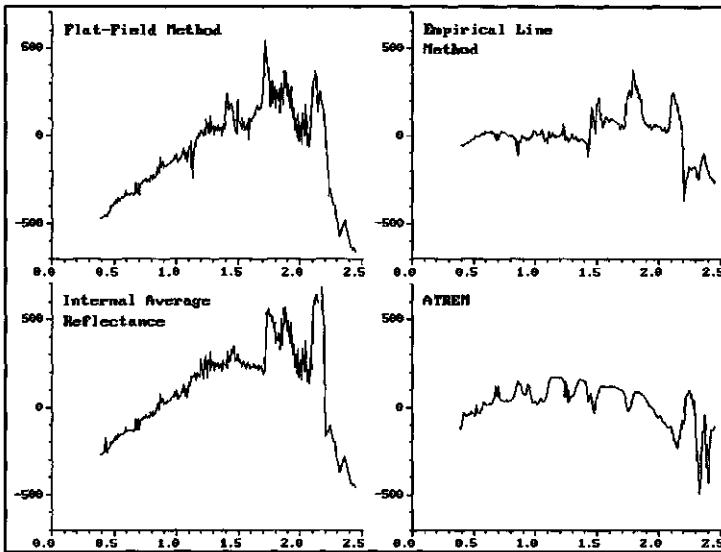


Fig. 7.10: Example of Alunite difference spectra calculated by subtracting the calibrated spectrum from the laboratory spectrum.

spectra were fitted onto the AVIRIS spectra and a difference spectrum (Fig. 7.10) was calculated by subtracting the laboratory spectrum from the pixel spectrum. In the ideal case, the difference spectrum should be zero over the entire wavelength region and the correlation should be equal to 1.0. The difference spectrum is very suitable in recognizing whether solar irradiance and atmospheric features are removed properly. If solar irradiance is not removed entirely, the difference spectrum will show a trend of decreasing values towards longer wavelengths. Atmospheric absorption features, not related to the mineral absorption features will produce positive bulges on the difference spectrum. In Table 7.8, the statistics are shown for the difference spectra calculated.

The IARR technique using the IAR spectrum for calibration performed moderately in removing atmospheric absorption features and removing the solar irradiance as can be seen from the difference spectrum. A severe amount of noise was introduced into the data, possibly related to the fact that the area has a wide variety in ground elevation or that the atmosphere has non-uniform conditions over the area in which circumstances the global average spectrum will not completely remove atmospheric effects (Kruse, 1988; p. 39).

The Flat-field correction and the empirical line method are more effective in removing both solar irradiance and atmospheric effects. The resulting spectra are very well interpretable. By increasing the number of spectra averaged to produce the calibration targets for both methods, the noise in the calibrated data cubes can be reduced. Some artifacts can be seen in the calibrated spectra which result from absorption features in the spectra obtained over the calibration areas. These calibration spectra should ideally be spectrally flat or have only minor

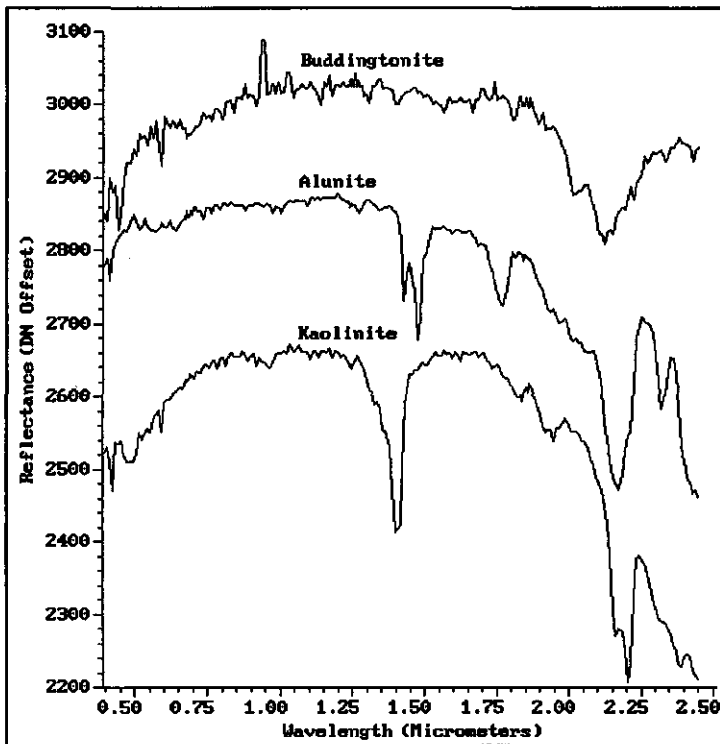


Fig. 7.11: AVIRIS pixel spectra for minerals Kaolinite, Alunite, and Buddingtonite (see Fig. 7.2 for location). Spectra are offset vertically for clarity.

absorption features. A way to improve the result of the empirical line algorithm is to use more than one dark and light target.

The spectral interpretability of all five method used was good except for the ATREM method for which absorption features were slightly offset in wavelength with respect to the laboratory spectra (Fig. 7.11). The wavelength positions of the double OH absorption with the weaker feature at 2.160 $\mu$ m and the stronger feature at 2.200 $\mu$ m for kaolinite is well known from laboratory studies (Hunt & Salisbury, 1970; Van der Marel & Beutelspacher, 1976; Hunt, 1979). This OH doublet was well resolved in all calibrated spectra extracted from the area B in Fig. 7.2 known as Kaolinite Hill. Buddingtonite occurs as replacement mineral in hydrothermally altered andesite, where ammonium substitutes alkali cations bound with the crystal structure (Krohn & Altaner, 1987). An absorption feature at 2.020 $\mu$ m and a vibrational absorption feature due to  $\text{NH}_4$  (Krohn & Altaner, 1987) at 2.110 $\mu$ m are the main diagnostic features distinguishing Buddingtonite spectrally from other clay minerals. Alunite is characterized by absorption features at 2.160 and 2.200 $\mu$ m due to OH frequency stretching (Hunt *et al.*, 1971) and a nearly symmetrical shape in the 2.080-2.280 $\mu$ m region. A second

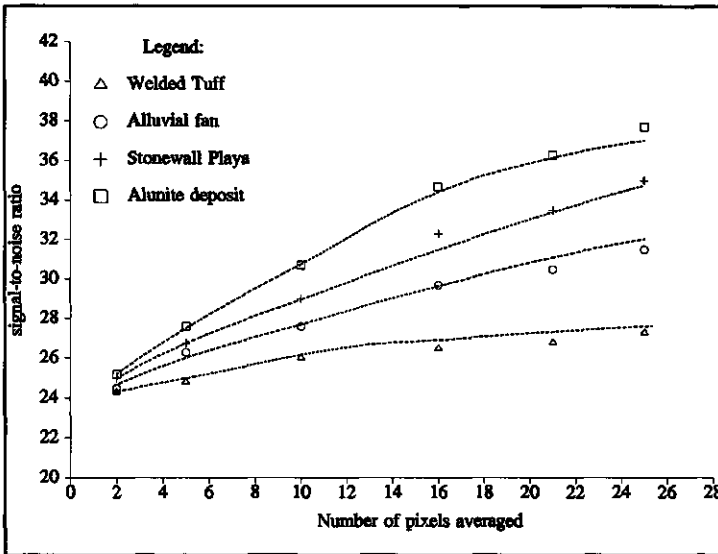


Fig. 7.12: Experimentally calculated SNR values (indicated by symbols) for four targets with different albedo. The model curves (dotted lines) are empirically determined based on the relative brightness of the targets and the signal-to-noise ratio of a single pixel in the target region using Eq.(12). See text for explanation (after: Van der Meer, 1994c).

broad absorption feature occurs at 2.320 $\mu$ m.

The calibrated data cube resulting from normalization with the Empirical Line method has been used to quantify the increase of the signal-to-noise ratio (SNR) with increasing number of pixel spectra averaged. Four targets with increasing albedo have been selected: a dark tuff, an intermediate dark alluvial fan, the moderately bright Stonewall Playa area, and an very bright Alunite deposit. Results of calculating the signal-to-noise ratio for a number of pixel spectra averaged ranging from 2 to 25 are shown in Fig. 7.12. The increase of SNR is clearly dependent on the relative brightness of the target: SNR increases more rapidly for bright targets. The experimentally calculated values could be approximated by an empirically determined model of the form (Van der Meer, 1994j):

$$\text{SNR} = N_1 + \text{NSA}^a \quad (12)$$

where SNR is the signal-to-noise ratio calculated as the ratio of the mean and standard deviation of the pixel spectra averaged over the wavelength range of 0.4-2.45 $\mu$ m,  $N_1$  is the signal-to-noise ratio of a single pixel over the target region, NSA is the number of pixel spectra averaged, and  $a$  is the relative albedo of the target expressed as the mean reflectivity of the target divided by 1000, if the data are normalized to a standard reflectance of DN 1000. An example of a raw and atmospherically calibrated pixel spectrum of a Kaolinite deposit is shown in Fig. 7.13. Note also the difference in spectral resolution of GERIS and AVIRIS as observed in this Figure.

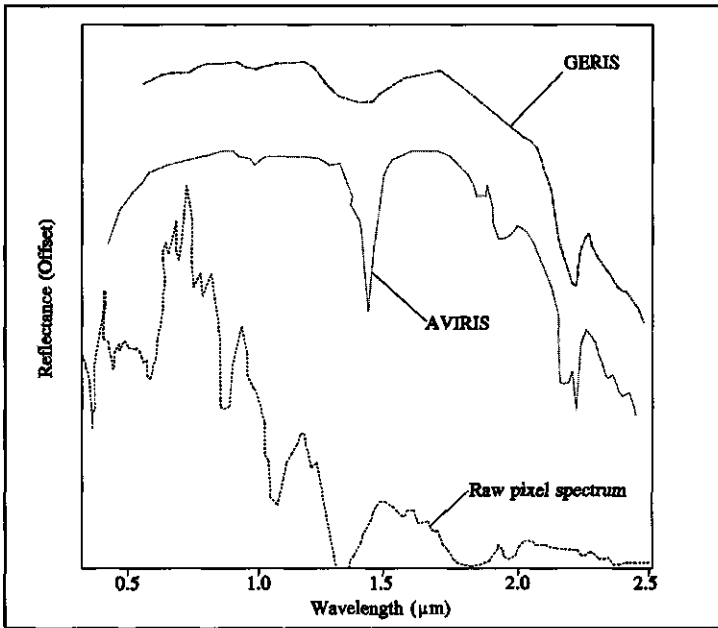


Fig. 7.13: Raw and calibrated Kaolinite pixel spectrum produced from GERIS and AVIRIS data.

Similarly, the performance of atmospheric calibration techniques for the GERIS data set from southern Spain has been evaluated. First, the raw data were reduced to reflectance using the entire data set. Thereafter, the raw data set was divided into two subsets: one covering the limestone area (subset A) and one covering the peridotite area (subset B). For these three data cubes, atmospheric calibration was conducted using the Flat-field method, the Empirical line method, the Internal Average Reflectance method, and the atmospheric removal method (ATREM). The input parameters for ATREM were the same in all three cases. The IARR does not require any user input. The Flat-field chosen for the entire data set was a small alluvial fan which was the best field possible in terms of spectral flatness. The same field was also used for the calibration of subset A using the Flat-field correction. For subset B, another alluvial fan was used as calibration target in Flat-field correction of the data. For the Empirical Line method, the targets selected as calibration areas for Flat-field calibration were used as 'bright' targets, whereas the 'dark' targets was a asphalt road for the entire data set, subset A and subset B, respectively. Gain and offset spectra used for the regression function in the Empirical Line method are shown in Figs. 7.14 and 7.15, respectively.

A pure calcite pixel spectrum was used to evaluate the results of the calibration and a spectrum of a dunite pixel spectrum along a gently sloping road-cut. The results are summarized in Table 7.9. The most important conclusions to be derived from Table 7.9 are

- Chapter 7 -

**Table 7.9:** Overall removal characteristics of calibration techniques for the GERIS data set.

processing technique	removal of solar irradiance	removal of atmospheric absorption	noise	artefacts	spectral interpretability
<b>Entire data set</b>					
Flat-Field Method	good	moderate	high	numerous	moderate/good
Empirical Line Method	excellent	good	moderate	moderate	moderate/good
IARR method	moderate/good	moderate	high	numerous	moderate
ATREM	excellent	good	low	moderate	moderate/poor
<b>Subset A (limestone area)</b>					
Flat-field method	good/excellent	moderate	high	numerous	moderate
Empirical line method	excellent	good	high	moderate	good
IARR method	good	good	high	moderate	good
ATREM	good	good	moderate/ low	moderate	moderate
<b>Subset B (peridotite area)</b>					
Flat-field method	good	moderate	high	numerous	good
Empirical line method	good	good	low	moderate	moderate/good
IARR method	moderate	moderate	high	moderate	good
ATREM	good	moderate	moderate	moderate	moderate

that the noise increases for subset A and decreases for subset B when applying the IARR method in comparison with the noise measured for the entire calibrated data set. In most cases, the noise would increase when subsetting a data cube if lithologies are homogeneously distributed over the scene and no extreme absorption features are present simply because the IAR spectrum is averaged over a smaller number of pixels.

In the case of the southern Spain GERIS data set where two contrasting types of lithologies are sensed, limestones and ultramafic rocks, this principle is no longer valid. For both subsets the number of processing artefacts decreases and the spectral interpretability increases when using subsets as input for the IARR calibration. For the other three calibration methods, using subsets does not seem to improve the results of the calibration.

- Atmospheric calibration -

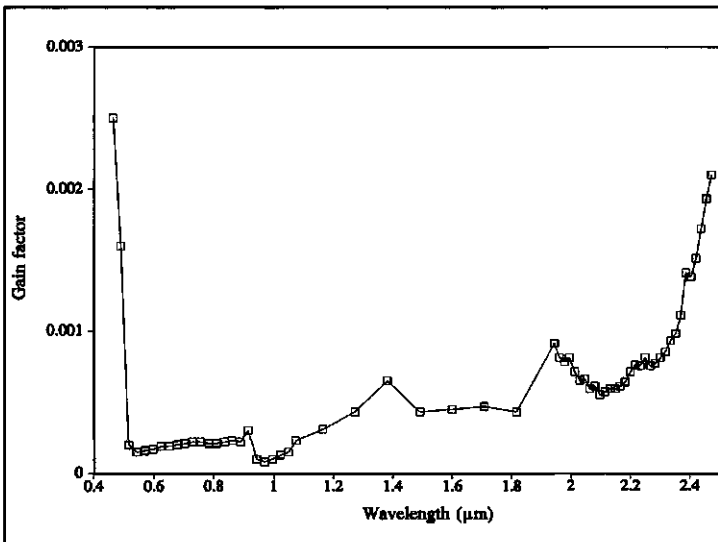


Fig. 7.14: Gain factor for the southern Spain GERIS data set.

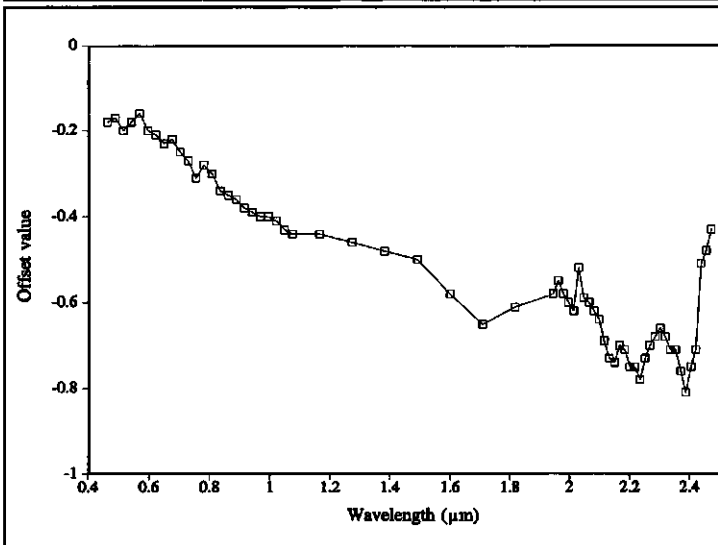


Fig. 7.15: Offset factor for the southern Spain GERIS data set.

### 7.5.7 Comparison of the AVIRIS Cuprite Mining District data set and GERIS data set from southern Spain

Similar investigations on the effectiveness of atmospheric calibration techniques have been conducted by Roberts *et al.* (1985) and Rast *et al.* (1991).

Roberts *et al.* (1985) evaluated the performance of the Flat-field correction and the log-residual correction method using AIS-I data over a clay alteration zone in the Yerington



area, Nevada. These authors concluded that the Flat-field correction performed moderately in terms of atmospheric correction whereas the spectra interpretability of the reduced spectra was moderate. The log-residual correction performed better producing excellent calibrated pixel spectra with high spectral interpretability. Roberts *et al.* (1985) also found that the spectral interpretability of calibrated spectra using the Flat-field method was moderate for sparsely vegetated areas and good for densely vegetated areas. The log-residual method, however, performed well in sparsely vegetated areas and poor in densely vegetated areas.

Rast *et al.* (1991) evaluated the performance of the Flat-field correction, the log-residual method, and the LOWTRAN 7 correction using the AVIRIS Cuprite Mining District data set. They concluded that the log-residual method produces the best results for atmospheric calibration in the absence of ground truth data. Log-residual spectra were found to contain much noise however the corrected spectra were very good interpretable. The Flat-field correction showed the least satisfactory results, whereas the LOWTRAN 7 corrected data set was the most effective technique for data calibration in the presence of external information. Van den Bosch & Alley (1991) noted that atmospheric models are more sensitive to errors in moisture content than to any other parameters due to inaccuracies in radiosonde data. These authors conclude that improper characterization of targets by wrongly chosen pixel samples contributes most of the error in the formulation of the regression model forming the basis of the Empirical Line correction (see also Conel *et al.*, 1988).

## 7.6 CONCLUSIONS

A one channel wavelength shift was found in the GERIS data set on the basis of the position of CO<sub>2</sub> absorption bands. A similar shift was found in other GERIS data sets by other workers, therefore careful radiometric calibration of GERIS data is needed prior to image analysis.

Signal-to-noise ratios were derived using three methods. The computed noise levels for the "homogeneous area method" were found to be higher than those for the "local means and standard deviation method". The "geostatistical method" produced high signal-to-noise ratios due to a lower estimate of the noise component. However, estimates for both the AVIRIS Cuprite Mining district data set and the GERIS southern Spain data set were good and values of 35:1 and 8:1 were found for GERIS and AVIRIS respectively in the 2.0-2.5 $\mu$ m wavelength region. In general, GERIS produced higher signal-to-noise values than AVIRIS.

The performance of the calibration techniques is dependent on many factors. In presence of vegetation, the Flat-field method performs better than in sparsely vegetated terrains. The results of the IAR method are dependent on selection of a homogeneous subset

*- Atmospheric calibration -*

of image data with respect to spectral features. In the case of southern Spain where contrasting lithologies occur, e.g., limestones with strong carbonate absorption bands and ultramafic rocks which have relatively dark and featureless spectra, subsetting improves the calibration. Calibration is also scene dependent in the sense that good calibration targets (e.g., for Flat-field and Empirical Line method) are required or external information (e.g. for ATREM). If good calibration targets are available, the Empirical Line method produces the best results as can be seen from the Cuprite Mining data set. However, if these targets are less properly chosen, one may prefer to use IAR.

## CHAPTER 8:

### *Mineral mapping and automatic feature extraction from imaging spectrometer data<sup>6</sup>*

#### ABSTRACT

Available techniques for mineral mapping based on the presence or absence of spectral absorption features in reflectance-mode imaging spectrometer data are discussed in this Chapter. Visual inspection of pixel spectra is tedious and both the use of colour-composite images (with bands on shoulders and center of absorption bands) as well as the use of colour-coded stacked spectra requires much manual input and yields imprecise results. Quantitative analysis techniques including Spectral Angle Mapping, Unmixing analysis, and Binary encoding may yield satisfactory results lacking however a probabilistic output result. A new non-parametric classification technique is introduced which builds on the concept of Indicator Kriging. The technique overcomes some inherent problems of classification algorithms in because: (1) it relies on spectral information from laboratory studies rather than on ground truth data only, (2) it yields a probability or portion of a pixel belonging to a certain class or mineralogy (3) through the kriging estimation an estimate of uncertainty is derived, (4) it incorporates spatial aspects rather than only spectral aspects, (5) it is distribution free, and (6) may be applied on different supports. The Indicator Kriging classifier requires a number of steps to be followed: (1) define key spectral bands, (2) set upper and lower limit in these bands, (3) transform the data to 0 and 1 if the spectral response of the pixel falls inside or outside the indicated range, (4) estimate the quasi-point support values within a local area from which a probability of a pixel belonging to a class can be deduced, (5) integrate all probabilities obtained from all bands used into a final probability map. and (6) threshold this map to produce the final classification. Comparison of the Indicator Kriging classifier with conventional classification techniques shows that accuracy is higher for the new method. Furthermore, a quantification of visual aspects of classified images shows that the Indicator Kriging classifier produces less isolated classes with more spatial continuity.

---

<sup>6</sup>Parts of this Chapter have been published as:

Van der Meer, F. 1994. Extraction of mineral absorption features from high-spectral resolution data using non-parametric geostatistical techniques. *International Journal of Remote Sensing*, 15(11): 2193-2214.

Van der Meer, F. 1994. Classification of remotely sensed imagery using an indicator kriging approach: Application to the problem of calcite-dolomite mineral mapping, *International Journal of Remote Sensing*, submitted.

## 8.1 INTRODUCTION

In this chapter, techniques will be discussed for mineral identification and mapping based on their spectral characteristics as observed in imaging spectrometer pixel spectra. Existing mineral mapping techniques, which mostly yield a qualitative estimate of surface mineralogy, will be briefly discussed. A new mineral mapping technique is introduced combining non-parametric geostatistical techniques a statistical zonation algorithms. Results of mineral mapping using this indicator kriging classifier are compared with classified images using conventional classification algorithms.

## 8.2 EXISTING TECHNIQUES FOR MINERAL MAPPING FROM IMAGING SPECTROMETER DATA

### 8.2.1 Comparison of pixel and laboratory spectra

Fig. 8.1 shows spectra from areas B, C and D in Fig. 7.2 using AVIRIS data normalized to reflectance using the Empirical Line method described in Chapter 7. These spectra are the result of averaging 25 spectra over the indicated area and smoothing using a fast fourier transform. Area B is known as Kaolinite Hill for its extensive and well exposed deposit of the clay mineral Kaolinite. The wavelength positions of the double OH absorption with the weaker feature at  $2.16\mu\text{m}$ . and the stronger feature at  $2.20\mu\text{m}$ . is well known from laboratory studies (Hunt & Salisbury, 1970; Van der Marel & Beutelspacher, 1976). This OH doublet was the main criterium used for positive identification of Kaolinite. Furthermore, the characteristic asymmetric shape of the spectrum towards long wavelengths is well resolved in the AVIRIS spectrum. Other clay minerals which are difficult to distinguish from Kaolinite visually are Alunite and Buddingtonite. Alunite occurs widely throughout the Cuprite mining area while Buddingtonite has been observed at few locations at the site. The occurrence of Buddingtonite was first discovered through the analysis of AIS spectra (Goetz & Srivastava, 1985). Buddingtonite occurs as replacement mineral in hydrothermally altered andesite, where ammonium substitutes alkali cations bound with the crystal structure (Krohn & Altaner, 1987). An absorption feature at  $2.02\mu\text{m}$ . and a vibrational absorption feature due to  $\text{NH}_4$  (Krohn & Altaner, 1987) at  $2.11\mu\text{m}$ . are the main diagnostic features distinguishing Buddingtonite spectrally from other clay minerals. Alunite is characterized by absorption features at  $2160$  and  $2.20\mu\text{m}$ . due to OH frequency stretching (Hunt *et al.*, 1971) and a nearly symmetrical shape in the  $2.08$ - $2.28\mu\text{m}$ . region. A second broad absorption feature occurs at  $2.32\mu\text{m}$ . Mineral identification by comparison of pixel and laboratory spectra is throughout

- Mineral mapping -

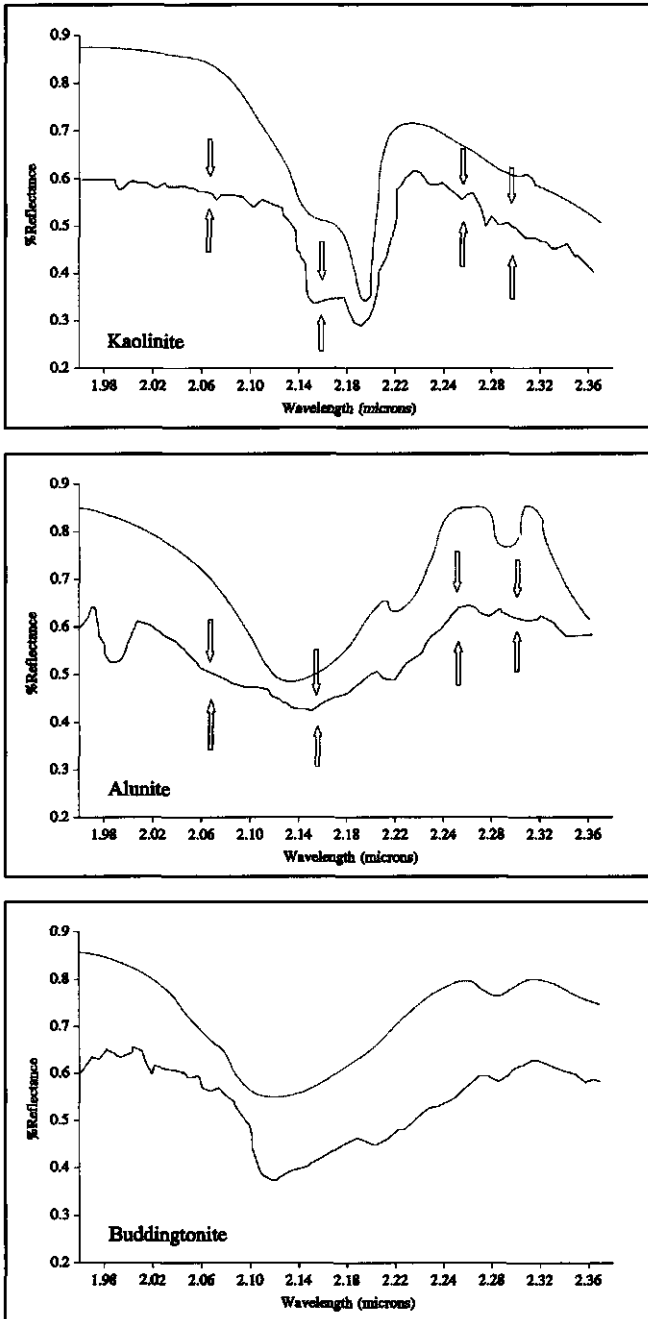


**Fig. 8.1:** AVIRIS pixel spectra of clay minerals (see Fig. 7.2 for location). Dotted curves represent laboratory spectra of the investigated minerals, solid curves represent the AVIRIS derived spectra. The arrows enclose the spectral range in each band used for indicator classification (see text for discussion). Spectra are vertically offset for clarity by factor 0.2.

This figure is displayed as colour plate 3 on page 314

**Fig. 8.2:** Colour-composite image with band centred at  $1.995\mu\text{m}$  in red (left shoulder of clay mineral absorption features), band centred at  $2.312\mu\text{m}$  in blue (right shoulder of clay mineral absorption features), and band centred at  $2.232\mu\text{m}$  in green (centre of the absorption feature). In this image, moderately altered opalized and argillized units containing hydrothermal clay minerals are represented in light blue colours. The unaltered Tertiary volcanic deposits are red coloured in the image.

possible, however requires enormous manual input. Therefore techniques for digital mapping of surface mineralogy will be explored in the remainder of this Chapter.

### 8.2.2 Colour-composite images

An alternative for manual inspection of pixel spectra is the use of colour-composite images constructed using known spectral absorption features minerals from laboratory spectra. The three clay minerals present in the AVIRIS Cuprite Mining District data set (Kaolinite, Alunite, and Buddingtonite) all have distinct absorption features near a wavelength of  $2.20\mu\text{m}$ . A colour-composite image (Fig. 8.2) has been made with bands centered at  $1.995\mu\text{m}$  and  $2.312\mu\text{m}$  at the shoulders of the absorption features (displayed in red and blue respectively)

This figure is displayed as colour plate 4  
on page 314

Fig. 8.3: Example of a colour-coded stacked spectrum for the GERIS data set from southern Spain. The x-axis of the plot is the spectral band and the y-axis represents the pixel position along a line running parallel to the strike through the limestone area (A-B) and along a line crossing the peridotite-marble contact (C-D).

and  $2.232\mu\text{m}$  in the centre of the absorption features (displayed in green). In this image, clay minerals are represented in light blue colours. Although colour-composite images in some cases may yield satisfactory results, subtle spectral differences will often not be discernable. For general characterization purposes, however, such images are very useful.

### 8.2.3 Colour-coded stacked spectra

Colour-coded spectra (Kruse *et al.*, 1985; Marsh & McKeon, 1983; Huntington *et al.*, 1986) show all spectra along a predefined line (e.g. a scanline or an arbitrary line crossing the

image) stacked side by side and coloured according to the intensity of the reflectance. The x-axis of the plot represents the spectral direction ranging from 0.4 $\mu$ m to 2.45 $\mu$ m, and the y-axis represents the location of the pixel. Each line in the image is a full spectrum. The colour-coding is done with respect to the average spectrum calculated for the scene. Black, purple, and blue colours represent reflectance lower than the average spectrum (absorption features), green and yellow represent reflectance similar to the average spectrum, and orange, red and white represent reflectance higher than the average spectrum. Fig. 8.3 shows a colour-coded stacked spectrum for an arbitrary line through the GERIS image from southern Spain. The first line runs parallel to the strike of the limestones (A-B), the second (C-D) passes straight into the peridotites. The spectra are extracted from a GERIS data cube which was calibrated using the Empirical Line Method. Atmospheric water absorption bands centered at 1.4 $\mu$ m and 1.9 $\mu$ m show as black colours. In the middle-left of the line C-D, the boundary between the marbles and peridotites is visible. Thus colour-coded stacked spectra provide a fast mean of investigating a data set and allow to visualize spectral information from many spectral bands in one plot. Data extraction and mineral mapping from such plots is tedious and requires manual input and knowledge on the site.

#### 8.2.4 Binary encoding

In this technique, pixel spectra are encoded such that a one-zero representation of the brightness of a pixel in various spectral bands results using a threshold level equal to the average brightness of the pixel over all channels. A simple binary code for a reflectance spectrum can be described as (Goetz *et al.*, 1985)

$$\begin{aligned} h(n) &= 0 \text{ if } x(n) \leq T \\ &= 1 \text{ if } T < x(n) \end{aligned} \quad (1)$$

where  $x(n)$  is the brightness value of a pixel in the  $n$ th channel,  $T$  is the user specified threshold which often equals the average brightness value of the spectrum, and  $h(n)$  is the resulting binary code for the pixel in the  $n^{\text{th}}$  band.

A variation to this simple encoding is to break the spectral range into a number of subregions and to code separately within these subregions following the same procedure as described above. A modification to the simple encoding has been proposed by Jia & Richards (1993) who exploit multiple thresholds. Their method consist of determining the mean brightness of a pixel vector and then setting additionally upper and lower thresholds. The binary code in two bit format can now take four different values



$$\begin{aligned}h(\mathbf{n}) &= 00 \text{ if } x(\mathbf{n}) \leq T_1 \\&= 01 \text{ if } T_1 < x(\mathbf{n}) \leq T_2 \\&= 10 \text{ if } T_2 < x(\mathbf{n}) \leq T_3 \\&= 11 \text{ if } T_3 < x(\mathbf{n})\end{aligned}\quad (2)$$

where  $T_1$  is the lower threshold,  $T_2$  is the mean brightness of the spectrum, and  $T_3$  is the higher threshold.

Binary encoding provides a simple mean of analyzing data sets for the presence of absorption features, however, with the simple 0-1 coding much depends on the threshold chosen. Comparison of 0-1 coded pixel and laboratory spectra yields a qualitative indication for the presence or absence of absorption features where the depth and thus the significance of the absorption feature is not considered.

### 8.2.5 Waveform characterization

In waveform characterization (Okada & Iwashita, 1992), first the imaging spectrometer data are normalized to produce reflectance-type images. The upper convex Hull is calculated as an enveloping curve on the pixel spectra having no absorption features. Next, the Hull-quotient reflectance spectrum is derived by taking the ratio between the pixel reflectance spectrum and the enveloping upper convex Hull (Green & Graig, 1985). These Hull quotient spectra are used to characterize absorption features, known to be attributed to a certain mineral of interest, in terms of their position, depth, width, asymmetry, and slope of the upper convex Hull.

The absorption band position,  $\lambda$ , is defined as the band having the minimum reflectance value over the wavelength range of the absorption feature. The relative depth,  $D$ , of the absorption feature is defined as the reflectance value at the shoulders minus the reflectance value at the absorption band minimum. The width of the absorption feature,  $W$ , is given by

$$W = A_{\text{all}} / 2D \quad (3)$$

where  $A_{\text{all}}$  is the sum of the area left of the absorption band minimum,  $A_{\text{left}}$ , and the area right of the absorption band minimum,  $A_{\text{right}}$ , forming the total area under the convex hull enclosing the absorption feature. The symmetry factor,  $S$ , of the absorption feature is defined as

$$S = 2(A_{\text{left}}/A_{\text{all}}) - 1 \quad (4)$$

where  $A_{\text{left}}$  is again the area of the absorption from starting point to maximum point. Values for  $S$  range from -1.0 to 1.0 where  $S$  equals 0 for a symmetric absorption feature. The slope of the upper hull,  $\theta$ , characterizes the slope of the upper hull over the absorption feature and is defined as

$$\theta = \tan^{-1} \{ (R_e - R_s) / (\lambda_e - \lambda_s) \} \quad (5)$$

where  $R_e$  and  $R_s$  are the reflectance at the ending and starting point of the absorption feature, respectively, and  $\lambda_e$  and  $\lambda_s$  are the wavelength at the ending and starting point of the absorption feature, respectively.

As a result of the waveform characterization, five images (e.g., an position, depth, width, symmetry, and slope of upper Hull image for each absorption feature selected) can be generated defining the similarity between a pixel spectrum and an laboratory spectrum of a mineral of interest based on the presence of characteristic absorption features in both spectra. However, Okada & Iwashita (1992) give no solution to the mineral mapping from these images. Techniques need to be developed to quantitatively estimate the probability of a mineral occurrence from the waveform characteristics.

In Chapter 7 it was shown that data normalization using a single, internally derived, reference spectrum can result in spectral curves that are distorted from those observed in true reflectance spectra. To avoid this problem, Crowley *et al.* (1989) developed a method of mineral mapping from imaging spectrometer using Relative Absorption Band-Depth Images (RBD) generated directly from radiance data. In essence, RBD images provide a local continuum correction (Clark & Roush, 1984) removing any small channel to channel radiometric offsets, as well as variable atmospheric absorption and solar irradiance drop off for each pixel in the data set. To produce a RBD image, several data channels from both absorption band shoulders are summed and then divided by the sum of several channels from the absorption band minimum. The resulting absorption band-depth image gives the depth of an absorption feature relative to the local continuum which can be used to identify pixels having stronger absorption bands indicating that these may represent a certain mineral.

### 8.2.6 Spectral Angle Mapping (SAM)

Spectral Angle Mapping (Boardman, 1994; Kruse *et al.*, 1993) calculates the spectral similarity between a test reflectance spectrum and a reference reflectance spectrum assuming that the data is correctly calibrated to apparent reflectance with dark current and path radiance removed. The spectral similarity between the test (or pixel) spectrum and the reference (or

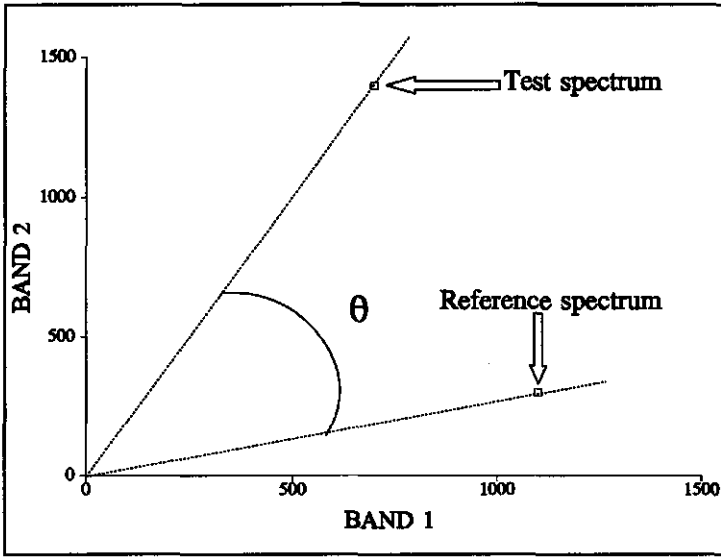


Fig. 8.4: Concept of Spectral Angle Mapping (after: Kruse *et al.*, 1993).

laboratory) spectrum is expressed in terms of the average angle between the two spectra (Fig. 8.4). In this approach, the spectra are treated as vectors in a space with dimensionality equal to the number of bands. The spectral angle mapping-algorithm determines the similarity between a test spectrum  $t$  and a reference spectrum  $r$  from the arc-cosine of the dot product of the two spectra defined as

$$\cos^{-1} \frac{t \cdot r}{\|t\| \cdot \|r\|} \quad (6)$$

which can also be written as

$$\cos^{-1} \frac{\sum_{i=1}^{nb} t_i r_i}{\sqrt{\sum_{i=1}^{nb} t_i^2} \sqrt{\sum_{i=1}^{nb} r_i^2}} \quad (7)$$

where  $nb$  is the number of bands.

The spectral angle measured by the spectral angle mapping-algorithm is insensitive to gain factors because the angle between the two vectors is invariant with respect to the lengths of the vectors. Therefore laboratory spectra can be compared directly with pixel spectra which have an unknown gain factor dependent on topography and illumination. The outcome of the spectral angle mapping for each pixel is an angular difference measured in radiance ranging from zero to  $\pi/2$  which gives a qualitative estimate of the presence of absorption features which can be related to mineralogy. Mineral mapping using Spectral Angle Mapping is discussed within the framework of the Ronda peridotites in Chapter 9.

### 8.2.7 Spectral Unmixing

Spectral unmixing is based on the assumption that a pixel is composed of the spatial mixing of materials within the volume bounded by the pixel all having a characteristic spectral signature together resulting in the reflected electromagnetic radiation observed in imaging spectrometer data. If a single incident photon is multiply scattered and encounters more than one material then nonlinear mixing describes the resulting spectral signature (Hapke, 1981; Johnson *et al.*, 1983). If one single material is encountered, linear mixing models can describe the spectral reflectance characteristics (Singer & McCord, 1979; Adams & Smith, 1986). Linear mixing models have been proven to be successful in spectral analysis (see Chapters 4 and 5). In the nonlinear models, the problem is linearized through a change of variables. Thus both model types use a linear relationship between an observed spectrum and a library composed of endmember spectra to find the individual mixing components and their abundances. In simplified form this is achieved by solving the following:

$$\mathbf{A} * \mathbf{X} = \mathbf{B} \quad (8)$$

thus

$$\mathbf{X} = \mathbf{A}^{-1} * \mathbf{B} \quad (9)$$

where  $\mathbf{A}$  is an  $M$  by  $N$  endmember library matrix,  $\mathbf{X}$  is an  $N$  by 1 unknown abundance vector, and  $\mathbf{B}$  is an  $M$  by 1 observed data vector with  $M$  as the total number of bands and  $N$  the total number of mixing endmembers.

Spectral unmixing using Singular Value Decomposition is described in detail by Boardman (1989; 1990; 1991). The spectral unmixing results in an abundance image for each

endmember in the mixing model giving the relative abundance of a mineral at every pixel. In addition, an image of the sum of the abundances at each pixel and an image of the root-mean square error at each pixel are calculated. The error image displays how well the mixing library can be used to model each observed spectrum, and can be used to assess the validity of the endmember spectra. Improved error mitigation due to image restoration is discussed in Hsien-Huang & Schowengerdt (1992). Results of unmixing for the southern Spain GERIS data set are discussed in Chapter 9.

### **8.3 A NEW INDICATOR KRIGING CLASSIFICATION METHOD FOR MINERAL MAPPING**

Results of mineral mapping with the Spectral Angle Method and by means of unmixing analysis are further discussed in Chapter 9 using the GERIS data set from southern Spain. The remainder of this Chapter deals with the introduction and evaluation of a new mineral mapping technique based on non-parametric geostatistics. In this Chapter, this technique is used for clay mineral mapping from the Cuprite AVIRIS data set, however, it will be shown that similar analysis can be conducted using conventional remotely sensed image types. The results will be compared with conventional classified images modified for the analysis of hyperspectral data. In contrast with all the earlier described techniques for mineral mapping, indicator kriging classification yields a probability of a pixel belonging to a certain class mineralogy and an estimate of the reliability of this probability rather than a qualitative assessment of surface mineralogy.

Classification of remotely sensed imagery into groups of pixels having similar spectral reflectance characteristics is often an integral part of digital image analysis. On basis of the spectral reflectance which training pixels (e.g. pixels known to represent a ground class of interest) exhibit, pixels for which the ground cover type is unknown are classified. Classification routines aim at comparing the observed spectral reflectance of pixels with unknown composition with that of training pixels, and assign the unknown pixel to that group which resembles most their spectral reflectance characteristics. Techniques making use of training data sets are referred to as supervised classification algorithms as opposed to unsupervised classification techniques in which no foreknowledge of the existence of ground classes is required.

Supervised and unsupervised image classification techniques have been widely used in the analysis of conventional remote sensing data type (e.g., Landsat MSS and TM, and SPOT) and several studies have been undertaken to develop algorithms based on classification for hyper-spectral data types. Cetin *et al.* (1993a+b) and Cetin & Levandowski (1991) use n-

Dimensional Probability Density Functions based on the principle of the maximum likelihood classifier to analyze AVIRIS, TIMS, and Landsat TM images. Lee & Landgrebe (1993) give algorithms for the Minimum Distance Classifier in high-spectral resolution imagery. Conventional supervised classification techniques currently available have a number of drawbacks which limit their use and application:

- 1) ground information is needed to train the classifier which is not always available or difficult to obtain.
- 2) most classifiers assign unknown (to be classified) pixels to a ground cover class from a set of user defined classes without quantifying the uncertainty or the likelihood that the pixel actually belongs to that class.
- 3) classification methods use only the *spectral* characteristics of an unknown pixel in comparison with that of a set of training samples to classify unknown pixels without considering the *spatial* aspects or the relative location of an unknown pixel with respect to pixels from the training data set.
- 4) most classifiers rely on a Gaussian probability distribution of the spectral signature of the training data which often exhibit a non-Gaussian distribution.
- 5) classification methods work on a pixel support without allowing estimation on larger or smaller volumes.

The new image classification technique based on non-parametric geostatistics in conjunction with statistical zonation techniques, requires no ground knowledge because it uses spectral characteristics of ground cover classes as known from laboratory reflectance studies. Since the classifier applies indicator kriging, it will provide through the estimation variances a means of quantifying the accuracy of the classification. Furthermore, it encompasses both spectral information and spatial information and intrinsically could be applied to data at various supports. Finally, the indicator transformed variables are distribution free and therefore overcome the assumptions made in most classifiers which rely on Bayesian statistics using Gaussian probability density functions. Though the technique presented can intrinsically be used for the analysis of both standard remotely sensed products and high-spectral resolution data, a comparison is made of classification results derived from high spectral resolution data.

### **8.3.1 Conventional classification techniques in the hyperspectral space**

Image classification techniques are well known in pattern recognition and standard image analysis. Classification is based on computer-assisted recognition of surface materials from their characteristic spectral properties in various wavelength bands. Supervised classification

techniques are used for the extraction of information from remotely sensed imagery where spectral information of ground classes is known. An important assumption is that each spectral class can be described by a probability distribution defining the chance of finding a pixel belonging to that class at any given location in the multispectral space. Irrespective of the particular method used in supervised classification, the essential practical steps to be followed are (Richards, 1993):

- 1) Identify a set of ground cover types into which the image needs to be segmented.
- 2) Choose for each of these classes representative pixels characterizing the spectral reflectance behaviour of the class. This set of training data can be established from field knowledge. If a pixel,  $f$ , is represented in two different spectral bands  $X$  and  $Y$ , its spectral reflectance characteristics can be shown in a graph known as the feature space which has the spectral range of the first band as x-axis and the spectral range of the second band as y-axis. By plotting representative pixels  $f(x,y)$  in this graph, the two-dimensional feature space is defined characterizing the reflectivity of the ground cover classes. The size of the feature space depends on the number of spectral bands. In case of  $N$  bands, an  $N$ -dimensional feature space defines the spectral characteristics of pixels.
- 3) Use the training data to estimate the parameters of the particular classifier algorithm to be used defining the properties of the probability model (e.g., the signature of the class).
- 4) Use the training classifier, to label or classify every pixel in the image into the desired ground cover class.
- 5) Produce a thematic map summarizing the results of the classification.

A wide range of classifier algorithms exists to perform step 4 mentioned above. Here we consider the most often used techniques: the parallelepiped (or box) classifier, the K-nearest neighbours classifier, and the maximum-likelihood classifier.

Parallelepiped classification is the simplest classifier that is trained by inspecting histograms of the individual spectral components of the available training data. The upper and lower limits of the histograms are identified to describe the brightness value range for the class in each band. Together, the range in all bands describe a multidimensional parallelepiped or parallelepiped. If throughout classification unknown pixels are found to lie within the parallelepiped they are labelled as belonging to that class. The parallelepiped classifier has several drawbacks:

- 1) there can be considerable gaps between the parallelepiped and therefore pixels in those region will not be classified
- 2) for correlated data, overlap of the parallelepipeds can occur and consequently there is some data that cannot be separated

- 3) prior probabilities of class membership are not considered
- 4) parallelepipeds are only a crude representation of the elliptical surfaces usually defining spectral class signatures.

The K-nearest neighbour classifier uses the distance in the feature space from a point to be classified to the K-nearest points in each cluster of training data points for ground cover classes. The unknown pixel is assigned to that ground cover class for which the average distance to the K-nearest neighbouring points is smallest. K can be any ordinal value larger than 0. In case of using 1 neighbouring point ( $K=1$ ), the feature space can be divided into representative areas for each ground cover class based on the distances between points in each cluster, thus defining the decision boundaries. The K-nearest neighbour algorithm is discussed in more detail in Fix & Hodges (1952), Sebestyen (1962), Nilsson (1965), Cover & Hart (1967), Cover (1968), Tou & Gonzalez (1974), and Hart (1968).

Maximum-likelihood classification (see Strahler, 1980, Swain & Davis, 1978; Nilsson, 1965; Andrews, 1972; Duda & Hart, 1973; Tou & Gonzalez, 1974) uses a Gaussian probability distribution derived from the statistics of the training data to construct ellipses of equal probability radiant around the center of the cluster. An unknown pixel is assigned to the class for which the probability is largest based on the intersection of the position of the unknown pixel in the feature space and the probability surfaces of the training classes.

### 8.3.2 the Indicator Kriging Classifier

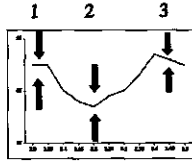
The indicator kriging classifier (van der Meer, 1993; 1994d) introduced here uses both spectral information and spatial information in the classification process. The derivation of the ordinary point and block kriging estimator used is described in detail in Appendix 1 to this Chapter. Classification using the indicator kriging approach starts by defining the spectral bands that contain "key information" on the spectral response of a certain ground class of interest (Step I, Fig. 8.5). This step is done by extracting absorption features characterizing a mineral of interest from laboratory measurements. Bands on the shoulders of the absorption feature and bands on the centre of the feature are subsequently used for further analysis (in the next section, statistical zonation techniques are discussed for automatically finding

---

Fig. 8.5 (*facing page*): Outline of the new indicator kriging based classification technique for extraction of absorption features and mineral mapping from image data. See text for explanation.



*- Mineral mapping -*



Step I: Define key-bands  
Step II: Define upper and lower limits indicated by the arrows

Step III: Transform the selected band images to indicators

1	1	0
1	1	0
0	0	0

band 1

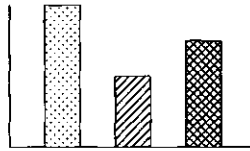
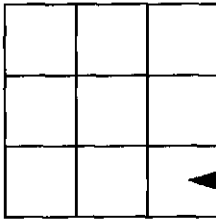
0	0	0
1	1	1
1	0	1

band 2

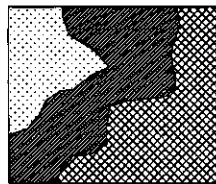
1	0	0
1	1	0
1	1	0

band 3

Step IV: Estimate quasi-point support distributions within block areas

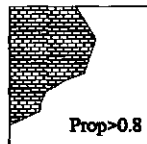


Step V: Integrate the estimates in each band by averaging

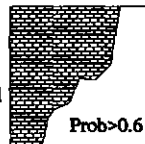


average > 0.8  
average > 0.6  
average > 0.4

Step VI: Classify by setting a tolerance on the average proportion



Classified  
Not-classified



shoulder and center bands of absorption features). This first step requires information on the spectral characteristics of certain minerals and not necessary on field geology which is obligatory for proper selection of training areas. The next step is to define the spectral range in each band by means of setting upper and lower limits for the DN values in those spectral bands (Step II, Fig. 8.5). For all locations  $s$  in the selected bands,  $b$  ( $b$  being any number of bands out of the entire set of 224 spectral bands), the data are being transformed into indicator variables (Step III, Fig. 8.5). Binary indicator values  $i(s_b; z_b)$  for cutoffs  $z_b$  at location  $s$  are defined as

$$i(s_b; z_b) = \begin{cases} 1, & \text{if } z_{bl} < z_b(s) \leq z_{bu} \\ 0, & \text{otherwise} \end{cases} \quad (10)$$

where  $z_{bl}$  and  $z_{bu}$  are the lower and upper threshold value for cutoff  $z_b$  respectively and  $z(s)$  the data value at location  $s$  for band  $b$ . Indicator kriging (Journel, 1983) will provide an estimate of the conditional expectation of the indicator transformation of the random variable  $z_b$  given the realizations of  $n$  other neighbouring random variables or data values resulting in a cumulative distribution function for each cutoff  $z_b$

$$\begin{aligned} [i(s_b; z_b)]^* &= E\{I(s_b; z_b)|(n)\}^* \\ &= Prob^* \{ (Z_{bl} < Z_b(s) \leq Z_{bu})|(n) \} \end{aligned} \quad (11)$$

where  $(n)$  is the conditioning information available in the neighbourhood of location  $s$ . Subsequently, indicator estimation is performed for each of the class indicators in the different bands to obtain estimates of the local mean indicator giving an estimate of the quasi-point support values within a local area (Fytas *et al.*, 1989; Dagbert, 1990; Step IV, Fig. 8.5). If the process is stationary and independent of  $s$ , then the indicator kriging predictor is

$$[i(s_b; z_b)]^* = \sum_{i=1}^n \lambda_i(s_b; z_b) i(s_{bi}, z_b) \quad (12)$$

where

$$\sum_{i=1}^n \lambda_i(s_b; z_b) = 1 \quad (13)$$

- Mineral mapping -

Journal (1983) proposes that the weights,  $\lambda_i(s_b; z_b)$ , corresponding to cutoffs  $z_b$ , be calculated from a simple kriging system through the calculation of residual indicator data  $[i(s_{bi}, z_b) - F^*(z_b)]$  where  $F^*(z_b)$  is the stationary cumulative distribution function of the random function  $Z(s)$ . Note that these weights in simple kriging are not required to sum up to 1. The simple kriging estimate of the indicator transform  $i(s_{bi}, z_b)$  is thus written as

$$[i(s_{bi}, z_b)]_{SK}^* = \sum_{i=1}^n \lambda_i(s_b; z_b) i(s_{bi}, z_b) + [1 - \sum_{i=1}^n \lambda_i(s_b; z_b)] F^*(z_b) \quad (14)$$

using  $n$  observed data values. The simple kriging system of equations is

$$\sum_{i=1}^n \lambda_i(s_b; z_b) C_I(s_{bj} - s_{bi}; z_b) = C_I(s_{bi}; A; z_b), i=1, 2, \dots, n \quad (15)$$

where  $C_I(s_{bj} - s_{bi}; z_b)$  are indicator correlogram values for the distance between  $s_{bj} - s_{bi}$ , and  $C_I(s_{bi}; A; z_b)$  are average indicator correlogram values between location  $s_{bi}$  and the area to be estimated,  $A$ , at cutoff  $z_b$ . Since data is abundant, I considered ordinary indicator kriging within moving data neighbourhoods. A block indicator kriging algorithm was used thus discretizing the block area into point samples yielding

$$i_v(s_b; z_b) \neq \frac{1}{|V|} \int_V i(s_b'; z_b) ds' \equiv \frac{1}{N} \sum_{j=1}^N i(s_{bj}'; z_b) \quad (16)$$

where  $v(s)$  is a block of measure  $|V|$  centered at  $s$ , and the  $i(s_{bj}'; z_b)$  are the  $N$ -points discretizing the volume  $v(s)$ . The result of this block indicator kriging is the average  $1/N \sum [i(s_{bj}; z_b)]_{ik}^*$  which is an estimate of the proportion of point values  $z(s_{bj}')$  within the block area  $v(s)$  that are outside the class interval enclosed by the lower and upper thresholds ( $z_{bl}$  and  $z_{bu}$  from Eq.(10)) defined for band  $b$ . The ordinary block indicator kriging (*OBIK*) estimator using  $n$  control points takes on the form

$$[i(s_b; z_b)]_{obik}^* = [prob\{z_{bl} < z_b(s) \leq z_{bu}\} | (N)]_{obik}^* \\ = \sum_{j=1}^n \lambda_j(s_b; z_b) \gamma([i(s_{bi}; z_b)], [i(s_{bj}; z_b)]) + \mu = \gamma([i(s_{bi}; z_b)], v(s)) \text{ for all } i=1, n \quad (17)$$

and its estimation variance

$$\sigma_{obik}^2 = \sum_{i=1}^n \lambda_j(s_b; z_b) \gamma([i(s_{bi}; z_b)], v(s)) + \mu - \gamma(v(s), v(s)) \quad (18)$$

where the weights  $\lambda_j(s_b; z_b)$  are required to sum up to 1. The terms  $\gamma([i(s_{bi}; z_b)], [i(s_{bj}; z_b)])$  are the point-to-point (or sample-to-sample) semivariances,  $\mu$  is the lagrange multiplier, the terms  $\gamma([i(s_{bi}; z_b)], v(s))$  are the point-to-block semivariances, and the term  $\gamma(v(s), v(s))$  is the block-to-block semivariance. In the actual calculation, covariances were used for numerical stability. In matrix form the system of equations becomes  $[C] \cdot [\lambda] = [D]$  where  $[C]$  is the point-to-point covariance matrix,  $[\lambda]$  is the vector containing the kriging weights, and  $[D]$  is the point-to-block covariance matrix defined as

$$[\lambda] = \begin{bmatrix} \lambda_1(s_b; z_b) \\ \lambda_2(s_b; z_b) \\ \vdots \\ \lambda_n(s_b; z_b) \\ \mu \end{bmatrix}$$

$$[D] = \begin{bmatrix} C([i(s_{b1}; z_b)], v(s)) \\ C([i(s_{b2}; z_b)], v(s)) \\ \vdots \\ C([i(s_{bn}; z_b)], v(s)) \\ 1 \end{bmatrix} \quad (19)$$

$$[C] = \begin{bmatrix} C([i(s_{b1}; z_b)], [i(s_{b1}; z_b)]) & \dots & C([i(s_{b1}; z_b)], [i(s_{bn}; z_b)]) & 1 \\ \vdots & \ddots & \vdots & \vdots \\ C([i(s_{bn}; z_b)], [i(s_{b1}; z_b)]) & \dots & C([i(s_{bn}; z_b)], [i(s_{bn}; z_b)]) & 1 \\ 1 & \dots & 1 & 0 \end{bmatrix}$$

The point-to-block covariances and the block-to-block covariance were approximated by a discrete summation rather than an integration achieved by discretizing the block areas into 6-by-6 arrays of discretizing points. It can be shown using Eq.(16) that the point-to-block covariances are the average covariances between samples and the discretizing points within the block. Similarly, the block-to-block covariance is approximated by the average of the covariances between the  $N$ -points discretizing the block area  $v(s)$ . Since the original sample

values are not at point support but at pixel support, the sample covariances need to be regularized to point support. This was done in the same manner as the discretization of block areas discussed above. In matrix [C] the covariance between any two samples at quasi-point support is replaced by the average covariance between the two sample volumes obtained by discretizing the sample volumes over an 6-by-6 array of discretizing points. The covariance matrix [D] between the sample points and the volume  $v(s)$ , which in fact is an average covariance between a sample point and a number of discretizing points, is replaced by the average covariance between the sample and the point being estimated. Another more formal means of support correction is treated in Appendix 2 of this Chapter.

Summarizing, indicator variables are obtained in several bands on the shoulders and centers of key-absorption features for a ground cover class of interest by thresholding the spectral DN-values at certain upper and lower threshold levels. If an unknown pixel has a spectral DN-value within designated spectral range the indicator value is 1 otherwise 0. Block indicator kriging yields an estimate of the distribution of quasi-point support values within the block for each spectral band chosen. These values for all bands used in the analysis are integrated by simple averaging (Step V; Fig. 8.5). The final classification follows from thresholding these averaged proportions at a user-defined value. The level of accuracy of the classification is proportional to the average proportion of an block area chosen as a threshold level.

### 8.3.3 Statistical Zonation techniques for Automatic Detection of absorption features

In order to extract automatically spectral bands characterizing mineral absorption features (step I, Fig. 8.5), the ability of statistical zonation techniques was tested. These techniques rely on analysis of variance thus evaluating whether two or more populations have significant different mean values. A sequence is subdivided into relatively uniform segments, each which is distinct from adjacent segments. Several authors have proposed methods for statistical zonation of sequential data (e.g. Testermann, 1962; Trudgen & Hoffmann, 1967; Hawkins & Merriam, 1973). Two contrasting approaches often referred to as "local boundary hunting (Webster, 1973)" and "global zonation (Gill, 1970)" were used.

Local boundary hunting searches for abrupt changes in average values or steep gradients in sequences. Webster (1973) introduced a split-moving-window approach for defining boundaries between soil zones along a transect. The sequence, according to this procedure, is examined by iteratively moving a window across it which is split into two part ( $i+h$ ) and ( $i-h$ ) centered around its midpoint  $i$ . Within the window, the Mahalanobis' generalized distance,  $D^2$ , is calculated as

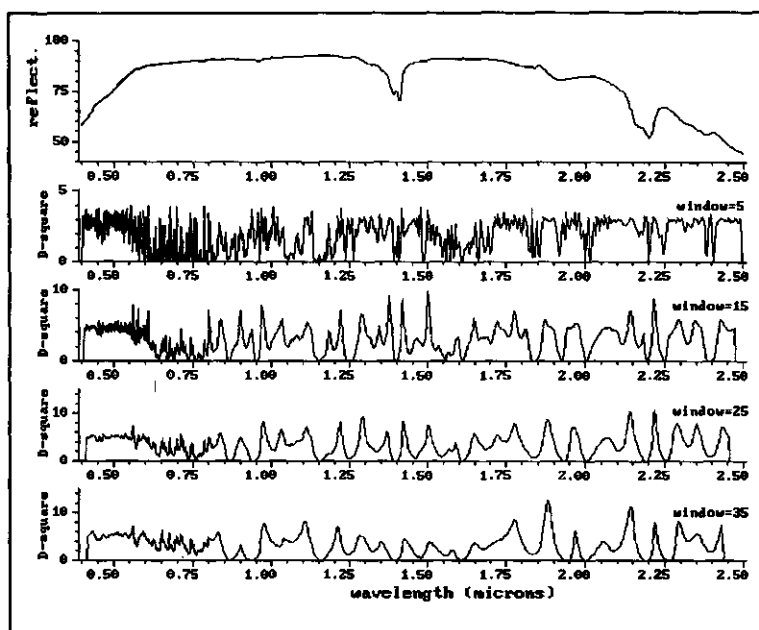


Fig. 8.6: Kaolinite spectrum (top) segmented using local boundary hunting (Webster, 1973). The laboratory spectrum is composed of a total of 826 bands. The generalized distance,  $D^2$ , shows a very erratic plot when using a small window but tends to over-generalize the variability and thus may not detect important boundaries when using a large window.

$$D^2 = \mathbf{d}' \mathbf{W}^{-1} \mathbf{d} \quad (20)$$

where  $\mathbf{d}$  is the vector of differences between the means of the two halves, and  $\mathbf{W}$  is the pooled within-halves variance-covariance matrix calculated from principal components (Webster, 1973). Since the principal components are linearly independent over the entire transect, this reduces to

$$D^2 = \sum_{i=1}^p d_i^2 / s_i^2 \quad (21)$$

where  $d$  is the difference between means, and  $s^2$  is the pooled within-halves variance, and  $p$  is the number of principal components.

The results of applying the local boundary hunting technique for absorption feature detection are shown in Fig. 8.6. For window sizes from 5 to 35 bands, a Kaolinite laboratory spectrum is segmented. This laboratory spectrum consists of 826 spectral bands in the 0.4-2.45 $\mu\text{m}$  wavelength region. Clearly, a small window results in a very erratic plot, whereas a large window tends to generalize the variability and miss important absorption features. Thus, local boundary hunting is very dependent on the proper selection of the window and as such

not very suitable for implementation in automatic image classification routines.

An alternative method iterative zonation procedure was developed by Gill (1970). According to this procedure, the sequence is first divided into a short initial part and the remainder of the sequence. For the two segments, the variance between the zones,  $B$ , and the variance within the zones,  $W$ , are calculated as

$$B = \frac{1}{z-1} \sum_{i=1}^z n_i (M_i - M)^2 \quad (22)$$

and

$$W = \frac{1}{N-z} \sum_{i=1}^z \sum_{j=1}^{n_i} (X_{ij} - M_i)^2 \quad (23)$$

where

$B$	=	between zone variance ("mean square between"; Gill, 1970)
$z$	=	number of zones
$n_i$	=	number of observations in zone $i$
$M_i$	=	mean of zone $i$
$M$	=	mean of the entire sequence
$W$	=	pooled within zone variance ("mean square within"; Gill, 1970)
$N$	=	total number of observations
$X_{ij}$	=	$j^{\text{th}}$ observation in the $i^{\text{th}}$ zone

The effectiveness of the proposed zonation in minimizing the variance within the zones,  $W$ , and maximizing the variance between the zones,  $B$ , can be estimated by calculating the zonation index,  $R$ , (Testermann, 1962) defined as

$$R = (B - W)/B \quad (24)$$

For a homogeneous data set,  $B$  equals zero and  $R$  is undefined, whereas for an optimal zonation  $W$  equals zero and  $R$  equals 1. Any proposed zonation which does not yield  $B \geq W$  is statistically arbitrary. In practice, the boundary between the two zones is moved along the

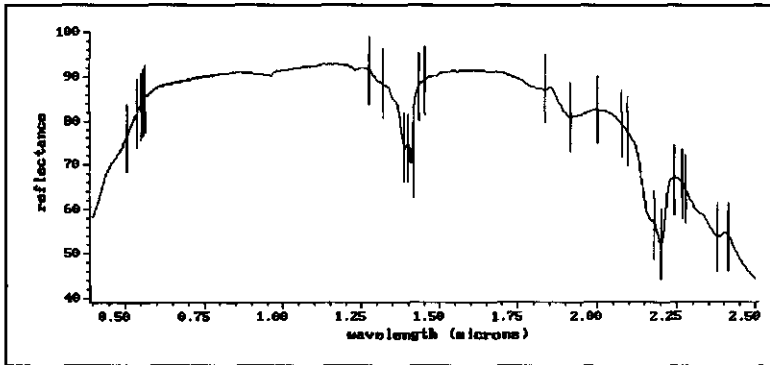


Fig. 8.7 :  
Boundaries  
(vertical bars)  
detected by the  
global zonation  
algorithm (Gill,  
1970).

sequence and the values of B, W, and R are recomputed until the value of R maximizes indicating a zone boundary. The remainder of the sequence itself is partitioned by splitting it up into two parts, a short initial part and the rest of the sequence, and the procedure is repeated. Fig. 8.7 shows the result of applying global zonation to the reflectance spectrum of Kaolinite. The technique detected all possible absorption features and doublets were successfully split into intervals. Van der Meer (1994d) showed that statistical zonation can be improved by using Hull quotient spectra.

### 8.3.4 Results

To test the performance of the indicator kriging based method for feature extraction, we have used a small area from the Cuprite data set was used for a pilot study. The area is 50 by 20 pixels in size contains both Kaolinite and Alunite outcrops. Three bands were used to characterize the mineral absorption features of both Kaolinite and Alunite in the 2.10-2.20 $\mu$ m. wavelength range (see Fig. 8.1).

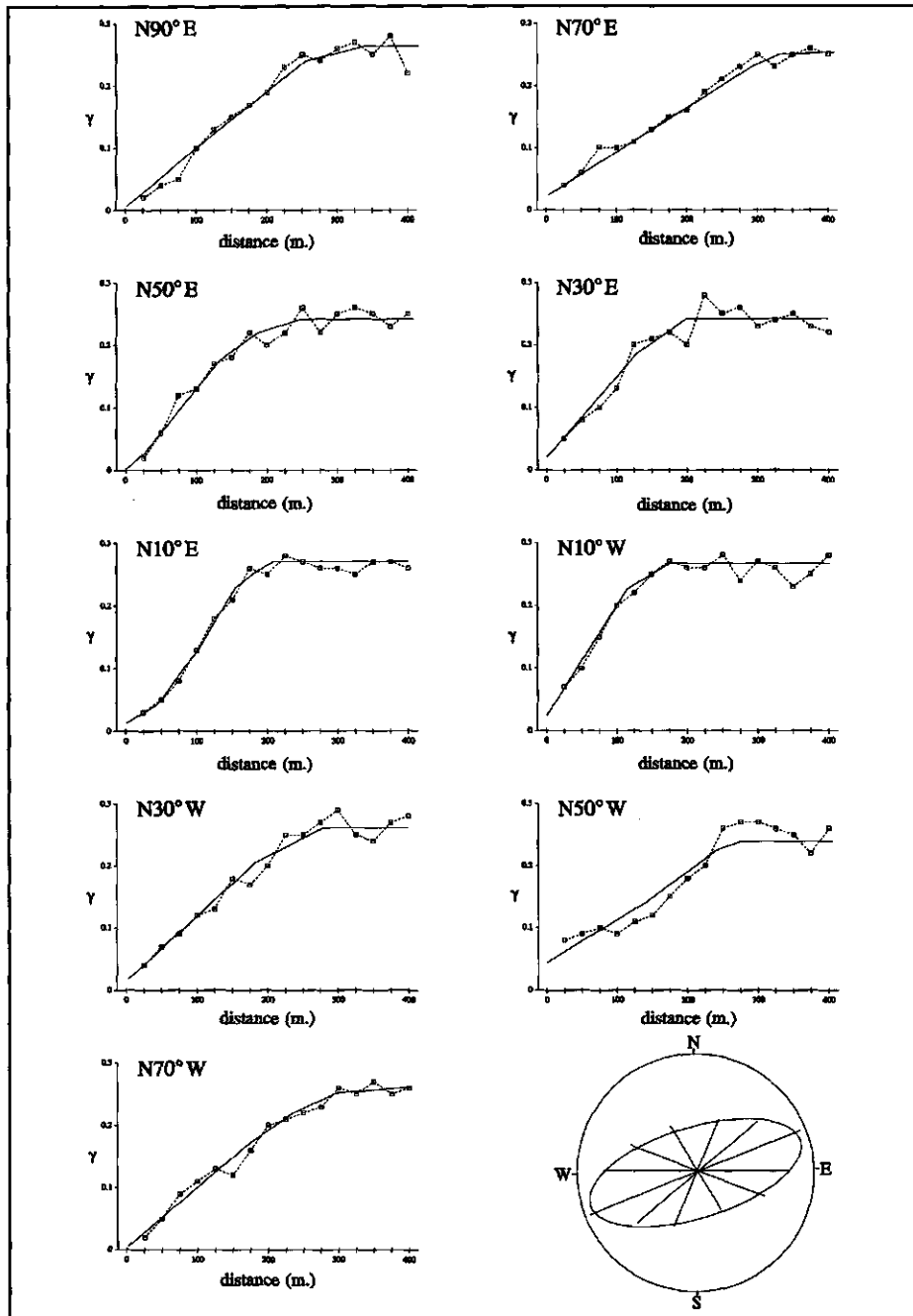
Directional indicator variograms for binary maps of band 2.30 $\mu$ m. thresholded using the DN values indicated by arrows are shown in Fig. 8.8. These variograms were calculated with an directional tolerance angle of 45 degrees. The variograms are well defined and exhibit a geometrical anisotropy with maximum variance in the NW-SE direction and maximum continuity in the NE-SW direction.

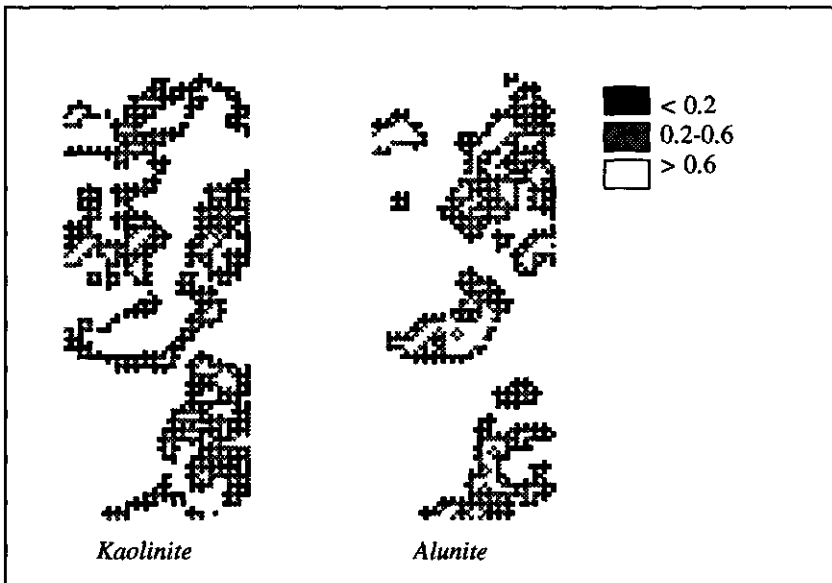
---

Fig. 8.8 (*facing page*): Directional variograms for indicator variable  $i(s_0; z_0)$  (1, if  $z_{bl} < z_0(s) \leq z_{bu}$ , otherwise 0) at the band centered at 2.30 $\mu$ m.



- Mineral mapping -





**Fig. 8.9:** Proportion of a pixel belonging to class kaolinite (left) or alunite (right). By setting tolerances on these values, pixels can be classified. From these images, the final classification was deduced by setting tolerances on the proportions (e.g.  $P > 0.5$  for indicator minimum and  $P > 0$  for indicator maximum classification).

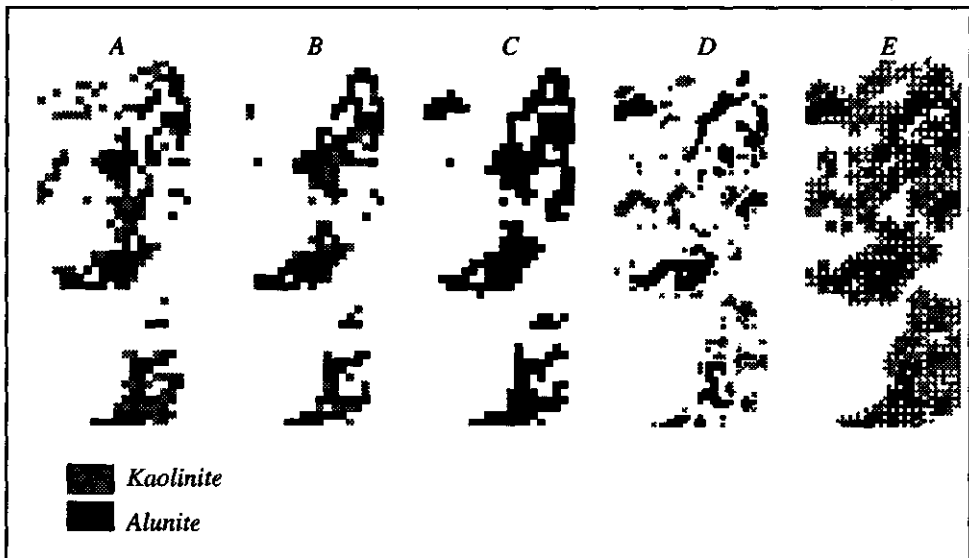


**Fig. 8.10:** Classification results for ground classes Kaolinite and Alunite using (A) Parallelepiped classification, (B) K-Nearest neighbour analysis, (C) maximum-likelihood decision rules, (D) indicator kriging using proportion values greater than 0.5, and (E) indicator kriging using proportion values greater than 0.

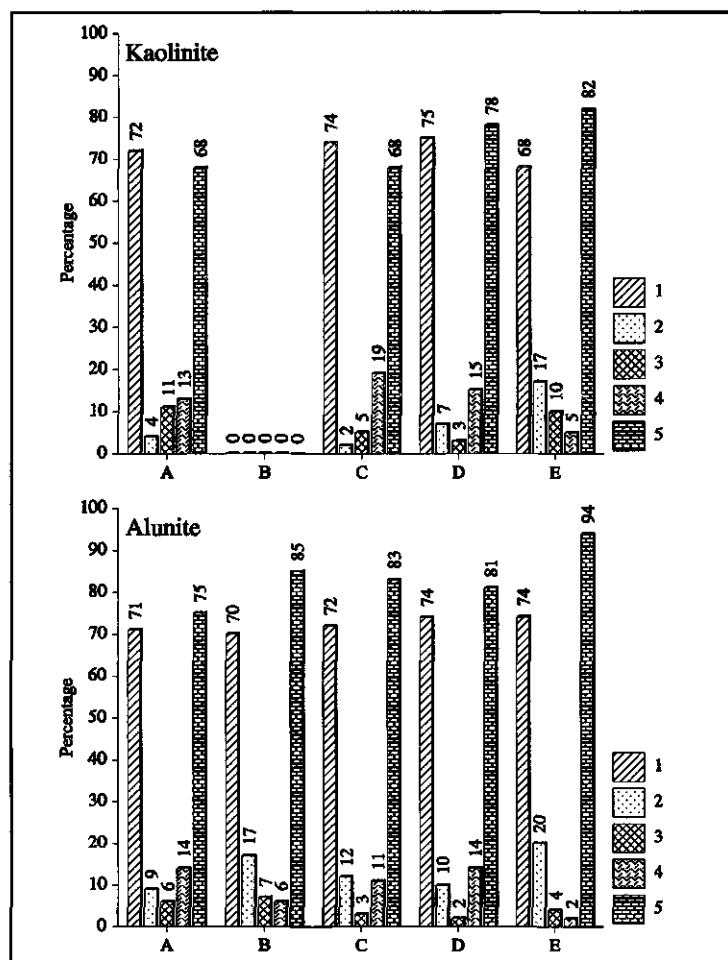


Fig. 8.11: Results of comparing pixels classified as Kaolinite (top) and Alunite (bottom) with known field occurrences of these minerals (A = Parallellepipied classification, B = maximum-likelihood decision rules, C = K-Nearest neighbour analysis, D = indicator kriging using proportion values greater than 0.5, and E = indicator kriging using proportion values greater than 0, 1 = pixel classified in the field not in the image, 2 = pixel classified in the image not in the field, 3 = pixel classified in both image and field, 4 = pixel not classified in image and field, 5 = accuracy).

The resulting estimated proportion maps for Kaolinite and Alunite occurrences are shown in Fig. 8.9. These maps show the proportion of a pixel representing Kaolinite and Alunite, respectively. These were combined by taking all pixels with a proportion of more than zero (referred to as the indicator maximum result) and by using all pixels with proportions exceeding 0.5 (referred to as the indicator minimum results). The classified images for the indicator kriging based method are shown in Fig. 8.10 together with results from conventional classification methods.

The classification results have been evaluated by comparing the classified images with the field information from Albers & Stewart (1972) and Ashley (1977). Fig. 8.11 shows the results of the comparison between classification and field evidence for the distribution of Kaolinite and Alunite, respectively. Four different combinations can occur

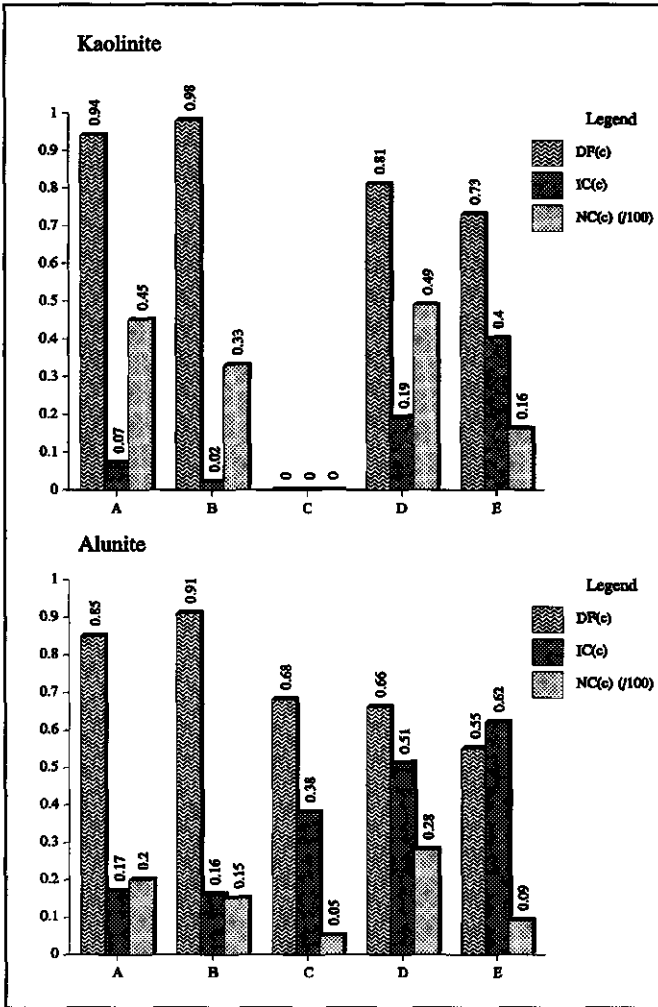


Fig. 8.12: Calculation of synthetic measurements of shape for classes Kaolinite (top) and Alunite (bottom; A = Parallelepiped classification, B = maximum-likelihood decision rules, C = K-Nearest neighbour analysis, D = indicator kriging using proportion values greater than 0.5, and E = indicator kriging using proportion values greater than 0, IC(C) = index of morphologic compactness, NC(c) = connectivity number, and DF(c) = boundary density function.

- 1) in both the classified image and the field geologic map the pixel is classified as mineral
- 2) only in the field the mineral occurrence is detected not in the classified image
- 3) only in the classified image the pixel is assigned to the class representing the mineral to occur although no evidence was found in the field geologic map
- 4) the pixel in the image and in the field geologic map were not considered to belong to the class of the mineral investigated.

The classification results for Kaolinite are in general poor although the indicator kriging technique adopting a probability of zero scores relatively good with respect to the

conventional classification methods. For the class Alunite surprisingly good results were obtained by the maximum-likelihood decision rules and by the indicator kriging technique using all probability values greater than zero.

In order to evaluate the results of different feature extraction algorithms, visual aspects of the resulting images were quantified using synthetic measures of shape derived from mathematical morphology. Mathematical morphology (Serra, 1982) quantifies the geometrical structure and texture of an object by introducing the concept of the structuring element. This element interacts with the object under study, modifying its shape and reducing it to a caricature which is more expressive than the initial phenomenon. Basic transformations of binary patterns are erosion, opening and closing (Fabbri, 1984) from which synthetic measurements of shape are derived quantifying the visual aspects of a class (Fabbri *et al.*, 1993). In this study, measurements used were (Durand & Flouzat, 1985)

- 1) the index of morphologic compactness
- 2) the connectivity number
- 3) the boundary density

The index of morphologic compactness ( $IC(c)$ ) is an indication for the roundness of particles in a class. The index varies from 0 to 1 where  $IC(c)=1$  is a class composed of entities with rounded edges and  $IC(c)=0$  is a class composed of entities with a blocky character. The connectivity number ( $NC(c)$ ) defines the number of particles in class  $c$  minus the number of holes in them. The higher the number of entities, the greater the disseminated aspect of the class. The boundary density ( $DF(c)$ ) represents application to a given class of the shape coefficient for isolated objects, and provides information on the physiognomy of edges in that class. The results of calculating these synthetic measures of shape are shown in Fig. 8.12. The morphological compactness of classes Alunite and Kaolinite in the parallelepiped classified image and the K-nearest neighbour image are low giving them a blocky aspect. Maximum-likelihood classification yields better results, however, the indicator kriging classified images score best with this respect. The connectivity number of all methods is high, especially for the class Kaolinite, although maximum-likelihood classification and the indicator kriging based methods perform best with this respect. The boundary density for the indicator kriging based methods is significantly lower than for the conventional classification techniques, thus indicating less isolated objects. In general, the indicator kriging classifier produces classification results with more rounded classes, less isolated objects, and a smaller disseminated aspect of classes. These results can be attributed to the fact that the indicator kriging classifier uses both spectral and spatial information from the image data. Therefore the resulting classified images show more continuous clusters of pixels containing less holes in the clusters.

An experiment has been performed to investigate the accuracy of the different

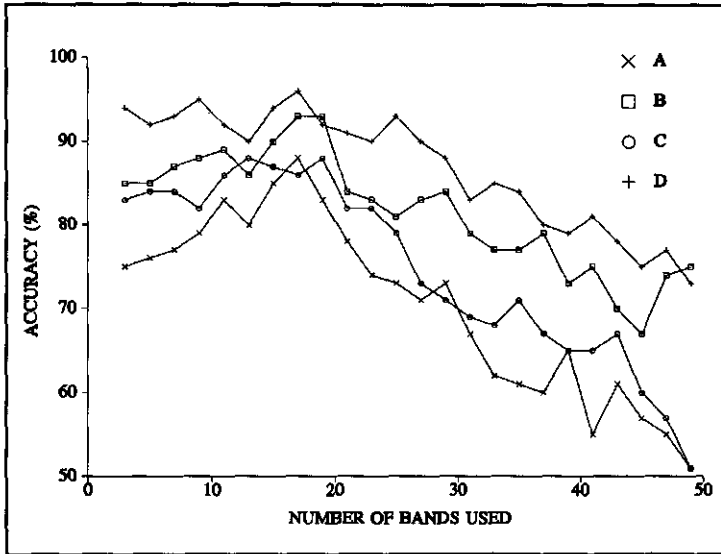


Fig. 8.13: Performance of classifiers with increasing dimensionality (A = Parallelepiped classification, B = maximum-likelihood decision rules, C = K-Nearest neighbour analysis, D = indicator kriging using proportion values greater than 0).

classifiers when increasing the dimensionality of the data. The AVIRIS spectral band marking the center of the absorption features characterizing Kaolinite, Alunite, and Buddingtonite was determined. For Kaolinite the double absorption feature at  $2.20\mu\text{m}$  and  $2.16\mu\text{m}$  was used. The center was marked by AVIRIS band 197 centered at  $2.183\mu\text{m}$ . Alunite was characterized by the broad absorption feature at  $2.16\mu\text{m}$  marked by AVIRIS band 195 centered at  $2.163\mu\text{m}$ . Spectral bands on the shoulders of absorption features were AVIRIS bands 205 and 189 centered at  $2.262\mu\text{m}$  at  $2.104\mu\text{m}$  respectively for Kaolinite and AVIRIS bands 205 and 185 centered at  $2.262\mu\text{m}$  and  $2.064\mu\text{m}$  respectively for Alunite. Classification was performed using a standard training data set of pixels with increasing number of spectral bands starting with three spectral bands (e.g. two shoulders and one center band) by adding two bands next to the central band during each iteration. Thus the maximum number of bands which could be used to fully characterize the absorption feature for the three clay minerals were 17 for Kaolinite, 21 for Alunite, and 33 for Buddingtonite. More bands were added until a maximum of fifty bands was reached to perform the classification. For each classification result, the accuracy was calculated as the normalized mis-classification (e.g. the number of pixels improperly classified divided by the total number of pixels properly classified subtracted from 100%). This quantitative measure of accuracy is 100 for a perfect classification.

The results of this experiment are summarized in Fig. 8.13. Clearly from this figure it can be seen that the classification accuracy increases when adding more bands to image data set to characterize more properly the absorption feature. The increase in accuracy is less

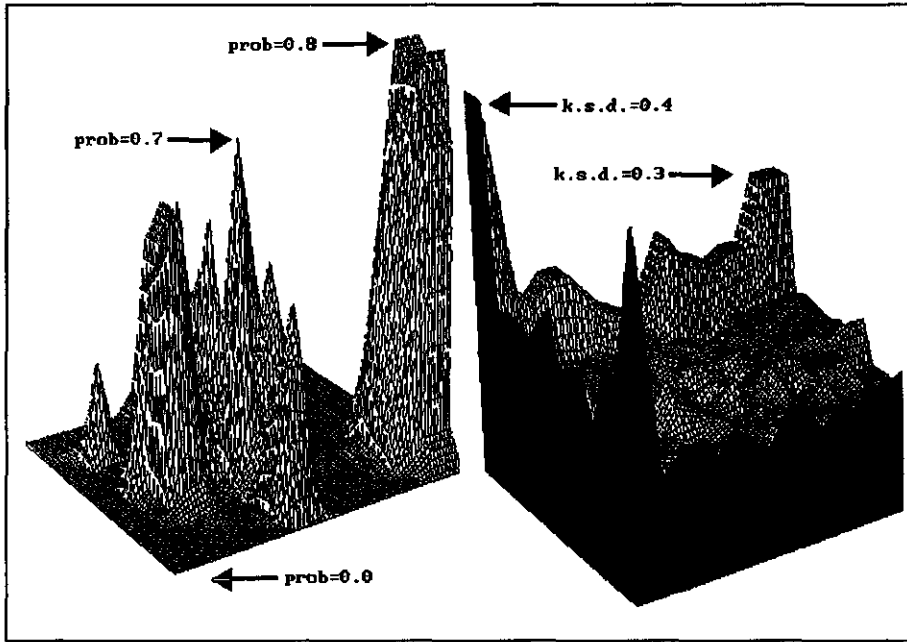


Fig. 8.14: Proportion of a pixel represents Kaolinite (left) and average kriging standard deviation or error of the probability for central part of the Cuprite Mining district.

prominent for the parallelepiped and K-nearest neighbour classifiers than for the Maximum likelihood and Indicator Kriging classifiers. This can be explained by considering the theoretical basis of these techniques. When dimensionality increases (e.g. the number of spectral bands used in classification), second-order statistics become more important than first-order statistics. Thus in the low-dimensional case, class mean differences play a more important role in discriminating between classes than the covariance differences especially when adjacent spectral bands are highly correlated as is often the case in imaging spectrometer data as opposed to conventional remotely sensed data. Therefore, classifiers using Euclidean distances such as the parallelepiped classifier and the K-nearest neighbour classifier are less accurate in high dimensional data sets than other classifiers. Surprising is the fact that classification accuracy reaches a maximum value when a number of spectral bands are used approximately equal to the total number of bands covering the wavelength range between left and right shoulder of an absorption band. When exceeding this value (e.g. bands outside the absorption feature) classification accuracy decreases dramatically for conventional classification techniques which may be attributed to the fact that these bands do not capture any 'useful' spectral information regarding the absorption feature or may even

This figure is displayed as colour plate 5 on page 315

**Fig. 8.15:** Mineral map produced by indicator kriging classification showing Kaolinite in red and Alunite in blue.

characterize other absorption features related to other minerals (deconvolution of absorption features is addressed by Sunshine *et al.*, 1990; 1993). Thus spectral noise is added to the training data set obscuring the classification results. The Indicator Kriging classifier seems to be less affected by this effect possibly because it also incorporates spatial information. Lee & Landgrebe (1993) showed that the performance in terms of accuracy for a number of ground cover classes of the classifiers in the hyperspectral image space increases when adding more spectral bands. Similarly, it was found that small uncorrelated noise added to each band caused greater decrease in classification accuracy than larger correlated noise.

Fig. 8.14 shows the proportion of a pixel representing a Kaolinite occurrence for the central part of the Cuprite Mining district and the corresponding estimation variance produced by the block indicator kriging estimator. This estimation variance can be interpreted as an indication for the reliability of the estimate, thus indicator kriging classification produces estimates of accuracy of the classified images. The final classification is shown in Fig. 8.15 where Kaolinite and Alunite occurrences identified by the indicator kriging classifier with proportions of the pixel belonging to these classes exceeding 50% are shown on the AVIRIS band 68 centered at 1.013 $\mu\text{m}$ .



## 8.4 CONCLUSIONS

Available techniques for mineral mapping from imaging spectrometer data yield qualitative assessments of the surface mineralogy based on the presence or absence of absorption features in pixel reflectance spectra. The application of conventional classification techniques in the hyperspectral space has some inherent complications: (1) ground information is needed to train the classifier which is not always available or difficult to obtain, (2) most classifiers assign unknown (to be classified) pixels to a ground cover class from a set of user defined classes without quantifying the uncertainty or the likeliness that the pixel actually belongs to that class, (3) classification methods use only the *spectral* characteristics of an unknown pixel in comparison with that of a set of training samples to classify unknown pixels without considering the *spatial* aspects or the relative location of an unknown pixel with respect to pixels from the training data set, (4) most classifiers rely on a Gaussian probability distribution of the spectral signature of the training data which often exhibit a non-Gaussian distribution, (5) classification methods work on a pixel support without allowing estimation on larger or smaller volumes.

A new non-parametric classification technique is introduced in this Chapter which builds on the concept of Indicator Kriging. The technique overcomes some of the problems of classification algorithms because: (1) it relies on spectral information from laboratory studies rather than on ground truth data only, (2) it yields a probability or portion of a pixel belonging to a certain class or mineralogy (3) through the kriging estimation an estimate of uncertainty is derived, (4) it incorporates spatial aspects rather than only spectral aspects, (5) it is distribution free, and (6) may be applied on different supports.

The performance of the new classifier has been evaluated on a small test area in the AVIRIS Cuprite Mining District data set containing occurrences of both Kaolinite and Alunite which were mapped in detail. The accuracy of the classification was calculated by comparing with field occurrences and normalized by taking the ratio of the total misclassified pixels over the total of properly classified pixels subtracted from 100%. Calculation of this index for the classified images of Kaolinite and Alunite showed that the Indicator Kriging classifier performed slightly better than the conventional methods. Furthermore, it was found that increasing the number of spectral bands in the classification improves the accuracy until the absorption feature is entirely sampled. Adding bands at wavelengths shorter than the left shoulder and higher than the right shoulder reduces the classification accuracies.

## APPENDIX 1: Ordinary kriging of points and blocks

Geostatistics studies a variable that varies in space where not only the value but also the location of the variable is important. The main idea in estimation is to consider a variable  $z(\mathbf{x})$  at one point  $\mathbf{x}$  in space as a realization of a random function  $Z(\mathbf{x})$ ,  $\mathbf{x}$  being any point in a volume of interest (David, 1977). A regionalized variable is a realization of a random field. The spatial variations of the variable  $z(\mathbf{x})$  at point  $\mathbf{x}$  are considered as one realization of a stochastic process, that is a random function  $Z(\mathbf{x})$ . The second-order stationarity assumption consists of two parts. First, the expected value of  $Z(\mathbf{x})$  is independent of the location and equal to the mean

$$E[Z(\mathbf{x})] = m(\mathbf{x}) = m \quad (1)$$

Second, the covariance of the random variable at two points is only a function of the distance between these points

$$E\{[Z(\mathbf{x}) - m][Z(\mathbf{x}+\mathbf{h}) - m]\} = K(\mathbf{x}, \mathbf{x}+\mathbf{h}) = K(\mathbf{h}) \quad (2)$$

where  $\mathbf{h}$  is the distance between points  $\mathbf{x}$  and  $\mathbf{y}$  (David, 1977). The spatial dependence between individual points is characterized by the variance of its increments of order 0, called the variogram

$$\text{VAR}[Z(\mathbf{x}+\mathbf{h}) - Z(\mathbf{x})] = 2 \gamma(\mathbf{h}) \quad (3)$$

It can be shown that the variogram can be estimated by (Journel & Huijbregts, 1978)

$$\hat{\gamma}(\mathbf{h}) = 1/2N(\mathbf{h}) \sum [Z(\mathbf{x}_i) - Z(\mathbf{x}_i + \mathbf{h})]^2 \quad (4)$$

where  $N(\mathbf{h})$  is the number of pairs of points  $[Z(\mathbf{x}_i) - Z(\mathbf{x}_i + \mathbf{h})]$  available for distance  $\mathbf{h}$ . The best linear unbiased estimator (BLUE) of the value of the variable at any unknown location, given by  $Z_v(\mathbf{x})$ , can be obtained by kriging. The name of this interpolation technique was coined by George Matheron in recognition of the early work done by D.G. Krige. The problem is to estimate  $Z_v(\mathbf{x})$  from a linear combination  $Z_v^*$  of available sample values  $(Z\mathbf{x}_\alpha, \alpha=1 \dots N)$ . Two conditions are required: the estimator is unbiased

$$E(Z_v(\mathbf{x}) - Z_v^*) = 0 \quad (5)$$

- Mineral mapping -

and it will have a minimum estimation variance. Using the estimation variance we want to find a set of weights ( $\lambda_i$ ) assigned to the various points so that the kriging error ( $\sigma_k^2$ ) is minimized

$$\sigma_k^2 = 2 \sum \lambda_i \gamma(x_i, x_0) - \sum \sum \lambda_i \lambda_j \gamma(x_i, x_j) \quad (6)$$

where  $\lambda(x_i, x_0)$  is the semivariance between location  $x_0$  to be estimated and location  $x_i$  at which the value of the variable is known, and  $\gamma(x_i, x_j)$  is the semivariance between the observations at locations  $x_i$  and  $x_j$ . The weights are chosen so that they sum up to 1 (ensuring unbiasedness) and that the error variance is minimized

$$\sigma_k^2 = \sum \lambda_i \gamma(x_i, x_j) + \mu - \gamma(x_i, x_0) \text{ for all } i \quad (7)$$

where  $\mu$  is the lagrange multiplier associated with the minimization. This yields

$$\sigma_k^2 = \sum \lambda_i \gamma(x_i, x_0) - \mu \quad (8)$$

where  $\lambda_i$  and  $\mu$  are obtained by solving the following matrix equations

$$c = A^{-1} b \quad (9)$$

where  $A = \begin{bmatrix} \gamma(x_1, x_1) & \gamma(x_2, x_1) & \dots & \gamma(x_n, x_1) & 1 \\ \gamma(x_1, x_2) & \gamma(x_2, x_2) & \dots & \gamma(x_n, x_2) & 1 \\ \cdot & \cdot & \cdot & \cdot & 1 \\ \cdot & \cdot & \cdot & \cdot & 1 \\ \cdot & \cdot & \cdot & \cdot & 1 \\ \gamma(x_1, x_n) & \gamma(x_2, x_n) & \dots & \gamma(x_n, x_n) & 1 \\ 1 & 1 & \cdot & 1 & 0 \end{bmatrix}$

$$B = \begin{bmatrix} \gamma(x_1, x_0) \\ \gamma(x_2, x_0) \\ \cdot \\ \cdot \\ \cdot \\ \gamma(x_n, x_0) \\ 1 \end{bmatrix} \quad (10)$$

$$C = \begin{bmatrix} \lambda_1 \\ \lambda_2 \\ \cdot \\ \cdot \\ \cdot \\ \lambda_n \\ \mu \end{bmatrix}$$

In these equations, point  $x_0$  is the point to be estimated using the values at known locations  $x_1, \dots, x_n$ . The kriged estimate of variable  $Z$  at location  $Z(x_0)$  becomes

$$Z(x_0) = \sum \lambda_i Z(x_i) \quad (11)$$

For block estimation, the estimation variance  $\sigma_{kb}^2$  becomes

$$\sigma_{kb}^2 = \sum \lambda_i \gamma(x_i, V) + \mu_b \gamma(V, V) \quad (12)$$

where  $\gamma(x_i, V)$  is the average semivariance between the observation points and block  $V$  and  $\gamma(V, V)$  is the average semivariance between points within block  $V$ . The parameter  $\mu_b$  is the lagrange multiplier. The system of equations for ordinary block kriging in matrix form is

$$[W] \cdot [\lambda] = [B] \quad (13)$$

where

$$[\lambda] = \begin{bmatrix} \lambda_1 \\ \lambda_2 \\ \lambda_3 \\ \cdot \\ \cdot \\ \lambda_n \\ -\mu \end{bmatrix} \quad (14)$$

and

$$[B] = \begin{bmatrix} \gamma(v_1, V) \\ \gamma(v_2, V) \\ \gamma(v_3, V) \\ \vdots \\ \gamma(v_n, V) \\ 1 \end{bmatrix} \quad (15)$$

and

$$[W] = \begin{bmatrix} \gamma(v_1, v_1) & \gamma(v_1, v_2) & \gamma(v_1, v_n) & 1 \\ \gamma(v_2, v_1) & & & \\ \gamma(v_3, v_1) & & & \\ \vdots & & & \\ \vdots & & & \\ \gamma(v_n, v_1) & \dots & \gamma(v_n, v_n) & 1 \\ 1 & & 1 & 0 \end{bmatrix} \quad (16)$$

In this, the matrix  $[W]$  is a sample-to-sample semivariance, the matrix  $[B]$  is the sample-to-block semivariance, and  $[\lambda]$  are the weights assigned to each of the sample locations. In practice, the sample-to-block semivariances are found through a discrete summation rather than through an integration. The block volume,  $V$ , is represented by a number of discretizing points and the semivariance between each point discretizing the block and the sample  $v_i$  is computed and averaged to yield a value for  $\gamma(v_i, V)$ .

## APPENDIX 2: Support correction

From the above, it can be seen that the kriging estimator does not necessary have to produce estimates on the same spatial area as the sample values; estimation on smaller blocks or subpixel areas is possible (Van der Meer, 1994d). However in doing so, prior to performing indicator transformation on the pixel data, a correction for the change of pixel size or support between input and output data need to be made. A relation exists between the support or size of the data, and the distribution of their values. For example, measuring the depth of an absorption feature from rock samples of 5\*5 cm (typical for laboratory measurements) will yield more variability than the analysis of the same depth feature using 1\*1 m outcrop with a field spectrometer. Therefore, before applying the indicator kriging method to the image data we have to correct this data for the support or pixel size on which we produce our estimates. Regarding the image data as point estimates at the center of a pixel we have to transform this original point distribution to the distribution expected for several sizes of block estimates. It can be shown that increasing the support mainly affects the variance and spread of the distribution leaving the mean unchanged. The range at which the spread decreases and the distribution becomes more symmetric depends on the spatial arrangement of the data. Several methods of support correction have been proposed of which the affine transformation and the lognormal transformation are the simplest and most straightforward. The affine correction transforms the original distribution  $q$  to another distribution  $q'$  using the following linear transformation

$$q' = \sqrt{f} * (q-m) + m \quad (1)$$

where  $f$  is the variance adjustment factor and  $m$  is the mean of the original point distribution. Note that the mean is forced to remain unchanged and that the spread decreases while the skewness remains the same. The indirect lognormal correction is a method that uses a transformation of original point support to block support assuming a lognormal distribution. The transformed values are obtained by

$$q' = aq^b \quad (2)$$

with  $a$  and  $b$  defined as

$$\begin{aligned} a &= [m/\sqrt{(f CV^2 + 1)}] * [(\sqrt{CV^2 + 1})/m]^b \\ b &= \sqrt{[(\ln(f CV^2 + 1))/(\ln(CV^2 + 1))]} \end{aligned} \quad (3)$$

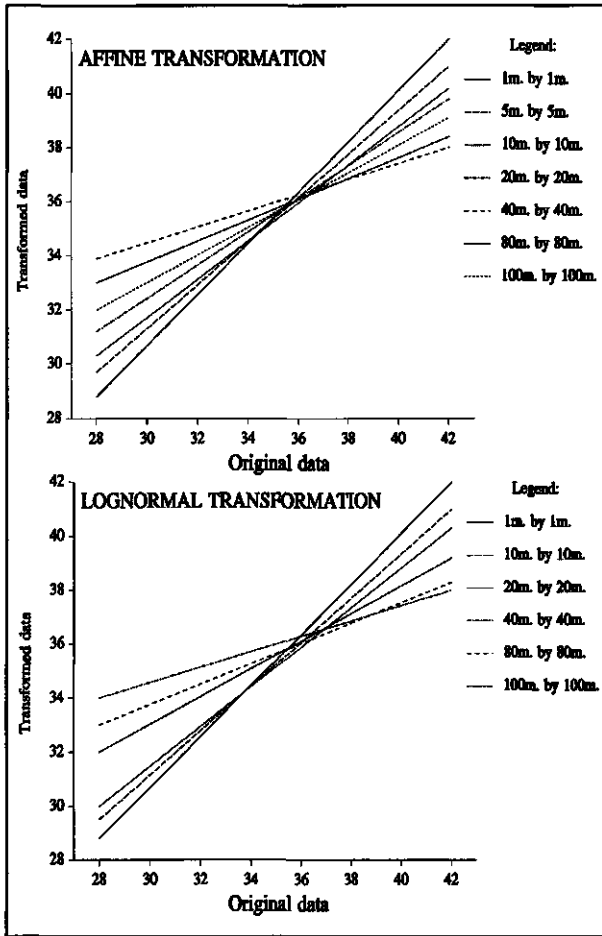


Fig. A2.1: Original distribution and distribution of data after support correction for various block sizes using the Affine correction (top) and the Indirect Lognormal correction (bottom).

where CV is the coefficient of variation of the original point distribution (standard deviation divided by the mean). However, if the original distribution is not exactly lognormal, the method does not necessarily preserve the mean value. The variance adjustment factor ( $f$ ) can be derived by introducing the dispersion variance. The dispersion variance is an average squared difference that has the support of the individual values ( $a$ ) and the support of the mean ( $b$ ) explicitly stated

$$\sigma^2(a,b) = \frac{1}{n} \sum_{i=1}^n (v_i + m_0)^2 \quad (4)$$

- Chapter 8 -

Table A2.1: Dispersion variances calculated for different support.  $\sigma^2(.,A)$ =dispersion variance of the points;  $\sigma^2(.,B)$ =dispersion variance within the blocks;  $\sigma^2(B,A)$ =dispersion variance between the blocks;  $f$ =variance adjustment factor.

	$\sigma^2(.,A)$	$\sigma^2(.,B)$	$\sigma^2(B,A)$	$f$
points	5.3394	----	----	----
1*1m.	5.3394	0.2811	5.0583	0.947
5*5m.	5.3394	1.8403	3.4991	0.655
10*10m.	5.3394	1.8557	3.4837	0.652
20*20m.	5.3394	1.8751	3.4643	0.649
40*40m.	5.3394	4.6846	0.6548	0.123
80*80m.	5.3394	4.4340	0.9054	0.170
100*100m.	5.3394	3.7861	1.5533	0.291

where  $v_1, \dots, v_n$  are the  $n$  point values and  $m$  is their arithmetic mean. Thus, the dispersion variance of the original point data ( $\sigma^2(.,A)$ ) equals the dispersion variance between the estimated block support ( $\sigma^2(B,A)$ ) plus the dispersion variance within the blocks ( $\sigma^2(.,B)$ ).

$$\sigma^2(.,A) = \sigma^2(.,B) + \sigma^2(B,A) \quad (5)$$

The variance adjustment factor is the ratio of the block variance to the point variance

$$f = \sigma^2(B,A)/\sigma^2(.,A) = 1 - \sigma^2(.,B)/\sigma^2(.,A) \quad (6)$$

The dispersion variance of the points within the entire area can be written as

$$\sigma^2(.,A) = 1/n \sum_{i=1}^n (v_i - m)^2 \quad (7)$$

where  $v_1, \dots, v_n$  are the  $n$  point values in volume  $V$  and  $m$  is their arithmetic mean. This equals the following expression



- Mineral mapping -

Table A2.2: Statistics of data distribution after affine transformation for support correction.

	mean	$\sigma^2$	minimum	maximum	skewness	C.V.
point	36.44	5.34	31	43	-0.411	6.34
1*1m.	36.44	5.05	31.14	42.82	-0.411	6.17
5*5m.	36.44	3.43	32.08	41.69	-0.411	5.08
10*10m	36.44	3.48	32.05	41.73	-0.411	5.12
20*20m	36.44	3.47	32.06	41.72	-0.411	5.11
40*40m	36.44	0.66	34.53	38.74	-0.411	2.26
80*80m	36.44	0.91	34.20	39.14	-0.411	2.61
100m.	36.44	1.16	33.51	39.98	-0.411	3.42

Table A2.3: Statistics of data distribution after lognormal transformation for support correction.

	mean	$\sigma^2$	minimum	maximum	skewness	C.V.
point	36.44	5.34	31	43	-0.411	6.34
1*1m.	36.44	5.04	31.15	42.80	-0.416	6.16
5*5m.	36.42	3.53	31.96	41.66	-0.446	5.15
10*10m	36.42	3.51	31.96	41.65	-0.446	5.14
20*20m	36.43	3.49	31.98	41.64	-0.446	5.13
40*40m	36.44	0.67	34.45	38.64	-0.530	2.25
80*80m	36.44	0.93	34.10	39.04	-0.529	2.65
100m.	36.43	1.58	33.41	39.86	-0.495	3.45

$$\sigma^2(.,A)=1/2n^2 \sum_{i=1}^n \sum_{j=1}^n (v_i - v_j)^2 \quad (8)$$

which is intrinsically similar to the definition of the variogram. Therefore the dispersion variance for point values can be derived directly from the variogram, the dispersion variance of points within the block ( $\sigma^2(.,B)$ ) can be estimated by discretizing the block into several points and calculating the average variogram value between all possible pairs of points. From this the variance adjustment factor (f) can be obtained.

The average experimental variogram for the image data is fitted using a double exponential model with a small nugget component following the expression

$$\gamma(h) = 0.5 + 3[1 - \exp(-h/400)] + 3.5[1 - \exp(-h/600)] \quad (9)$$

The estimated dispersion variances using the method described above are listed in Table A2.1. The statistics of the resulting distributions after applying the affine correction are summarized in Table A2.2. The distributions are shown in Fig. A2.1. Clearly, the affine correction preserves the mean and skewness of the distribution and reduces the spread. The resulting statistics of the data distributions after applying the lognormal transformation are shown in Table A2.3. The method nearly preserves the mean value indicating that the original distribution of points was nearly lognormal. The skewness, however, decreases as does the variance. However, both correction methods result in nearly identical re-distribution of the data.

## CHAPTER 9:

### *Imaging Spectrometry and the Ronda peridotites*<sup>7</sup>

#### ABSTRACT

Spectral unmixing and mineral mapping from GERIS data reveals several metamorphic minerals in marbles bordering the peridotites. The peridotite body itself is shown to be zoned into a garnet-, spinel-, and plagioclase-lherzolite facies reflecting decreasing pressures and temperatures related to diapiric uprise and subsequent cooling of the body. This zonation is overprinted by two phases of late-stage serpentinization which are interpreted as resulting from regional metamorphism related to northwestward thrusting of the peridotite body. Two Case Studies are presented demonstrating the use of imaging spectrometry in mineral exploration. The first deals with calcite-dolomite mineral mapping, of importance for oil exploration. The semi-linear model for the position of the carbonate absorption-band related to the calcite content of the sample derived in Chapter 4 forms the basis for this analysis. The second case studies yields the estimation of the degree of serpentinization, important in asbestos mining, based in spectral reflectance spectroscopy presented in Chapter 5. In both cases, a newly developed methodology for mineral mapping in the presence of vegetation is used. This methodology consists of four principal steps: (1) vegetation masking, (2) calculating the absorption band-depth using a Hull quotient spectrum, (3) translating this into mineral occurrence value using a semi-empirical linear model, and (4) estimating the degree of mineral occurrence at the pixel support using geostatistical techniques. In this approach, estimation and simulation techniques are used to gain data at densely vegetated areas. Comparison with field data in both cases shows that the methodology can be used within reasonable statistical fluctuations.

---

<sup>7</sup>Parts of this Chapter have been published as:

Van der Meer, F. 1994. Sequential Indicator Conditional Simulation and Indicator Kriging applied to discrimination of dolomitization in GER 63-Channel imaging spectrometer data. *Nonrenewable Resources*, 3(2): 146-164.

Van der Meer, F. 1994. Mapping the degree of serpentinization within ultramafic rock bodies using imaging spectrometer data. *International Journal of Remote Sensing*, 15(18): 3851-3857.

Van der Meer, F. 1995. Estimating and simulating the degree of serpentinization of peridotites using hyperspectral remotely sensed imagery. *Nonrenewable Resources*, 4(1): 84-98.

Van der Meer, F. 1994. Metamorphic facies zonation in the Ronda peridotites mapped from GER imaging spectrometer data. *International Journal of Remote Sensing*, submitted.

## 9.1 INTRODUCTION

This final Chapter deals with the application of mineral mapping techniques to imaging spectrometer data of southern Spain. Spectral Angle Mapping and linear unmixing analysis are used to map surface mineralogy of the Ronda peridotites and adjacent metamorphic rocks with emphasis on the mineralogical composition of the massif as related to the mode and timing of its emplacement. Two Case Studies are presented to demonstrate the use of imaging spectrometry for mineral exploration in vegetated areas. The first Case Study deals with calcite-dolomite mineral mapping based on the quantitative model found in Chapter 4 describing the position of the carbonate absorption band in relation to the relative calcite content of a sample. This application is in particular important in oil exploration. The second Case Study addresses the problem of mapping the degree of serpentinization within ultramafic rock bodies based on the discussion and models derived in Chapter 5. Knowledge of weathering characteristics of both carbonate and ultramafic rocks as discussed in Chapter 6 is incorporated as well as the spectral signature of vegetation. A methodology is proposed for these two studies to overcome the problems related to vegetation cover. This methodology consists of four principal steps: (1) vegetation masking, (2) calculating the absorption band-depth using a Hull quotient spectrum, (3) translating this into mineral occurrence value using a semi-empirical linear model, and (4) estimating the degree of mineral occurrence at the pixel support using conditional simulation techniques or ordinary block kriging.

A number of recent studies have demonstrated the usefulness of geostatistics in the analysis of remotely sensed imagery (Curran, 1994). Many workers have used the semivariogram to characterize spatial variability of digital images (Curran, 1988; Duggin *et al.*, 1985; Webster *et al.*, 1989). Cohen *et al.* (1990) use the semivariogram for the analysis of conifer canopy structure, Jupp *et al.* (1988; 1989) developed techniques for calculating the autocorrelation function in digital images, and Woodcock *et al.* (1988a+b) use the semivariogram for the characterization of different ground cover classes. Several authors have demonstrated the use of geostatistical estimation techniques for quantification of measurement error in remotely sensed images (Lunetta *et al.*, 1991; Curran & Williamson, 1985; 1986; Curran & Hay, 1986) and in Chapter 8 of this thesis a technique for mineral mapping was derived using geostatistical estimation theory yielding accuracy or reliability estimates for ground cover classes. Recently, Rossi *et al.* (1994) demonstrate that geostatistical techniques can be used for re-sampling remotely sensed images when distortion occurs or information is missing. Landgrebe (1992) showed that signal of remotely sensed data can be treated as a stochastic process and thus allows the application of simulation techniques in remote sensing.

In this Chapter, geostatistical techniques are exploited for re-sampling remote sensing data at unknown locations where signal is obscured by, in this case, vegetation.

## 9.2 MINERAL MAPPING AND THE RONDA PERIDOTITES

### 9.2.1 Spectral unmixing

In order to model the spectral variability of the GERIS data, spectral unmixing is used. Six spectral endmembers were required to model the continuum reflectance of each pixel in the data set: three soil types, green vegetation (and grass), senescent vegetation, and decayed vegetation. These endmembers explain approximately 93% of the spectral variability on the average at a pixel resolution. The remaining unexplained variability may be attributed to shade or albedo variations that are due to the effects of variable illumination and shading which are not properly compensated in the atmospheric calibration process. Constrained unmixing was used (Smith *et al.*, 1994; see also Chapter 8) thus forcing the abundance estimates for each endmember to be greater or equal to zero and the sum of the abundances less or equal to one. The outcome of the unmixing analysis is an abundance image for each endmember, one image for the sum of all abundances, and a root-mean-square (RMS) image. The RMS image is the error between the original, mixed spectrum and the best-fit spectrum calculated from the resulting endmember abundances. The solution of the unmixing was considered valid when the abundance values across the image were mostly between one and zero, the average RMS error is low and in the order of magnitude of the noise component of the image, and the RMS error image shows a low spatial correlation.

Soil samples and the method of sampling of these samples is described in detail in Chapter 6. Three different types of soil spectral profiles were used as endmembers. The spectral reflectance characteristics of soils are dominated by 1.4 $\mu\text{m}$  and 1.9 $\mu\text{m}$  absorption features due to water also causing the general decrease in reflectance at wavelengths longer than 2.2 $\mu\text{m}$  (Singh & Sirohi, 1994). Narrow absorption features near 2.2 $\mu\text{m}$  and 2.3 $\mu\text{m}$  are due to Al-OH and Mg-OH combination tones. Absorption features in the visible part of the spectrum are due to  $\text{Fe}^{2+}$  and  $\text{Fe}^{3+}$ . Spectra of soil samples from the peridotites show strong absorption features near 0.5 $\mu\text{m}$  and 0.9 $\mu\text{m}$  and a strong and positive continuum slope in the visible toward shorter wavelengths pointing to the presence of iron. The water absorption bands as well as the Al-OH and Mg-OH features are relative weak and the overall reflectivity is moderate. The soil samples taken from areas underlain by limestone are characterized by weak or nearly absent iron absorption bands and strong water and hydroxyl absorption bands. The absorption band near 2.3 $\mu\text{m}$  is usually very strong compared to those of soils from the peridotite terrain. The third group of soil samples are the soils having a low albedo and weak absorption features due to the spectral masking effect possibly caused by the presence of finely disseminated organic carbon. Spectra of healthy, green vegetation and senescent

This figure is displayed as colour plate 6 on page 315

**Fig. 9.1:** Color-composite image with the peridotite soil endmember displayed in red, the limestone soil endmember displayed in green, and the spectrally quenched soil endmember displayed in blue.

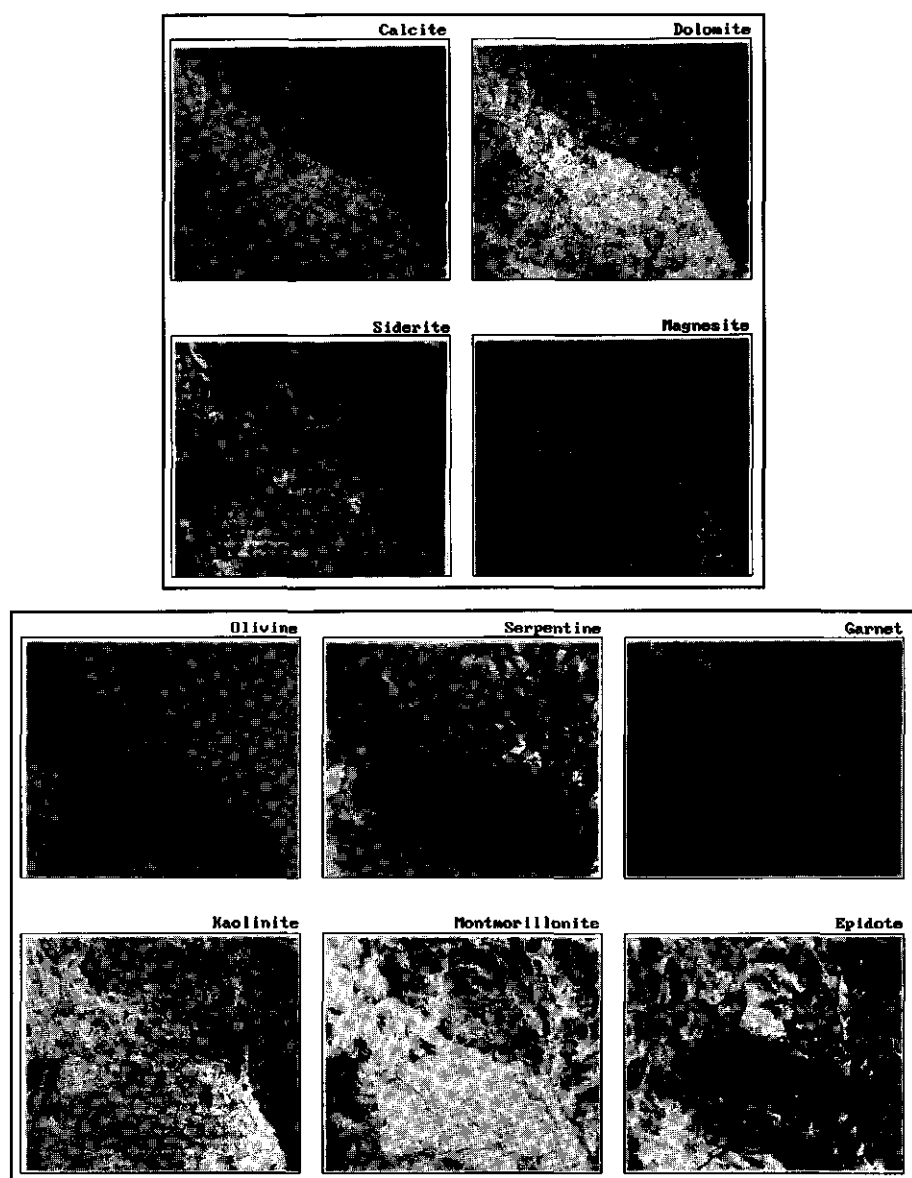
vegetation differ primarily in the shape of the spectrum between  $0.4\mu\text{m}$  and  $1.0\mu\text{m}$ . Green vegetation has low reflectivity between  $0.4\mu\text{m}$  and  $0.65\mu\text{m}$  and a very steep rise in reflectivity from  $0.65\mu\text{m}$  to the plateau reflectance reached at  $0.75\mu\text{m}$ . Senescent vegetation shows a spectrum dominated by a gradual increase in reflectivity between  $0.4\mu\text{m}$  and  $0.75\mu\text{m}$  where it reaches its plateau. Partly decayed vegetation has a spectrum converging towards that of soils, however detailed water absorption features at wavelengths longer than  $1.2\mu\text{m}$  can be used to discriminate decayed vegetation from soil.

Fig. 9.1 is a color-composite with the peridotite soil endmember in red, the limestone soil endmember displayed in green, and the spectrally quenched soil endmember displayed in blue. It should be noted that the soil spectra characterized by weak absorption features and low reflectivity are found predominantly along the marble-peridotite contact. These are interpreted as being mylonitic in origin related to the late-stage thrust emplacement of the peridotites. The vegetation endmember spectra are later in this Chapter used for vegetation masking.

### 9.2.2 Mineral mapping

The peridotites in the Sierra Bermeja are bordered to the west by a HP-HT series of phyllites, garnet-staurolite mica schists, and gneisses of what is known as the Casares Unit (Lundeen,

*- Imaging spectrometry and the Ronda peridotites -*



**Fig. 9.2:** Examples of mineral maps for several minerals resulting from Spectral Angle Mapping (grey scale ranges from zero to  $\pi/2$  radiance). More similar pixels are bright whereas un-similar pixels are dark.

1978), "Gneiss series" (Loomis, 1972) or Los Reales Nappe (Tubía & Cuevas, 1986). This series is a contact metamorphic aureole surrounding the peridotite complex which grades from

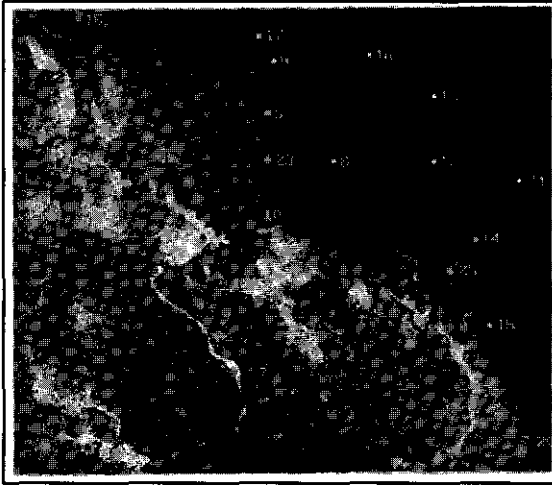


Fig. 9.3: Location of 25 pixel spectra for minerals mapped (legend: 1 = calcite, 2 = dolomite, 3 = siderite, 4 = magnesite, 5 = graphite, 6 = brucite, 7 = goethite, 8 = hematite, 9 = magnetite, 10 = wollastonite, 11 = tremolite, 12 = diopside, 13 = augite, 14 = hypersthene, 15 = enstatite, 16 = olivine, 17 = serpentine, 18 = garnet, 19 = kaolinite, 20 = montmorillonite, 21 = epidote, 22 = chlorite, 23 = spinel, 24 = plagioclase, 25 = muscovite).

greenschist facies to high-grade granulite facies. At the eastern contact of the Sierra Bermeja peridotite, a second metamorphic facies series is observed, related to LP-HT ( $700-800^{\circ}$ ,  $\pm 3.5$  kbar, Lundeen 1978) contact metamorphism resulting in garnet-staurolite mica schists and gneisses grading into leucocratic cordierite gneisses and mylonitized hornfelses. The southern contact, separating the peridotite from the underlying units, has been shown to be a gently undulating thrust surface (Lundeen, 1978). Mylonitization, which occurs in a zone of 100m along the contact, resulted in the development of "cordierite gneisses" indicating HP-LT conditions (Lundeen, 1978). The rock units forming the southern and eastern contact with the peridotites are locally known as the Blanca unit (Lundeen, 1978), the "Hornfels series" (Loomis, 1972) and the Guadaiza Nappe (Tubía & Cuevas, 1986).

Chabrilat *et al.* (1994) mapped different peridotite types from ISM and AVIRIS data over the Ronda peridotite massif. Mineral occurrences in the Sierra Bermeja peridotite were mapped from GERIS data in order to identify the major surface constituents on the basis of spectral properties using Spectral Angle Mapping and unmixing analysis (Boardman, 1994; Kruse *et al.*, 1993; Smith *et al.*, 1994) as described in Chapter 8. Mineral maps for 25 different minerals were prepared using the Spectral Angle Mapping-algorithm of which examples are shown in Fig. 9.2. Pixel spectra were extracted at locations mapped as having high spectral similarity with laboratory mineral spectra. The location of these pixel spectra is shown in Fig. 9.3 and some examples are shown in Fig. 9.4. Fig. 9.5 shows a compilation of the resulting mineral maps by assigning the pixels to the mineral having the lowest spectral angle. The contact metamorphic aureole, as present in the GERIS data set, is formed by a series of marbles which grade into limestones and dolomitic limestones with distance from



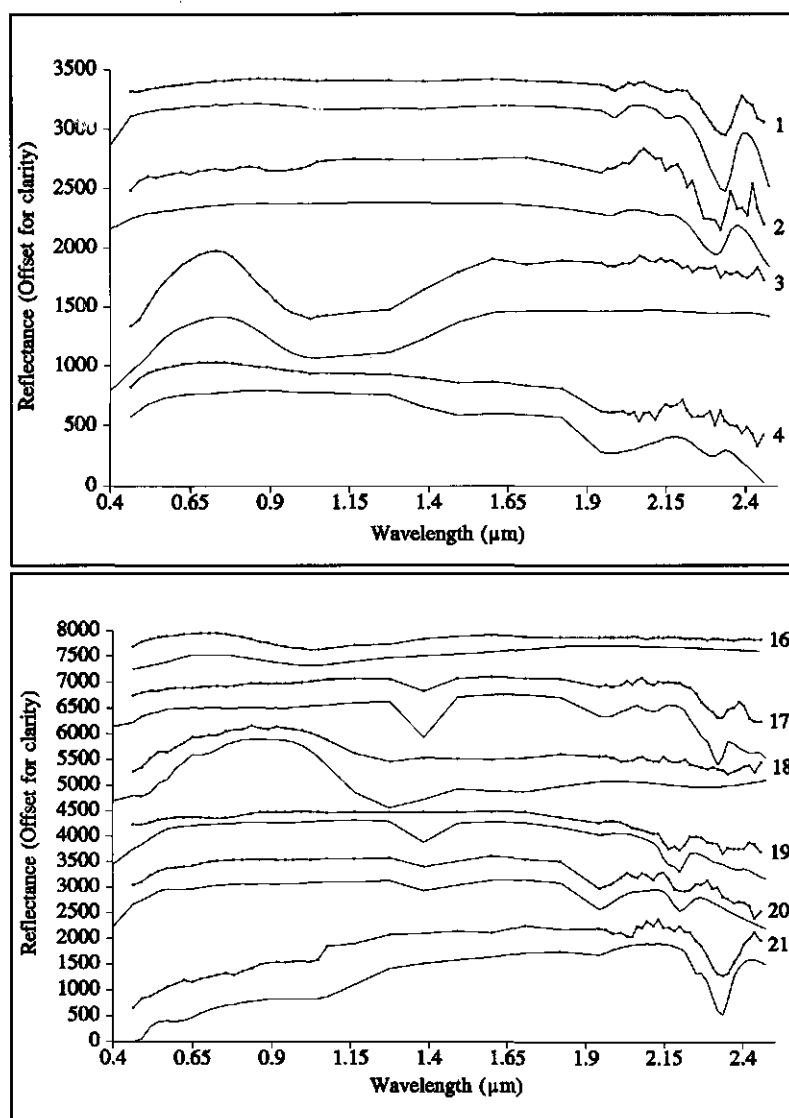


Fig. 9.4: Pixel spectra (point-dot lines) and laboratory spectra (solid-lines) for minerals of Fig. 9.2. See Fig. 9.3 for location and mineral name. Laboratory spectra are re-sampled to the GERIS band channel position and width.

the peridotite contact. The marbles show the strongest carbonate absorption bands and contain accessory metamorphic minerals of which tremolite could be mapped from the GERIS data. Tremolite is a magnesium hydroxyl silicate mineral of the amphibole group indicating relative low-grade regional metamorphism in the dolomitic marbles. In the area where the marbles border the gneiss series (e.g., towards the dolomitized front of the ancient carbonate platform, Van der Meer, 1994f), magnesite occurs. This magnesite, may indicate alteration of forsterite

This figure is displayed as colour plate 7 on page 316

**Fig. 9.5:** GERIS band 30 centered at  $1.7099\mu\text{m}$  with mineral occurrences of major mineral assemblages overlain. Top is the thermal aureole and limestone country rock, bottom is the ultramafic body.

to serpentine with formation of magnesite where forsterite is interpreted as resulting from thermal metamorphism of dolomitic limestones. Locally, siderite was mapped in the limestone-marble series. Siderite is an iron carbonate mineral often occurring as replacement in limestones.

The Ronda peridotite massif itself is composed of lherzolites, harzburgites and dunites in which the extent of late-stage serpentinization varies widely. The harzburgites are characterized by spectra dominated by the mineral enstatite, whereas the lherzolites are dominated by the spectral features of diopside. Mineral mapping in the ultramafic body

permits a metamorphic zonation into garnet-, spinel-, and plagioclase-lherzolite facies (Fig. 9.6). The highest pressures and temperatures are reflected by the garnet-lherzolite facies, intermediate pressure and temperature conditions by the spinel-lherzolite facies, and low pressure and temperature conditions by the plagioclase-lherzolite facies. The garnet is of pyrope-almandine composition with important amounts of grossular. Obata (1980) interpreted this metamorphic zonation in terms of a diapiric rising upper mantle body. This author proposed that the interior of the diapir, being hotter than the exterior, followed a different pressure-temperature path during ascent. The cooler exterior part, represented by the garnet-lherzolite facies, equilibrated at greater depth before the hotter interior part, represented by the plagioclase-lherzolite facies equilibrated at a shallower depth and thus at lower pressures. Clearly, from the facies distributions it can be seen that the peridotite massif itself is tilted towards the southeast and must have therefore undergone considerable tectonic deformation and transportation.

Serpentine and magnetite, mapped within the peridotite body, are the result of the serpentization-process by which anhydrous ferromagnesian silicate minerals (olivine, enstatite) are converted to hydrous ferromagnesian serpentine-group minerals. In the case of the Sierra Bermeja peridotites, Fe-bearing anhydrous phases are involved yielding besides serpentine also magnetite. Interestingly, the occurrence of serpentine is not related to the metamorphic facies distribution in the peridotites and seems to occur mainly near the boundary of the peridotite massif. This may indicate that serpentization is related to a latter phase of low-grade metamorphism overprinting the initial metamorphic facies of the peridotites related to their crustal emplacement. The temperatures and pressures for the production of various serpentine mineral assemblages have been determined by reversed bracketing experiments in the presence of water by Moody (1976). At low temperatures (300-400°), an association of lizardite and chrysotile occurs, whereas antigorite replaces lizardite or chrysotile at higher temperatures (>500°). The higher temperature associated with antigorite formation occurs when dehydration of the mineralogy produces a lower activity of water which results in the formation of antigorite with less  $Mg(OH)_2$  than found in either lizardite or chrysotile (Evans & Frost, 1975). This points to an upper crustal environment for serpentization at relatively low oxygen fugacity (Evans & Frost, 1975). Wenner & Taylor (1974) conclude from isotopic studies that serpentization in the peridotite parts of ophiolites occurred after continental emplacement. These authors further conclude that pervasive lizardite-chrysotile serpentization is caused by fluids of meteoric-hydrothermal origin or by waters emanating from sedimentary formations, whereas antigoritic serpentization takes place as a result of regional metamorphism in the presence of non-meteoric waters. In the Sierra Bermeja peridotites, both lizardite-chrysotile and antigorite occur. These are interpreted as representing two subsequent phases of serpentization; low-temperature serpentization,

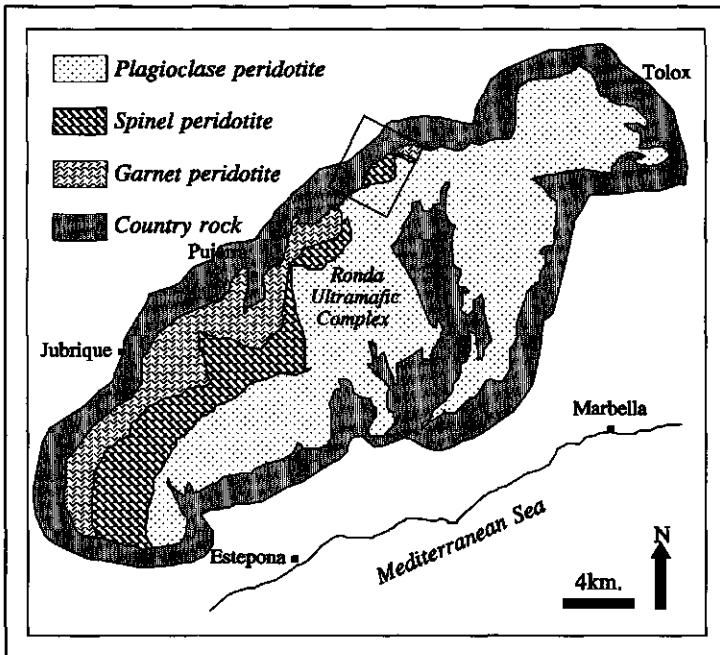


Fig. 9.6: Map of the Ronda ultramafic complex (partly after Obata, 1980; Lundeen, 1978; Reisberg *et al.*, 1989) showing metamorphic facies boundaries mapped from GERIS imagery within the investigated area (indicated by the box).

producing lizardite and chrysotile, and higher-temperature serpentinization producing antigorite as a result of regional metamorphism related to the "cold" phase of emplacement of the peridotites. Both phases of serpentinization postdate the crustal emplacement of the peridotites. Another argument supporting this hypothesis is the source of water needed for the hydration process. This cannot be derived from crustal rocks, however could be derived from the phyllite-schist-gneiss series bordering the peridotites.

### 9.3 CASE STUDY I: CALCITE-DOLOMITE MINERAL MAPPING

Mapping calcite and dolomite mineral occurrences is of economic interest for various reasons. Replacement of carbonate lithologies by calc-silicates such as garnet and pyroxene often occurs associated with granitic plutons. The resulting skarns can host high-grade deposits of copper, gold, iron, lead, zinc, or tungsten. Dolomitization of limestones increases the porosity of the rock by 12% making these lithologies possible targets for oil exploration.

Discriminating calcite from dolomite in laboratory reflectance spectra is possible because both minerals show absorption features in the near-infrared which are slightly displaced (see Chapter 4). The center of the calcite absorption feature is found at a few

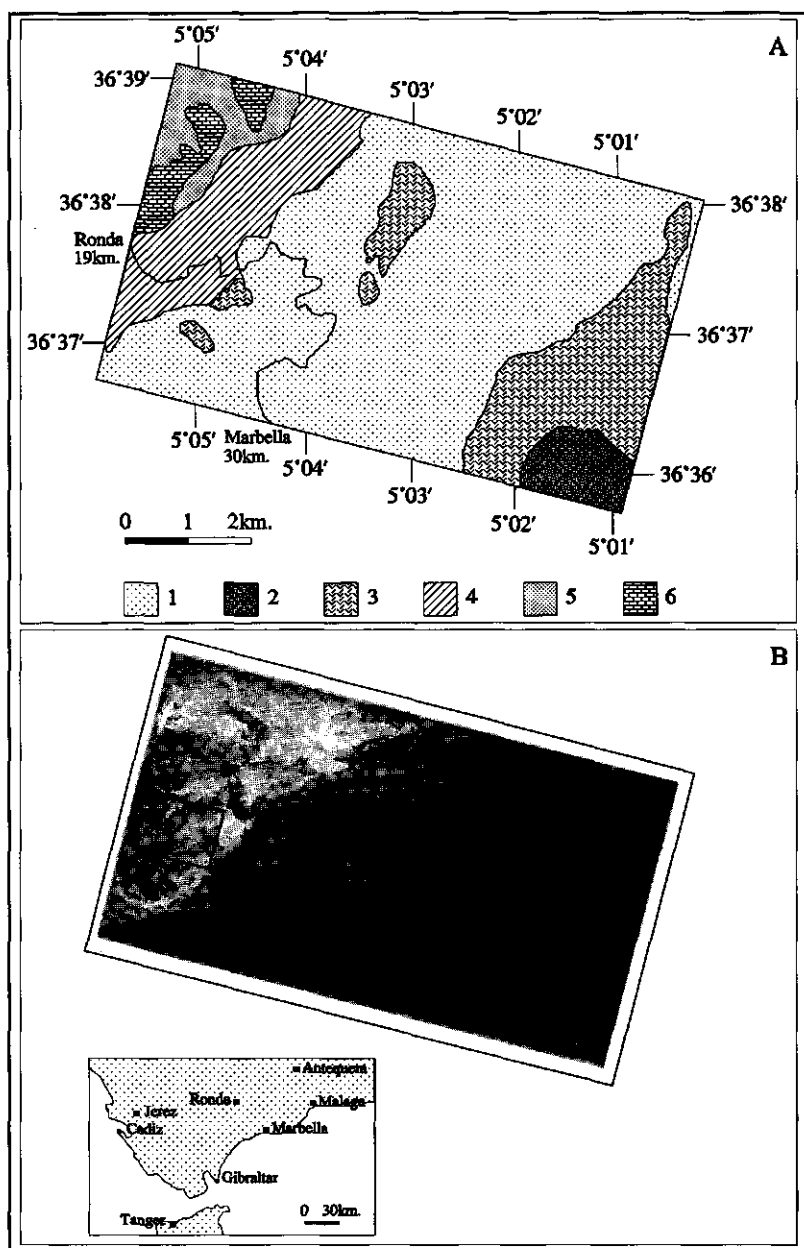


Fig. 9.7: (A) Lithologic map and (B) GERIS band 30 centered at 1.7099 μm of the strip covered. The box indicates the 100-by-100 pixel area used as a test-field for the mapping of dolomitization. Letters indicate the location of GERIS pixel spectra shown in Fig. 9.9.

nanometers higher wavelength than that of dolomite. In Chapter 4, a nearly linear relationship was established between the calcite-dolomite content of synthetic mixtures and the position of the carbonate absorption band. This relation was also predicted using mineral mixture models. Below, the linear model derived in Chapter 4 will be used to map the degree of dolomitization in GER 63-channel imaging spectrometer data from southern Spain.

### 9.3.1 GERIS Data preparation

A 100-by-100 pixel window (Fig. 9.7) was selected from the calibrated GERIS data set consisting only of carbonate rocks and vegetation. Calibration was done using the Empirical Line method as described in Chapter 7. The area covered by the window was sampled in detail in the field. Pixels showing characteristic carbonate absorption-bands in the GERIS images were identified within the window through the following steps:

1) Masking of vegetation:

Dense vegetation masks the spectral signal of the underlying rocks thus obscuring the carbonate absorption-band in pixel spectra. In order to remove pixels consisting mainly of vegetation from the data set, a vegetation index for the GERIS image was calculated following the procedure outlined by Okada *et al.* (1993). Approximately 86% of the pixels were removed after masking.

2) Determining the carbonate absorption-band position:

For the remaining pixels, the position of the carbonate absorption-band was determined using the procedure of continuum removal outlined earlier (see also Clark & Roush, 1984; Okada & Iwashita, 1992). Using this approach, the GERIS band in which the absorption center falls could be determined.

3) Conversion of the absorption-band centers to calcite-dolomite abundances:

From Table 9.1 it can be seen that the full range of pixels for characterizing calcite/dolomite mineral mixtures is covered by the spectral bands 53 to 56 of the GERIS data set. As mentioned earlier, the bands are  $0.017\mu\text{m}$  wide. Using the semi-linear model for the calcite-dolomite weight percentages the absorption-band centers ( $\lambda_{\text{Carb}}$ ) occurring in any GERIS spectral band (e.g.,  $\lambda_{53}$ ) could be converted to weight percentages calcite ( $z(x)$ ) for a pixel at location  $x$  as:

$$\begin{aligned}\lambda_{\text{Carb}} \in \lambda_{53} : 0\% < z(x) \leq 26\% \\ \lambda_{\text{Carb}} \in \lambda_{54} : 26\% < z(x) \leq 57\% \\ \lambda_{\text{Carb}} \in \lambda_{55} : 57\% < z(x) \leq 86\% \\ \lambda_{\text{Carb}} \in \lambda_{56} : 86\% < z(x) \leq 100\%\end{aligned}\tag{1}$$

Table 9.1: GERIS spectral band positions and corresponding weight percentages of calcite.

GERIS band number	wavelength (μm)			weight % calcite	
	minimum	center	maximum	minimum	maximum
53	2.2935	2.3020	2.3105	0	26
54	2.3105	2.3190	2.3275	27	57
55	2.3275	2.3360	2.3445	58	86
56	2.3445	2.3530	2.3615	87	100

By this definition, the variable  $z(\mathbf{x})$  takes on a range of values and can therefore best be treated as a category indicator variable. The resulting classes are shown in Fig. 9.8. In order to estimate the calcite-dolomite abundance at unknown locations (e.g., the pixels identified earlier as vegetation), indicator kriging and indicator based simulation techniques are exploited below.

### 9.3.2 Estimating calcite-dolomite abundances using Indicator Kriging

Indicator kriging (Journel, 1983; see also Appendix 1 of Chapter 7) aims at estimating a conditional cumulative distribution function at each cutoff  $z_b$  from a set of indicator transforms  $i(\mathbf{x}; z_b)$  at locations  $\mathbf{x}$  set to 1 if  $z(\mathbf{x}) \leq z_b$ , else 0 (assuming a continuous variable). The indicator variables are defined in Eq.(1) according to the presence or absence of an carbonate absorption-band center in a specific GERIS spectral band. Indicator kriging (Journel, 1983) will provide an estimate of the conditional expectation of the indicator transformation of the random variable  $z_b$  given the realizations of  $n$  other neighbouring random variables or data values resulting in a cumulative distribution function for each cutoff  $z_b$

$$\begin{aligned}
 [i(\mathbf{x}; z_b)]^* &= E\{I(\mathbf{x}; z_b)|(n)\}^* \\
 &= Prob^* \{(Z(\mathbf{x}) \leq z_b)|(n)\}
 \end{aligned}
 \quad (2)$$

where  $(n)$  is the conditioning information available in the neighbourhood of location  $\mathbf{x}$ . Indicator estimation is performed for each of the class indicators to obtain estimates of the local mean indicator giving an estimate of the quasi-point support values within a local area. If the process is stationary and independent of  $\mathbf{x}$ , the indicator kriging predictor is

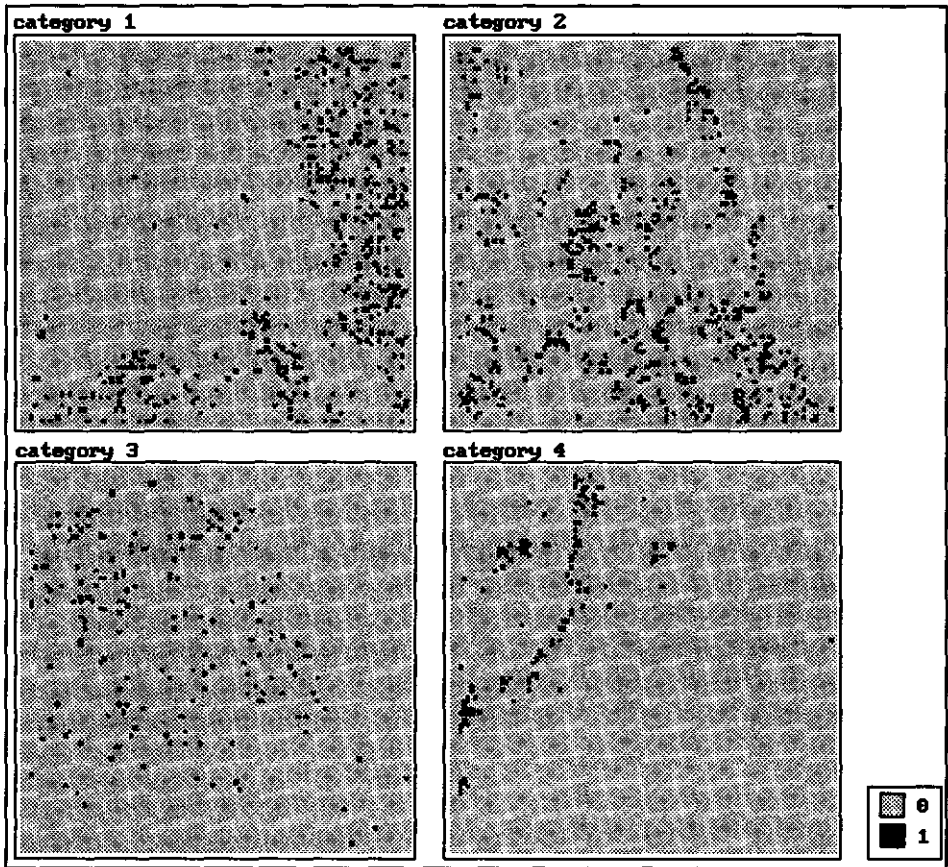


Fig. 9.8: Variable  $z(x)$  data set used as input for SCIS (category and continuous variable) and IK estimation ( $n=1316$ ).

$$[i(x; z_b)]^* = \sum_{i=1}^n \lambda_i(x; z_b) i(x_i, z_b) \quad (3)$$

Journal (1983) proposes that the weights,  $\lambda_i(x; z_b)$ , corresponding to cutoffs  $z_b$ , to be calculated from a simple kriging system through the calculation of residual indicator data  $[i(x, z_b) - F^*(z_b)]$  where  $F^*(z_b)$  is the stationary cumulative distribution function of the random function  $Z(x)$ . Note that these weights in simple kriging are not required to sum up to 1. The simple kriging estimate of the indicator transform  $i(x, z_b)$  is thus written as



$$[i(\mathbf{x}, z_b)]_{SK}^* = \sum_{i=1}^n \lambda_i(\mathbf{x}; z_b) i(\mathbf{x}_i; z_b) + [1 - \sum_{i=1}^n \lambda_i(\mathbf{x}; z_b)] F^*(z_b) \quad (4)$$

using  $n$  observed data values. The simple kriging system of equations is

$$\sum_{i=1}^n \lambda_i(\mathbf{x}_i; z_b) C_f(\mathbf{x}_j - \mathbf{x}_i; z_b) = C_f(\mathbf{x}_j; A; z_b), \quad i=1, 2, \dots, n \quad (5)$$

where  $C_f(\mathbf{x}_j - \mathbf{x}_i; z_b)$  are indicator correlogram values for the distance between  $\mathbf{x}_j - \mathbf{x}_i$ , and  $C_f(\mathbf{x}_j; A; z_b)$  are average indicator correlogram values between location  $\mathbf{x}_j$  and the area to be estimated,  $A$ , at cutoff  $z_b$ . Since data is abundant, ordinary indicator kriging within moving data neighbourhoods was considered using an block indicator kriging algorithm thus discretizing the block area into point samples yielding

$$i_v(\mathbf{x}; z_b) \equiv \frac{1}{|V|} \int_V i(\mathbf{x}'; z_b) d\mathbf{x}' \equiv \frac{1}{N} \sum_{j=1}^N i(\mathbf{x}_j'; z_b) \quad (6)$$

where  $v(s)$  is a block of measure  $|V|$  centered at  $s$ , and the  $i(\mathbf{x}_j'; z_b)$  are the  $N$ -points discretizing the volume  $v(s)$ . The result of this block indicator kriging is the average  $1/N \sum [i(\mathbf{x}_j; z_b)]_{ik}^*$  which is an estimate of the proportion of point values  $z(\mathbf{x}_j')$  within the block area  $v(s)$  that are less than the cutoff  $z_b$ . The ordinary block indicator kriging (*OBIK*) estimator using  $n$  control points takes on the form

$$[i(\mathbf{x}; z_b)]_{obik}^* = [prob\{Z(\mathbf{x}) \leq z_b\} | (N)]_{obik}^* \\ = \sum_{j=1}^n \lambda_j(\mathbf{x}; z_b) \gamma([i(\mathbf{x}_i; z_b)], [i(\mathbf{x}_j; z_b)]) + \mu = \gamma([i(\mathbf{x}; z_b)], v(s)) \text{ for all } i=1, n \quad (7)$$

where the weights  $\lambda_j(\mathbf{x}; z_b)$  are required to sum up to 1. The terms  $\gamma([i(\mathbf{x}_i; z_b)], [i(\mathbf{x}_j; z_b)])$  are the point-to-point (or sample-to-sample) semivariances,  $\mu$  is the lagrange multiplier, and the terms  $\gamma([i(\mathbf{x}; z_b)], v(s))$  are the point-to-block semivariances. The point-to-block covariances and the block-to-block covariance were approximated by a discrete summation achieved by discretizing the block areas into 6-by-6 arrays of discretizing points. Order relation problems

were corrected for following the procedure outlined by Deutsch & Journel (1992, p.77-81). The mean value at each location was derived from the conditional cumulative distribution function estimated assuming the mean value for each cutoff is the average of the minimum and maximum weight percent calcite defined in Eq.(1), thus assuming normally distributed data within a class.

### 9.3.3 Simulating calcite-dolomite abundances using Conditional Simulation

Sequential conditional indicator simulation algorithms (see Appendix 1 to this Chapter) work on binary [0,1] data, which may be transformed categorical or continuous variables, aiming at the reproduction of the indicator covariance model. The nature of the data used in this study, allowed to simulate both categorical variables and continuous variables. The following discussion is based on Deutsch & Journel (1992) and Journel (1989).

Through stochastic simulation, a series of alternative equally probable models of the spatial distribution of a indicator variable  $i(x)$  are produced that honour the conditioning data. If a binary indicator  $i(x)$  for a location  $x$  belonging to a category  $A$  ( $x \in A$ ) is simulated then the probability frequency function to be estimated becomes  $Prob\{I(x)=1|n\}=E\{I(x)|n\}$ . In case a continuous variable  $z(x)$ , the estimated conditional cumulative distribution function (ccdf) results in  $Prob\{Z(x)\leq z|n\}=E\{I(x;z)|n\}$  with the indicator  $I(x;z)=1$  if  $z(x)\leq z$ , else 0, where  $z$  is the cutoff value.

*Simulating categorical variables (SCIS category variable)* - Consider the spatial distribution of  $K$  mutually exclusive categories  $s_k, k=1,2,...,K$ . Let the indicator of class  $s_k$  be 1 if  $x \in s_k$ , else 0. Mutual exclusion yields  $i_k(x)i_{k'}(x)=0, k \neq k'$  and

$$\sum_{k=1}^K i_k(x) = 1 \quad (8)$$

Direct (SK or OK) kriging of the indicator variable  $i_k(x)$  provides an estimate for the probability that  $s_k$  prevails at location  $x$ . Using SK this yields

$$Prob^*\{I_k(x)=1|n\}=p_k + \sum_{a=1}^n \lambda_a [I_k(x_a) - p_k] \quad (9)$$

where  $p_k = E\{I_k(x)\} \in [0,1]$ , and  $\lambda_{\alpha}$  the weights of the SK system of equations. Sequential simulation of a category variable, further denoted as *SCIS* (category variable), now proceeds as follows (Deutsch & Journel, 1992)

- 1) Define a random path that visits each node  $x$  of a grid covering a field  $A$  to be simulated.
- 2) Correct the data for order relation problems (Journel & Posa, 1990) and apply indicator kriging (Journel, 1983) to estimate  $K$  probabilities  $p_k^*(x|(\bullet))$ ,  $k=1,2,\dots,K$ , where the conditioning data  $(\bullet)$  consist of both original  $i_k$ -data and previously simulated  $i_k$ -values.
- 3) Define any ordering of the  $K$  categories giving a cumulative distribution function of the probability interval  $[0,1]$  with  $K$  intervals.
- 4) Draw a random number  $p$  uniformly distributed in  $[0,1]$ . The interval in which  $p$  falls determines the simulated category at location  $x$ .
- 5) Update all  $K$  indicator data sets with the simulated values and proceed to the next node  $x'$ .
- 6) Repeat these steps until all nodes are visited. A simulated image, honouring the conditioning data and statistics and dispersion of the data, is now obtained.

In this study, the program *SISIMPDF* (Deutsch & Journel, 1992) was used for the conditional simulation of categorical variables.

*Simulating continuous variables SCIS (continuous variable)* - A continuous variable  $z(x)$  discretized into  $K$  mutually exclusive classes  $s_k$  gives a spatial distribution of  $K$  class indicators and allows to model each class by a different indicator variogram. Cumulative class indicators are defined in a common way by  $i(x; z_k) = 1$ , if  $z(x) \leq z_k$ , else 0. Sequential conditional simulation of continuous indicators, further denoted as *SCIS* (continuous variable) follows the following steps (Deutsch & Journel, 1992)

- 1) Define a random path that visits each node  $x$  of a grid covering a field  $A$  to be simulated.
- 2) Apply indicator kriging (SK or OK; Journel, 1983) to provide a *ccdf* through  $K$  probabilities at a node  $x$  to be simulated as

$$F^*(x; z_k | (n)) = \text{Prob}^* \{ Z(x) \leq z_k | (n) \}, k=1,2,\dots,K \quad (10)$$

where  $F^*(x; z_k | (n))$  is the non-stationary conditional cumulative distribution function of the indicator of cutoff  $k$  conditioned by the realizations of  $n$  neighbouring random variables defining a probability of  $Z(x) \leq z_k$ .

- 3) A Monte-Carlo simulation of realization  $z^{(b)}(x)$  is obtained by drawing a random

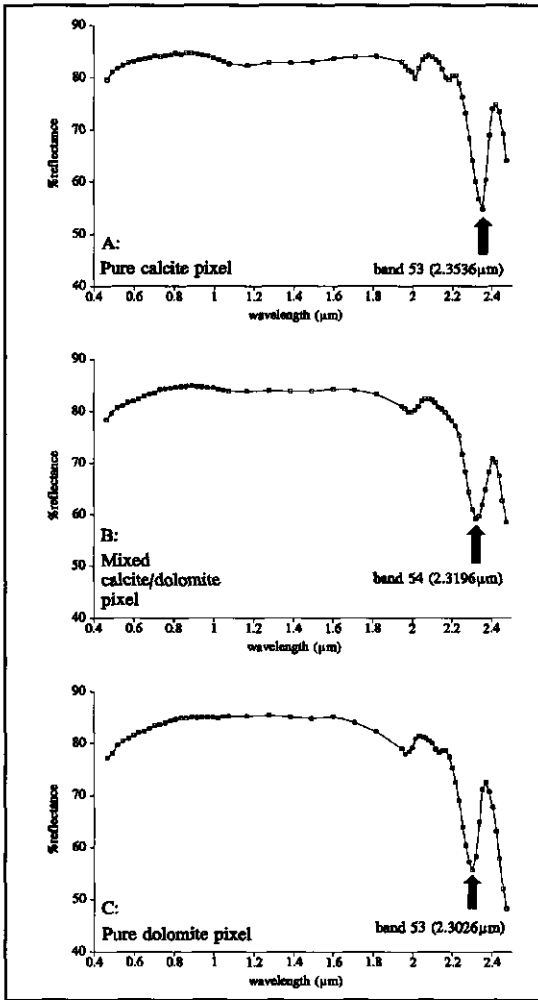


**Fig. 9.9:** GERIS pixel spectra of (A) a pure calcite, (B) a mixed calcite/dolomite pixel, and (C) a pure dolomite pixel. The position of the center of the carbonate absorption-band is indicated as GERIS channel and corresponding wavelength.

number  $p^{(i)} \in [0,1]$  and retrieving the  $ccdf$   $p^{(i)}$ -quantile  $z^{(i)}(x) = F^{*-1}(x; p^{(i)} | (n))$  where  $F^{*-1}(x; p^{(i)} | (n)) = p^{(i)}$ .

4) Update the indicator data sets with the simulated value  $z^{(i)}(x)$  and perform indicator kriging at the next node  $x'$ .

5) Repeat the process until all nodes are visited resulting in a stochastic image for the entire field  $A$ .

In this study, the sequential indicator simulation program *SISIM* from Deutsch & Journel (1992) was used.

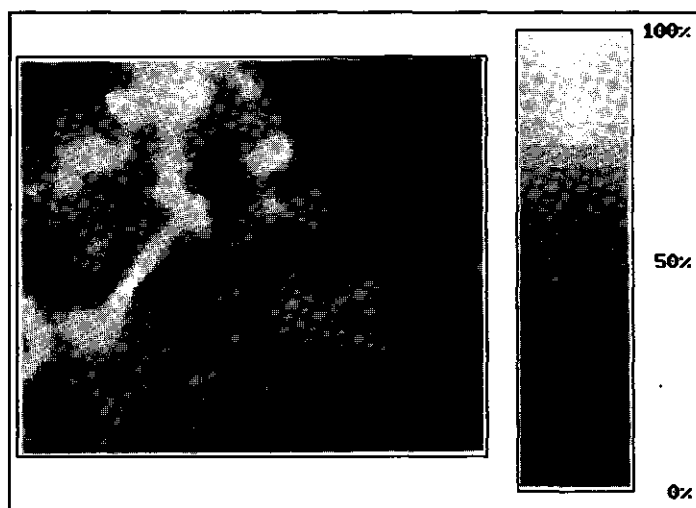


Fig. 9.10: Indicator kriged estimated calcite percent values. Note that kriging tends to smooth the data thus reproducing less of the spatial dispersion and statistical distribution of the original data. The scale ranges from 0% calcite (in black) to 100% calcite in white.

### 9.3.4 Results

In Fig. 9.9, reflectance spectra obtained by averaging 10 GERIS pixel spectra at locations marked A-C in Fig. 9.7 are shown. These spectra simply demonstrate that the carbonate absorption-bands in laboratory spectra are reproduced in the pixel spectra, and that pixels with intermediate mixtures of calcite and dolomite can be identified in the GERIS data set.

The results of indicator kriging of the variable and cutoffs shown in Fig. 9.8 are presented in Fig. 9.10. The corresponding omnidirectional indicator variograms for cutoffs used (Fig. 9.11) are well-defined and could be modelled with simple spherical models. Directional variograms were modelled using a  $22.5^\circ$  angular tolerance. These show a weak geometrical anisotropy with better correlation in NE-SW directions. The ranges fluctuate between 200 and 175 meters. In Fig. 9.12, directional variograms for cutoff 2 ( $z(x) \leq 57\%$ ) are shown. The effect of incorporating anisotropy in the kriging was evaluated by means of a cross-validation, in which the omnidirectional variogram and the anisotropic model were compared. The results (not shown here) indicated only a minor improvement of the estimation, therefore the analysis was carried out using the omnidirectional variograms.

Next, *SCIS* (continuous variable) and *SCIS* (category variable) was attempted. Four realizations of a *SCIS* (category variable) for the four categories defined in Eq.(1) are shown in Fig. 9.13. The corresponding indicator variograms are presented in Fig. 9.14. From Table 9.2 it can be concluded that the percentages of each category in the four realizations is similar to that of the conditioning data. To enhance the differences between the realizations, cross

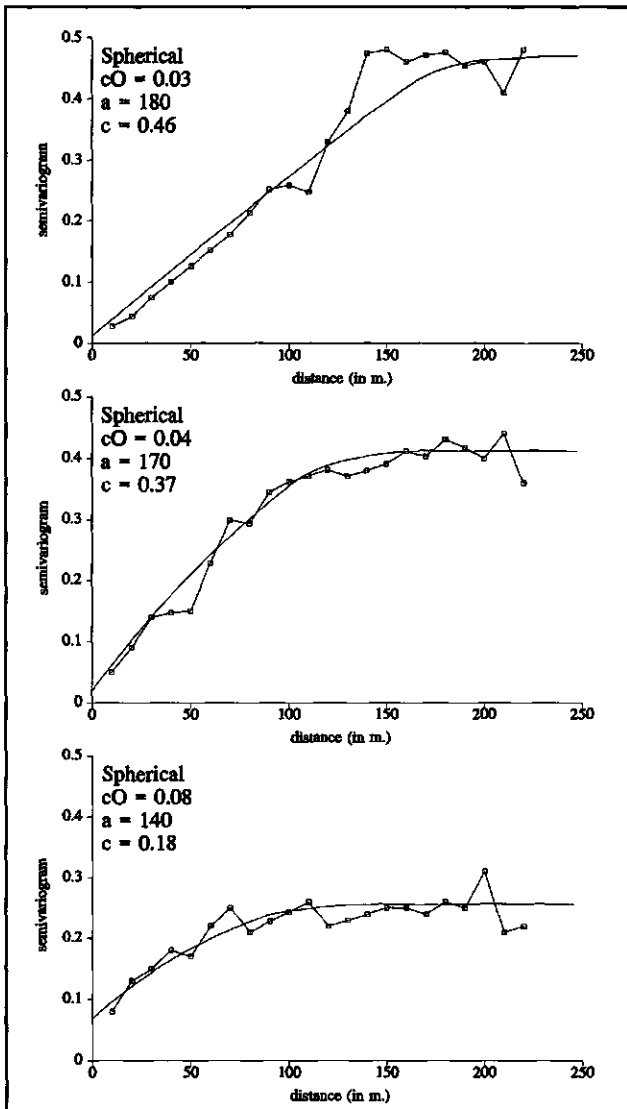


Fig. 9.11: Experimental indicator variograms for cutoffs used in direct *IK* estimation and *SCIS* (continuous variable). Their structure is well-defined, however, the total variance decreases and the nugget variance increases for high cutoff values (legend: type=spherical,  $cO$ =nugget variance,  $a$ =range,  $c$ =sill). Fitted models are indicated by solid lines.

tables were calculated tabulating the frequency of pixel value combinations occurring in two realizations (Tables 9.3 and 9.4). Table 9.3 is a cross table of *SCIS* (category variable) realization 1 and 2. From this Table it can be deduced that 58.5% of the simulated nodes fall in the same category in both of the realizations, 32.5% differ by one category, 8.4% differ by two categories, and 0.6% differ by three categories. Realization 2 and 4 are more similar:

- Imaging spectrometry and the Ronda peridotites -

**Table 9.2:** Percentage of pixels in each category for the four realizations of the *SCIS* (category variable).

Realization	Category 1: $0 < Z(x) \leq 26\%$	Category 2: $26\% < Z(x) \leq 57\%$	Category 3: $57\% < Z(x) \leq 86\%$	Category 4: $86\% < Z(x) \leq 100\%$
1	29.6	34.9	17.6	17.9
2	27.0	33.8	22.3	17.0
3	27.8	34.6	20.9	16.6
4	26.5	33.5	25.5	14.5
Conditioning data ( $n=1316$ )	28.1	34.1	21.3	16.5

**Table 9.3:** Cross table for realization 1 and 2 resulting from the *SCIS* (category variable). Horizontal are the categories simulated in realization 2, vertical are the categories simulated in realization 1. The numbers are percentages.

	1	2	3	4
1	22.1	5.6	1.5	0.5
2	4.4	19.4	7.9	3.2
3	0.4	5.5	7.8	4.0
4	0.1	3.3	5.1	9.2

**Table 9.4:** Cross table for realization 2 and 4 resulting from the *SCIS* (category variable). Horizontal are the categories simulated in realization 4, vertical are the categories simulated in realization 2. The numbers are percentages.

	1	2	3	4
1	23.8	3.0	0.2	0.0
2	2.6	22.3	7.8	1.0
3	0.1	6.6	12.0	3.6
4	0.0	1.6	5.5	9.9

68% of the pixels are of the same class, 29.1% differ by one class, 2.9% differ by two classes. No differences of three classes occurred between these realizations.

Four realizations of a *SCIS* (continuous variable) are shown in Fig. 9.15. To evaluate the performance of the simulation, the differences between individual realizations was calculated on a pixel by pixel basis by subtracting the simulated value in one realization from that of another. Table 9.5 documents the results of calculating  $z^{(1)}(x) - z^{(2)}(x)$ ,  $z^{(2)}(x) - z^{(3)}(x)$ , and  $z^{(3)}(x) - z^{(4)}(x)$ . These indicate that on the average, 95% of the pixels show differences between  $\pm 30\%$  calcite and 50% lie between  $\pm 10\%$  calcite (Fig. 9.16).

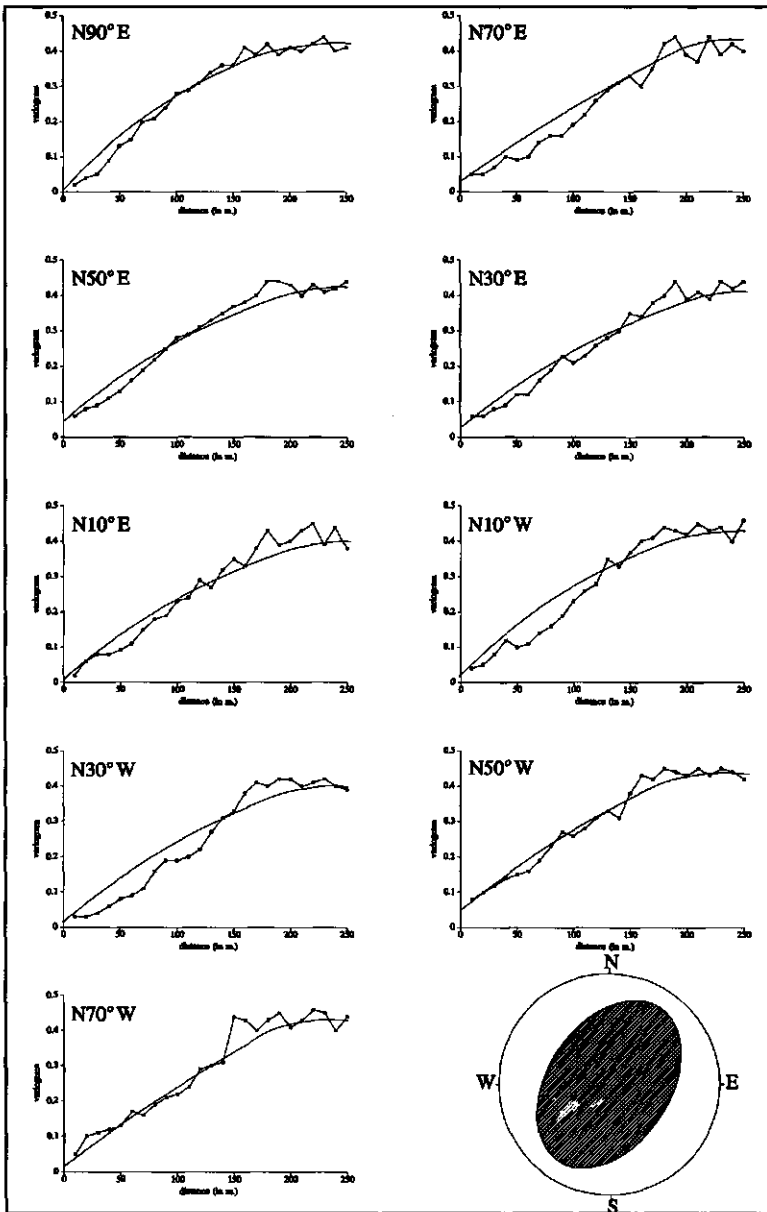


**Fig. 9.12:** Experimental directional variograms (tolerance =  $22.5^\circ$ ) for cutoff 2 ( $z(x) \leq 57\%$ ) showing a weak geometrical anisotropy with better correlation in NE-SW direction (major range  $N30^\circ E = 200m.$ ; minor range  $N70^\circ W = 175m.$ ). The diagram in the bottom right of the Figure indicates the approximate distribution of ranges. Solid lines indicate the fitted spherical models.



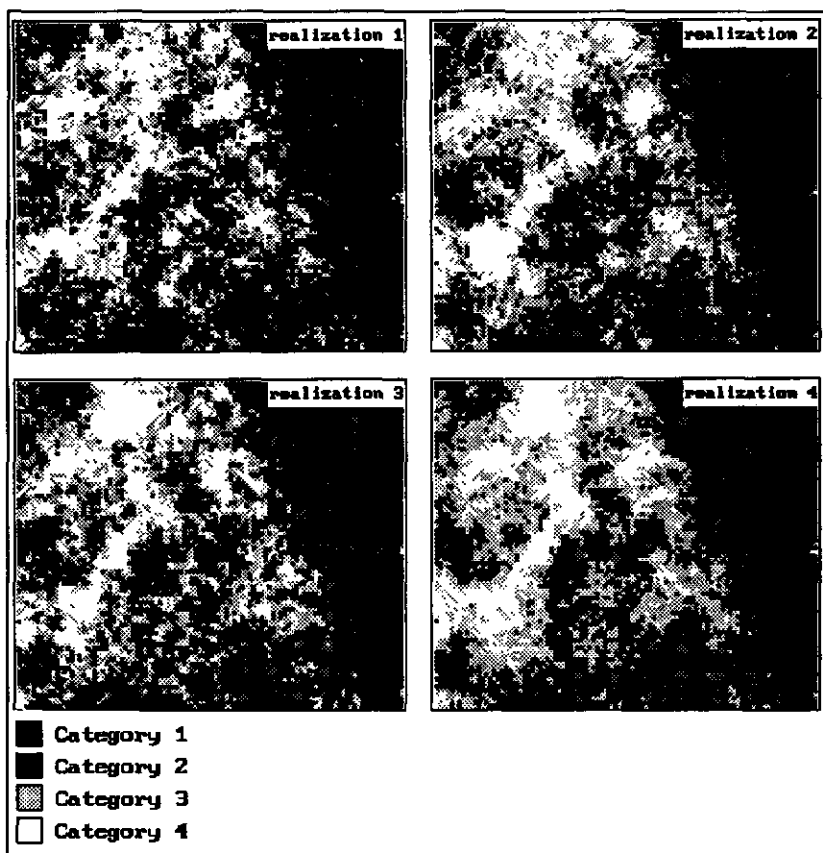


Fig. 9.13: Four realizations of a SCIS (category variable) on a small 100-by-100 pixel area indicated in Fig. 9.7.

Table 9.5: Statistics of differences between four realizations produced by the SCIS (continuous variable).

Statistic	$z^{(1)} - z^{(2)}$	$z^{(2)} - z^{(3)}$	$z^{(3)} - z^{(4)}$
mean	-0.82	-0.41	0.51
st. dev.	22.34	18.91	15.21
maximum	74.81	69.76	58.93
upper quartile	9.96	7.41	6.23
median	-0.05	-0.01	0.00
lower quartile	-11.15	-8.23	-5.03
minimum	-91.00	-78.51	-62.40

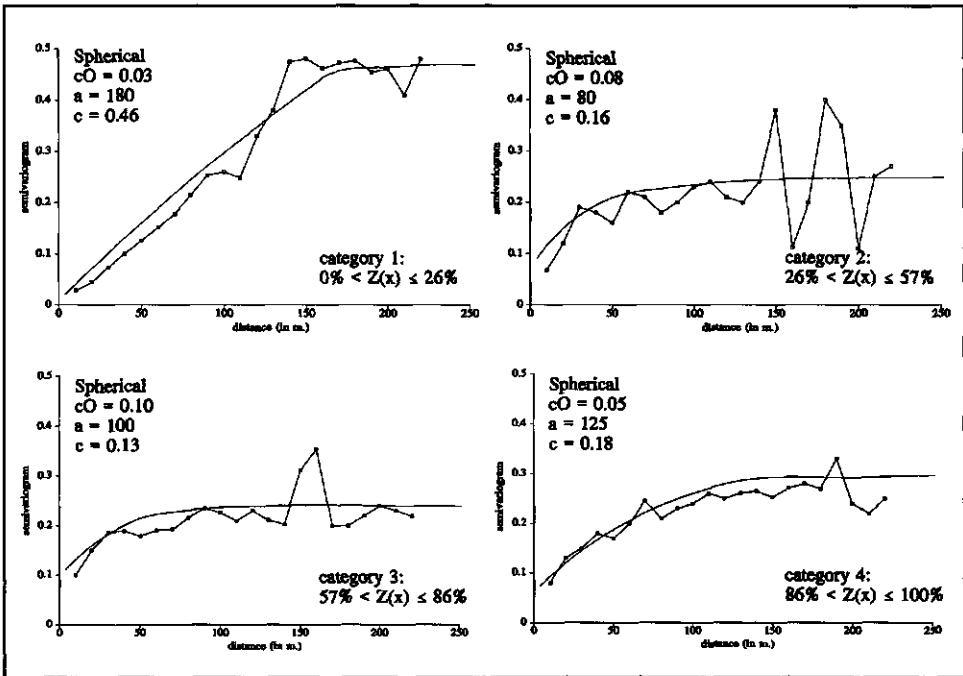


Fig. 9.14: Experimental indicator variograms of category variables (legend: type = spherical, cO = nugget variance, a = range, c = sill). Fitted models are indicated by solid lines.

Table 9.6: Statistics of IK and the first four realizations of the SCIS (continuous variable; calcite estimates in percent).

Statistic	$z^*(x)$	$z^{(1)}(x)$	$z^{(2)}(x)$	$z^{(3)}(x)$	$z^{(4)}(x)$
mean	47.99	44.12	45.03	45.13	44.33
std. dev.	26.38	30.23	29.15	28.45	28.40
maximum	90.97	99.83	98.71	97.81	97.95
upper quartile	71.73	69.83	70.23	70.44	70.31
median	49.74	34.90	36.25	37.95	41.31
lower quartile	21.81	17.10	19.95	20.21	20.01
minimum	8.01	1.40	0.31	1.14	1.00

Note: Column  $z^*(x)$  are 10.000 IK estimates.

Columns  $z^{(l)}(x)$ , denote the  $l=1, \dots, 4$  realizations of the SCIS (continuous variable) considered on 10.000 nodes  $x$ .

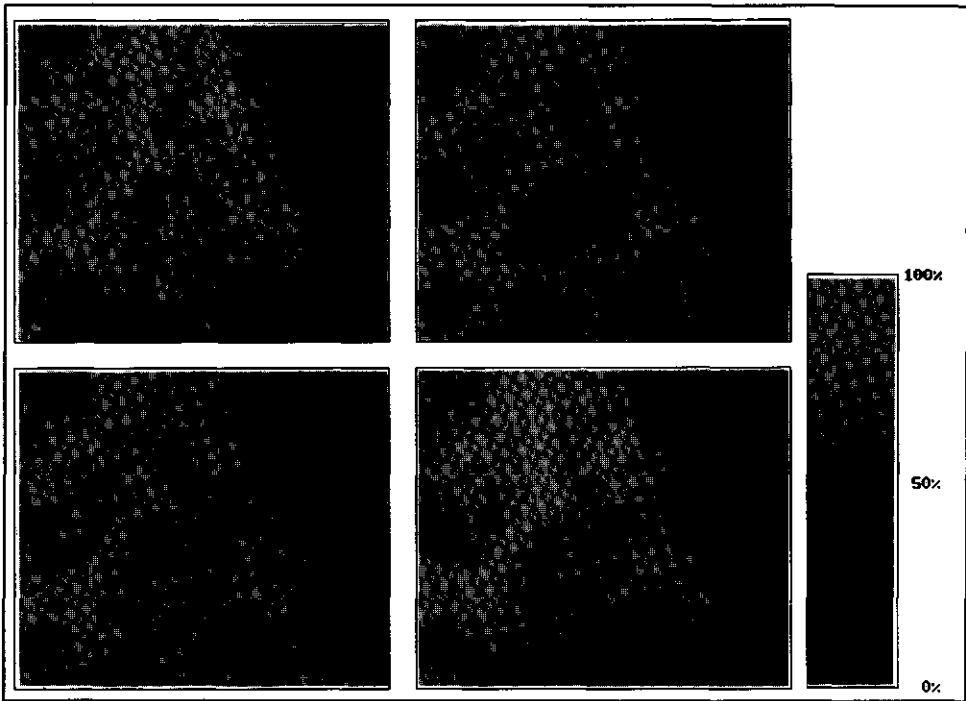


Fig. 9.15: Four realizations of a *SCIS* (continuous variable). The scale ranges from 0% calcite (in black) to 100% calcite in white. (realization 1=top left; realization 2=top right; realization 3=bottom left; realization 4=bottom right).

The statistics of *SCIS* (continuous variable) and *IK* are compared in Table 9.6. As expected, *IK* tends to smooth the variance of the data set and produces a more statistically symmetric estimated distribution than the four realizations.

The ultimate performance test of *IK* and *SCIS* (continuous variable) was done by comparing the estimated and simulated pixel values with a set of 163 hand-specimen sampled at the same locations. Identification of carbonate minerals calcite and dolomite from thin sections was done using staining methods described by Friedman (1959). Calcite percent was estimated from staining with alizarine red S (using 0.1 g in 100ml 0.2% hydrochloric acid) giving a deep red color for calcite whereas dolomite does not stain. Additional organic stains were used for dolomite: alizarine red S, alizarine cyanine green, and titan yellow each prepared by dissolving 0.2 g dye in 25ml methanol adding 15 ml of 30% NaOH. Dolomite is stained purple in alizarine red, deep green in alizarine cyanine green, and deep orange-red in titan yellow alkaline solution (Friedman, 1959). The results of the comparison of *IK* estimated values, *SCIS* (continuous variable) simulated values, and the field measurements is

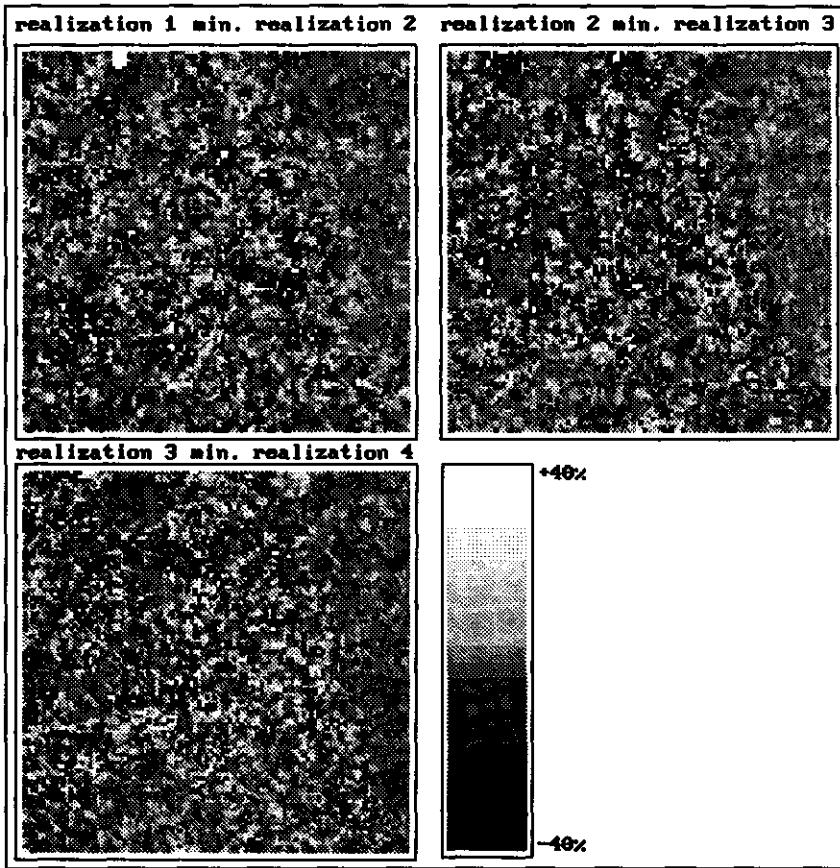


Fig. 9.16: Difference images for the four realizations of the SCIS (continuous variable).

Table 9.7: Statistics of the comparison calcite fraction measured from stained thin sections,  $z$ , and calculated value from direct  $IK$  estimation,  $z^*$ , and the first four SCIS (continuous variable) realizations  $z^{(l)}$ ,  $l=1, \dots, 4$ .

statistic	$z$	$z^*$	$z^* - z$	$\Sigma z^{(l)}/l$	$\Sigma z^{(l)}/l - z$
mean	48.00	48.89	1.47	48.32	-0.16
std. dev.	30.00	29.65	5.84	28.79	12.17
maximum	97.00	100.00	17.10	96.55	26.21
median	50.00	49.90	0.31	42.10	0.01
minimum	2.00	2.11	-20.31	1.01	-46.81

Note:  $z^* - z = IK$  estimate minus the measured value.

$\Sigma z^{(l)}/l - z$  is the difference between the average simulated value of the first four SCIS (continuous variable) realizations and the measured value. The number of observation,  $n$ , equals 163.

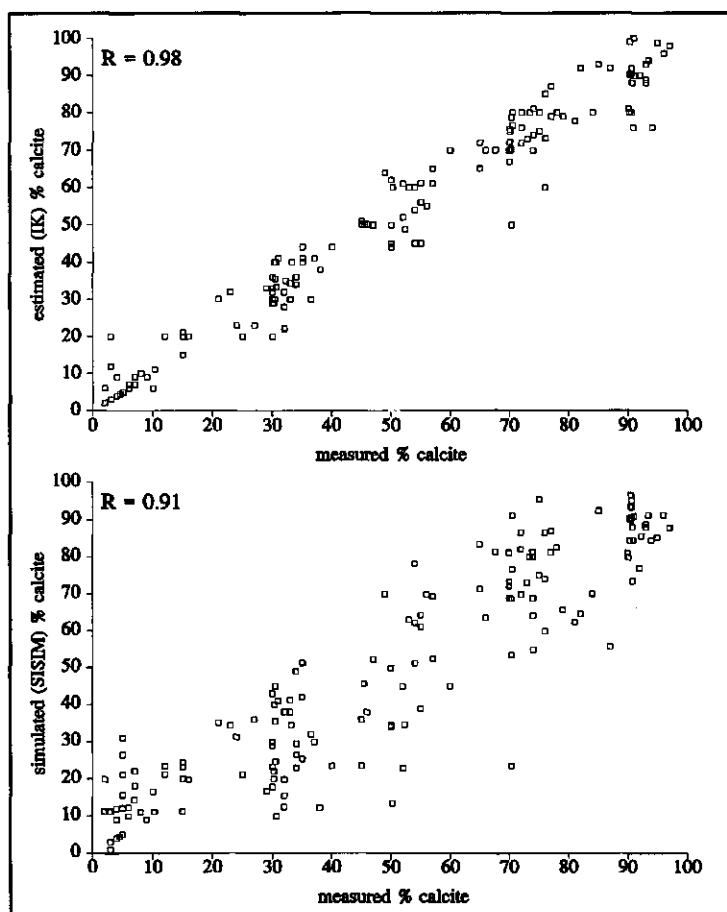
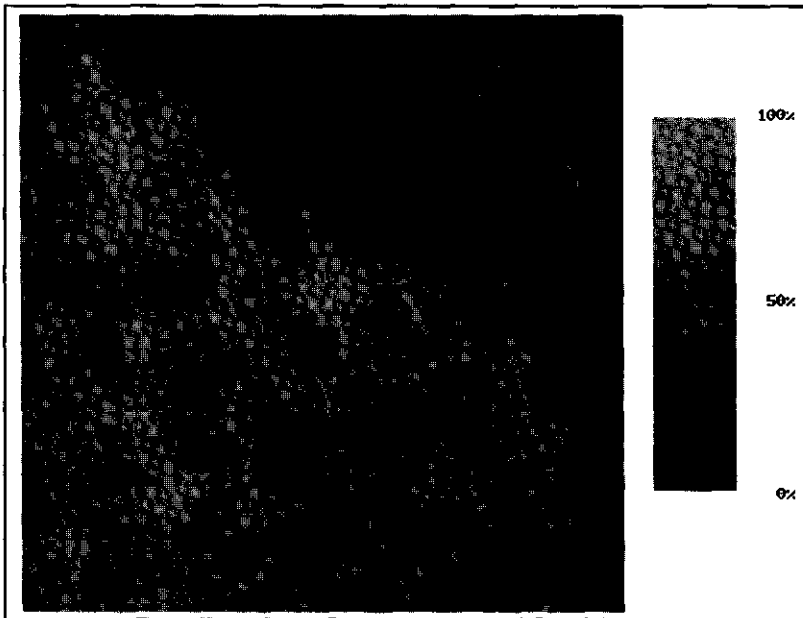


Fig. 9.17: IK derived calcite percentage (top) and SCIS (continuous variable) derived calcite percentage (bottom) versus calcite percentage measured in stained thin sections ( $n=163$ ).

shown in Fig. 9.17 and Table 9.7. These indicate that *IK* globally yields significant better results than the *SCIS* (continuous variable). Although the mean difference for the simulations is nearly zero, their standard deviation and spread is almost double that of the *IK* produced estimates.

Fig. 9.18 shows a realization of the dolomitization pattern for the carbonate portion of the GERIS image bordering the Ronda peridotites. This realization consist of 500-by-500 grid nodes, the road from Ronda to the coast at San Pedro (the C-339) has been plotted for reference. Note that the dolomitization pattern follows the trend of the geologic units and tends to increase toward both the peridotites and the gneiss/schist series.



**Fig. 9.18:** Conditional simulation of the carbonate portion in the GERIS image bordering the Ronda Peridotites. The dolomitization pattern follows roughly the structural trend of the geology and increases toward the gneiss/schist series and toward the peridotite.

#### **9.4 CASE STUDY II: MAPPING THE DEGREE OF SERPENTINIZATION**

As a result of the hydrothermal serpentinization process, magnesian silicate minerals (especially olivines and pyroxenes) in ultramafic rocks are often replaced by hydrous minerals of the serpentine group composed mainly of flaky antigorite and fibrous chrysotile plus lesser amounts of brucite, talc, tremolite and magnetite. Approximately 93 percent of the worlds global production of asbestos can be contributed to chrysotile hosted in Alpine-type peridotites. Estimating and mapping the degree of serpentinization within peridotite bodies is very complicated and requires detailed sampling and laboratory analyses. A technique based on quantitative analysis of remotely sensed imagery to rapidly characterize highly serpentinized rocks would therefore be a valuable tool in exploration for asbestos deposits. Such a tool is described in this Case Study.

The results of the analysis of laboratory reflectance spectra of serpentinized peridotites were presented in Chapter 5 demonstrating an increase in overall reflectivity and an increase in the depth of the 2.3 $\mu$ m and 1.4 $\mu$ m absorption bands with increasing abundance of

serpentine-group minerals. Laboratory spectra of mixtures of olivine-serpentine-magnetite were shown to investigate the effect of magnetite on the depths of these absorption bands. From this analysis presented in Chapter 5, a linear relationship was deduced to model the degree of serpentinization on basis of the depth of serpentine absorption bands. This relationship is used here to map the degree of serpentinization from GERIS data covering partly the Ronda peridotites. An approach is used similar to the methodology proposed in Van der Meer (1994f) to map dolomitization patterns in the previous Case Study which consist of four basic steps: (1) masking vegetation, (2) determining the absorption band-depth of the 2.3 $\mu$ m absorption feature, (3) converting this value into a measure of the degree of serpentinization, and (4) estimating the degree of serpentinization at unknown locations (e.g. pixels removed during the vegetation masking; Van der Meer, 1995). Calibration of the data to reflectance was done applying the Empirical Line method as described in Chapter 7.

#### 9.4.1 Data preparation

In order to map the degree of serpentinization, first pixels representing vegetation were removed from the GERIS data set. A training set of pixels known to represent various types of vegetation present throughout the scene were used as end-members of a mixture model assuming linear mixture systematics (Mustard & Pieters, 1987). This approach is similar to the method described by Zamudio (1993) for removing vegetation influences from imaging spectrometer data using unmixing. For the remaining pixels, the absorption-band depth of the 2.3 $\mu$ m absorption feature was estimated by fitting and removing by division a continuum over the pixel reflectance spectrum (Clark & Roush, 1984). This step is particularly important because wavelength dependent scattering may impart a slope to the spectrum causing apparent shifts in the absorption-band minima. Removing the slope thus corrects the band minimum to that of the true band center (Clark & Roush, 1984). Next, the absorption-band depth ( $D_b$ ) for the 2.3 $\mu$ m absorption feature was calculated following the definition by Clark & Roush (1984)

$$D_b \equiv \frac{R_c - R_b}{R_c} \quad (11)$$

where  $R_b$  is the reflectance at the band center, and  $R_c$  is the reflectance of the continuum at the band center. These absorption-band depth values were converted into degree of serpentinization (expressed as estimated percent serpentine minerals of a pixel) using the

linear relation established earlier. The degree of serpentinization at pixels which were excluded from the data set (because of dense vegetation) was estimated using an ordinary kriging-type of estimator described in Appendix 1 of Chapter 7 and simulated using conditional simulation techniques described below.

#### 9.4.2 Sequential Gaussian Conditional Simulation (SGCS)

In sequential Gaussian simulation (see also Appendix 1 to this Chapter), all *ccdf*'s are assumed Gaussian and their means and variances are found from a series of  $N$  simple kriging systems as described below.

If a continuous variable  $\{z(x), x \in A\}$  can be generated by the sum of a number of independent sources  $\{y_k(x), x \in A\}, k=1,2,\dots,K$ , with similar spatial distributions, then its spatial distribution can be modeled by a multivariate Gaussian random function defined as

$$Z(x) = \sum_{k=1}^K Y_k(x) \approx \text{Gaussian} \quad (12)$$

The random function (RF)  $Y(x)=\{Y(x), x \in A\}$  is multivariate normal and can be considered a multivariate Gaussian RF if

- A) all subsets of that RF are also multivariate normal.
- B) all linear combinations of the random variable components of  $Y(x)$  are normally distributed.
- C) zero covariance entails full independence.

The conditional Gaussian simulation of a continuous variable  $z(x)$  modeled by a Gaussian related stationary RF  $Z(x)$  proceeds as follows

- 1) Determine the univariate cumulative distribution function (*ccdf*)  $F_z(z)$  representative of the entire study area.
- 2) Transform the  $z$ -data with a transform standard normal *ccdf* to normal scored data (see Deutsch & Journel, 1992, p. 138).
- 3) Check the normal scored data for bivariate normality (see Deutsch & Journel, 1992, p. 139-141).

In step (2),  $z$ -data are transformed (by means of a normal score transform) to  $y$ -data which are by definition normally distributed. However, this not necessarily means that the spatially distributed  $Y(x), x \in A$  values are multivariate normal (as was required earlier). Bivariate normality checks whether the bivariate cumulative distribution function (*cdf*) of any pairs of



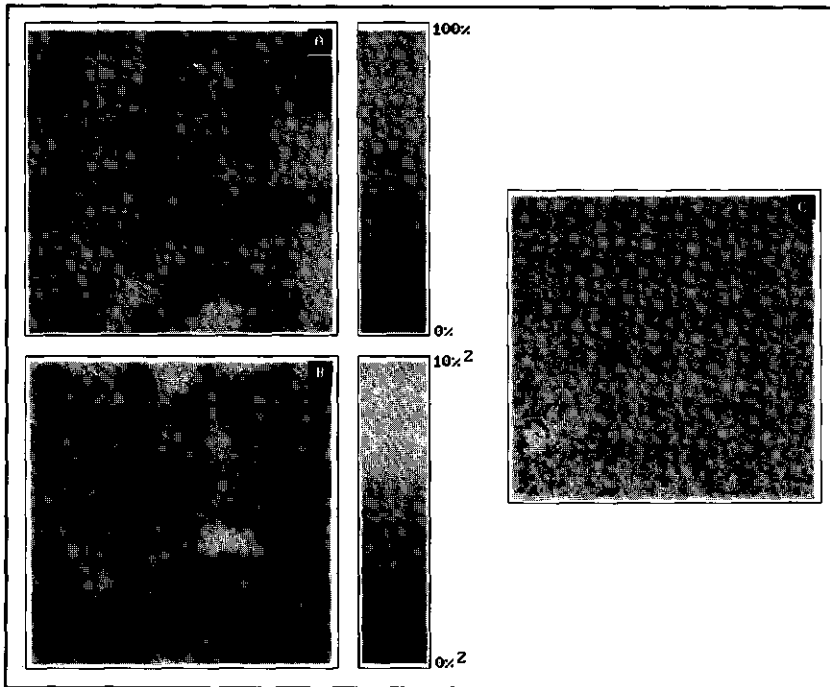


Fig. 9.19: GERIS band 30 centered at  $1.7099\mu\text{m}$ . The degree of serpentinization is estimated within the indicated window.

values  $y(\mathbf{x})$ ,  $y(\mathbf{x}+\mathbf{h})$  are normal. If steps (1)-(3) are valid, sequential conditional Gaussian simulation proceeds as follows (Deutsch & Journel, 1992)

- 4) Define a random path that visits each node  $\mathbf{x}$  of a grid covering a field  $A$  to be simulated and retain at each node a specified number of neighbouring conditioning data including both original  $y$ -data and simulated grid node  $y$ -values.
- 5) Use either simple kriging (*SK*) or ordinary kriging (*OK*) with the normal score variogram model to determine the parameters (i.e., the mean and variance) of the *ccdf* of the *RF*  $Y(\mathbf{x})$  at node  $\mathbf{x}$ .
- 6) Draw a simulated  $y^{(i)}(\mathbf{x})$  value from that *ccdf*.
- 7) Add the simulated value  $y^{(i)}(\mathbf{x})$  to the data set.
- 8) Proceed to the next node until all nodes are simulated.
- 9) Backtransform (see Deutsch & Journel, 1992, p. 211-213) the simulated normal values  $\{y^{(i)}(\mathbf{x}), \mathbf{x} \in A\}$  into simulated values of the original variable  $\{z^{(i)}(\mathbf{x}), \mathbf{x} \in A\}$ .

Now a stochastic simulated image is generated that honours the hard conditioning data values and reproduces the statistics and spatial dispersion of the input conditioning data. In this study, the program *SGSIM* (Journel & Alabert, 1989; Deutsch & Journel, 1992) was used to perform sequential conditional Gaussian simulation.



**Fig. 9.20:** Results of Ordinary Kriging for estimating the degree of serpentinization within the window indicated in Fig. 9.19. (A) ordinary kriged estimates, (B) ordinary kriging estimation error, and (C) distribution of data locations ( $n=1181$ ).

### 9.4.3 Results

A small image window of 100 by 100 pixels was selected to test the methodology developed for mapping the degree of serpentinization (Fig. 9.19). After vegetation masking, a data set consisting of 1181 pixels (out of 10000; Fig. 9.20c) resulted for which the percent serpentinization was calculated on basis of the depth of the  $2.3\mu\text{m}$  absorption feature. The percent serpentinization for the remaining pixels was determined using sequential Gaussian simulation. Variograms were modelled in nine directions with angular tolerances of  $22.5^\circ$ . These showed that the data set is nearly isotropic and could be modelled with a spherical variogram (nugget=62.9; range=22 pixels; sill=97.2).

The results of ordinary block kriging applied to the  $n=1181$  data locations for which the degree of serpentinization was estimated are shown in Fig. 9.20. Both the kriging estimates as well as the corresponding estimation variances are shown. In Table 9.8 the

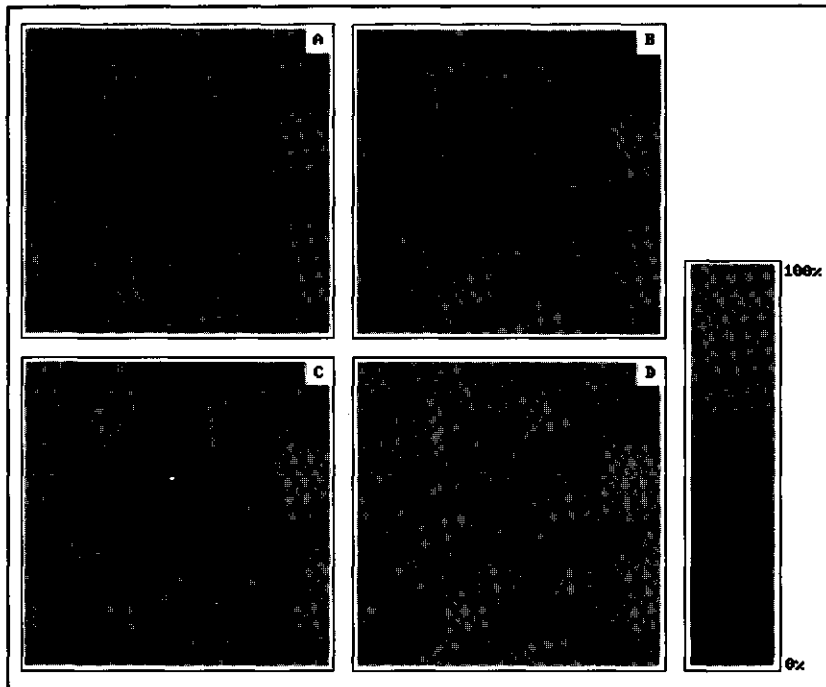


**Fig. 9.21:** Four realizations of a conditional Gaussian sequential simulation of percent serpentine minerals per pixel (legend: A=realization 1; B=realization 2; C=realization 3; D=realization 4). See Fig. 9.19 for location of the window.

statistics of the kriging are documented together with the statistics of the original conditioning data. It is clear from this table that ordinary kriging preserves the mean of the data, however the standard deviation and variance and also the minimum and maximum estimated values are much lower than those of the original data. Thus kriging acts as a low-pass filter by suppressing local and global variation as was also demonstrated by Carr (1990). The spatial distribution of kriging error values (Fig. 9.20b) seems determined mainly by the distribution of data values (compare with Fig. 9.20c).

The first four realizations of the Gaussian simulation are shown in Fig. 9.21. The statistics of these realizations is given in Table 9.9 together with the statistics of the conditioning data. From this Table it can be seen that the statistics of the conditioning data is reproduced within reasonable statistical fluctuations. Difference images were calculated by subtracting the realizations from each other excluding the conditioning data for which the realizations are forced to be identical by the simulation algorithm (Fig. 9.22). Table 9.10 demonstrates that on the average, 68% of the simulated nodes differ  $\pm 15\%$  serpentinization,

- Chapter 9 -

Table 9.8: Statistics of kriging.

	condit. data	$z^*(x)^1$	$\sigma_{OK}^2$	$z_*(x)-z(x)^3$
mean	67.97	67.91	4.24	-0.24
variance	288.84	140.65	1.18	760.63
std. dev.	16.96	11.86	1.16	26.46
%C.V.	25.00	17.46	25.59	110.33
skewness	-0.31	0.06	0.059	-0.28
kurtosis	2.87	3.30	4.52	3.78
minimum	12.31	25.96	2.11	-68.92
lower quartile	57.22	60.57	3.49	-18.18
median	69.45	67.67	4.01	-2.21
upper quartile	80.11	74.69	4.76	13.57
maximum	100.00	98.26	9.92	75.47

<sup>1</sup>kriging estimates ( $n=10000$ ). <sup>2</sup>kriging standard deviation ( $n=10000$ ).

<sup>3</sup>estimated minus measured value from cross validation ( $n=1181$ ).

Table 9.9: Statistics of the first four realizations,  $z^{(1)}(x)$ - $z^{(4)}(x)$ , of the conditional Gaussian sequential simulation.

	condit. data <sup>1</sup>	$z^{(1)}(x)$	$z^{(2)}(x)$	$z^{(3)}(x)$	$z^{(4)}(x)$
mean	67.97	68.95	67.93	67.85	67.51
variance	288.84	292.71	276.80	295.55	305.39
std. dev.	16.96	17.11	16.64	17.19	17.48
% C.V. <sup>2</sup>	25.00	24.81	24.19	25.34	25.87
skewness <sup>3</sup>	-0.31	-0.18	-0.19	-0.04	-0.08
kurtosis	2.87	3.20	2.95	10.41	7.91
minimum	12.31	0.21	10.33	12.00	7.76
lower quartile	57.22	57.95	57.43	56.93	56.67
median	69.45	69.97	68.69	68.10	67.98
upper quartile	80.11	80.78	79.00	79.11	79.05
maximum	100.00	100.00	99.81	101.05	101.01

<sup>1</sup>number of conditioning points equals 1181 ( $n=1181$ ). <sup>2</sup>%C.V. is the coefficient of variation expressed in percent and calculated as (std. dev./mean)\*100%. <sup>3</sup>skewness is calculated as  $3*(\text{mean}-\text{median})/\text{std. dev.}$

- Imaging spectrometry and the Ronda peridotites -

Table 9.10: Statistics of differences between realizations.

	$z^{(1)}(\mathbf{x}) - z^{(2)}(\mathbf{x})$	$z^{(2)}(\mathbf{x}) - z^{(3)}(\mathbf{x})$	$z^{(3)}(\mathbf{x}) - z^{(4)}(\mathbf{x})$
mean	1.16	0.093	0.392
variance	237.46	238.21	255.92
std. dev.	15.41	15.43	15.99
%C.V.	1324.54	16634.50	4078.54
skewness	0.09	-0.03	0.06
kurtosis	4.04	14.76	15.75
minimum	-83.52	-69.11	-60.81
lower quartile	-8.24	-9.20	-9.36
median	0.69	0.23	0.06
upper quartile	10.57	9.55	9.76
maximum	94.59	62.13	63.51

Note: the number of observations is 8819 ( $n=8819$ ) and excludes the conditioning data.

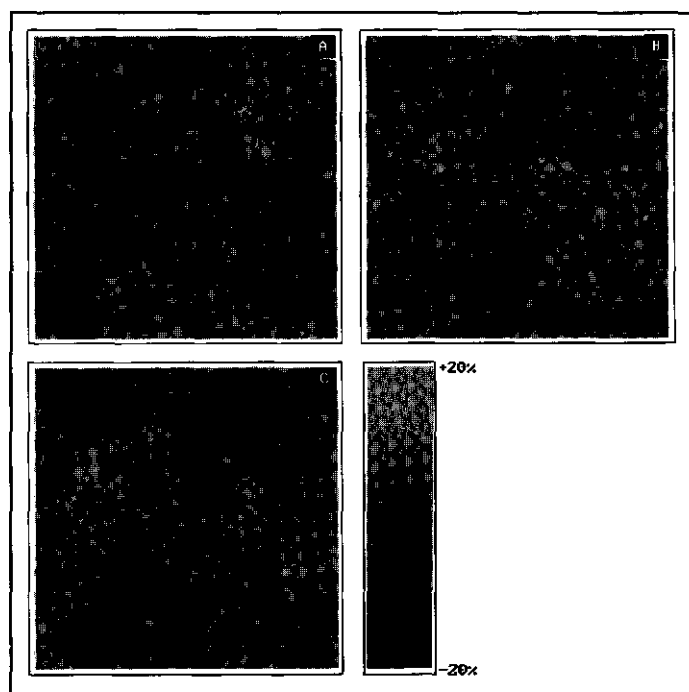


Fig. 9.22: Difference images for the four realizations of the conditional gaussian sequential simulation of percent serpentine minerals of Fig. 9.21. (A) Realization 1 minus realization 2, (B) realization 2 minus realization 3, and (C) realization 3 minus realization 4.

- Chapter 9 -

*Table 9.11: Statistics of simulated and estimated %serpentinization and measured %serpentinization for 49 observations (n=49).*

	measured	simulated	difference
mean	52.47	42.43	9.94
variance	490.00	841.96	190.77
std.dev.	22.14	29.02	13.81
%C.V.	42.27	68.39	138.97
skewness	-0.36	-0.06	-0.24
kurtosis	2.58	1.74	2.24
minimum	4.00	0.00	-23.00
lower quartile	38.00	12.25	-3.51
median	55.00	43.01	11.04
upper quartile	68.00	68.76	22.12
maximum	98.00	100.00	33.14

thus showing that the realizations are statistically similar. The minimum and maximum differences simulated differ from +94.6 to -83.5 for realization 1 minus realization 2, to approximately -60 to +60 for the other two difference images.

In order to evaluate the results, samples were gathered in the field at 49 locations. Thin sections were prepared and the bulk mineralogy of the samples was determined from thin section analysis and chemical analysis. The degree of serpentinization of each sample was expressed as the percent of secondary serpentine-group minerals and compared with the estimates obtained through a conditional simulation. The results of this comparison (Table 9.11) indicate that simulating the degree of serpentinization is feasible since the maximum and minimum difference were found to be +33% and -23%, respectively. Note that for moderately serpentinized samples the simulation tends to underestimate the true value due to the linear relationship assumed. Estimating the degree of serpentinization using ordinary kriging yields much better results although the estimation does not preserve local and global variability.

## 9.5 CONCLUSIONS

Mineral mapping from GERIS data permits a metamorphic zonation of the Sierra Bermeja peridotite body from northwest to southeast into a garnet-, spinel-, and a plagioclase-lherzolite

facies. These metamorphic facies record the cooling of these ultramafic rocks with the "hot" phase of emplacement at crustal levels. This zonation is overprinted by two subsequent phases of serpentinization producing an assemblage of lizardite-chrysotile and antigorite. The lizardite-chrysotile serpentinization is caused by fluids of meteoric-hydrothermal origin derived from sedimentary formations at low temperatures (300-400°), whereas antigoritic serpentinization takes place as a result of regional metamorphism in the presence of non-meteoric waters at higher temperatures (>500°). The latter, may be related to a late-phase of "cold" deformation related to northwestward thrusting of the peridotite body.

A methodology has been presented through which imaging spectrometer data sets can be analyzed despite abundant vegetation. Two Case Studies demonstrate the use of imaging spectrometry for mineral exploration purposes. The carbonate absorption-band can be resolved in GERIS pixel spectra as well as the shift to shorter wavelength with increasing dolomitization. This allows to characterize the calcite content of a pixel in four categories ( $0\% < z(x) \leq 26\%$ ,  $26\% < z(x) \leq 57\%$ ,  $57\% < z(x) \leq 86\%$ ,  $86\% < z(x) \leq 100\%$ ) using GERIS bands 53-56 for pixels with low degree of vegetation. Estimating the degree of dolomitization (expressed as the percent dolomite minerals) using *SCIS* (category variable) yields at 60% of the nodes the same category for four realizations. In 90% of the cases the differences is 0 or 1 class. Estimating the degree of dolomitization using *IK* yields results which show a difference of  $\pm 20\%$  calcite (maximum) with 163 field samples. *SCIS* (continuous variable) produces differences between +26% and -47%. *SCIS* (continuous variable) better preserves the variability of the data and should be used to visualize the spatial pattern of dolomitization rather than to estimate it. Multiple realizations allow to reduce and characterize the error of the values produced by the simulation. Studies of laboratory spectra of both serpentinized rock samples and synthetic mixtures of olivine-serpentine-magnetite demonstrate that the degree of serpentinization can be quantified using the depth of the 2.3 $\mu$ m absorption band indicative for the presence of serpentine-group minerals. From the results of this study it can be concluded that mapping the degree of serpentinization from high-spectral resolution imagery is possible within 20% accurate. Conditional simulation reproduces the spatial and statistical variability of the data set, however it sacrifices the local accuracy. Direct estimation using ordinary kriging provides a better local estimate but does not honour the statistics and spatial dispersion of the original data.

## APPENDIX 1: Sequential Conditional Simulation.

Geostatistics is concerned with the study of phenomena that fluctuate in space and/or time. Stochastic simulation in geostatistics is the process of generating alternative, equally probable, models of the spatial distribution of an attribute  $z(\mathbf{x})$  over a field or area  $A$  ( $\mathbf{x} \in A$ ) where each realization,  $z^j(\mathbf{x})$  is an element of  $A$ . In case the realizations honour the data values, the simulation is said to be conditional, else non-conditional. Simulation differs from estimation (e.g., kriging) in two ways: (1) in simulation the global statistics is considered more important than the local accuracy that estimation provides, and (2) simulation provides many alternative models of a single variable that have in common that they reproduce the statistics and spatial dispersion (e.g., the histogram and variogram) of the conditioning data, whereas kriging only provides one such model. Sequential simulation builds on the principle of drawing values of a variable  $Z(\mathbf{x})$  from its conditional distribution using all data within the neighbourhood of  $\mathbf{x}$  including original (conditioning data) and previously simulated data (Journel, 1989). Consider the joint distribution of  $N$  random variables (RV's)  $Z_i$  which represent the same attribute at the  $N$  nodes of a dense grid discretizing field  $A$ . Next, consider the conditioning of these random variables by a set of  $n$  data of any type (symbolized by  $l(n)$ ). The corresponding  $N$ -variate conditional cumulative distribution function (*ccdf*) is denoted

$$F_{(n)}(z_1, \dots, z_N | l(n)) = \text{Prob}\{Z_i \leq z_i, i=1, \dots, N | l(n)\} \quad (1)$$

Successive application of the conditional probability relation shows that conditioning is done as follows

- 1) draw a value  $z_1^{(0)}$  from the univariate *ccdf* of  $Z_1$  given  $(n)$  original data values where  $z_1^{(0)}$  is considered a conditioning datum for all subsequent drawings. The information data set  $(n)$  is now updated to  $(n+1) = (n) \cup \{Z_1 = z_1^{(0)}\}$ .
- 2) Draw a value  $z_2^{(0)}$  from the univariate *ccdf* of  $Z_2$  given the updated set  $(n+1)$ , then update the information set to  $(n+2) = (n+1) \cup \{Z_2 = z_2^{(0)}\}$ .
- 3) Continue until all  $N$  RV's  $Z_i$  are considered.

The resulting set  $\{z_i^{(0)}, i=1, 2, \dots, N\}$  represents the joint realization of the  $N$  dependent RV's  $Z_i$ . Other realizations can be produced in another random process. The sequential simulation procedure requires the determination of  $N$  univariate *ccdf*'s namely

$$\begin{aligned} &\text{Prob}\{Z_1 \leq z_1 | l(n)\} \\ &\text{Prob}\{Z_2 \leq z_2 | l(n+1)\} \\ &\dots \\ &\text{Prob}\{Z_N \leq z_N | l(n+N-1)\} \end{aligned} \quad (2)$$



## References

- Abrams, M.J., Ashley, R.P., Rowan, L.C., Goetz, A.F.H. & Kahle, A.B. 1977. Mapping of hydrothermal alteration in the Cuprite mining district, Nevada using aircraft scanner images for the spectral region 0.46-2.36 $\mu$ m. *Geology*, **5**: 713-718.
- Adams, J.B. 1974. Visible and near-infrared diffuse reflectance: Spectra of pyroxenes as applied to remote sensing of solid objects in the solar system. *J. Geophys. Res.*, **79**: 4829-4836.
- Adams, J.B. 1975. Interpretation of visible and near-infrared diffuse reflectance spectra of pyroxenes and other rock forming minerals. In: C. Karr (Ed.), *Infrared and Raman Spectroscopy of Lunar and Terrestrial Materials*, Academic Press: pp. 91-116.
- Adams, J.B. & Smith, M.O. 1986. Spectral mixture modelling: a new approach to analysis of rock and soil types at the Viking lander 1 site. *J. Geophys. Res.*, **91**: 8098-8112.
- Agbor, B. 1992. *Some aspects of the emplacement of the Ronda peridotite (Sierra Bermeja), Málaga Province, Spain*. Unpublished M.Sc. thesis, ITC, Enschede: 71 pp.
- Aines, R.D. & Rossman, G.R. 1984. Water in minerals? A peak in the infrared. *J. Geophys. Res.*, **89**: 4059-4071.
- Albers, J.P. & Stewart, J.H. 1972. Geology and mineral deposits of Esmeralda County, Nevada. *Nevada Bur. Mines and Geology Bull.*, **78**: 1-80.
- Allerton, S., Reicherter, K. & Platt, J.P. 1994. A structural and paleomagnetic study of a section through the eastern Subbetic, Southern Spain. *J. Geol. Soc. London*, **151**: 659-668.
- Almela, A., Alvarado, M., Coma, E., Felgueroso, C. & Quitero, I. 1962. Estudio geológico de la Región de Almadén. *Bol. Inst. Géol. Min. España*, **73**: 193-327.
- Andrews, H.C. 1972. *Introduction to Mathematical Techniques in Pattern Recognition*. Wiley, New York: 242 pp.
- Andrieux, J., Fontboté, J.M. & Mattauer, M. 1971. Sur un modèle explicatif de l'Arc de Gibraltar. *Earth Planet. Sci. Lett.*, **12**: 191-198.
- Angelier, J. 1984. Tectonic analysis of fault slip data sets. *J. Geophys. Res.*, **89**: 5835-5848.
- Angelier, J. 1989. From orientation to magnitudes in paleostress determinations using fault slip data. *J. Struct. Geol.*, **11**: 37-50.
- Aronson, J.R. & Emslie, A.G. 1973. Spectral Reflectance and Emittance of particulate materials, 2, Application and results. *App. Opt.*, **12**: 2573-2584.
- Arthaud, F. & Choukroune P. 1972. Methode d'analyse de la tectonique cassante a l'aide des microstructures dans les zones pue deformees: exemple de la plate-forme Nord

- References -

- Aquitaine. *Rev. Inst. Fr. Pet.*, **27**(5): 715-732.
- Ashley, P.M. 1975. Opaque mineral assemblage formed during serpentinization in the Coolac Ultramafic Belt, New South Wales. *J. Geol. Soc. London*, **131**: 91-102.
- Ashley, R.P. 1977. *Geologic map and alteration map, Cuprite mining district, Nevada* (unpublished).
- Ashley, R.P. & Abrams, M.J. 1980. *Alteration Mapping using Multispectral Images-Cuprite Mining District, Esmeralda County, Nevada*. U.S. Geological Survey Open File Report 80-367, Denver CO: 17 pp.
- Ave Lallemant, H.G. & Carter, N.L. 1970. Syntectonic recrystallization of olivine and modes of flow in the upper mantle. *Geol. Soc. Am. Bull.*, **81**: 2203-2220.
- Azéma, J. 1961. Étude géologique des abords de Málaga (Espagne). *Estudios Geol.*, **27**(2): 131-160.
- Azéma, J., Fourcault, A., Fourcade, E., García-Hernández, M., Gonzalez-Donoso, J.M., Linares, A., López-Garrido, A.C., Rivas, P. & Vera, J.A. 1979. *Las Microfacies del Jurásico y Cretácico de las Zonas Externas de las Cordilleras Béticas*. Univ. Granada: 83 pp.
- Baena Perez, J & Jerez Mir, L., 1982. *Síntesis para un ensayo Paleogeográfico entre la Meseta y la zona Bética (s.str.)*. IGME (Instituto Geológico y Minero de España), Madrid: 256 pp.
- Bakker, H.E., De Jong, K., Helmers, H. & Biermann, C. 1989. The geodynamic evolution of the Internal Zone of the Betic Cordilleras (south-east Spain): a model based on structural analysis and geothermobarometry. *J. Metamorph. Geol.*, **7**: 359-381.
- Balanya, J.C. & Garcia-Dueñas, 1987. Les directions structurales dans la Domaine d'Alborán de part et d'autre du Détroit de Gibraltar. *C.R. Se. Ac. Sc. Paris*, **304**: 923-933.
- Baret, F. 1994. Imaging spectroscopy in agriculture, comparison of modellistic approaches and experimental data. In: J. Hill & J. Mégier (Eds.), *Imaging spectrometry - a tool for environmental observations*. Dordrecht, Kluwer Academic Publishers: pp. 1-20.
- Barranco, L.M., Ansorge, J. & Banda, E. 1990. Seismic refraction constraints on the geometry of the Ronda peridotitic massif (Betic Cordillera, Spain). In: G. Boillot & J.M. Fontboté (Eds.), *Alpine evolution of Iberia and its Continental Margins. Tectonophysics*, **184**: 379-392.
- Basset, K.H., Liang, C.Y. & Marchessault, R.H. 1963. The infrared spectrum of crystalline polyaccharides. IX. The near infrared spectrum of cellulose. *Journal of polymer science*, **1**: 1687-1692.
- Baumgardner, M.F., Stoner, E.R., Silva, L.F. & Biehl, L.L. 1985. Reflectance properties of soils. In: N. Brady (Ed.), *Advances of Agronomy*, Academic Press, New York: pp. 1-44.
- Behrmann, J.H. & Platt, J.P. 1982. Sense of nappe emplacement from quartz c-axis fabrics; an example from the Betic Cordilleras (Spain). *Earth Planet. Sci. Lett.*, **59**: 208-215.
- Ben-Dor, E. & Kruse, F.A. 1994. The relationship between the size of spatial subsets of GER 63 channel scanner data and the quality of the Internal Average Relative Reflectance (IARR) Atmospheric correction technique. *Int. J. Remote Sens.*, **15**: 683-690.
- Berthé, D., Choukroune, P. & Jegouzo, P. 1979. Orthogneiss, mylonite and non-coaxial deformation of granites: the example of the South Armorican Shear Zone. *J. Struct. Geol.*, **1**: 31-42.

- References -

- Besems, R.E. & Simon, O.J. 1982. Aspects of Middle and Late Triassic Palynology 5. On the Triassic of the Subbetic Zone in the province of Murcia (Betic Cordilleras, southeastern Spain). *Proc. Kon. Ned. Akad. Wetensch., Ser. B.*, **85**: 29-51.
- Blanco, M.J. & Spakman, W. 1993. The P-wave velocity structure of the mantle below the Iberian Peninsula: evidence for subducted lithosphere below southern Spain. *Tectonophysics*, **221**: 13-34.
- Blow, W. 1969. Late middle Eocene to Recent planktonic foraminiferal biostratigraphy. In: P. Bronnimann & H.H. Renz (Eds.), In: *Proceedings First Internat. Conf. Planktonic Microfossils*, Geneva, 1967, Brill, Leiden: pp. 119-142.
- Blumenthal, M. 1933. Geologie der Bergen um Ronda. *Ecl. Geol. Helv.*, **26**: 44-92.
- Boardman, J.W. 1989. Inversion of imaging spectrometry data using singular value decomposition. In: *Proceedings of the 9<sup>th</sup> International Geoscience & Remote Sensing Symposium*, IGARSS '89, 10-14 july, Vancouver, Canada: pp. 2069-2072.
- Boardman, J.W. 1990. Inversion of high-spectral resolution data. In: *Proceedings of the Technical Symposium on Optical Engineering and Photonics in Aerospace Sensing*, Society of Photo-Optical Instrument Engineering, SPIE, Vol. 1298: pp. 222-233.
- Boardman, J.W. 1991. Sedimentary facies analysis using imaging spectrometry. In: *Proceedings of the Ninth Thematic Conference on Geologic Remote Sensing*, ERIM, 29 april-2 may, Denver, USA: pp. 1189-1199.
- Boardman, J.W. 1994. Spectral angle mapping: a rapid measure of spectral similarity (in preparation).
- Bon, A., Biermann, C., Koenen, D.B. & Simon, O.J. 1989. Middle Miocene strike-slip tectonics in the Aguilas-Mazarrón region, SE Spain. *Proc. Kon. Ned. Akad. Wetensch.*, **92(2)**: 143-157.
- Bond, G.C. & Kominz, M.A. 1984. Construction of tectonic subsidence curves for the early Paleozoic miogeocline, southern Canadian Rocky mountains: Implications for subsidence mechanisms, age of breakup, and crustal thinning. *Geol. Soc. Am. Bull.*, **95**: 155-173.
- Bond G.C., Kominz, M.A. & Deulin, W.J. 1983. Thermal subsidence and eustasy in the lower Paleozoic miogeocline of western North America. *Nature*, **306**: 775-779.
- Bonini, W.E., Loomis, T.P. & Robertson, D. 1973. Gravity anomalies, ultramafic intrusions and the tectonics of the region around the Strait of Gibraltar. *J. Geophys. Res.*, **76**: 1372-1382.
- Bouchez, J.L. 1977. Plastic deformation of quartzites at low temperature in an area of natural strain gradient. *Tectonophysics*, **39**: 25-50.
- Bouchez, J.L., Lister, G.S. & Nicolas, A. 1983. Fabric asymmetry and shear sense in movement zones. *Geol. Rundsch.*, **72**: 401-419.
- Bouillin, J.P., Durand-Delga, M. & Olivier, Ph. 1986. Betic-Rifian and Tyrrhenian Arcs: distinctive features, genesis and development stages. In: F.C. Wezel (Ed.), *The Origin of Arcs*. Elsevier, Amsterdam: pp. 281-304.
- Bourgeois, J. 1978. *La transversale de Ronda, Cordillères Bétiques, Espagne, Données géologiques pour un modèle d'évolution de l'Arc du Gibraltar*. Ph.D. thesis, Université de Besançon: 445 pp.
- Boutin, H. & Basset, W. 1963, A comparison of OH<sup>-</sup> motions in brucite and micas. *Am. Mineral.*, **48**, 639-651.
- Brunel, M., 1980. Quartz fabrics in shear-zone mylonites. Evidence for a major imprint due

- References -

- to late strain increments. *Tectonophysics*, **64**: 133-144.
- Buchanan, L.J. 1981. Precious metal deposits associated with volcanic environments in the southwest. In: W.R. Dickinson & W.D. Payne (Eds.), *Relations of tectonics to ore deposits in the southern cordillera*. Arizona Geological Society Digest, **24**: pp. 237-262.
- Buform, E., Udias, A. & Colombas, M.A. 1988. Seismicity, source mechanisms and tectonics of the Azores-Gibraltar plate boundary. *Tectonophysics*, **152**: 89-118.
- Burns, R.G. 1970. *Mineralogical Application to Crystal Field Theory*. Cambridge University Press, Cambridge: 224 pp.
- Burrus, J., Bessis, F. & Doligez, B. 1987. Heat flow, subsidence and crustal structure of the Gulf of Lions (NW Mediterranean): a quantitative discussion of the classic passive margin model. *Mem. Can. Soc. Petrol. Geol.*, **12**: 1-15.
- Carder, K.L., Reinersman, P., Chen, R.F., Muller-Karger, F., Davies, C.O. & Hamilton, M. 1993. AVIRIS calibration and application in coastal environments. *Remote Sens. Environ.*, **44**: 205-216.
- Carr, J.R. 1990. Application of spatial filtering theory to kriging. *Math. Geol.*, **22**(8): 1063-1074.
- Carrere, V. & Abrams, M.J. 1988. An assessment of AVIRIS data for hydrothermal alteration mapping in the Goldfield mining district. In: G. Vane (Ed.), *Proceedings of the Airborne Visible/Infrared Imaging Spectrometer (AVIRIS) Performance Evaluation Workshop*, Pasadena, USA, NASA-JPL Publication, 88-38: pp. 134-154.
- Carrere, V. & Conel, J.E. 1993. Recovery of atmospheric water vapour total column abundance from imaging spectrometer data around 940 nm - sensitivity analysis and application to Airborne Visible/Infrared Imaging Spectrometer (AVIRIS) data. *Remote Sens. Environ.*, **44**: 179-204.
- Cetin, H. & Levandowski, D.W. 1991. Interactive classification and mapping of multi-dimensional remotely sensed data using n-dimensional probability density function (nPDF). *Photogramm. Eng. and Remote Sensing*, **57**(12): 1579-1587.
- Cetin, H., Warner, T.A. & Levandowski, D.W. 1993a. Data Classification, Visualization, and Enhancement Using n-Dimensional Probability Density Functions (nPDF): AVIRIS, TIMS, TM, and Geophysical Applications. In: *Proceedings of the Ninth Thematic Conference on Geologic Remote Sensing*, ERIM, 8-11 february, Pasadena, USA: pp. 331-342.
- Cetin, H., Warner, T.A. & Levandowski, D.W. 1993b. Data Classification, Visualization, and Enhancement Using n-Dimensional Probability Density Functions (nPDF): AVIRIS, TIMS, TM, and Geophysical Applications. *Photogramm. Eng. and Remote Sensing*, **59**(12): 1755-1764.
- Chabrilat, S., Pinet, P., Ceuleneer, G., Mustard, J.F., Smith, M.O., Sutin, C., Gondet, B. & Bibring, J.P. 1994. Lithologic discrimination across the Ronda peridotite massif from preliminary calibration of Airborne Hyperspectral data. In: *Proceedings of the First International Airborne Remote Sensing Conference and Exhibition*, 12-15 september, Strasbourg, France, Vol. III: p. 339-345.
- Chernosky, J.V. 1973. The stability of chrysotile,  $\text{Mg}_3\text{Si}_2\text{O}_5(\text{OH})_4$  and the free energy of formation of talc,  $\text{Mg}_3\text{Si}_4\text{O}_{10}(\text{OH})_2$ . *Geol. Soc. Am. Abstracts*.
- Chiu, H.Y. & Collins, W. 1978. A spectroradiometer for airborne remote sensing.

- References -

- Photogramm. Eng. and Remote Sensing*, **44**: 507-517.
- Choukroune, P. 1969. Un exemple d'analyse microtectonique d'une serie calcaire affectee de plis isopaques ("concentriques"). *Tectonophysics*, **7**(1): 57-70.
- Chrien, T.G., Green, R.O. & Eastwood, M.L. 1990. Accuracy of the spectral and radiometric laboratory calibration of the Airborne Visible/Infrared Imaging Spectrometer (AVIRIS). In: *Proceedings of the Technical Symposium on Optical Engineering and Photonics in Aerospace Sensing*, Society of Photo-Optical Instrument Engineering, SPIE, Vol. 1298: pp. 37-49.
- Christie-Blick, N. & Biddle, K.T. 1985. Deformation and basin formation along strike-slip faults. In: K.T. Biddle & N. Christie-Blick (Eds.), *Strike-slip deformation, basin formation, and sedimentation*. SEPM Special Publication, no. 37: pp. 1-34.
- Chung, W.Y. & Kanamori, H. 1976. Source process and tectonic implications of the Spanish deep-focus earthquake of March 29, 1954. *Physics of the Earth and Planetary Interiors*, **13**: 85-96.
- Clark, R.N. 1981. Water frost and ice: The near-infrared spectra reflectance 0.65-2.5µm. *J. Geophys. Res.*, **86**: 3087-3096.
- Clark, R.N. 1983. Spectral properties of mixtures of montmorillonite and dark carbon grains: Implications for remote sensing minerals containing chemically and physically absorbed water. *J. Geophys. Res.*, **88**: 10635-10644.
- Clark, R.N., King, T.V.V., Kleijwa, M., Swayze, G.A. & Vergo, N. 1990. High spectral Resolution Reflectance Spectroscopy of Minerals. *J. Geophys. Res.*, **95**: 12653-12680.
- Clark, R.N. & Lucey, P.G. 1984. Spectral properties of ice-particulate mixtures for remote sensing, I, Intimate mixtures. *J. Geophys. Res.*, **89**: 6329-6348.
- Clark, R.N. & Roush, T.L. 1984. Reflectance spectroscopy: Quantitative analysis techniques for remote sensing applications. *J. Geophys. Res.*, **89**: 6329-6340.
- Cloetingh, S., Gradstein, F., Kooi, H., Grant, A.C. & Kaminski, M. 1990. Did plate reorganization cause rapid late Neogene subsidence around the Atlantic? *J. Geol. Soc. London*, **147**: 495-506.
- Cloetingh, S., McQueen, H. & Lambeck, K. 1985. On a tectonic mechanism for regional sealevel variations. *Earth Planet. Sci. Lett.*, **75**: 157-166.
- Cloutis, E.A., Gaffey, M.J., Jackowski, T.L. & Reed, K.L. 1986. Calibrations of Phase Abundance, Composition, and Particle size distribution for Olivine-Orthopyroxene mixtures from reflectance spectra. *J. Geophys. Res.*, **91**: 11641-11653.
- Cloutis, E.A., Gaffey, M.J., Smith, D.G.W. & Lambert, R.St.J. 1990. Metal Silicate Mixtures: Spectral Properties and Applications to Astroid Taxonomy. *J. Geophys. Res.*, **95**, 8323-8338.
- Cohen, W.B., Spies, T.A. & Bradshaw, G.A. 1990. Semivariograms of digital imagery for analysis of conifer canopy structure. *Remote Sens. Environ.*, **34**: 167-178.
- Collins, W.E. & Chang, S.H. 1988. Application of Geophysical Environmental Research (GER) Airborne scanner data for detection of hydrothermal alteration in Nevada. In: *Proceedings of the Sixth Thematic Conference on Remote Sensing for Exploration Geology*, ERIM, may 16-19, Houston, Texas, USA: pp. 123-124.
- Collins, W.E. & Chang, S.H. 1990. Commercial spectroscopy with the geophysical research imaging spectrometer (GERIS). In: *Proceedings of the Technical Symposium on Optical Engineering and Photonics in Aerospace Sensing*, Society of Photo-Optical Instrument Engineering, SPIE, Vol. 1298: pp. 61-72.

- References -

- Condit, H.R. 1970. The spectral reflectance of American soils. *Photogramm. Eng. and Remote Sensing*, **36**: 955-966.
- Condit, H.R. 1972. Application of characteristic vector analysis to the spectral energy distribution of daylight and the spectral reflectance of American soils. *App. Opt.*, **11**: 74-86.
- Conel, J.E., Adams, S., Alley, R.E., Hoover, G. & Schultz, S. 1988. AIS Radiometry and the problem of Contamination from Mixed Spectral Orders. *Remote Sens. Environ.*, **24**(1): 179-200.
- Conger, S.D., Green, H.W. & Lipps, J.H. 1977. Test ultrastructure of some calcareous foraminifers. *J. Foraminiferal Res.*, **7**: 278-296.
- Coulson, K.L. & Reynolds, D.W. 1971. The spectral reflectance of natural surfaces. *J. Appl. Meteorol.*, **10**: 1285-1295.
- Cover, T.M. 1968. Estimation by the Nearest Neighbor rule. *IEEE Trans. on Information Theory*, **IT-14**(1).
- Cover, T.M. & Hart, P.E. 1967. Nearest Neighbor Pattern Classification, *IEEE Trans. on Information Theory*, **IT-13**(1): 21-27.
- Crowley, J.K. 1986. Visible and near-infrared spectra of carbonate rocks: reflectance variations related to petrographic texture and impurities. *J. Geophys. Res.*, **91**: 5001-5012.
- Crowley, J.K. 1991. Visible and near-infrared (0.4-2.5 $\mu$ m) Reflectance spectra of playa evaporite minerals. *J. Geophys. Res.*, **96**: 16231-16240.
- Crowley, J.K. 1993. Mapping playa evaporite minerals with AVIRIS data: a first report from Death Valley, California. *Remote Sens. Environ.*, **44**: 337-356.
- Crowley, J.K., Brickey, D.W. & Rowan, L.C. 1989. Airborne Imaging Spectrometer Data of the Ruby Mountains, Montana: Mineral Discrimination Using Relative Absorption Band-Depth Images. *Remote Sens. Environ.*, **29**: 121-134.
- Curran, P.J. 1988. The semivariogram in remote sensing: an introduction. *Remote Sens. Environ.*, **24**: 493-507.
- Curran, P.J. 1994. Imaging Spectrometry - its present and future role in environmental research. In: J. Hill & J. M  gier (Eds.), *Imaging Spectrometry - a Tool for Environmental Observations*. Kluwer Academic Publishers, Dordrecht: pp. 1-23.
- Curran, P.J. & Dungan, J.L. 1989. Estimation of Signal-to-Noise: A new Procedure Applied to AVIRIS Data. *IEEE Trans. Geosci. Rem. Sens.*, **27**(5): 620-628.
- Curran, P.J. & Hay, A.M. 1986. The importance of measurement error for certain procedures in remote sensing at optical wavelengths. *Photogramm. Eng. and Remote Sensing*, **52**: 229-241.
- Curran, P.J. & Milton, E.J. 1983. The relationship between the chlorophyll concentration, LAI and reflectance of a simple vegetation canopy. *Int. J. Remote Sens.*, **4**(2): 247-255.
- Curran, P.J. & Williamson, H.D. 1985. The accuracy of ground data used in remote sensing investigations. *Int. J. Remote Sens.*, **6**: 1637-1651.
- Curran, P.J. & Williamson, H.D. 1986. Sample size for ground and remotely sensed data. *Remote Sens. Environ.*, **20**: 31-41.
- Dagbert, M., 1990. Nested indicator approach for ore reserve estimation in highly variable mineralization, In: *Proceedings of the 92nd Annual General meeting of the Canadian institute of Mining and Metallurgy*, may 6-16, Ottawa, Canada, Paper 101.

- References -

- David, M. 1977. *Geostatistical ore reserve estimation*. Elsevier, New York: 364 pp.
- Davies, G.R. Nixon, P.H., Pearson, D.G. & Obata, M. 1993. Tectonic implications of graphitized diamonds from the Ronda peridotite massif, southern Spain. *Geology*, **21**: 471-474.
- De Charpal, O., Tremolieres, P., Jean, F. & Masse, P., 1974. Un exemple de tectonique de plate-forme: les Causses Majeurs (Sud du Massif Central, France). *Rev. Inst. Fr. Pet.*, **29**(5): 641-659.
- Deer, W.A., Howie, R.A. & Zussman, J. 1962. *Rock-forming Minerals, Vol.5. Non-Silicates*. Longman Group, London.
- Deer, W.A., Howie, R.A. & Zussman, J. 1967. *An introduction to rock-forming minerals*. London, Longman, Green and Co. Ltd.: 528 pp.
- De Jong, K. 1991. *Tectono-metamorphic studies and radiometric dating in the Betic Cordilleras (SE Spain) - with implications for the dynamics of extension and compression in the western Mediterranean area*. Ph.D. thesis, Vrije Universiteit, Amsterdam: 204 pp.
- De Jong, K. 1993. The tectono-metamorphic evolution of the Veleta Complex and the development of the contact with the Mulhacen Complex (Betic Zone, SE Spain). *Geol. Mijnbouw*, **71**: 227-237.
- De Jong, K. & Bakker, H.E. 1991. The Mulhacen and Alpujarride Complex in the Sierra de los Filabres, SE Spain: Litho-stratigraphy. *Geol. Mijnbouw*, **70**: 93-103.
- De Jong, S.M. 1992. The analysis of Spectroscopical data to map soil types and soil crusts of Mediterranean eroded soils. *Soil Technology*, **5**: 199-211.
- Delgado, F. & Sanz de Galdeano, C. 1981. Estudio geológico de la Sierra de Gíbalto y sectores próximos (provincias de Granada y Málaga). *Estudios Geol.*, **37**: 69-75.
- Dercourt, J., Zonenshain, L.P., Ricou, L.E., Kazmin, V.G., Le Pichon, X., Knipper, A.L., Grandjacquet, C., Sbertshikov, I.M., Geyssant, J., Lepvrier, C., Pechersky, D.H., Boulín, J., Sibuet, J.C., Savostin, L.A., Sorokhtin, O., Westphal, M., Bazhenov, M.L., Lauer, J.P. & Biju-Duval, B. 1986. Geological evolution of the Tethys belt from the Atlantic to the Pamirs since the Lias. In: J. Aubouin, X. Le Pichon & A.S. Monin (Eds.), *Evolution of the Tethys. Tectonophysics*, **123**: 241-315.
- De Ruig, M.J. 1992. *Tectono-sedimentary evolution of the Prebetic Fold Belt of Alicante (SE Spain) - a study of stress fluctuations and foreland deformation*. Ph.D. thesis, Vrije Universiteit, Amsterdam: 207 pp.
- De Ruig, M.J., Smit, J., Geel, T. & Kooi, H. 1991. Effects of the Pyrenean collision on the Paleocene stratigraphic evolution of the southern Iberian margin (southeast Spain). *Geol. Soc. Am. Bull.*, **103**: 1504-1512.
- De Smet, M.E.M. 1984. Wrenching in the External Zone of the Betic Cordilleras, Southern Spain. *Tectonophysics*, **107**: 57-79.
- Deutsch, C.V. & Journel, A.G. 1992. *GSLIB: Geostatistical Software Library and User's Guide*. Oxford University Press, New York: 340 pp.
- Díaz de Federico, A., Gómez-Pugnaire, M.T., Puga, E. & Sassi, F.P. 1979. New problems in the Sierra Nevada Complex (Betic Cordilleras, Spain). *N. Jb. Geol. Pal. Mh.*, **10**: 577-585.
- Dickey, J.S. 1970. Partial fusion products in Alpine-type peridotites: Serranía de la Ronda and other examples. *Mineralogical Society of America Special Paper*, **3**: 33-49.
- Didon, J. 1960. Le flysch gaditan au Nord et au Nord-est d'Algésiras (Province de Cadix,

- References -

- Espagne). *Bull. Soc. Géol. France*, **2(7)**: 352-361.
- Didon, J. 1969. *Étude géologique du Campo de Gibraltar (Espagne Méridionale)*. Ph.D. thesis, Université de Paris: 539 pp.
- Didon, J., Durand-Delga, M. & Kornprobst, J. 1973. Homologies géologiques entre les deux rives du détroit de Gibraltar. *Bull. Soc. Géol. France*, **15**: 77-104.
- Doblas, M. & Oyarzun, R. 1989. Mantle core complexes and Neogene extensional detachment tectonics in the Western Betic Cordilleras, Spain: an alternative model for the emplacement of the Ronda peridotite. *Earth Planet. Sci. Lett.*, **93**: 76-84.
- Donoghue, D.N.M., Robinson, D.W.C. & Hook, S.J. 1990. Analysis of High spectral resolution data on a Personal Computer. In: R.O. Green (Ed.), *Proceedings of the Second Airborne Visible/Infrared Imaging Spectrometer (AVIRIS) Workshop*, Pasadena, USA, NASA-JPL Publication 90-54: pp. 216-223.
- Dowty, E. 1971. Crystal chemistry of titanian and zirconian garnet: I-Review and spectral studies. *Am. Mineral.*, **56**: 1983-2009.
- Dubois, M. & Magre, J. 1972. Présence de Burdigalien dans la région d'Ubrique (Province de Cadix, Espagne Méridionale). *Ann. Sc. Univ. Besançon*, 3ème série, fasc. **17**: 113-116.
- Duda, R.O. & Hart, P.E. 1973. *Pattern Classification and Scene Analysis*. Wiley, New York: 482 pp.
- Duggin, M.J., Sakhavat, H. & Lindsay, J. 1985. Systematic and random variations in Thematic Mapper digital radiance data. *Photogramm. Eng. and Remote Sensing*, **51**: 1427-1434.
- Dunham, R.J. 1962. Classification of carbonate rocks according to depositional texture. *Memoir Amer. Assoc. Petrol. Geol.*, **1**: 108-121.
- Durand-Delga, M. 1980. La Méditerranée occidentale: étapes de sa genèse et problèmes structuraux liés à celle-ci. *Mém. hors. sér. Soc. géol. France*, **10**: 203-224.
- Durand-Delga, M., Magne, J. & Peyne, Y. 1959. Découverte du Cretacé moyen dans le Bétique de Málaga et le Pénibétique d'Antequera (Andalousie). *C.R. Se. Ac. Sc. Paris*, **249**: 2796-2798.
- Durand, M.A. & Flouzat, G. 1985. Quantification de l'aspect visuel des images classées. *Photo interpretation*, **3(5)**: 47-51.
- Durand, B. & Monin, J.C. 1980. Elemental analysis of kerogens (C, H, O, N, S, Fe). In: B. Durand (Ed.), *Kerogen: Insoluble Organic matter from Sedimentary Rocks*. Technip, Paris: pp. 113-142.
- Dürr, S.H. 1967. Geologie der Serrania de Ronda und ihrer Südwestlichen ausläufer (Andalusien). *Geol. Romana*, **6**: 1-73.
- Egeler, C.G. & Simon, O.J. 1969. Sur la tectonique de la Zone Bétique (Cordillères bétiques, Espagne). *Verh. Kon. Ned. Akad. Wetensch.*, **XXV(3)**: 90 pp.
- Eichmann, R., Saupé, F. & Schidlowsky, M. 1977. Carbon and oxygen isotope studies of rocks in the vicinity of the Almadén mercury deposits (Province of C. Real, Spain). In: D. Klemm & H.J. Schneider (Eds.), *Time and stratabound ore deposits*, Berlin, Springer Verlag: pp. 171-189.
- Elvidge, C.D. 1990. Visible and near infrared reflectance characteristics of dry plant material. *Int. J. Remote Sens.*, **11(10)**: 1775-1795.
- Elvidge, C.D., Chen, Z. & Groeneveld, D.P. 1993. Detection of trace quantities of green vegetation in 1990 AVIRIS data. *Remote Sens. Environ.*, **44**: 271-279.



- References -

- Emslie, A.G. & Aronson, J.R. 1973. Spectral reflectance and emittance of particulate materials, 1, Theory. *Appl. Opt.*, **12**: 2563-2572.
- Esteban, M. 1974. Caliche Textures and 'Microcodium'. *Bull. Soc. Geol. Ital.*, **92**: 105-125.
- Evans, B.W. & Frost, B.R. 1975. Chrome spinel in progressive metamorphism - a preliminary analysis. *Geochim. Cosmochim. Acta.*, **39**: 959-972.
- Evans, B.W., Johannes, W., Otterdoorn, H. & Trommsdorff, V. 1976. Stability of chrysotile and antigorite in the serpentine multisystem. *Schweiz. Mineral. Petrogr. Mitt.*, **56**: 79-93.
- Fabbri, A.G. 1984. *Image processing of geologic data*. Van Nostrand Reinhold publishers, New York: 244 pp.
- Fabbri, A.G., van der Meer, F.D., Valenzuela, C.R. & Kushigbor, C.A. 1993. Shape analysis and Multispectral Classification in Geological Remote Sensing. *Math. Geol.*, **25**: 773-793.
- Fallot, P. 1948. Les Cordillères Bétiques. *Estudios Geol.*, **8**: 83-172.
- Ferns, D.C., Zara, S.J. & Barber, J. 1984. Application of high spectral resolution spectroradiometry to vegetation. *Photogramm. Eng. and Remote Sensing.*, **50(12)**: 1725-1735.
- Fix, E. & Hodges, U.L. 1952. *Discriminatory Analysis: Small Sample Performance*. Project No. 21-49-004, Report No. 11, USAF School of Aviation Medicine, Randolph Field, Texas.
- Fontboté, J.M. 1984. La Cordillera Bética. In: *Libro Jubilar J.M. Ríos*, Geología de España, II, IGME (Instituto Geológico y Minero de España), Madrid: pp. 251-343.
- Forsman, J.P. 1963. The geochemistry of kerogen. In: I.A. Breger (Ed.), *Organic Geochemistry*. Macmillan, New York: pp. 148-182.
- Freund, J.E. & Walpole, J.E. 1987. *Mathematical Statistics*. Prentice Hall, Englewood Cliffs: 608 pp.
- Frizon de Lamotte D., Andrieux, J. & Geuzou, J.C. 1991. Cinématique des chevauchements néogènes dans l'Arc bético-rifain: discussion sur les modèles géodynamiques. *Bull. Soc. Géol. France*, **162**: 611-626.
- Frouin, R., Deschamps, P.Y. & Lecomte, P. 1990. Determination from space of atmospheric total water amounts by differential absorption near 940 nm: Theory and airborne verification. *J. Appl. Meteorol.*, **29**: 448-460.
- Frye, K. 1981. *The Encyclopedia of Mineralogy*. Hutchinson Ross Publishing Company, Stroudsburg: 794 pp.
- Fujimoto, N., Takahashi, Y., Moriyama, T., Shimada, M., Wakabayashi, H., Nakatani, Y. & Obayashi, S. 1989. Evaluation of SPOT HRV image data received in Japan. In: *Proceedings of the 9th International Geoscience & Remote Sensing Symposium, IGARSS '89*, 10-14 July, Vancouver, Canada: pp. 467-470.
- Frey, F.A., Suen, C.J. & Stockman, H.W. 1985. The Ronda high temperature peridotite: Geochemistry and petrogenesis. *Geochim. Cosmochim. Acta.*, **49**: 2469-2491.
- Friedman, G.M. 1959. Identification of carbonate minerals by staining methods: *J. Sed. Petrol.*, **29**: 87-97.
- Fytas, K., Chaouai, N.E., & Lavigne, M. 1989. Indicator kriging performance in gold deposit evaluation. In: *Proceedings of the 91th Annual General meeting of the Canadian Institute of Mining and Metallurgy*, 30 April-3 May, Quebec City, Canada, Paper 58.

- References -

- Gaffey, S.J. 1984. *Spectral reflectance of carbonate minerals in the visible and near-infrared (0.35-2.55 microns): Applications in carbonate petrology*. Ph.D. Thesis, University of Hawaii: 236 pp.
- Gaffey, S.J. 1985. Reflectance spectroscopy in the visible and near infrared (0.35-2.55 microns): Applications in carbonate petrology. *Geology*, **13**: 270-273.
- Gaffey, S.J. 1986. Spectral reflectance of carbonate minerals in the visible and near-infrared (0.35-2.55 microns): calcite, aragonite, and dolomite. *Am. Mineral.*, **71**: 151-162.
- Gaffey, S.J. 1987. Spectral reflectance of carbonate minerals in the visible and near-infrared (0.35-2.55 microns): Anhydrous carbonate minerals. *J. Geophys. Res.*, **92**: 1429-1440.
- Gao, B.C. 1993. An Operational Method for Estimating Signal to Noise Ratios from Data Acquired with Imaging Spectrometers. *Remote Sens. Environ.*, **43**: 23-33.
- Gao, B.C., Heidebrecht, K.B. & Goetz, A.F.H. 1993. Derivation of scaled surface reflectances from AVIRIS data. *Remote Sens. Environ.*, **44**: 165-178.
- García-Casco, A. 1986. *Petrologia, geoquímica y mineralizaciones asociadas del plutón de Santa Eufemia (Batolito de Los Pedroches, Córdoba)*. PhD Thesis University of Granada: 303 pp.
- García-Casco, A. & Pascual, E. 1987. El Plutón de Santa Eufemia (Batolito de Los Pedroches, Córdoba, España): un granitoide epizonal de tipo S. *Geogaceta*, **2**: 56-59.
- García-Hernandez, M., Lopez-Garrido, A.C., Rivas, P., Sanz de Galdeano, C. & Vera, J.A., 1980. Mesozoic paleogeographic evolution of the External Zone of the Betic Cordilleras. *Geol. Mijnbouw*, **59**: 155-168.
- Gates, D.M., Keegan, H.J., Schleter, J.C. & Weidner, V.R. 1965. Spectral properties of plants. *App. Opt.*, **4**(1): 11-20.
- Gausman, H.W. 1974. Leaf reflectance of near infrared. *Photogramm. Eng. and Remote Sensing.*, **40**(2): 57-62.
- Gausman, H.W., Allen, W.A. & Cardenas, R. 1969. Reflectance of cotton leaves and their structure. *Rem. Sens. Environ.*, **1**: 19-22.
- Gausman, H.W., Allen, W.A. Cardenas, R. & Richardson, A.J. 1970. Relation of light reflectance to histological and physical evaluation of cotton leaf maturity. *App. Opt.*, **9**(3): 545-552.
- Geel, T. 1973. *The geology of the Betic of Málaga, the Subbetic, and the zone between these two units in the Vélez Rubio area (southern Spain)*. Ph.D. thesis, Universiteit van Amsterdam: 179 pp.
- Geel, T., Roep, Th.B., ten Kate, W. & Smit, J. 1992. Early-Middle Miocene stratigraphic turning points in the Alicante region (SE Spain): reflections of Western Mediterranean plate-tectonic reorganizations. *Sed. Geol.*, **75**: 223-239.
- Geiser, P.A. & Sansone, S. 1981. Joints, microfractures, and the formation of solution cleavage in limestone. *Geology*, **9**: 280-285.
- Gill, D. 1970. Application of a Statistical Zonation Method to Reservoir Evaluation and Digitized-Log analysis. *Am. Assoc. Petrol. Geol. Bull.*, **54**: 719-729.
- Gillespie, A.R. 1980. Digital techniques of image enhancement. In: B.S. Siegal & A.R. Gillespie (Eds.), *Remote Sensing in Geology*, New York, Wiley: pp. 139-226.
- Gillespie, A.A., Kahle, A.B. & Walker, R.E. 1986. Color enhancement of Highly Correlated Images. I. Decorrelation and HSI Contrast stretch. *Rem. Sens. Environ.*, **20**: 209-235.
- Gillespie, A.A., Kahle, A.B. & Walker, R.E. 1987. Color enhancement of Highly Correlated

- References -

- Images. II. Channel Ratio and "Chromaticity" Transformation Techniques. *Rem. Sens. Environ.*, **22**: 343-365.
- Goetz, A.F.H. 1991. Imaging Spectrometry for studying Earth, Air, Fire and Water. *EARSel Advances in Remote Sensing*, **1**: 3-15.
- Goetz, A.F.H. 1992. Imaging Spectroscopy for Earth Remote Sensing. In: F. Toselli & J. Bodechtel (Eds.), *Imaging Spectroscopy: Fundamentals and Prospective Applications*. Kluwer Academic Publishers, Dordrecht: pp. 1-19.
- Goetz, A.H. & Herring, M. 1989. The High Resolution Imaging Spectrometer for EOS. *IEEE Trans. Geosci. Rem. Sens.*, **27**(2): 136-144.
- Goetz, A.F.H. & Rowan, L.C. 1981. Geologic remote sensing. *Science*, **211**: 781-791.
- Goetz, A.F.H., Rowan, L.C. & Kingston, M.J. 1982. Mineral identification from orbit: initial results from the Shuttle Multispectral Infrared Radiometer. *Science*, **218**: 1020-1031.
- Goetz, A.F.H. & Srivastava, V. 1985. Mineralogical mapping in the Cuprite mining district, Nevada. In: G. Vane & A.F.H. Goetz (Eds.), *Proceedings of the Airborne Imaging Spectrometer (AIS) Data analysis Workshop*, Pasadena, USA, NASA-JPL Publ. 85-41: pp. 22-31.
- Goetz, A.F.H., Vane, G., Solomon, J.E. & Rock, B.N. 1985. Imaging spectrometry for earth remote sensing. *Science*, **228**: 1147-1153.
- Goffé, B., Michard, A., Garcia-Dueñas, V., Gonzalez-Lodeiro, F., Monié, P., Campos, J., Galindo-Zaldivar, J., Jabaloy, A., Martínez-Martínez, J.M. & Simancas, J.F. 1989. First evidence of high-pressure, low-temperature metamorphism in the Alpujarride nappes, Betic Cordilleras (S.E. Spain). *Eur. J. Mineral*, **1**: 139-142.
- Goldsmith, J.R. 1983. Phase relations of rhombohedral carbonates. In: R.J. Reeder (Ed.), *Carbonates: Mineralogy and Chemistry. Mineralogical Society of America Reviews in Mineralogy*, **11**: pp. 49-76.
- González-Donoso, J.M. & Serrano-Lozano, F. 1977. Sobre la presencia de materiales de edad Messiniense en la región de Ronda (Málaga). *Studia Geol.*, **13**: 163-183.
- Gradie, J. & Veverda, J. 1982. When are spectral reflectance curves comparable? *Icarus*, **49**: 109-119.
- Green, R.O. 1992a. Retrieval of reflectance from calibrated radiance imagery measured by the Airborne Visible/Infrared Imaging Spectrometer (AVIRIS) for lithological mapping of the Clark Mountains, California. In: F. Toselli & J. Bodechtel (Eds.), *Imaging Spectrometry: Fundamentals and Prospective Applications*. Kluwer Academic Publishers, Dordrecht: pp. 61-71.
- Green, R.O. 1992b. Determination of the in-flight spectral and radiometric characteristics of the Airborne Visible/Infrared Imaging Spectrometer (AVIRIS). In: F. Toselli & J. Bodechtel (Eds.), *Imaging Spectrometry: Fundamentals and Prospective Applications*. Kluwer Academic Publishers, Dordrecht: pp. 103-123.
- Green, A.A. & Graig, M.D. 1985. Analysis of aircraft spectrometer data with logarithmic residuals. In: G. Vane & A.F.H. Goetz (Eds.), *Proceedings of the Airborne Imaging Spectrometer Data Analysis Workshop*, Pasadena, USA, NASA-JPL Publication 85-41: pp. 111-119.
- Green, H.W., Lipps, J.H. & Showers, B.W. 1980. Test ultrastructure of fusulinid Foraminifers. *Nature*, **283**: 853-855.
- Green, R.O., Vane, G. & Conel, J.E. 1988. Determination of in-flight AVIRIS spectral,

- References -

- radiometric, spectral and signal-to-noise characteristics using atmospheric and surface measurements from the vicinity of the rare-earth-bearing carbonatite at Mountain Pass, California. In: G. Vane (Ed.), *Proceedings of the Airborne Visible/Infrared Imaging Spectrometer (AVIRIS) Performance Evaluation Workshop*, Pasadena, USA, NASA-JPL Publication, 88-38: pp. 162-184.
- Gresens, R.L. 1967. Composition-volume relationships of metasomatism. *Chem. Geol.*, 2: 47-65.
- Grove, C.I., Hook, S.J. & Paylor II, E.D. 1992. *Laboratory Reflectance Spectra of 160 minerals, 0.4 to 2.5 Micrometers*. NASA-JPL Publication 92-2, Pasadena: 300pp.
- Guyot, G., Baret, F. & Jacquemond, S. 1992. Imaging spectroscopy for vegetation studies. In: F. Toselli & J. Bodechtel, *Imaging spectroscopy: Fundamentals and Prospective Applications*, Dordrecht, Kluwer Academic Publishers: pp. 145-165.
- Hamzah, A. 1992. *Structural Geology of the External Zone of the Betic Cordilleras of the Ronda area, Málaga Province, Spain*. Unpublished M.Sc. thesis, ITC, Enschede: 60 pp.
- Hapke, B. 1981. Bidirectional reflectance spectroscopy, 1, theory. *J. Geophys. Res.*, 86: 3039-3054.
- Hapke, B. 1984. Bidirectional reflectance spectroscopy, 3, Correction for macroscopic roughness. *Icarus*, 59: 41-59.
- Hapke, B. 1987. Bidirectional reflectance spectroscopy, 4, The extinction coefficient and the opposition effect. *Icarus*, 67: 264-280.
- Hapke, B. & Wells, E. 1981. Bidirectional reflectance spectroscopy, 2, Experiments and observations. *J. Geophys. Res.*, 86: 3055-3060.
- Harland, W.B., Armstrong, R.L., Cox, A.V., Craig, L.E., Smith, A.G. & Smith, D.G. 1990. *A geologic time scale 1989*. Cambridge Univ. Press, Cambridge, 263 pp.
- Hart, P.E. 1968. The condensed Nearest Neighbor Rule. *IEEE Trans. on Information Theory*, IT-14(3).
- Hawkins, D.M. & Merriam, D.F. 1973. Optimal Zonation of Digitized Sequential Data. *Math. Geol.*, 5(4): 389-395.
- Hegarty, K.A., Weissel, J.K. & Mutter, J.C. 1988. Subsidence history of Australia's southern margin: constraints on basin models. *Am. Assoc. Petrol. Geol. Bull.*, 72: 615-633.
- Heller, P.L., Wentworth, C.M. & Poag, C.W. 1982. Episodic post-rift subsidence of the United States Atlantic continental margin. *Bull. Geol. Soc. Am.*, 93: 379-390.
- Hermes, J.J. 1977. Late Burdigalian folding in the Subbetic north of Vélez Blanco, Province of Almería, Southeastern Spain. *Proc. Kon. Ned. Akad. Wetensch., Ser. B.*, 80(2): 89-99.
- Hermes, J.J. 1978. The stratigraphy of the Subbetic and southern Prebetic of the Vélez Rubio-Caravaca area and its bearing on the transcurrent faulting in the Betic Cordilleras in southern Spain. *Proc. Kon. Ned. Akad. Wetensch., Ser. B.*, 81: 1-54.
- Hermes, J.J. 1985. Algunos aspectos de la estructura de la zona Subbética (Cordilleras Béticas, España Meridional). *Estudios Geol.*, 41: 157-176.
- Hermes, J.J. & Smit, J. 1975. New data on "silexites" of the west Mediterranean area. *Proc. Kon. Ned. Akad. Wet.*, Ser. B., 79(2): 115-122.
- Hill, J. 1991. Analysis of GER imaging spectrometer data acquired during the European imaging spectrometry aircraft campaign (EISAC) '89. Quality assessments and first

- References -

- results. *Earsel Advances in Remote Sensing*, 1(1): 64-77.
- Hook, S.J., Elvidge, C.D., Rast, M. & Watanabe, H. 1991. An evaluation of short-wave-infrared (SWIR) data from the AVIRIS and GEOSCAN instruments for mineralogical mapping at Cuprite, Nevada. *Geophysics*, 56(9): 1432-1440.
- Hostetler, P.B., Coleman, R.G., Mumpton, F.A. & Evans, B.W. 1966. Brucite in Alpine serpentinites. *Am. Mineral.*, 51: 75-98.
- Hsien-Huang, W. & Schowengerdt, R.A. 1992. Image restoration for improved spectral unmixing. In: *Proceedings of the 9<sup>th</sup> International Geoscience & Remote Sensing Symposium*, IGARSS '92, Houston, USA: pp. 558-560.
- Hunt, G.R. 1977. Spectral signatures of particulate minerals in the visible and near-infrared. *Geophysics*, 42: 501-513.
- Hunt, G.R. 1980. Electromagnetic radiation: the communication link in remote sensing. In: B. Siegal & A. Gillespie (Eds.), *Remote sensing in Geology*, New York, Wiley: 702 pp.
- Hunt, G.R. & Evarts, R.C. 1981. The use of near-infrared spectroscopy to determine the degree of serpentinization of ultramafic rocks. *Geophysics*, 46, 316-321.
- Hunt, G.R. & Salisbury, J.W. 1970. Visible and near-infrared spectra of minerals and rocks, I. Silicate Minerals. *Modern Geology*, 1: 283-300.
- Hunt, G.R. & Salisbury, J.W. 1971. Visible and near-infrared spectra of minerals and rocks, II. Carbonates. *Modern Geology*, 2: 23-30.
- Hunt, G.R., Salisbury, J.W., & Lenhoff, C.J. 1971a. Visible and near-infrared spectra of minerals and rocks, III. Oxides and Hydroxides. *Modern Geology*, 2: 195-205.
- Hunt, G.R., Salisbury, J.W., & Lenhoff, C.J. 1971b. Visible and near-infrared spectra of minerals and rocks, IV. Sulphides and sulphates. *Modern Geology*, 3: 1-14.
- Hunt, G.R., Salisbury, J.W., & Lenhoff, C.J. 1972. Visible and near-infrared spectra of minerals and rocks, V. Halides, arsenates, vanadates, and borates. *Modern Geology*, 3: 121-132.
- Hunt, G.R., Salisbury, J.W., & Lenhoff, C.J. 1973a. Visible and near-infrared spectra of minerals and rocks, VI. Additional Silicates. *Modern Geology*, 4: 85-106.
- Hunt, G.R., Salisbury, J.W., & Lenhoff, C.J. 1973b. Visible and near-infrared spectra of minerals and rocks, VII. Acidic Igneous Rocks. *Modern Geology*, 4: 217-224.
- Hunt, G.R., Salisbury, J.W., & Lenhoff, C.J. 1973c. Visible and near-infrared spectra of minerals and rocks, VIII. Intermediate Igneous Rocks. *Modern Geology*, 4: 237-244.
- Hunt, G.R., Salisbury, J.W., & Lenhoff, C.J. 1974. Visible and near-infrared spectra of minerals and rocks, IX. Basic and Ultrabasic igneous rocks. *Modern Geology*, 5: 15-22.
- Hunt, G.R., Salisbury, J.W., & Lenhoff, C.J. 1975. Visible and near-infrared spectra of minerals and rocks, X. Stoney Meteorites. *Modern Geology*, 5: 115-126.
- Hunt, G.R. & Salisbury, J.W. 1976a. Visible and near-infrared spectra of minerals and rocks: XI. Sedimentary rocks. *Modern Geology*, 5: 211-217.
- Hunt, G.R. & Salisbury, J.W. 1976b. Visible and near-infrared spectra of minerals and rocks: XII. Metamorphic rocks. *Modern Geology*, 5: 219-228.
- Huntington, J.F., Green, A.A. & Graig, M.D. 1986. Preliminary Geological Investigation of AIS Data at Mary Kathleen, Queensland, Australia. In: G. Vane (Ed.), *Proceedings of the second Airborne Imaging Spectrometer (AIS) Data Analysis Workshop*,

## - References

- Pasadena, USA, NASA-JPL Publication 86-35: pp. 109-131.
- Hutsinpillar, A., 1988. Discrimination of Hydrothermal Alteration Mineral Assemblages at Virginia City, Nevada, Using the Airborne Imaging Spectrometer. *Remote Sens. Environ.*, **24**: 53-66.
- Ingle, J.C. 1980. *Cenozoic paleobathymetry and depositional history of selected sequences within the southern California continental borderland*. Cushman Foundation Spec. Publ. 19: pp. 163-195.
- Instituto Geológico y Minero de España (IGME), 1972. *Mapa Geológico de España*, Hoja 1.065(15-45) Marbella: 65 pp.
- Instituto Tecnológico GeoMinero de España (ITGE), 1990. *Mapa Geológico de España*, Escala 1:50.000, Hoja 1051 (15-44) Ronda, Segunda Serie, Madrid
- Jabaloy, A., Galindo-Zaldivar, J. & Gonzalez-Lodeiro, F. 1993. The Alpujarride-Nevado-Filabride extensional shear zone, Betic Cordillera, SE Spain. *J. Struct. Geol.*, **15**: 555-569.
- Jansen, W.T. 1993. *General Imaging Spectrometry Interpretation Systems: GenIsis*. San Mateo, WTJ-Software.
- Jensen, J.R. 1986. *Introductory Digital Image Processing (A remote Sensing perspective)*. Englewood Cliffs, N.J., Prentice-Hall: 379 pp.
- Jia, X. & Richards, J.A. 1993. Binary Coding of Imaging Spectrometer Data for Fast Spectral Matching and Classification. *Remote Sens. Environ.*, **43**: 47-53.
- Johannes, W. 1969. An experimental investigation of the system  $MgO-SiO_2-H_2O-CO_2$ . *Am. J. Sci.*, **267**: 1083-1104.
- Johnson, T.V. & Fanale, F.P. 1973. Optical properties of carbonaceous chondrites and their relationship to asteroids. *J. Geophys. Res.*, **78**: 8507-8518.
- Johnson, P.E., Smith, M.O., Taylor-George, S. & Adams, J.B. 1983. A semiempirical method for analysis of the reflectance spectra of binary mineral mixtures. *J. Geophys. Res.*, **88**: 3557-3561.
- Journel, A.G. 1983. Nonparametric estimation of spatial distributions. *Math. Geol.*, **17**: 445-468.
- Journel, A.G. 1989. *Fundamentals of Geostatistics in Five Lessons (Short Course in Geology: Volume 8)*. American Geophysical Union, Washington D.C.: 40 pp.
- Journel, A.G. & Alabert, F. 1989. Non-Gaussian data expansion in the earth science. *Terra Nova*, **1**: 123-134.
- Journel, A.G. & Huijbregts, G.H. 1978. *Mining geostatistics*. Academic Press, New York: 600 pp.
- Journel, A.G. & Posa, D. 1990. Characteristic behaviour and order relations for indicator variograms. *Math. Geol.*, **22**(8): 1011-1025.
- Jupp, D.L.B., Strahler, A.H. & Woodcock, C.E. 1988. Autocorrelation and regularization in digital images I. Basic theory. *IEEE Trans. Geosci. Remote Sens.*, **26**: 463-473.
- Jupp, D.L.B., Strahler, A.H. & Woodcock, C.E. 1989. Autocorrelation and regularization in digital images II. Simple image models. *IEEE Trans. Geosci. Remote Sens.*, **27**: 247-258.
- Kahle, A.B. & Goetz, A.F.H. 1983. Mineralogical information from a new airborne thermal infrared multispectral scanner. *Science*, **222**: 24-27.
- Kahle, A.B., Palluconi, F.D., Hook, S.J., Realmuto, V.J. & Bothwell, G. 1991. The Advanced

- References -

- Spaceborne Thermal Emission and Reflectance Radiometer (ASTER). *International Journal of Imaging Systems and Technology*, **3**: 144-156.
- Kaufman, H., Weisbrich, W., Beyth, M., Bartov, Y., Itamar, A., Ronen, S. & Kafri, U. 1991. Mineral identification using GER-II data acquired from Makhtesh Ramon/Negev, Israel. *Earsel Advances in Remote Sensing*, **1**(1): 82-92.
- Keirein-Young, K.S. & Kruse, F.A. 1989. Comparison of Landsat Thematic Mapper Images and Geophysical Environmental Research Imaging Spectrometer data for alteration mapping. In: *Proceedings of the Seventh Thematic Conference on Remote Sensing for Exploration Geology*, ERIM, 2-6 october, Calgary, Canada: pp. 349-359.
- Kenter, J.A.M., Reymer, J.J.G., Van der Straaten, H.C. & Peper, T. 1990. Facies patterns and subsidence history of the Jumilla-Cieza region (southeastern Spain). *Sed. Geol.*, **67**: 263-280.
- Kerekes, J.P. & Landgrebe, D.A. 1991. Parameter Trade-offs for Imaging Spectroscopy Systems. *IEEE Trans. Geosci. Rem. Sens.*, **29**(1): 57-65.
- King, T.V.V. & Clark, R.N. 1989. Spectral Characteristics of Chlorites and MG-Serpentinities Using High-Resolution Spectroscopy. *J. Geophys. Res.*, **94**: 13997-14008.
- King, T.V.V. & Ridley, W.I. 1987. Relation of the Spectroscopic Reflectance of Olivine to Mineral Chemistry and Some Remote Sensing Implications. *J. Geophys. Res.*, **92**, 11457-11469.
- Klappa, C.F. 1978. Biolithogenesis of Microcodium: elucidation. *Sedimentology*, **25**: 105-125.
- Kleverlaan, K. 1989. Neogene history of the Tabernas Basin (SE Spain) and its Tortonian submarine fan development. *Geol. Mijnbouw*, **68**: 421-432.
- Kneizys, F.X., Anderson, G.P., Shettle, E.P., Gallery, W.O., Abreu, L.W., Selby, J.E.A., Cetwynd, J.H. & Clough, S.A. 1988. *Users guide to LOWTRAN 7*. Air Force Geophysics Laboratory, Hanscom AFB, Massachusetts AFGL-TR-88-0177.
- Kockel, F. 1960. *Die Geologie des gebietes zwischen Rio Guadalhorce und dem Plateau von Ronda (Südspanien)*. Ph.D. thesis, Universität Bonn: 341 pp.
- Kominz, M.A. 1984. Oceanic ridge volumes and sealevel change- and error analysis. *Am. Assoc. Petrol. Geol. Mem.*, **36**: 109-127.
- Kooi, H., Cloetingh, S. & Remmelts, G. 1989. Intraplate stresses and the stratigraphic evolution of the North Sea Central Graben. *Geol. Mijnbouw*, **68**: 49-72.
- Kornprobst, J. 1976. Signification structurale des peridotites dans l'orogène bético-rifain: arguments tirés de l'étude des détritites observés dans les sédiments paléozoïques. *Bull. Soc. Géol. France*, **18**: 607-618.
- Kortum, G. 1969. *Reflectance Spectroscopy*. Springer-Verlag, New York: 366 pp.
- Krohn, M.D. & Altaner, S.P. 1987. Near Infrared detection of ammonium minerals. *Geophysics*, **52**: 924-930.
- Kruse, F.A. 1988. Use of Airborne Imaging Spectrometer Data to Map Minerals Associated with Hydrothermally Altered Rocks in the Northern Grapevine Mountains, Nevada, and California. *Remote Sens. Environ.*, **24**: 31-51.
- Kruse, F.A., Keirein-Young, K.S. & Boardman, J.W. 1990. Mineral Mapping at Cuprite, Nevada with a 63-channel Imaging Spectrometer. *Photogramm. Eng. and Remote Sensing*, **56**: 83-92.
- Kruse, F.A., Lefkoff, A.B., Boardman, J.W., Heidebrecht, K.B., Shapiro, A.T., Barloon, P.J. & Goetz, A.F.H. 1993. The Spectral Image Processing System (SIPS) - Interactive

- References -

- Visualization and Analysis of Imaging Spectrometer Data. *Remote Sens. Environ.*, **44**: 145-163.
- Kruse, F.A., Raines, G.L. & Watson, K. 1985. Analytical techniques for extracting geologic information from multichannel airborne spectroradiometer and airborne imaging spectrometer data. In: *Proceedings of the Fourth Thematic Conference on Remote Sensing for Exploration Geology*, ERIM, 1-4 april, San Francisco, USA: pp. 309-324.
- Kubelka, P. 1948. New contribution to the optics of intensely light scattering materials. *Journ. Opt. Soc. Am.*, **38**: 448-457.
- LaBaw, C. 1987. Airborne Imaging Spectrometer 2: The optical design. In: G. Vane, A.F.H. Goetz & D.D. Norris (Eds.), *Proceedings of the Society of Photo-optical Instrumentation Engineers*, SPIE, Vol. 834.
- Lanaja, J.M., Querol, R. & Navarro, A. 1987. *Contribución de la exploración petrolífera al conocimiento de la geología de España*. IGME (Instituto Geológico y Minero de España), Madrid: 465 pp.
- Landgrebe, D.A. 1992. On the use of stochastic process-based methods for the analysis of Hyperspectral data. In: *Proceedings of the 12<sup>th</sup> International Geoscience and Remote Sensing Symposium*, IGARRS '92, 26-29 May, Houston, USA: pp. 552-554.
- Lang, H.R., Bartholomew, M.J., Grove, C.I. & Paylor, E.D. 1990. Spectral Reflectance characterization (0.4 to 2.5 and 8.0 to 12.0µm) of Phanerozoic strata, Wind River Basin and southern BigHorn Basin Areas, Wyoming. *J. Sed. Petrol.*, **60**(4): 504-524.
- Lazarev, A.N. 1974. The dynamics of crystal lattices. In: V.C. Farmer (Ed.), *The infrared spectra of minerals*. Mineralogical Society, London: pp. 69-85.
- LeBlanc, D. & Olivier, Ph. 1984. The role of strike-slip in the Betic-Rifian orogeny. *Tectonophysics*, **101**: 345-355.
- Lee, J.L. & Hoppel, K. 1989. Noise modelling and estimation of remotely-sensed images. In: *Proceedings of the 9<sup>th</sup> International Geoscience & Remote Sensing Symposium*, IGARSS '89, 10-14 july, Vancouver, Canada: pp. 2912-2917.
- Lee, C. & Landgrebe, D.A. 1993. Analyzing High-Dimensional Multispectral Data. *IEEE Trans. Geosci. Rem. Sens.*, **31**(4): 792-800.
- Lehmann, F., Rothfuß, H. & Richter, R. 1990. Evaluation of imaging spectrometer data (GER) for the spectral analysis of an old vegetation covered waste deposit. In: *Proceedings of the 10<sup>th</sup> International Geoscience & Remote Sensing Symposium*, IGARSS '90, may 20-24, Washington D.C., USA: pp. 1613-1616.
- Lemoine, M. & Trümpy, R. 1987. Pre-oceanic rifting in the Alps. In: C. Froidevaux & Tan Tjong Kie (Eds.), *Deep Internal Processes and Continental Rifting*. *Tectonophysics*, **133**: 305-320.
- Lister, G.S. & Domsiepen, U.F. 1982. Fabric transitions in the Saxony Granulite terrain. *J. Struct. Geol.*, **4**: 81-93.
- Lister, G.S. & Williams, P.F. 1979. Fabric development in shear zones: theoretical controls and observed phenomena. *J. Struct. Geol.*, **1**: 283-297.
- Loneragan, L., Platt, J.P. & Gallagher, L. 1994. The Internal-External Zone Boundary in the eastern Betic Cordillera, SE Spain. *J. Struct. Geol.*, **16**(2): 175-188.
- Long, G., Neglia, S. & Favretto, L. 1968. The metamorphism of the kerogen from Triassic black shales, southeast Sicily. *Geochim. Cosmochim. Acta.*, **23**: 647-656.
- Loomis, T.P. 1972a. Contact metamorphism of pelitic rock by the Ronda ultramafic intrusion,



- References -

- Southern Spain. *Geol. Soc. Am. Bull.*, **83**: 2449-2474.
- Loomis, T.P. 1972b. Diapiric emplacement of the Ronda high-temperature ultramafic intrusion, southern Spain. *Geol. Soc. Am. Bull.*, **83**: 2475-2496.
- Loomis, T.P. 1975. Tertiary mantle diapirism, orogeny and plate tectonics east of the Strait of Gibraltar. *Am. J. Sci.*, **275**: 1-30.
- Lucazeau, F. & Le Douaran, S. 1985. The blanketing effects of sediments in basins formed by extension: a numerical model. Applications to the Gulf of Lyon and Viking Graben. *Earth Planet. Sci. Lett.*, **40**: 92-102.
- Lundeen, M.T. 1978. Emplacement of the Ronda peridotite, Sierra Bermeja, Spain. *Geol. Soc. Am. Bull.*, **88**: 172-180.
- Lunetta, R.S., Congalton, R.G., Fenstermaker, L.K., Jensen, J.R., McGwire, K.C. & Tinney, L.R. 1991. Remote Sensing and Geographic Information System Data Integration: Error sources and research issues. *Photogramm. Eng. and Remote Sensing*, **57**: 677-687.
- Lyon, R.J.P. & Lanz, K. 1985. Field Utilization and analysis of AIS 128-channel imagery using microcomputers: application to Yerington, Nevada, field area. In: G. Vane and A.F.H. Goetz (Eds.), *Proceedings of the Airborne Imaging Spectrometer Data Analysis Workshop*, Pasadena, USA, NASA-JPL Publication 85-41: pp. 35-40.
- Mäkel, G.H. 1985. *The geology of the Malaguide Complex and its bearing on the geodynamic evolution of the Betic-Rif orogen (southern Spain and northern Morocco)*. Ph.D. thesis, Universiteit van Amsterdam, GUA papers of Geology, Ser. 1, **22**: 263 pp.
- Malkmus, W. 1967. Random Lorentz band model with exponential-tailed S line intensity distribution function. *Journ. Opt. Soc. Am.*, **57**: 323-329.
- Malpas, J. 1992. Serpentine and the geology of serpentinized rocks. In: B.A. Roberts & J. Procter (Eds.), *The Ecology of Areas with Serpentinized Rocks: A World Review*. Kluwer Academic Publishers, Dordrecht: pp. 7-30.
- Marconnet, B., Leymarie, P. & Monget, J. 1984. La teledetection spatiale utilisee comme moyen de prospection miniere sur une region a gisements etain-tungstene (Province de Zamora, Espagne). *Zeitschrift der Deutschen Geologische Gesellschaft*, **135**: 373-381.
- Marsh, S.E. & McKeon, J.B. 1983. Integrated Analysis of High-Resolution Field and Airborne Spectroradiometer Data for Alteration Mapping. *Econ. Geol.*, **78**: 618-632.
- Martín-Algarra, A. 1980. Rasgos de la sedimentación y su evolución a lo largo del Mesozoico en el dominio de la Unidad de las Nieves (Cordillera Bética, Andalucía). In: *Proceedings of the IX. Congreso Nac. de Sedimentología (Resúmenes y Comunicaciones)*, Salamanca: p. 88.
- Mather, P.M. 1987. *Computer processing of remotely sensed images*. Chichester, Wiley: 352 pp.
- Matossi, F. 1928. Absorption linear polarisierter ultraroter Strahlung im Kalkspat ( $2\mu$ - $16\mu$ ). *Zeitschrift für Physik*, **48**: 616-623.
- Maucher, A. & Saupé, F. 1967. Sedimentärer Pyrit aus der Zinnerlagerstätte Almadén (Provinz Ciudad Real, Spanien). *Mineral Deposita*, **2**: 312-317.
- Mazer, A.S., Martin, M., Lee, M. & Solomon, J.E. 1988. Image processing software for imaging spectrometry data analysis. *Rem. Sens. Environ.*, **24**(1): 201-210.
- McCauley, J.F., Schaber, G.G., Breed, C.S., Grolier, M.J., Haynes, C.V., Issawi, B. & Blom, R. 1982. Subsurface valleys and geoarcheology of the Eastern Sahara revealed by Shuttle Radar. *Science*, **218**: 1004-1021.

- References -

- McKenzie, D. 1978. Some remarks on the development of sedimentary basins. *Earth Planet. Sci. Lett.*, **40**: 25-32.
- Meer, P., Jolion, J.M. & Rosenfield, A. 1990. A fast parallel algorithm for blind estimation of noise variance. *IEEE Trans. Pattern Anal. Machine Intelligence*, **12**: 216-223.
- Michael, A.J. 1984. Determination of stress from slip data: faults and folds. *J. Geophys. Res.*, **89**: 11517-11526.
- Mollat, H. 1965. *Die Geologie der Sierra Blanca und ihrer Umgebung*. Ph.D. Thesis, University of Bonn: 75pp.
- Mollat, H. 1968. Schichtenfolge und tektonischer Bau der Sierra Blanca und ihrer Umgebung (Betische Kordilleren, Südsanien). *Geol. Jahrb.*, **86**: 471-521.
- Montenat, C., Ott d'Estevou, P. & Masse, P. 1987. Tectono-sedimentary characters of the Betic Neogene basins evolving in a crustal transcurrent shear zone (SE Spain). *Bull. Centres Rech. Explor. Prod. Elf-Aquit.*, **11**(1): 1-22.
- Moody, J.B. 1976. Serpentinization: a review. *Lithos*, **9**: 125-138.
- Moore, R.K. & White, W.B. 1971. Intervalence electron transfer effects in the spectra of melanite garnets. *Am. Mineral.*, **56**: 826-840, 1971.
- Mulders, M.A. 1987. *Remote Sensing in Soil Science*. Amsterdam, Elsevier: 379 pp.
- Mustard, J.F. & Pieters, C.M. 1987. Quantitative abundance estimates from bidirectional reflectance measurements. *J. Geophys. Res.*, **92**: 617-626.
- Nash, D.B. & Conel, J.E. 1974. Spectral reflectance systematics for mixtures of powdered hypersthene, labradorite, and ilmenite. *J. Geophys. Res.*, **79**: 1615-1621.
- Navarro-Vila, F. & Tubía, J.M. 1983. Essai d'une nouvelle differenciation des nappes Alpujarrides dans le secteur occidental des Cordilleres Betiques (Andalousie, Espagne). *C.R. Se. Ac. Sc. Paris*, **296**: 111-114.
- Nicolas, A. & Poirier, J.P. 1976. *Crystalline Plasticity and Solid State Flow in Metamorphic Rocks*. Wiley, London: 445 pp.
- Nilsson, N.J. 1965. *Learning Machines*. McGraw-Hill, New York: 137 pp.
- Obata, M. 1980. The Ronda peridotite: garnet-, spinel-, and plagioclase lherzolite facies and P-T trajectories of a high-temperature mantle intrusion. *J. Petrol.*, **21**: 533-572.
- O'Hanley, D.S. 1992. Solution to the volume problem in serpentinization. *Geology*, **20**: 705-708.
- O'Hanley, D.S., Chernosky, J.V., Jr. & Wicks, F.J. 1989. The stability of lizardite and chrysotile. *Can. Mineral.*, **27**: 483-493.
- Okada, K., & Iwashita, A. 1992. Hyper-multispectral image analysis based on waveform characteristics of spectral curve. *Adv. Space Res.*, **12**(7): 433-442.
- Okada, K., Segawa, K. & Hayashi, I. 1993. Removal of the vegetation effect from LANDSAT TM and GER imaging spectroradiometer data. *ISPRS J. Photogram. Remote Sensing*, **48**(6): 16-27.
- Ortega-Gironés, E. & Hernandez-Sobrinio, A. 1992. The Mercury deposits of the Almadén syncline, Spain. *Chron. Recherche Minière*, **506**: 3-24.
- Osete, M.L., Freeman, R. & Vegas, R. 1988. Preliminary paleomagnetic results from the Subbetic Zone (Betic Cordilleras, southern Spain): kinematic and structural implications. *Physics of the Earth and Planetary Interiors*, **52**: 283-300.
- Page, N.J. 1967. Serpentinization at Burro Mountain, California. *Contr. to Miner. and Petr.*, **14**: 321-342.

- References -

- Paquet, J. 1967. *Étude géologique de l'Ouest de la Province de Murcie (Espagne)*. Ph.D. thesis, Université de Lille: 593 pp.
- Park, W.C. & Schot, E.H. 1968. Stylolites: their nature and origin. *J. Sed. Petr.*, **38**: 175-191.
- Pearson, D.G., Davies, G.R., Nixon, P.H. & Milledge, H.J. 1989. Graphitized diamonds from a peridotite in Morocco and implications for anomalous diamond occurrences. *Nature*, **338**: 60-62.
- Peper, T. & Cloetingh, S. 1992. Lithospheric dynamics and tectono-stratigraphic evolution of the Mesozoic Betic rifted margin (southeastern Spain). In: E. Banda & P. Santanach (Eds.), *Geology and Geophysics of the Valencia Trough, Western Mediterranean. Tectonophysics*, **203**: 345-361.
- Peyre, Y. 1974. *Géologie d'Antequera et de sa région (Cordillères Bétiques), Espagne*. Ph.D. thesis, Université de Paris: 538 pp.
- Platzman, E.S. 1992. Paleomagnetic rotations and the kinematics of the Gibraltar arc. *Geology*, **20**: 311-314.
- Platzman, E.S., Platt, J.P. & Olivier, P. 1993. Paleomagnetic rotations and fault kinematics in the Rif Arc of Morocco. *J. Geol. Soc. London*, **150**: 707-718.
- Porter, W.M., Chrien, T.G., Hansen, E.G. & Sarture, C.M. 1990. Evolution of the Airborne Visible/Infrared Imaging Spectrometer (AVIRIS) flight and ground data processing systems. In: *Proceedings of the Technical Symposium on Optical Engineering and Photonics in Aerospace Sensing*, Society of Photo-Optical Instrument Engineering, SPIE, Vol. 1298: pp. 11-17.
- Porter, W.M. & Enmark, H.T. 1987. A system overview of the Airborne Visible/Infrared Imaging Spectrometer (AVIRIS). In: *Proceedings of the 31th annual International Technical Symposium*, 16-21 august 1987, Society of Photooptical Instrumentation Engineers Vol. 834: pp. 22-31.
- Povarennykh, A.S. 1978. The use of infrared spectra for the determination of minerals. *Am. Mineral.*, **63**: 956-959.
- Price, A. 1977. *Beckman instructions 015-555416*. Fullerton, California.
- Priem, H.N., Boelrijk, N.A., Hebeda, E.H., Oen, I.S., Verdurmen, E.A. & Verschure, R.H. 1979. Isotopic dating of the emplacement of the ultramafic masses in the Serrania de Ronda, southern Spain. *Contrib. Mineral. Petrol.*, **70**: 103-109.
- Puga, E., Portugal, M., Diaz de Federico, A., Bargossi, G.M. & Morten, L. 1989a. The evolution of the magmatism in the External Zones of the Betic Cordilleras during the Mesozoic. *Geodyn. Acta (Paris)*, **3**: 253-266.
- Puga, E., Diaz de Federico, A., Bargossi, G.M. & Morten, L. 1989b. The Nevado-Filabride metaophiolite association in the Cobdar region (Betic Cordillera, SE Spain): preservation of pillow structures and development of coronitic eclogites. *Geodyn. Acta (Paris)*, **3**: 17-36.
- Puigdefàbregas, C. & Souquet, P. 1986. Tectono-sedimentary cycles and depositional sequences of the Mesozoic and Tertiary from the Pyrenees. In: E. Banda & S.M. Wickman (Eds.), *The geological evolution of the Pyrenees. Tectonophysics*, **129**: 173-203.
- Puschmann, H. 1967a. Das Paläozoikum in gebiet zwischen San Benito und Torrecampo, Sierra Morena, Spanien. *Geol. Mijnbouw*, **46**: 383-391.
- Puschmann, H. 1967b. Zum problem der schichtlim Devon der Sierra Morena (Spanien). *Geol. Rundsch.*, **56**: 528-542.

# - References -

- Rast, M. 1992. ESA's Activities in the field of imaging spectroscopy. In: F. Toselli & J. Bodechtel (Eds.), *Imaging Spectroscopy: Fundamentals and Prospective Applications*. Dordrecht, Kluwer: pp. 167-191.
- Rast, M., Hook, S.J., Elvidge, C.D. & Alley, R.E. 1991. An evaluation of techniques for the extraction of mineral absorption features from high spectral resolution remote sensing data. *Photogramm. Eng. and Remote Sensing*, **57**(10): 1303-1309.
- Reeder, R.J. 1983. Crystal chemistry of the rhombohedral carbonates. In: R.J. Reeder (Ed.), *Carbonates: Mineralogy and Chemistry. Mineralogical Society of America Reviews in Mineralogy*, **11**: pp. 1-47.
- Rehault, J.P., Boillot, G. & Mauffret, A. 1984. The Western Mediterranean Basin geological evolution. *Mar. Geol.*, **55**: 447-477.
- Reimer, J.H., Heyada, J.R., Carpenter, S.C., Deich, W.T.S. & Lee, M. 1987. Airborne Visible/Infrared Imaging Spectrometer (AVIRIS) ground data processing system. In: *Proceedings of the Technical Symposium on Optical Engineering and Photonics in Aerospace Sensing*, Society of Photo-Optical Instrument Engineering, SPIE, Vol. 834: pp. 79-90.
- Reisberg, L., Zindler, A. & Jagoutz, E. 1989. Further Sr and Nd isotopic results from peridotites of the Ronda Complex. *Earth Planet. Sci. Lett.*, **96**: 161-180.
- Reisberg, L., Allegre, C.J. & Luck, J.M. 1991. The Re-Os systematics of the Ronda ultramafic complex of southern Spain. *Earth Planet. Sci. Lett.*, **105**: 196-213.
- Richards, J.A. 1993. *Remote Sensing Digital Image Analysis: An Introduction*. Springer-Verlag, Berlin: 340 pp.
- Richardson, A.J. & Wiegand, C.L. 1977. Distinguishing vegetation from soil background information. *Photogramm. Eng. and Remote Sensing*, **43**: 1541-1552.
- Roberts, D.A., Smith, M.O. & Adams, J.B. 1993. Green vegetation, Nonphotosynthetic vegetation, and soils in AVIRIS data. *Rem. Sens. Environ.*, **44**: 255-269.
- Roberts, D.A., Yamaguchi, Y. & Lyon, R.J.P. 1985. Calibration of Airborne Imaging Spectrometer Data to percent reflectance using field spectral measurements. In: *Proceedings of the 19<sup>th</sup> International Symposium on Remote Sensing of Environment*, ERIM, 21-25 october, Ann Arbor, USA: pp. 679-688.
- Rockwell, B.W. 1991. Evaluation of GERIS Airborne Spectrometer data analysis for disseminated gold exploration: A case study from the Getchell Trend/Potosi Mining District, Nevada, USA. In: *Proceedings of the Eighth Thematic Conference on Geologic Remote Sensing*, ERIM, april 29-may 2, Denver, USA: pp. 837-850.
- Rodriguez-Estrella, T. 1977. Síntesis geológica del Prebético de la Provincia de Alicante. *Bol. Geol. Min. España*, **T.LXXXVIII-3**: 183-214.
- Roep, Th.B. 1972. Stratigraphy of the "Permo-Triassic" Saladilla formation and its tectonic setting in the Betic of Málaga (Vélez Rubio region, SE Spain). *Proc. Kon. Ned. Akad. Wetensch.*, Ser. B, **75**: 223-247.
- Rossi, R.E., Dungan, J.L. & Beck, L.R. 1994. Kriging in the Shadows: Geostatistical Interpolation for Remote Sensing. *Remote Sens. Environ.*, **49**: 32-40.
- Rowan, L.C., Anton-Pancheco, C., Brickey, D.W., Kingston, M.J. Payas, A., Vergo, N. & Crowley, J.K. 1987. Digital classification of contact metamorphic rocks in Extremadura, Spain using Landsat thematic mapper data. *Geophysics*, **52**: 885-897.
- Rowan, L.C., Jones, O.D. & Parlewicz, M.J. 1990. The use of Visible and Near-Infrared

- References -

- Spectral Reflectance for estimating the thermal maturity of organic matter in sedimentary rocks. In: *Proceedings Fifth Australasian Remote Sensing Conference*, 8-12 October, Perth, Australia.
- Rubin, T.D. 1993. Spectral Mapping with Imaging Spectrometers: *Photogramm. Eng. and Remote Sensing*, **59**(2): 215-220.
- Santos-García, J.A., Jerez-Mir, F. & Muñoz del Real, J.L. 1991. Los depósitos Miocenos en los alrededores de Andujar (depresión del Guadalquivir, Provincia de Jaen). *Estudios Geol.*, **47**: 33-42.
- Saupé, F. 1973. La géologie du gisement du mercure d'Almadén (Province de C. Real, Espagne). *Science de la Terre Mémoire*, **29**: 342 pp.
- Saupé, F. 1990. Geology of the Almadén Mercury Deposit, Province of C. Real, Spain. *Econ. Geol.*, **85**: 482-510.
- Saupé, F., Dunoyer, H. & Teichmüller, M. 1977. Étude du métamorphisme régional dans la zone d'Almadén (Province de C. Real, Espagne). *Science de la Terre*, **21**(3): 251-269.
- Savostin, L.A., Sibuet, J.C., Zonenshain, L.P., Le Pichon, X. & Roulet, M.J. 1986. Kinematic evolution of Tethys belt from the Atlantic Ocean to the Pamirs since the Triassic. *Tectonophysics*, **123**: 1-35.
- Schmid, S.M., Casey, M. & Starkey, J. 1981. The microfabric of calcite tectonites from the Helvetic Nappes (Swiss Alps). In: K.R. McClay & N.J. Price (Eds.), *Thrust and Nappe tectonics. Geological Society of London Special Publication*, **9**: pp. 151-158.
- Schroeder, R.A., Weir, C.E. & Lippencott, E.R. 1962. Lattice frequencies and rotational barriers for inorganic carbonates and nitrates from low temperature infrared spectroscopy. *Journal of Research of the National Bureau of Standards A. Physics and Chemistry*, **66a**: 407-434.
- Schubert, W. 1965. *Lignin Biochemistry*. New York, Academic press: 131 pp.
- Sclater, J.C. & Christie, P.A.F. 1980. Continental stretching: an explanation of the post-mid Cretaceous subsidence of the central North Sea basin. *J. Geophys. Res.*, **85**: 3711-3739.
- Sebestyen, G. 1962. *Decision-making Processes in Pattern Recognition*. MacMillan Company, New York: 162 pp.
- Sellers, P.J. 1989. Vegetation-Canopy spectral reflectance and biophysical processes. In: G. Asrar (Ed.), *Theory and Applications of optical Remote Sensing*, New York, Wiley: pp. 297-335.
- Serra, J. 1982. *Image analysis and Mathematical Morphology*. Academic Press, New York: 610 pp.
- Serrano-Lozano, F. 1979. *Los Foraminíferos planctónicos del Mioceno superior de la cuenca de Ronda y su comparación con los de otras áreas de las Cordilleras Béticas*. Ph.D. thesis, Universidad de Málaga: 272 pp.
- Serrano-Lozano, F. 1980. Los materiales del Mioceno Superior de la Cuenca de Ronda (Málaga). *Estudios Geol.*, **36**: 231-236.
- Shendy, M.M. 1992. *The application of Remote Sensing and soil survey in the establishment of a Geographical Information System for a part of the Guadalhorce Catchment*. Unpublished M.Sc. thesis, ITC, Enschede: 94 pp.
- Simon, O.J. 1987. On the Triassic of the Betic Cordilleras (Southern Spain). *Cuad. Geol. Ibérica*, **11**: 385-402.

- References -

- Simpson, C. & Schmid, S.M., 1983. An evaluation of criteria to deduce the sense of movement in sheared rocks. *Geol. Soc. Am. Bull.*, **94**: 1281-1288.
- Singer, R.B. 1981. Near-infrared spectral reflectance of mineral mixtures: Systematic combinations of pyroxenes, olivine, and iron oxides. *J. Geophys. Res.*, **86**: 7967-7982.
- Singer, R.B. & McCord, T.B. 1979. Mars: Large scale mixing of bright and dark surface materials and implications for analysis of spectral reflectance. In: *Proceedings of the 10th Lunar and Planetary Science Conference*, 19-23 March, Houston, USA: pp. 1835-1848.
- Singh, R.P. & Sirohi, A. 1994. Spectral properties of different types of soil surfaces. *ISPRS J. Photogram. Remote Sensing*, **49**(4): 34-40.
- Smid, A.G.F. & Heijke, P.J. 1987. *Three-dimensional stress analysis based on striated fault planes*. Internal Report of the University of Amsterdam: 80pp.
- Smit, J. 1979. Microcodium: its earliest occurrence and other considerations. *Revue de Micropaleontologie*, **22**(1): 44-50.
- Smith, M.O., Adams, J.B. & Sabol, D.E. 1994. Spectral Mixture Analysis: New strategies for the analysis of Multispectral Resolution data. In: J. Hill & J. M  gier (Eds.), *Imaging Spectrometry - a Tool for Environmental Observations*. Kluwer Academic Publishers, Dordrecht: 125-143.
- Soha, J.M. & Schwartz, A.A. 1978. Multispectral histogram normalization contrast enhancement. In: *Proceedings of the 5th Canadian Symposium on Remote Sensing*, Victoria BC, Canada: pp. 86-93.
- Spakman, W. 1990. Tomographic images of the upper mantle below central Europe and the Mediterranean. *Terra Nova*, **2**: 542-553.
- Speer, J.A. 1983. Crystal chemistry and phase relations of orthorhombic carbonates. In: R.J. Reeder (Ed.), *Carbonates: Mineralogy and Chemistry*. Mineralogical Society of America *Reviews in Mineralogy*, **11**: pp. 145-190.
- Srivastava, S.P., Roest, W.R., Kovacs, L.C., Oakley, G., L  vesque, S., Verhoef, J. & Macnab, R. 1990. Motion of Iberia since the Late Jurassic: Results from detailed aeromagnetic measurements in the Newfoundland basin. In: G. Boillot & J.M. Fontbot   (Eds.), *Alpine evolution of Iberia and its continental margins*. *Tectonophysics*, **184**: 229-260.
- Staplin, F.L. 1969. Sedimentary organic matter, organic metamorphism, and oil and gas occurrences. *Bull. Can. Petr. Geol.*, **17**: 47-66.
- Steckler M.S. & Watts, A.B. 1978. Subsidence of the Atlantic type continental margin off New York. *Earth Planet. Sci. Lett.*, **41**: 1-13.
- Strahler, A.H. 1980. The use of prior probabilities in Maximum Likelihood Classification of Remotely sensed data. *Remote Sens. Environ.*, **10**: 135-163.
- Streckeisen, A. 1973. Plutonic rocks. Classification and nomenclature recommended by the IUGS Subcommittee on the Systematics of Igneous Rocks. *Geotimes*, **18**: 26-30.
- Streckeisen, A. 1976. To each plutonic rock its proper name. *Earth Sci. Rev.*, **12**: 1-33.
- Suen, C.J. & Frey, F.A. 1987. Origins of the mafic and ultramafic rocks in the Ronda peridotite. *Earth Planet. Sci. Lett.*, **85**: 183-202.
- Sunshine, J.M., Mustard, J.F. & Pieters, C.M. 1993. Deconvolving overlapping absorption features to extract compositional information from reflectance data. In: *Proceedings of the Ninth Thematic Conference on Geologic Remote Sensing*, ERIM, 8-11 february, Pasadena, USA: pp. 151-155.

- References -

- Sunshine, J.M., Pieters, C.M. & Pratt, S.F. 1990. Deconvolution of mineral absorption bands: An improved approach. *J. Geophys. Res.*, **95**: 6955-6966.
- Swain, P.H. & Davis, S.M. 1978. *Remote Sensing: The Quantitative Approach*. McGraw-Hill, New York: 396 pp.
- Tabit, A., Kornprobst, J., Li, J.P. & Woodland, A.B. 1990. Origin and evolution of the massif at Beni Bousera, Morocco: petrological evidence. In: *International workshop on orogenic lherzolites and mantle processes (Abstract)*, Blackwell: 19 pp.
- Tanré, D., Deroo, C., Duhaut, P., Herman, M., Morcrette, J.J., Perbos, J. & Deschamps, P.Y. 1986. *Simulation of the Satellite Signal in the Solar Spectrum (5S), Users Guide* (UST de Lille, 59655 Villeneuve d'ascq, France: Laboratoire d'Optique Atmosphérique).
- Teillet, P.M. 1989. Surface reflectance retrieval using atmospheric correction algorithms. In: *Proceedings of the 9<sup>th</sup> International Geoscience & Remote Sensing Symposium, IGARSS '89*, 10-14 july, Vancouver, Canada: pp. 864-867.
- Testermann, J.D. 1962. A statistical reservoir zonation technique. *J. Petrol. Techn.*, **14**: 889-503.
- Thayer, T.P. 1966. Serpentinization considered as a constant-volume metasomatic process. *Am. Mineral.*, **51**: 685-710.
- Tibor, G., Ben-Avraham, Z., Steckler, M.S. & Fligelman, H. 1992. Late Tertiary subsidence history of the southern Levant margin and its implications for the Messinian event. *J. Geophys. Res.*, **97**: 17593-17605.
- Tjalsma, R.C. 1971. Stratigraphy and foraminifera of the Neogene of the Eastern Guadalquivir Basin (Southern Spain). *Utrecht Micropal. Bull.*, **4**: 161 pp.
- Torres-Roldán, R.L. 1979. The tectonic subdivision of the Betic Zone (Betic Cordilleras, southern Spain): its significance and one possible geotectonic scenario for the westernmost Alpine belt. *Am. J. Sci.*, **279**: 19-51.
- Tou, J.T. & Gonzalez, R.C. 1974. *Pattern recognition principles*. Addison-Wesley Publishing Group, Reading: 377 pp.
- Trudgen, P. & Hoffmann, F. 1967. Statistically analyzing core data. *J. Petrol. Techn.*, **13**(4): 497-503.
- Tubía, J.M. 1985. Significado de las deformaciones internas en las peridotitas de Sierra Alpujata (Málaga). *Estudios Geol.*, **41**: 369-380.
- Tubía, J.M. 1988a. Estructura de los Alpujarrides occidentales: Cinematica y condiciones de emplazamiento de las peridotitas de Ronda. Parte IV: Deformaciones de las peridotitas de Sierra Alpujata. *Boletín Geológico y Minero*, T. XCIX-V: 715-747.
- Tubía, J.M. 1988b. Estructura de los Alpujarrides occidentales: Cinematica y condiciones de emplazamiento de las peridotitas de Ronda. Parte III: Tectonica de la aureola dinamo-termica del manto de Ojén. *Boletín Geológico y Minero*, T. XCIX-IV: 490-515.
- Tubía, J.M. & Cuevas, J. 1986. High-temperature emplacement of the Los Reales peridotite nappe (Betic Cordillera, Spain). *J. Struct. Geol.*, **8**: 473-482.
- Tubía, J.M. & Cuevas, J. 1987. Structures et cinématique liées à la mise en place des peridotites de Ronda (Cordillères Bétiques, Espagne). *Geodin. Acta (Paris)*, **1**: 59-69.
- Tubía, J.M., Cuevas, J., Navarro-Vila, F., Alvarez, F. & Aldaya, F., 1992. Tectonic evolution of the Alpujarride Complex (Betic Cordillera, Southern Spain). *J. Struct. Geol.*, **14**: 193-203.
- Turcotte, D.L. & Ahern, J.L. 1977. On the thermal and subsidence history of sedimentary basins. *J. Geophys. Res.*, **82**: 3762-3766.

- References -

- Udias, A., Lopez Arroyo, A. & Mezcuca, J. 1976. Seismo-tectonics of the Azores-Alboran region. *Tectonophysics*, **31**: 259-289.
- Venable, W.H., Jr., Weidner, V.R. & Hsia, J.J. 1976. *Information sheet on optical properties of pressed Halon coating*. National Bureau of Standards, Washington D.C.
- Van den Bosch, J.M. & Alley, R.E. 1991. Comparison of three atmospheric correction models for a vegetated Airborne Visible/Infrared Imaging Spectrometer (AVIRIS) scene. In: *Proceedings of the Eighth Thematic Conference on Geologic Remote Sensing*, ERIM, april 29-may 2, Denver, USA: pp. 413-421.
- Van der Marel, H.W. & Beutelspacher, H. 1976. *Atlas of infrared spectroscopy of clay minerals and their admixtures*. Elsevier, New York: 396 pp.
- Van der Meer, 1993. Classification of high-spectral resolution imagery using an indicator kriging based technique. In: A. Soares (Ed.), *Geostatistics Trioa '92*. Kluwer Academic Press, Dordrecht: pp. 829-840.
- Van der Meer, F. 1994a. Triassic-Miocene paleogeography and basin evolution of the Subbetic zone between Ronda and Málaga, Spain. *Geol. Mijnbouw*, in press.
- Van der Meer, F. 1994b. Quantitative subsidence analysis and thermal-mechanical modelling: examples from southern Spain and Libya. *ITC-Journal*, **94**(1): 52-63.
- Van der Meer, F. 1994c Calibration of Airborne Visible/Infrared Imaging Spectrometer data (AVIRIS) to reflectance and mineral mapping in hydrothermal alteration zones: an example from the 'Cuprite Mining District'. *Geocarto International*, **9**(3): 23-37.
- Van der Meer, 1994d. Extraction of mineral absorption features from high-spectral resolution data using non-parametric geostatistical techniques. *Int. J. Remote Sens.*, **15**(11): 2193-2214.
- Van der Meer, F. 1994e. Quantification of particle shape and texture using mathematical morphology and geostatistical techniques. *ITC-Journal*, **94**(1): 13-22.
- Van der Meer, F. 1994f. Sequential Indicator Conditional Simulation and Indicator Kriging applied to discrimination of dolomitization in GER 63-channel Imaging Spectrometer data. *Nonrenewable Resources*, **3**(2): 146-164.
- Van der Meer, F. 1994g Spectral Reflectance of Carbonate Mineral Mixtures and Bidirectional Reflectance Theory: Quantitative Analysis Techniques for Application in Remote Sensing. *Remote Sensing Review*, submitted.
- Van der Meer, F. 1994h. ITC's research in Imaging Spectrometry. In: J.L. van Genderen (Ed.), *European Research in Remote Sensing, Earsel Newsletter*, **17**: 22-23.
- Van der Meer, F. 1994i. Mapping the degree of serpentinization within ultramafic rock bodies using imaging spectrometer data. *Int. J. Remote Sens.*, **15**(18): 3851-3857.
- Van der Meer, F. 1994j. Mineral identification and mapping of hydrothermal alteration zones using high-spectral resolution images (AVIRIS). *ITC-Journal*, **94**(2): 145-154.
- Van der Meer, F. 1995. Estimating and simulating the degree of serpentinization of peridotites using hyperspectral remotely sensed imagery. *Nonrenewable Resources*, **4**(1): 84-98.
- Van der Meer, F. & Cloetingh, S. 1993a. Intraplate stresses and the subsidence history of the Sirte Basin (Libya). In: S. Cloetingh, W. Sassi & F. Horváth (Eds.), *The origin of sedimentary basins: Inferences from quantitative modelling and basin analysis*. *Tectonophysics*, **226**: 37-58.
- Van der Meer, F. & Cloetingh, S. 1993b. Late Cretaceous and Tertiary subsidence history of the Sirte Basin (Libya); an example of the use of backstripping analysis. *ITC-Journal*,



- References -

93(1): 68-76.

- Van der Meer, F., Westerhof, A.B. & Van Dijk, P.M. 1994. Digital Classification of the Los Pedroches batholith, south-central Spain, using Landsat Thematic Mapper data. *Int. J. Remote Sens.*, in press.
- Van der Straaten, H.C. 1990. *The Abarán Basin - a Neogene pull-apart basin in SE Spain*. Ph.D. thesis, Vrije Universiteit, Amsterdam: 193 pp.
- Van der Straaten, H.C. 1993. Neogene strike-slip faulting in southeastern Spain: the deformation of the pull-apart basin of Abarán. *Geol. Mijnbouw*, **71**: 205-225.
- Van der Wal, D. 1993. *Deformation processes in Mantle Peridotites: with emphasis on the Ronda peridotite of SW Spain*. Ph.D. Thesis, University of Utrecht: 180 pp.
- Van der Wal, D. & Vissers, R.L.M. 1993. Uplift and emplacement of upper mantle rocks in the western Mediterranean. *Geology*, **21**: 1119-1122.
- Vane, G. 1989. First results from the Airborne Visible/Infrared Imaging Spectrometer (AVIRIS). In: G. Vane (Ed.), *Airborne Visible/Infrared Imaging Spectrometer (AVIRIS): A description of the sensor, ground data, processing facility, laboratory calibration and first results*. Pasadena, USA, NASA-JPL Publication, 87-38: pp. 89-97.
- Vane, G., Chrien, T.G., Reimer, T.G., Green, R.O. & Conel, J.E. 1988. Comparison of laboratory calibrations of the Airborne Visible/Infrared Imaging Spectrometer (AVIRIS) at the beginning and end of the first flight season. In: *Proceedings of the Technical Symposium on Optical Engineering and Photonics in Aerospace Sensing*, Society of Photo-Optical Instrument Engineering, SPIE, Vol. 924: pp. 168-178.
- Vane, G., Chrisp, M., Enmark, H., Macenka, S. & Solomon, J. 1984. Airborne Visible/Infrared Imaging Spectrometer (AVIRIS): an advanced tool for earth remote sensing. In: *Proceedings of the 1984 IEEE International Geoscience & Remote Sensing Symposium*, Vol. SP215, IEEE, New York: pp. 751-757.
- Vane, G. & Goetz, A.F.H. 1985. Introduction for the proceedings of the Airborne Imaging Spectrometer (AIS) Data analysis workshop. In: *Proceedings of the Airborne Imaging Spectrometer (AIS) data analysis workshop*, Pasadena, USA, NASA-JPL Publication 85-41.
- Vane, G. & Goetz, A.F.H. 1988. Terrestrial Imaging Spectroscopy. *Remote Sens. Environ.*, **24**: 1-29.
- Vane, G. & Goetz, A.F.H. 1993. Terrestrial Imaging Spectrometry: Current Status, Future Trends. *Remote Sens. Environ.*, **44**: 117-126.
- Vane, G., Green, R.O., Chrien, T.G., Enmark, H.T., Hansen, E.G. & Porter, W.M. 1993. Airborne Visible/Infrared Imaging Spectrometer (AVIRIS). *Remote Sens. Environ.*, **44**: 127-143.
- Vane, G., Porter, W.M., Reimer, J.H., Chrien, T.G. & Green, R.O. 1988. AVIRIS performance during the 1987 flight season: An AVIRIS project assessment and summary of the NASA-sponsored performance evaluation. In: G. Vane (Ed.), *Proceedings of the Airborne Visible/Infrared Imaging Spectrometer (AVIRIS) Performance Evaluation Workshop*, Pasadena, USA, NASA-JPL Publication, 88-38: pp. 1-20.
- Van Hinte, J.E. 1978. Geohistory analysis - Application of micropaleontology in exploration geology. *Am. Assoc. Petrol. Geol. Bull.*, **62**: 201-222.
- Van Wees, J.D., de Jong, K., & Cloetingh, S. 1992. Two-dimensional P-T-t modelling and the dynamics of extension and inversion in the Betic zone (SE Spain). *Tectonophysics*,

- References -

- 203: 305-324.
- Vegas, R. & Banda, E. 1982. Tectonic framework and Alpine evolution of the Iberian Peninsula. *Earth Evolution Sciences*, 4: 320-342.
- Vera, J.A., García-Hernández, M., López-Garrido, A.C., Comas, M.C., Ruiz-Ortiz, P.A. & Martín-Algarra, A. 1982. La Cordillera Bética. In: *El Cretácico de España*. Univ. Complutense, Madrid: pp. 515-632.
- Visser, R.L.M. 1981. *A structural study of the central Sierra de los Filabres (Betic Zone, SE Spain), with emphasis on deformational processes and their relation to the Alpine metamorphism*. Ph.D. thesis, Universiteit van Amsterdam: 154 pp.
- Watts, A.B., Karner, G.D. & Steckler, M.S. 1982. Lithospheric flexure and the evolution of sedimentary basins. *Phil. Trans. Roy. Soc. Lond., Ser. A*, 305: 249-281.
- Webster, R. 1973. Automatic soil-boundary location from transect data. *Math. Geol.*, 5(1): 27-37.
- Webster, R., Curran, P.J. & Munden, J.W. 1989. Spatial correlation in reflected radiation from the ground and its implication for sampling and mapping by Ground-Based radiometry. *Remote Sens. Environ.*, 29: 67-78.
- Weidner, V.R. & Hsia, J.J. 1981. Reflection properties of pressed polytetrafluoroethylene powder. *Journ. Opt. Soc. Am.*, 71: 856-859.
- Wendtland, M. & Hecht, H. 1966. *Reflectance Spectroscopy*. Wiley, New York: 298 pp.
- Wenner, D.B. & Taylor, H.P. 1974. D/H and O<sup>18</sup>/O<sup>16</sup> studies of serpentinization of ultramafic rocks. *Geochim. Cosmochim. Acta.*, 38: 1255-1286.
- Westerhof, A.B. 1975. *Genesis of Magnetite ore near Marbella, Southern Spain: Formation by oxidation of silicates in polymetamorphic gedrite-bearing and other rocks*. Ph.D. thesis, University of Amsterdam: 216pp.
- Westerhof, A.B. 1977. On the contact relation of high-temperature peridotites in the Serrania de Ronda, southern Spain. *Tectonophysics*, 39: 579-591.
- White, S.H., Burrows, S.E., Carreras, J., Shaw, N.D. & Humphreys, F.J. 1980. On mylonites in ductile shear zones. *J. Struct. Geol.*, 2: 175-187.
- Wicks, F.J. & O'Hanley, D.S. 1988. Serpentine minerals: structures and petrology. In: S.W. Bailey (Ed.), *Hydrous Phyllosilicates (Exclusive of Micas)*. *Rev. Mineral.*, 19: pp. 91-167.
- Wilson, C.J.L. 1975. Preferred orientation in quartz ribbon mylonites. *Geol. Soc. Am. Bull.*, 86: 968-974.
- Windeler, D.S. & Lyon, R.J.P. 1991. Discriminating Dolomitization of Marble in the Ludwig Skarn near Yerington, Nevada Using High-Resolution Airborne Infrared Imagery. *Photogramm. Eng. and Remote Sensing*, 57: 1171-1177.
- Woodcock, C.E., Strahler, A.H. & Jupp, D.L.B. 1988a. The use of variograms in remote sensing: I. Scene models and simulated images. *Remote Sens. Environ.*, 25: 324-348.
- Woodcock, C.E., Strahler, A.H. & Jupp, D.L.B. 1988b. The use of variograms in remote sensing: II. Real digital images. *Remote Sens. Environ.*, 25: 349-379.
- Yan, L. 1992. *TMU based versus SMU based data modelling for the design of an Environmental Management Data base*. Unpublished M.Sc. thesis, ITC, Enschede: 69 pp.
- Zamudio, J.A. 1993. Removal of the vegetation component from imaging spectrometer data. In: *Proceedings of the Ninth Thematic Conference on Geologic Remote Sensing*, ERIM, 8-11 February, Pasadena, USA: pp. 35-40.

- References -

- Zeck, H.P., Monie, P., Villa, I.M. & Hansen, B.T. 1992. Very high rates of cooling and uplift in the Alpine belt of the Betic Cordilleras, southern Spain. *Geology*, **20**: 79-82.
- Ziegler, P.A. 1988. *Evolution of the Arctic-North Atlantic and Western Tethys*. Am. Assoc. Petr. Geol. Mem., **43**: 198 pp.
- Ziegler, P.A. 1990. *Geological Atlas of Western and Central Europe*. Shell Internationale Petroleum Maatschappij, The Hague: 239 pp.
- Zindler, A., Staudigel, H., Hart, S.R., Endres, R. & Goldstein, S. 1983. Nd and Sr isotopic study of a mafic layer from Ronda ultramafic complex. *Nature*, **304**: 226-230.

## Acknowledgements

I would like to take the opportunity to thank all persons that contributed to the research reported in this thesis.

In the first place I wish to thank Prof. Dr. Salemon Kroonenberg and Prof. Dr. Andrea Fabbri for their willingness to act as promotor. Salle, I have many reasons to thank you. You accepted me as your student and guided me through my PhD study with an incredible amount of enthusiasm. Although I sometimes overloaded you with paper, you always had time to review my work and to provide constructive criticism yielding viewpoints which I had not yet considered. Our discussions really gave me the energy to continue my work. Your guidance and experience in fieldwork were very beneficial to my studies. I hope that in future I will have other opportunities to work with you. Andrea, you made it possible for me to conduct this research in imaging spectrometry. You put me in contact with various experts in the fields of remote sensing and quantitative geology which allowed me to conduct the research which is represented in this thesis. Also within ITC you made sure that I had the support and resources to carry out my studies. Throughout the years, you handed me the statistical and mathematical tools needed and suggested how these might be implemented in image analysis. I highly appreciate the constructive criticism and stimulating discussions we had on quantitative aspects related to remote sensing.

The spectral analyses presented in this thesis were carried out at the NASA Jet Propulsion Laboratory in Pasadena (California). I would like to thank Dr. Harold Lang for hosting me several times at JPL and for the numerous discussions on the measured spectra. Furthermore, I would like to thank Mrs. Cindy Grove and Dr. Elsa Abbot for their help in processing the samples. The members of the JPL Geology & Planetology section are thanked for creating a very pleasant working atmosphere for me.

I would like to thank my colleagues for their patience and in particular Dr. Bas Koopmans for suggesting the subject. Dr. Karl Stainz provided a thorough review of the PhD proposal.

Work on the Ronda-Málaga area of the following former ITC students has been most helpful: Mr. B. Agbor, MSc., Mr. A. Hamzah, MSc., Mrs. Li Yan, MSc., and Dr. M. Shendy, Mr. M. F. Njamu, Mr. C. Bedoya, and Mrs. A.I. Despaigne-Diaz.

Many persons reviewed part of my work in its present form or in the form of journal articles. Their critical comments and advice is highly appreciated: Dr. Koen de Jong and Dr. Dick Batjes (both Chapter 2), Dr. J.M. Tubía (Chapter 3), Dr. James E. Conel, Dr. John W. Salisbury, and Dr. Allan Gillespie (all Chapter 4), Dr. Roger Clark and Dr. John Mustard (Chapter 5), Dr. K.N. Au (Chapter 7), Dr. Roussos Dimitrakopoulos, Dr. Alfred Stein, Dr.

*- Acknowledgements -*

Chantal de Fouget, Dr. Michel Dagbert, and Dr. Edward Isaaks (all Chapter 8), Dr. James Carr, Dr. Mike Abrams, and Dr. Daniel H. Knepper Jr. (Chapter 9). Dr. Phil Westerhof and Dr. Paul van Dijk collaborated in the work on the Los Pedroches Batholith presented in Chapter 6.

Image processing of hyperspectral image data was carried out using the Spectral Image Processing Software developed at the University of Colorado. Dr. Kathy Heidebrecht and Dr. Fred Kruse are thanked for support provided on SIPS. Geostatistical estimation and simulation was done using the Geostatistical Software Library (GSLIB) from Stanford University.

The help of Wim Bakker and Martin Blankestijn in getting the IDL and the SIPS-software running and keeping it operational is very much appreciated.

Mrs. Ellen de Koning and Mr. Jan van Doesburg provided the chemical analyses of rock and soil samples, respectively.

Henk Frowijn, Benno Masselink, and Gert Lutke-Schipholt prepared many of the drawings.

Henk Scharrenborg and Andries Menning prepared camera-ready copies of the figures at numerous occasions.

I would like to thank Mr. Rafael Ramos López and Mr. Miguel Angel Catalina Mimendi from the Agencia Parque Natural Sierra de las Nieves for authorizing the study and admission to the National Park.

The research presented in this thesis was carried out within the scope of the project entitled 'Imaging spectrometry for mineralogical mapping of the Ronda peridotite and adjacent Neogene sedimentary basins' funded under the ITC Research Programme Theme No. 7: 'Exploration for and Environmentally sound Exploitation of Mineral and Water Resources'. I want to thank all those involved in evaluating and approving this project.

Finally I want to thank Marianne for relativizing my work and for her moral support.

## ***Bibliography***

### **Journal papers:**

- [1] Van der Meer, F. 1994. Sequential Indicator Conditional Simulation and Indicator Kriging applied to discrimination of dolomitization in GER 63-channel Imaging Spectrometer data. *Nonrenewable Resources*, **3**(2): 146-164.
- [2] Van der Meer, F. 1994. Extraction of mineral absorption features from high-spectral resolution data using non-parametric geostatistical techniques. *International Journal of Remote Sensing*, **15**(11): 2193-2214.
- [3] Van der Meer, F. 1994. Quantitative subsidence analysis and thermal mechanical modelling: examples from the Subbetic zone of southern Spain and the Sirte basin of Libya. *ITC-Journal*, **94**(1): 52-63.
- [4] Van der Meer, F. 1994. ITC's Research in Imaging Spectrometry. In: J.L. van Genderen (Ed.), *European Research in Remote Sensing*. *Earsel Newsletter*, **94**(17): 22-23.
- [5] Van der Meer, F. 1994. Mineral mapping in hydrothermal alteration zones using high-spectral resolution imagery (AVIRIS). *ITC-Journal*, **94**(2): 145-154.
- [6] Van der Meer, F. 1994. Mapping the degree of serpentization within ultramafic rock bodies using imaging spectrometer data. *International Journal of Remote Sensing*, **15**(18): 3851-3857.
- [7] Van der Meer, F. 1994. Calibration of Airborne Visible/Infrared Imaging Spectrometer data (AVIRIS) to reflectance and mineral mapping in hydrothermal alteration zones: an example from the Cuprite Mining District. *Geocarto International*, **9**(3): 23-37.
- [8] Van der Meer, F. 1994. Triassic-Miocene paleogeography and basin evolution of the Subbetic zone between Ronda and Málaga. *Geologie & Mijnbouw*, in press.
- [9] Van der Meer, F. 1994. Quantitative subsidence analysis and thermal mechanical modelling: examples from the Subbetic zone of southern Spain and the Sirte basin of Libya. In: A. Fabbri & J.J. Royer (Ed.), *Third CODATA Conference on Geomathematics and Geostatistics*, *Sciences de la Terre*, **32**: 666pp.

- Bibliography -

- [10] Van der Meer, F. 1994. Spectral reflectance of Carbonate mineral mixtures and Bidirectional Reflectance theory: Quantitative analysis techniques for application in remote sensing. *Remote Sensing Reviews*, in press.
- [11] Van der Meer, F., Westerhof, A.B. and Van Dijk, P.M. 1994. Digital Classification of the contact metamorphic aureole along the Los Pedroches Batholith, southern-central Spain, using Landsat Thematic Mapper data. *International Journal of Remote Sensing*, in press.
- [12] Van der Meer, F. 1994. Classification of remotely sensed imagery using an indicator kriging approach: application to the problem of calcite-dolomite mineral mapping. *International Journal of Remote Sensing*, submitted.
- [13] Van der Meer, F. 1994. Metamorphic facies zonation in the Ronda peridotites mapped from GER imaging spectrometer data. *International Journal of Remote Sensing*, submitted.
- [14] Van der Meer, F. 1995. Estimating and simulating the degree of serpentinization of peridotites using hyperspectral remotely sensed imagery. *Nonrenewable Resources*, 4(1): 84-98.
- [15] Fabbri, A.G., van der Meer, F., Valenzuela, C.R. and Kushigbor, C. 1993. Shape analysis and Multispectral Classification in Geological Remote Sensing. *Mathematical Geology*, 25(7): 773-793.

**Books:**

- [16] Van der Meer, F. 1993. Classification of high-spectral resolution imagery using an indicator kriging based technique. In: A. Soares (Ed.), *Geostatistics Trioa '92*, Kluwer Academic Press, Dordrecht, The Netherlands: pp. 829-840.

**Conference proceedings:**

- [17] Van der Meer, F. 1992. Comparison of conventional Multispectral Classification methods and a new indicator kriging based method using high-spectral resolution imagery. In: *Proceedings of the 17<sup>th</sup> Congress for Photogrammetry and Remote Sensing*, ISPRS, Commission VII, 2-14 august, Washington D.C., USA, International Archives of Photogrammetry and Remote Sensing, Vol. 29, Part B7: pp. 72-79.
- [18] Van der Meer, F. 1993. Mapping of hydrothermal alteration minerals using high-spectral resolution imagery (AVIRIS). In: J.L. van Genderen, R.A. van Zuidam, and C. Pohl (Eds.), *Proceedings of the International Symposium Operationalization of Remote Sensing*, 19-23 April, Enschede, The Netherlands, Vol. 3: pp. 43-54.
- [19] Van der Meer, F. 1994. Sequential Gaussian Conditional Simulation for mapping of dolomitization in GER 63 channel imaging spectrometer data (Ronda, southern Spain). Presented at the 2<sup>e</sup> Aardwetenschappelijk Congres, 21 & 22 april, Veldhoven, the Netherlands, Abstract Nr. 24.
- [20] Van der Meer, F. 1994. Mapping of calcite/dolomite mineral mixtures from GER 63

- Bibliography -

channel imaging spectrometer data in southern Spain. In: *Proceedings of the Tenth Conference Geologic Remote Sensing*, ERIM, 9-12 may, San Antonio, USA, Vol. 1: pp. 309-320.

[21] Van der Meer, F. 1994. Estimating the degree of serpentization of ultramafic rocks from GER 63 channel imaging spectrometer data. In: *Proceedings of the International Symposium on Resource and Environmental Monitoring ECO-RIO '94*, ISPRS, Commission VII, 26-30 september, Rio de Janeiro, Brazil, International Archives of Photogrammetry and Remote Sensing, Vol. 30, Part 7a: pp. 434-441.

**Symposium and conference presentations:**

[22] Van der Meer, F. 1991. A comparison of Conventional Multispectral Classification methods and a new indicator kriging based method using high-spectral resolution images. *Presented at the Environmental Geology Symposium*, 9-10 september, Enschede, The Netherlands.

[23] Van der Meer, F. 1992. Basic image processing techniques for Remote sensing of Natural Resources. *Presented at the Comett II Seminars on "Characterization and modelling of natural resources"*, 26-28 october, Rome, Italy.

[24] Van der Meer, F. 1992. Remote sensing and Image analysis. *Presented at the Comett II Seminars on "Characterization and modelling of natural resources"*, 26-28 October, Rome, Italy.



## ***Curriculum Vitae***

Freek Dirk van der Meer werd geboren op 26 mei 1966 te Amsterdam. In 1984 behaalde hij het Atheneum diploma aan het Snellius Lyceum te Amstelveen. In datzelfde jaar begon hij zijn studie geologie aan de Vrije Universiteit te Amsterdam. Voor zijn doctoraalscriptie deed hij onderzoek naar de tectonostratigrafische ontwikkeling van het Prébeticum in Zuidoost-Spanje. Hij studeerde af in augustus 1989 in de structurele geologie met als bijvakken geofysica, wiskunde, vaste stoffysica en milieukunde. Gedurende enkele maanden van zijn studie was hij werkzaam bij Grondmechanica Delft als geologisch assistent binnen de afdeling Geofysica waar hij zich bezig hield met onderzoek naar de toepassingen van ondiepe geofysische methoden voor het in kaart brengen van de ondergrond onder dijken langs het IJsselmeer. Tevens verrichte hij onderzoek naar de toepasbaarheid van grondradar voor breukanalyse in een karst gebied op Malta. In 1989 kwam hij in dienst van het ITC als docent in de geologie en remote sensing binnen de Afdeling Geological Survey. In 1992 werd het in dit proefschrift resulterende, door het ITC gefinancierde, onderzoek aangevangen. Sinds 1 mei 1993 werkt hij als universitair docent binnen de Afdeling Geological Survey van het ITC.

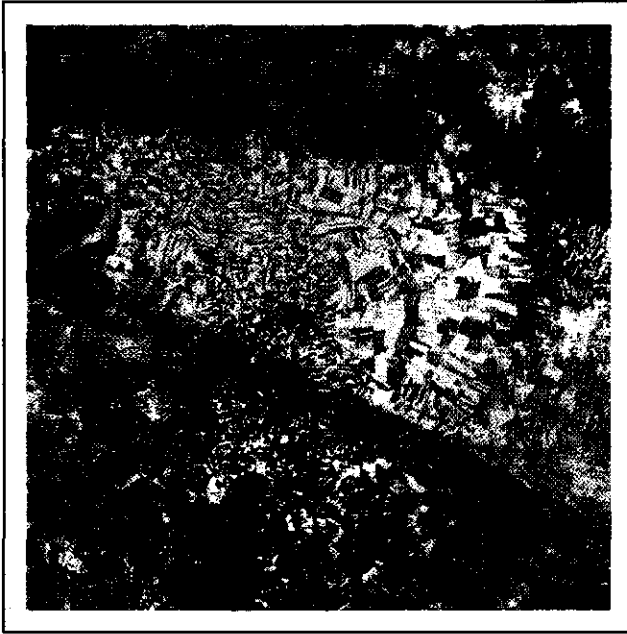


**Plate 1 (Fig. 6.22, page 154):** Colour Ratio component image with TM 5:7 displayed in red, TM 3:1 displayed in green, and TM 5 displayed in blue (see text for discussion).



**Plate 2 (Fig. 6.23, page 155):** Colour Ratio component image with TM 5:7 displayed in red, TM 3:1 displayed in green, and TM 5 displayed in blue. All ratios are normalized difference images (see text for discussion).

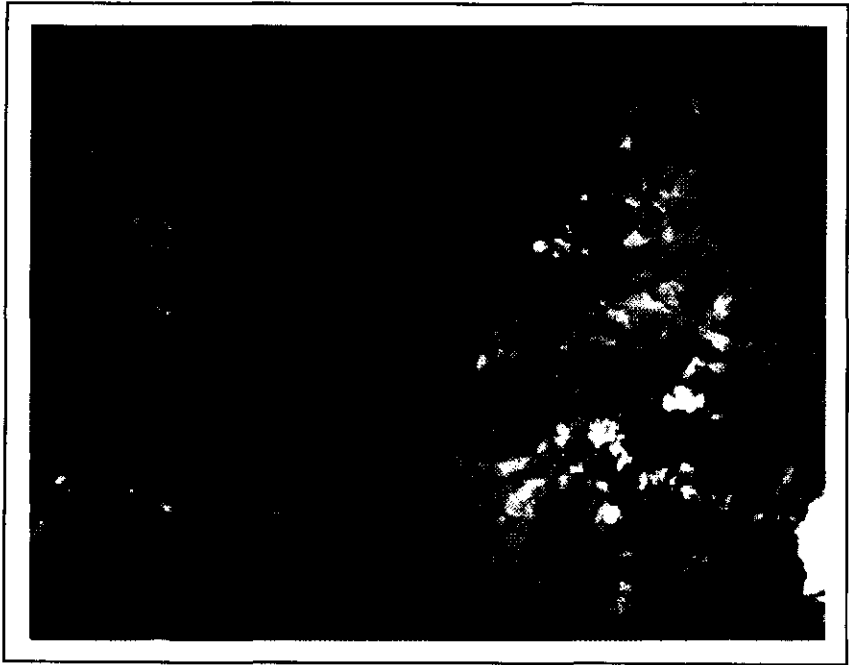


**Plate 3 (Fig. 8.2, page 200):** Colour-composite image with band centred at  $1.995\mu\text{m}$  in red (left shoulder of clay mineral absorption features), band centred at  $2.312\mu\text{m}$  in blue (right shoulder of clay mineral absorption features), and band centred at  $2.232\mu\text{m}$  in green (centre of the absorption feature). In this image, moderately altered opalized and argillized units containing hydrothermal clay minerals are represented in light blue colours. The unaltered Tertiary volcanic deposits are red coloured in the image.

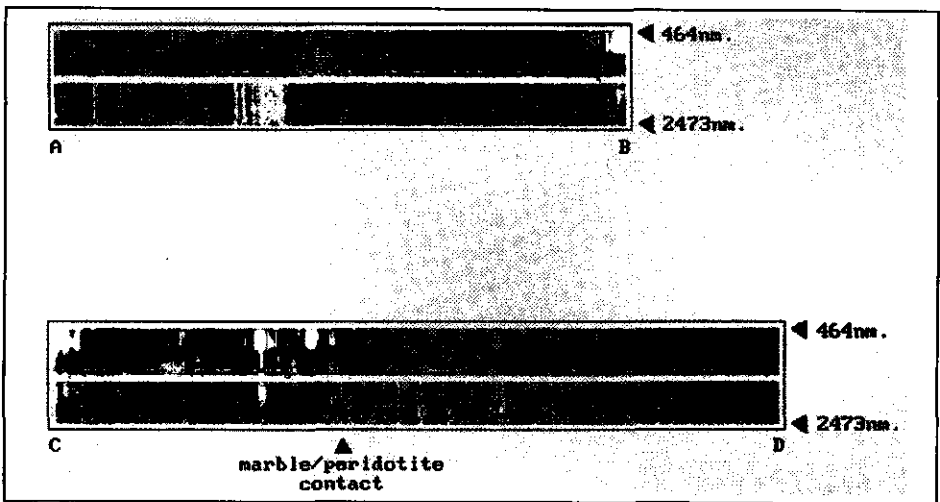


**Plate 4 (Fig. 8.3, page 201):** Colour-coded stacked spectrum for the GERIS data set from southern Spain. The x-axis of the plot is the spectral band and the y-axis represents the pixel position along a line running parallel to the strike through the limestone area (A-B) and along a line crossing the peridotite-marble contact (C-D).

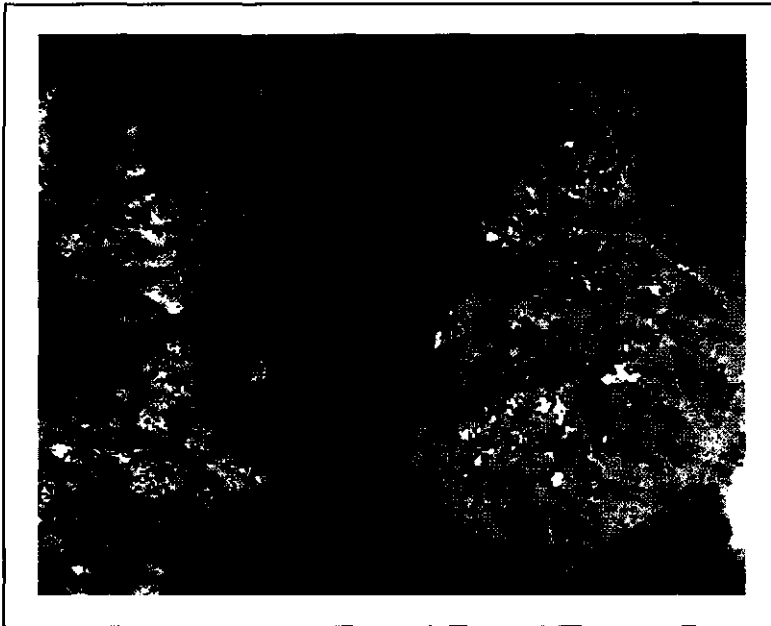


**Plate 5 (Fig. 8.15, page 226):** Mineral map produced by indicator kriging classification showing Kaolinite in red and Alunite in blue.

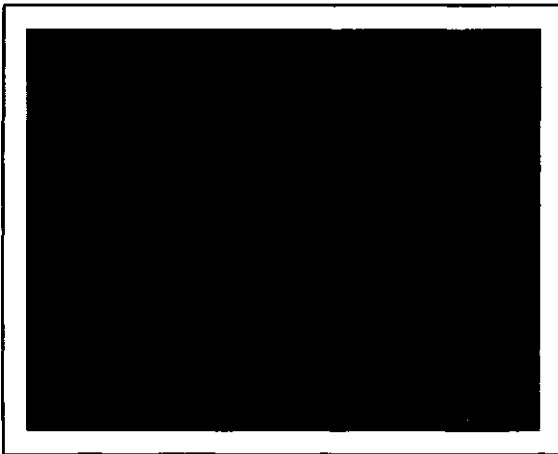


**Plate 6 (Fig. 9.1, page 240):** Color-composite image with the peridotite soil endmember displayed in red, the limestone soil endmember displayed in green, and the spectrally quenched soil endmember displayed in blue.

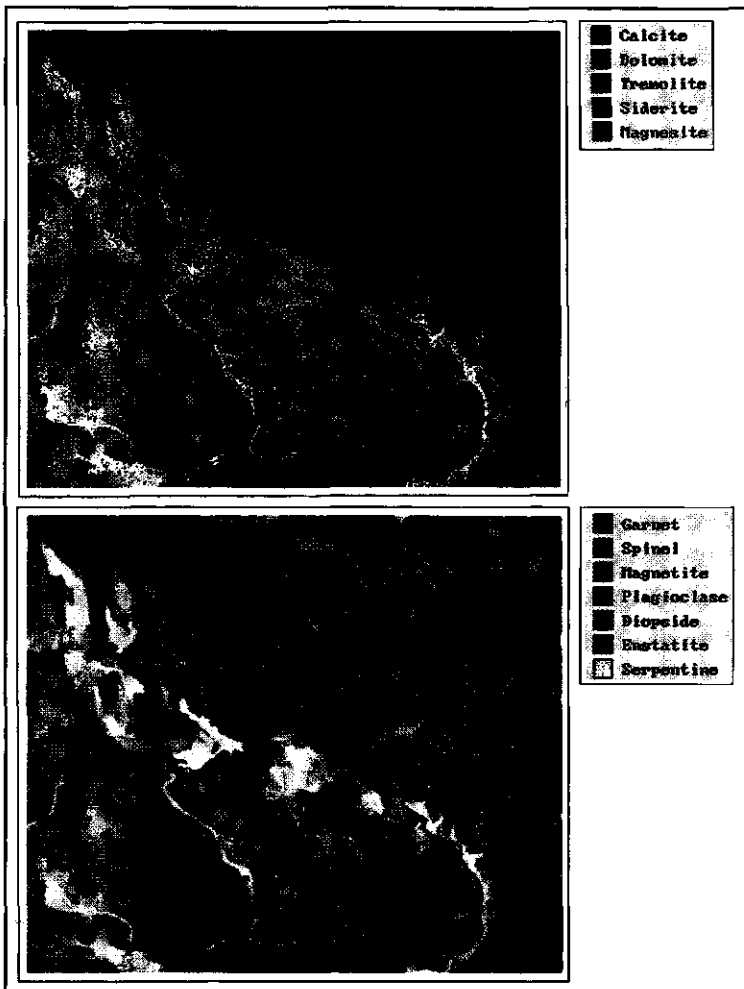


Plate 7 (Fig. 9.5, page 244): GERIS band 30 centered at 1.7099 $\mu$ m with mineral occurrences of major mineral assemblages overlain. Top is the thermal aureole and limestone country rock, bottom is the ultramafic body.